

LIGHT-ACTIVATED PROTIC RUTHENIUM ANTICANCER COMPOUNDS: STRUCTURE
FUNCTION RELATIONSHIPS AND DETERMINING WHICH FACTORS INFLUENCE
TOXICITY

by

JESSICA L. GRAY

ELIZABETH T. PAPISH, COMMITTEE CHAIR
PATRICK A. FRANTOM
YONGHYUN KIM
KEVIN H. SHAUGHNESSY
JOHN B. VINCENT

A DISSERTATION

Submitted in partial fulfillment of the requirements
for the degree of Doctor of Philosophy
in the Department of Chemistry and Biochemistry
in the Graduate School of
The University of Alabama

TUSCALOOSA, ALABAMA

2021

Copyright Jessica L. Gray 2021
ALL RIGHTS RESERVED

ABSTRACT

While research in the field of metallo-based chemotherapy drugs is extensive, understanding the effects of pH responsive ligands within these systems is limited. In 2017, the Papish group reported a new class of pH sensitive light-activated metallo drugs that are activated by light-triggered ligand dissociation also known as PACT or photoactivated chemotherapy. Three ruthenium complexes of the type $[(N,N')_2Ru(6,6'\text{-dhbp})]Cl_2$ (the photolabile ligand 6,6'-dhbp = 6,6'-dihydrobipyridine; **1_A**: N,N' = 2,2'-bipyridine (bpy) ; **2_A**: N,N = 1,10-phenanthroline (phen); **3_A**: N,N = 2,3-dihydro-[1,4]dioxino[2,3-f][1,10]phenanthroline (dop)) were synthesized and found to be toxic against various breast cancer cell lines upon irradiation ($\lambda = 450\text{ nm}$) with compound **3** eliciting EC_{50} values as low as $4\ \mu\text{M}$. Phototoxicity indices with **3** were as high as 120, which shows that dark toxicity is limited. The complexes exhibited low overall photodissociation (Φ_{PD}) despite good toxicity suggesting the mode of toxicity is not through a PACT driven pathway. Discussed herein, are the efforts to study the mode of action, physical properties, and which characteristics have the largest impact on light driven toxicity for compounds **1-3** and further investigation into newly developed compounds.

The hydrophobicity ($\text{Log}(D_{o/w})$) and uptake properties of **1-3** are reported. Due to the presence of the protic ligand, 6,6'-dhbp, all of the complexes studied increase in hydrophobicity with pH with **3** being the most hydrophobic (**3**>**2**>**1**). Cellular studies have demonstrated that passive diffusion is the dominant pathway for cellular uptake and compound **3** accumulates in the nuclei of cancer cells (MCF7, MDA-MB-231, and HeLa); however it competes with active transport out of the cell (efflux). Subsequent research has shown that an increase in

photodissociation does not result in an increase in toxicity and the primary mode of toxicity is likely via the production of singlet oxygen ($^1\text{O}_2$); a process known as photodynamic therapy (PDT). Singlet oxygen quantum yields (Φ_Δ) were higher for **1-3** upon deprotonation with values as high as 0.87(9) for complex **2**. New complexes are also reported which demonstrate improved Φ_Δ 's, toxicity, and light selectivity against breast cancer cells demonstrating the importance of studying protic anticancer metallo drugs.

DEDICATION

To my parents, David and Trisha, and my countless friends who have been there for the good times and the bad and without whom I would not be the person I am. Thank you.

LIST OF ABBREVIATIONS AND SYMBOLS

$^1\text{O}_2$	Singlet Oxygen
^3MC	Triplet Metal Centered Excited State
4,4'-dhbp	4,4'-dihydroxy-2,2'-bipyridine
5-CNU	5-Cyanouracil
5-FU	5-Fluorouracil
6,6'-dhbp	6,6'-dihydroxy-2,2'-bipyridine
6,6'-dmbp	6,6'-dimethoxy-2,2'-bipyridine
Å	Angstrom
BPhen	Bathophenanthroline (AKA DIP)
BPS	Bathophenanthrolinedisulfonic Acid
bpy	Bipyridine
CW-EPR	Continuous Wave Electron Paramagnetic Resonance
°	Degree
DI H ₂ O	Deionized Water
DMSO	Dimethyl Sulfoxide
DNA	Deoxyribose Nucleic Acid
dop	2,3-Dihydro-[1,4]dioxino[2,3-f][1,10]phenanthroline
DPBF	1,3-Diphenylisobenzofuran
EC ₅₀	Concentration of a drug that gives half-maximal response

EPR	Electron Paramagnetic Resonance
ESI-MS	Electrospray Ionization Mass Spectrometry
FDA	Food and Drug Administration
h	hour
IC ₅₀	Concentration of an inhibitor at which 50 % inhibition in its activity is achieved
ICP-MS	Inductively Coupled Plasma Mass Spectrometry
IR	Infrared
Log P	Partition Coefficient
Log(D _{o/w})	Distribution Coefficient
M	Molar
m/z	Mass to Charge Ratio
MALDI-ToF	Matrix-assisted Laser Desorption/Ionization Time of Flight Mass Spectrometry
MFI	Mean Fluorescence Intensity
MHz	Megahertz
μM	Micro Molar
min	minute
mM	Millimolar
NIH	National Institutes of Health
nm	Nanometer
NMR	Nuclear Magnetic Resonance
NSF	National Science Foundation
PACT	Photoactivated Chemotherapy
PBS	Phosphate-buffered Saline

PCT	Photochemotherapy
PDT	Photodynamic Therapy
pH	Potential of Hydrogen
pH _e	Extracellular pH
phen	1,10-Phenanthroline
PI	Phototoxicity Index
pK _a	Log of Ionization Constant
ppm	NMR Chemical Shift
RGC	Research Grants Committee
ROS	Reactive Oxygen Species
SOSG	Singlet Oxygen Sensor Green
TEMP	2,2',6,6'-Tetramethylpiperdine
tpy	2,2':6',2''-Terpyridine
TR-NIR	Time Resolved Near IR
UCRA	Undergraduate Creativity and Research Academy
UV-Vis	Ultraviolet-Visible Spectroscopy
X _A	The fully protonated [Ru] ²⁺ form of a complex
X _B	The fully deprotonated [Ru] ⁰ form of a complex
λ _{max}	Wavelength at which the maximum luminescence is observed
XRD	X-Ray Diffraction
Φ _{LUM}	Quantum Yield of Luminescence
Φ _{PD}	Quantum Yield of Photodissociation
Φ _Δ	Quantum Yield of Singlet Oxygen Production

ACKNOWLEDGEMENTS

Thank you to all my family, friends, and countless mentors who have helped me achieve a great deal and become the chemist I am today. I would like to extend a special thanks to my advisor Dr. Elizabeth Papish who has taught me a great deal and to my great friends and mentors, Dr. Deidra Gerlach and Dr. Sopheavy Siek, who guided me in becoming a true researcher, listened to me vent, and are the best Christmas cookies decorators of all time.

I would also like to thank my committee members Dr. Frantom, Dr. Kim, Dr. Shaughnessy, and Dr. Vincent for their guidance and support through graduate school. Dr. Kim especially has been an invaluable mentor and collaborator. Special thanks, also, go to Dr. Molly Lockart of the Bowman group, Mike Idhe of the Bonizzoni group, and Courtney Peterson of the Thompson for helping me with EPR and fluorescence measurements.

Special thanks go to Dr. Ken Belmore, Dr. Qiaoli Liang, and Dr. Fengrui Qu for their help and guidance on NMR, mass spectrometry, and XRD respectively.

Thank you to the University of Alabama Graduate Council Writing Fellowship for support as well as the NIH (R15-GM132803-01), National Science Foundation EPSCoR Track 2 Grant (OIA-1539035), the Undergraduate Creativity and Research Academy (UCRA) at UA, the Research Grants Committee (RGC) at UA, and the Alabama Commission on Higher Education Fellowship (to S.P.).

CONTENTS

ABSTRACT	ii
DEDICATION	iv
LIST OF ABBREVIATIONS AND SYMBOLS	v
ACKNOWLEDGEMENTS	viii
LIST OF TABLES	xv
LIST OF FIGURES	xviii
LIST OF SCHEMES	xxiii
LIST OF COMPOUNDS	xxiv
CHAPTER 1: INTRODUCTION	1
1.1 Abstract	1
1.2 Introduction	2
1.3 Summary of Dissertation	15
References	20
CHAPTER 2: CELLULAR UPTAKE OF PROTIC RUTHENIUM COMPLEXES IS INFLUENCED BY pH DEPENDENT PASSIVE DIFFUSION AND ENERGY DEPENDENT EFFLUX	27
2.1 Abstract	27

2.2 Introduction	28
2.3 Results and Discussion	31
2.3.1 Interpreting Log(D _{o/w}) values in terms of the pK _A values and the lipophilicity of each species	31
2.3.2 Variations in the pH External (pH _e) of the Cell Lines Studied and Implications for the Mechanism of Cellular Uptake.....	36
2.3.3 Cellular uptake and efflux mechanism for complex 3	37
2.3.4 Subcellular localization of the ruthenium complex 3	41
2.4 Conclusion	43
2.5 Materials and Methods	44
2.6 Acknowledgements	48
References	49
Appendix	52
CHAPTER 3: EFFORTS TOWARDS INCORPORATING A CYTOTOXIC LIGAND INTO RUTHENIUM COMPLEXES.....	60
3.1 Abstract	60
3.2 Introduction	61
3.3 Results and Discussion	64
3.3.1 Incorporating 5-Fluorouracil	64
3.3.2 Incorporating 5-Cyanouracil	67
3.4 Conclusion	73

3.4.1 Incorporating 5-Fluorouracil	73
3.4.2 Incorporating 5-Cyanouracil	74
3.5 Materials and Methods	75
3.5.1 Synthesis of ruthenium 5-FU complexes	75
3.5.2 Synthesis of ruthenium 5-CNU complexes	77
References	79
CHAPTER 4: INVESTIGATING MODE OF ACTION FOR RUTHENIUM COMPLEXES: MEASURING SINGLET OXYGEN PRODUCTION AND LUMINESCENT PROPERTIES	83
4.1 Abstract	83
4.2 Introduction	84
4.3 Results and Discussion	89
4.3.1 Detecting $^1\text{O}_2$ with EPR/TEMP	89
4.3.2 Detecting $^1\text{O}_2$ with UV-Vis/DPBF	93
4.3.3 Detecting $^1\text{O}_2$ with fluorescence/SOSG	95
4.3.4 Direct Detection of $^1\text{O}_2$ and Singlet Oxygen Quantum Yields	97
4.3.5. Development of new Protic Ru(II) PDT Complexes	98
4.3.6 Luminescent Measurements of compound 2	103
4.4 Conclusions	106
4.5 Materials and Methods	107

4.5.1 General Synthetic and Characterization Methods	107
4.5.2 Typical synthesis of 1B-3B	108
4.5.3 Singlet Oxygen Measurement via EPR/TEMPO	109
4.5.4 Singlet Oxygen Measurement Via UV-Vis/DPBF	109
4.5.5 Fluorescence/SOSG	109
4.5.6 Singlet Oxygen Quantum Yield Measurements	110
4.5.7 General Photodissociation Procedure for compounds 8_A and 3_A	110
4.5.8 Luminescence Measurements of compound 2	111
4.5.9 EC ₅₀ Measurements of Compound 8	111
References	112
Appendix	117
 CHAPTER 5: DEVELOPMENT OF NEW RUTHENIUM PDT AGENTS CONTAINING BATHOPHENANTHROLILNEDISULFONIC ACID AND BATHOPHENANTHROLINE LIGANDS	 135
5.1 Abstract	135
5.2 Introduction	136
5.3 Results and Discussion	139
5.3.1 Synthesis and Characterization of [(BPS) ₂ Ru(6,6'-dhbp)]Na ₂ (9_A)	139
5.3.2. Synthesis and Characterization of [(BPhen) ₂ Ru(6,6'-dhbp)]Cl ₂ (10_A) and [(BPhen) ₂ Ru(4,4'-dhbp)]Cl ₂ (11_A)	144

5.4 Conclusion	152
5.5 Materials and Methods	152
5.5.1 Synthesis of [(BPS) ₂ RuCl ₂]]Na ₄	152
5.5.2 Synthesis of [(BPS) ₂ Ru(6,6'-dhbp)]Na ₂ (9_A)	153
5.5.3 Synthesis of <i>trans</i> -(BPhen) ₂ RuCl ₂	153
5.5.4 Synthesis of [(BPhen) ₂ Ru(6,6'-dhbp)]Cl ₂ (10_A) & [(BPhen) ₂ Ru(4,4'-dhbp)]Cl ₂ (11_A)	154
5.5.5 EC ₅₀ measurements	155
References	156
CHAPTER 6: CRYSTAL STRUCTURE OF (PERCHLORATO- κ O)(1,4,7,10-TETRAAZACYCLODODECANE- κ^4 N)COPPER(II) PERCHLORATE	159
6.1 Abstract	159
6.2 Chemical Context	159
6.3 Structural Commentary	160
6.4 Supramolecular Features	161
6.5 Database Survey	162
6.6 Synthesis and Crystallization	163
6.7 Refinement	165
Acknowledgements	166

References	167
Appendix.....	169
CHAPTER 7: CONCLUSIONS AND FUTURE WORK.....	176
7.1 Summary of Findings and Future Works	176
7.2 Closing Remarks	180
References	181

LIST OF TABLES

1.1 Cell Viability Data for Complexes 1-3	12
1.2 Φ_{PD} and pK_A data for compounds 1-3	12
1.3 Φ_{PD} and EC_{50} Data for Compounds 2, 3, 2^{OMe} , and 3^{OMe}	13
2.1 Thermodynamic Acidity Data for Compounds 1, 2, and 3	30
2.2 Cell Viability Data for 1-3	31
2.3. $\text{Log}(D_{o/w})$ Values for Compounds 1, 2, and 3	32
2.4 Estimated $\text{Log}(D_{o/w})$ Values for Protonation States of 1, 2, and 3	35
2.5 The Change in pH_e over 48 h in Various Cell Lines and Uptake of Complex 3	37
2.6 Residual Sum of Squares for Complexes 1-3	46
2A.1 Molar Absorptivity Data for Complexes 1, 2, and 3	56
2A.2 $\text{Log}(D_{o/w})$ Data for 5-FU	57
2A.3 $\text{Log}(D_{o/w})$ Data for 1	58
2A.4 $\text{Log}(D_{o/w})$ Data for 2	58
2A.5 $\text{Log}(D_{o/w})$ Data for 3	58
4.1 Φ_{PD} , Toxicity, and pK_a Data for 2, 3, 2^{OMe} , and 3^{OMe}	86

4.2 Φ_{Δ} Data for 1-3 , 2^{OMe} , and 3^{OMe}	98
4.3 Selected Bond Lengths and Angles for 8_A	100
4.4 Φ_{Δ} Data for Complexes 1-3 and 8 in Acetonitrile	101
4A.1 Crystal Data for 8_A	123
4A.2 Data Collection for 8_A	123
4A.3 Refinement Information for 8_A	124
4A.4 Fractional Atomic Coordinates & Isotropic Displacement Parameters	124
4A.5 Atomic Displacement Parameters	127
4A.6 Geometric Parameters	129
4A.7 Hydrogen Bond Geometry	134
5.1 EC ₅₀ and PI Data for 10 & 11 Against Breast Cell Lines	152
6.1 Hydrogen Bond Geometry	162
6.2 Summary of Experimental Details	165
6A.1 Crystal Data	169
6A.2 Data Collection	170
6A.3 Refinement	170
6A.4 Fractional Atomic Coordinates & Isotropic Displacement Parameters	170
6A.5 Atomic Displacement Parameters	172

6A.6 Geometric Parameters173

LIST OF FIGURES

1.1 Structures of Current Chemotherapy Drugs	4
1.2 Structures of <i>trans</i> -Phototrexate and <i>cis</i> -Phototrexate	6
1.3 Structures of Ru(II) PCT agents studied by Turro and Dunbar	8
1.4 Structures of Ru(II) Dyads Studied by McFarland	9
1.5 Structures of Ru Complexes to Enter Clinical Trials	10
1.6 Complexes 1_A - 3_A Studied by Papish et al. <i>Inorg. Chem.</i> 2017	11
1.7 Uptake of 1-3 measured by ICP-MS	15
2.1 Log($D_{o/w}$) as a function of pH data for 1	33
2.2 Log($D_{o/w}$) as a function of pH data for 2	34
2.3 Log($D_{o/w}$) as a function of pH data for 3	35
2.4 Flow Cytometry Data for MCF10A, MCF7, MDA-MB-231, and HeLa cell lines	38
2.5 Cellular Uptake of 3 as a function of MFI	39
2.6 Light Induced Uptake of 3 Measured by Flow Cytometry	40
2.7 Uptake of 3 under metabolic inhibition conditions	41
2.8 Cellular Localization of 3	42

2A.1 Plotted Log($D_{o/w}$) residuals for complex 1	52
2A.2 Plotted Log($D_{o/w}$) residuals for complex 2	53
2A.3 Plotted Log($D_{o/w}$) residuals for complex 3	53
2A.4 UV-Vis spectra of 1 at pH 6.00 in Pre-Saturated 0.1M Phosphate Buffer	54
2A.5 ϵ Plot of 1 in pH 6.00 in Pre-Saturated 0.1M Phosphate Buffer	55
2A.6 ϵ Plot of 5-FU in pH 7.40 in Pre-Saturated 0.1M Phosphate Buffer	56
2A.7 Localization of Complex 3 (5 μ M) in MCF10A	59
3.1 PACT Reaction Pathway for 1-3	62
3.2 PACT Mechanism for 4 & 5	63
3.3 Structures of 5-CNU Complexes	64
3.4 ^{19}F NMR Spectrum of Reaction Solution 1	65
3.5 Structures of 4 and 5	65
3.6 MALDI-ToF Mass Spectrum of 4	66
3.7 ^{19}F NMR Spectrum of Reaction Solution 2	67
3.8 ^1H NMR Spectrum of the Crude Complex, 6	70
3.9 XRD Crystal Structure of 7	70
3.10 IR Spectrum of 7	71
3.11 ESI-MS (positive mode, $[\text{M}]^+$) Spectrum of 7	71

3.12. ^1H NMR Spectrum of Crude Product Mixture, 6 and 7	73
4.1 Reaction Between $^1\text{O}_2$ and TEMP to form TEMPO	87
4.2 UV-Vis Spectrum of DPBF Upon Reacting with $^1\text{O}_2$	88
4.3 Aerobic and Anerobic CW-EPR Spectra of 3_A and TEMP in Ethanol	90
4.4 CW-EPR Spectrum (+)-Control of $[\text{Ru}(\text{bpy})_3]^{2+}$	91
4.5 Electron Transfer Oxidation of TEMP to TEMPO	92
4.6 UV-Vis Spectra of 3_A (1 μM) and DPBF (100 μM) in Ethanol	94
4.7 UV-Vis Spectra: (-)-Control of DPBF	94
4.8 Fluorescence Control of SOSG and $[\text{Ru}(\text{bpy})_3]^{2+}$	96
4.9 Fluorescence of SOSG and 2 at pH 8.0	97
4.10 XRD Structure of 8_A vs 3_A	100
4.11 ^1H NMR Spectrum of $[(\text{dop})_2\text{Ru}(4,4'\text{-dhbp})]^{2+}$ (8_A) in DMSO- $[\text{d}_6]$	101
4.12 UV-Vis Spectra of Photodissociation of 8_A vs 3_A in Methanol	102
4.13 Jablonski Diagram of Light Emissive Relaxation Pathways	104
4.14 Emission Spectra of 2_A	104
4.15 Emission Spectra of 2_B	105
4.16 Emission Spectra of 2_A and 2_B in diH ₂ O	105
4A.1 UV-Vis Spectra of Photodissociation of 8_B in Methanol	118

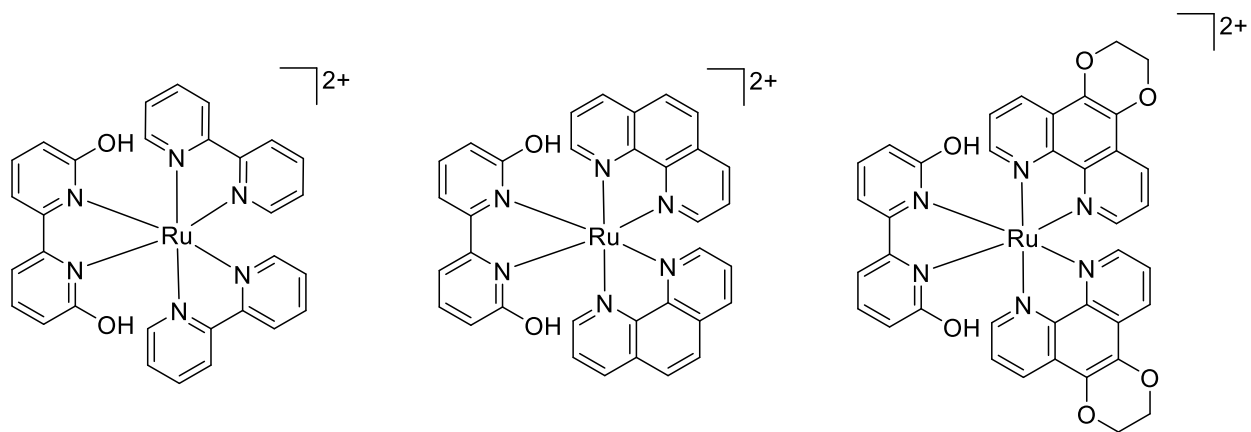
4A.2 UV-Vis Spectra of Photodissociation of 2_B at pH 8.0 with White Light	119
4A.3 Free Energy Diagram for 2_A & 3_A	120
4A.4 Orbital Depiction of ³ MC for 2_A	121
4A.5 Free Energy Diagram for 2_B & 3_B	121
4A.6 Simulated vs Experimental UV-Vis Spectra for 2 & 3	122
4A.7 Unit cell of 8_A as viewed along the <i>a</i> axis	123
5.1 Structures of BPS and BPhen Ru(II) Complexes, Including 9_A - 11_A	137
5.2 Structures of BPhen Complexes in the Literature	138
5.3 ¹ H NMR Spectrum of [(BPS) ₂ RuCl ₂] ⁴⁺ Intermediate in DMSO-[d ₆]	141
5.4 2D COSY ¹ H NMR Spectrum of [(BPS) ₂ Ru(6,6'-dhbp)] ²⁻ (9_A) in DMSO-[d ₆]	142
5.5 ESI-MS Spectrum of [(BPS) ₂ Ru(6,6'-dhbp)]Na ₂ (9_A)	143
5.6 UV-Vis Spectra of Photodissociation of [(BPS) ₂ Ru(6,6'-dhbp)] ²⁻ (9_A) diH ₂ O	144
5.7 ¹ H NMR Spectrum of [(BPhen) ₂ Ru(4,4'-dhbp)]Cl ₂ (11_A) in DMSO-[d ₆]	146
5.8 ¹ H NMR Spectrum of [(BPhen) ₂ Ru(6,6'-dhbp)]Cl ₂ (10_A) in DMSO-[d ₆]	147
5.9 2D COSY ¹ H NMR Spectrum of [(BPhen) ₂ Ru(6,6'-dhbp)]Cl ₂ (10_A) in DMSO-[d ₆]	148
5.10 XRD Crystal Structure of [(BPhen) ₂ Ru(6,6'-dhbp)] ²⁺ (10_A)	149
5.11 ESI-MS Spectrum of [(BPhen) ₂ Ru(6,6'-dhbp)] ²⁺ (10_A)	149
5.12 EC ₅₀ data plots for complexes 10 & 11	151

6.1 Chemdraw figure of [Cu(1,4,7,10-tetraazacyclododecane)](ClO ₄) ₂	160
6.2 Top and side view of the isolated [Cu(cyclen)](ClO ₄) ₂	161
6.3 Unit cell of the isolated [Cu(cyclen)](ClO ₄) ₂	162
6.4 A view of hydrogen bonding within a dimer pair	163
6.5 Packing of the complex cations, as viewed along the <i>c</i> axis of the unit cell	164
6.6 Hydrogen bonding between complex cations and anions, as viewed along the <i>c</i> axis	164

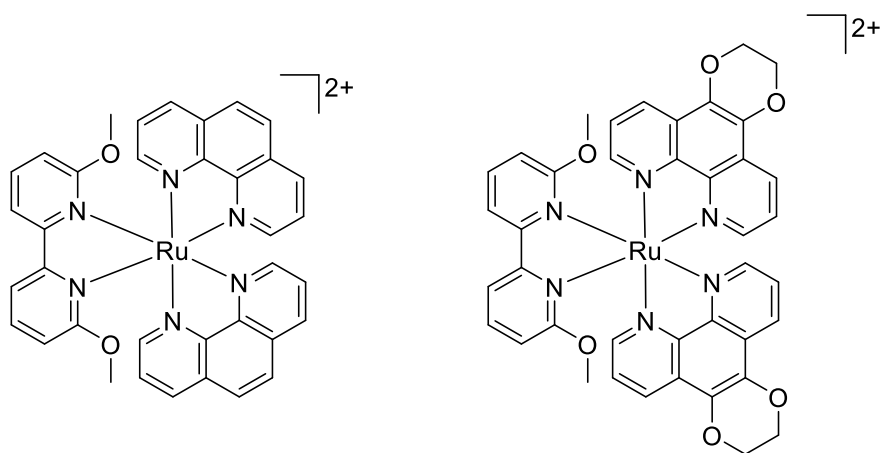
LIST OF SCHEMES

1.1 Relation Between PDT and PACT Pathways	6
2.1 Protonation/Deprotonation Pathway for Complexes 1 , 2 , and 3	29
3.1 Proposed Scheme Adapted from Shobana et al.	64
3.2 Synthesis of [(Ru(bpy) ₂ (thiouracil)](ClO ₄) ₂ Described by Lahiri et al.	67
3.3 Proposed Synthesis Route for 6	68
3.4 Synthesis Scheme for 4 and 5	75
4.1 Formation of ROS by Type I and II Processes	84
4.2 How Structural Changes Affect PDT and PACT Pathways	107
5.1 Synthesis of [(BPS) ₂ Ru(6,6'-dhbp)]Na ₂ (9_A)	140
5.2 Synthesis of [(BPhen) ₂ Ru(6,6'-dhbp)]Cl ₂ (10_A) and [(BPhen) ₂ Ru(4,4'-dhbp)]Cl ₂ (11_A)	145

LIST OF COMPOUNDS

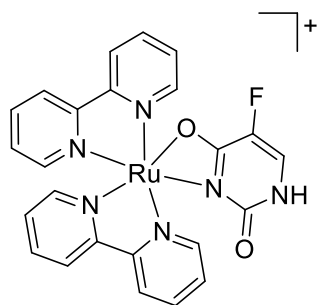


1_A: [(bpy)₂Ru(6,6'-dhbp)]Cl₂ **2_A**: [(phen)₂Ru(6,6'-dhbp)]Cl₂ **3_A**: [(dop)₂Ru(6,6'-dhbp)]Cl₂

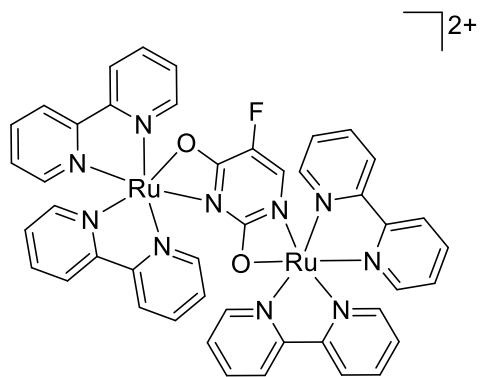


2^{OMe}: [(phen)₂Ru(6,6'-dmbp)]Cl₂

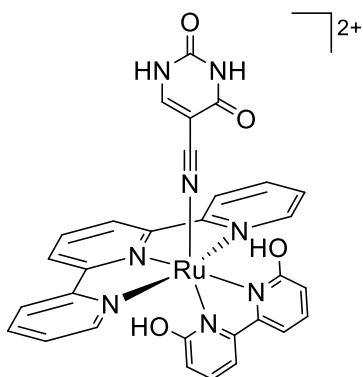
3^{OMe}: [(dop)₂Ru(6,6'-dmbp)]Cl₂



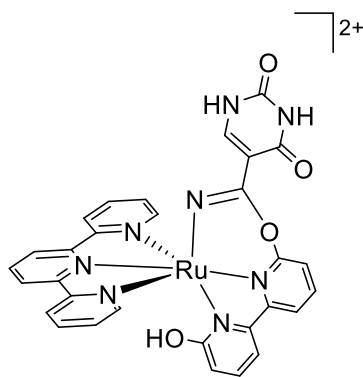
4: [(bpy)₂Ru(5-FU)](ClO₄)



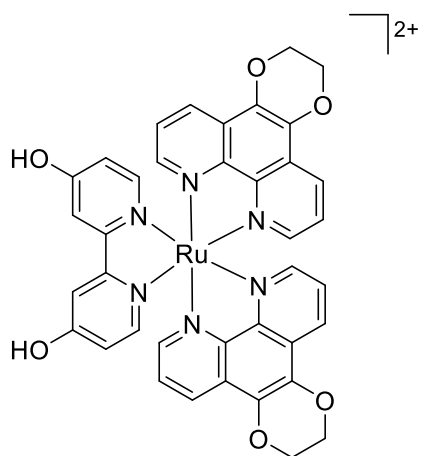
5: [((bpy)₂Ru)₂(5-FU)](ClO₄)₂



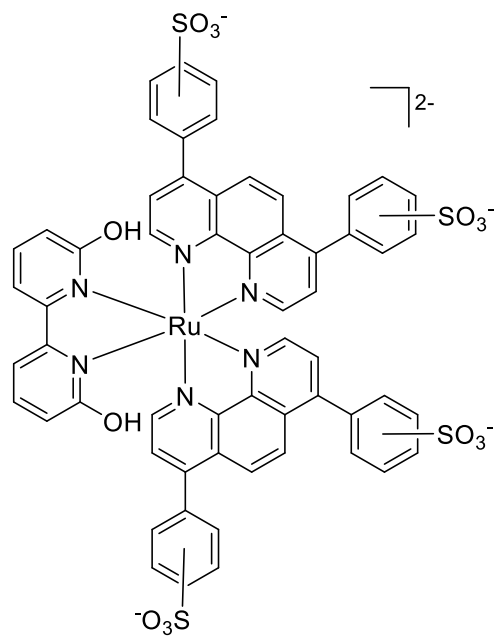
6: [(tpy)Ru(5-CNU)(6,6'-dhbp)](PF₆)₂



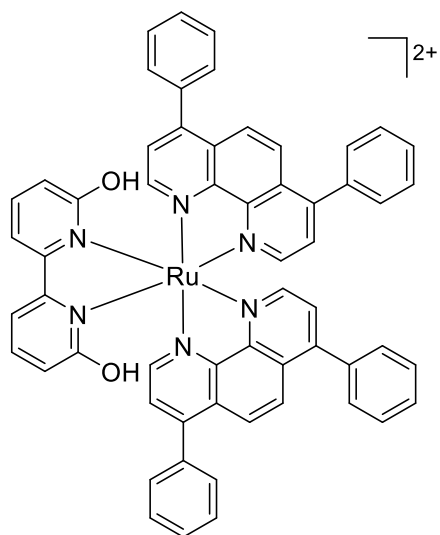
7: [(tpy)Ru(dhbp-CNU)](PF₆)₂



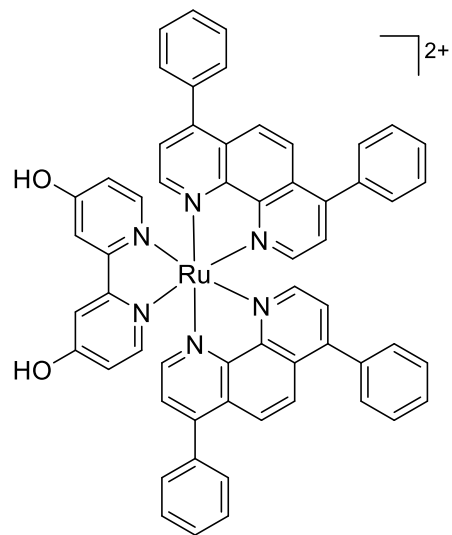
8A: [(dop)₂Ru(4,4'-dhbp)Cl₂]



9A: [(BPS)₂Ru(6,6'-dhbp)Na₂]



10A: [(BPhen)₂Ru(6,6'-dhbp)Cl₂]



11A: [(BPhen)₂Ru(4,4'-dhbp)Cl₂]

CHAPTER 1

INTRODUCTION

1.1 Abstract

In order to limit off-target side effects of chemotherapy agents, there is a need to develop targeted therapies. While research in the field of metallo-based chemotherapy drugs is extensive, understanding the effects of pH responsive ligands within these systems is limited. In 2017, the Papish group reported a new class of pH sensitive light-activated metallo drugs that are activated by light-triggered ligand dissociation, also known as PACT or photoactivated chemotherapy.¹ Three ruthenium complexes of the type $[(N,N')_2Ru(6,6'\text{-dhbp})]^{2+}$ were synthesized, characterized, and tested for cytotoxicity in cell culture (**1_A**: N,N' = 2,2'-bipyridine (bpy) and 6,6'-dhbp, the photolabile ligand, = 6,6'-dihydroxybipyridine; **2_A**: N,N = 1,10-phenanthroline (phen); **3_A**: N,N = 2,3-dihydro-[1,4]dioxino[2,3-f][1,10]phenanthroline (dop)). Due to 6,6'-dhbp's ability to transition between protonation states, the various species are denoted with the subscript A (**X_A**) for the fully protonated, $[Ru]^{2+}$ complex while the doubly deprotonated species ($[Ru]^0$) is denoted with the subscript B (**X_B**). All complexes have higher quantum yields of photodissociation (Φ_{PD} , λ of irradiation = 450 nm) when fully protonated (**X_A**) ; however, the overall Φ_{PD} was low for all complexes (and all protonation states). Despite limited photodissociation, all complexes had improved cytotoxicity upon irradiation. Complex **3** is the most cytotoxic complex of this series with EC₅₀ values as low as 4 μ M (with blue light, λ = 450

nm) versus two breast cancer cell lines. Phototoxicity indices ($PI = EC_{50 \text{ dark}}/EC_{50 \text{ light}}$) with **3** were as high as 120, which shows that dark toxicity is limited. Subsequent studies on analogous complexes show that increasing Φ_{PD} does not yield an increase in toxicity suggesting the mode of toxicity is not through a PACT driven pathway.² Uptake was measured by inductively coupled plasma mass spectrometry (ICP-MS), but no clear trend was found between uptake and toxicity. Further work is needed to determine the mode of toxicity, mode of uptake, and which characteristics have the greatest influence on toxicity in order to develop more potent light-activated ruthenium anticancer drugs.

1.2 Introduction

Cancer is a disease characterized by out of control cellular growth and spread that has been known to affect almost any portion of the body. While cancer has been present throughout human history, some of the earliest cases have been documented back to ancient Egypt in which mummified remains exhibited growths characteristic of osteosarcoma, a form of bone cancer.³ As scientists developed a better understanding of medicine, they were also able to improve their understanding of cancer and develop potential treatments. It was not until the 18th century in which the Scottish surgeon, John Hunter, suggested that cancer may be treated by surgical removal of tumors; however, this technique was not widely used in practice until further advancements in anesthesiology were made.³ Advancements in cancer treatment has improved greatly over the past 120 years including the development of radiation, hormone therapy, and chemotherapy treatments, however, an outright “cure” still remains elusive due to the multitude of risk factors that contribute to cancer and its ability to mutate.

According to the American Cancer Society, approximately 42 % of newly diagnosed cancers in the US in 2020 could have been prevented by limiting external risk factors such as

smoking, obesity, and UV exposure.⁴ Limiting exposure to these risk factors will reduce an individual's chance of getting cancer; however, genetic abnormalities may lead to an increase risk of other cancers such as leukemia, colorectal, and breast cancers. In some cases, these abnormalities can be detected or screened for, increasing the likelihood of early detection. Despite all preventative measures taken, it is estimated that there will still be 1.8 million new cases of cancer in the United States in 2020 with many of those requiring treatment.

Many treatments still used today were developed within the last century of oncology research. In the 1940s and 50s, a folic acid derivative, methotrexate, was developed (formerly known as amethopterin, Figure 1.1) for the treatment of leukemia and is widely considered to be one of the first chemotherapy agents.⁵⁻⁸ Not long after, Rosenberg and co-workers discovered that the platinum containing complex, cisplatin, had the ability to inhibit cell division in *E. coli* cells and later correctly hypothesized that this could be used to inhibit cell division in cancer.⁹

Metal complexes have at least one advantage over organic based chemotherapies like methotrexate: new derivatives can be more rapidly synthesized by replacing the ligands of the parent complex and the typical syntheses of metal complexes are only a few steps. This approach was used to develop a new generation of Pt-based chemotherapies including carboplatin, dicycloplaton, and oxaliplatin, which are all currently in use today (Figure 1.1).¹⁰ Many of the platinum complexes in use and in trials are able to kill cancer cells via interactions with DNA while methotrexate kills cells via metabolic inhibition.⁹⁻¹² While effective at killing cancer cells, both methotrexate and Pt-based drugs have serious side effects associated with their use.

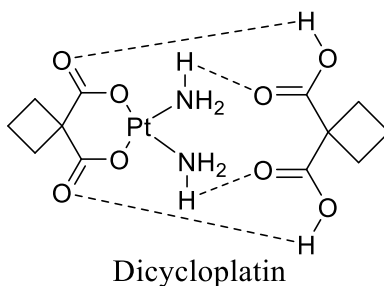
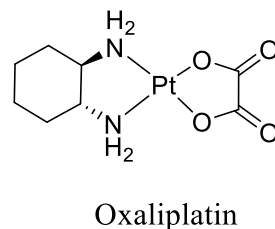
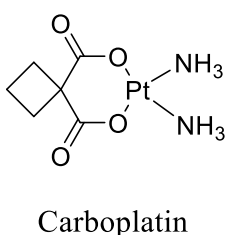
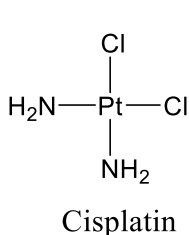
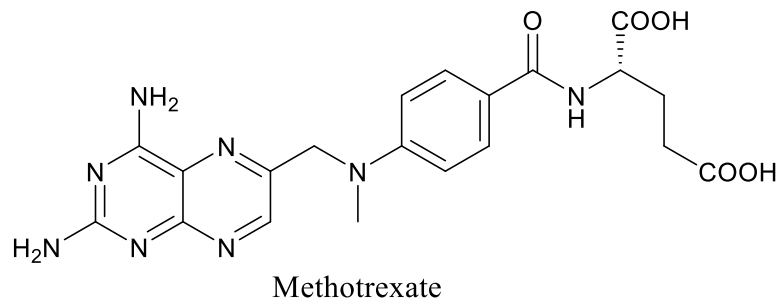
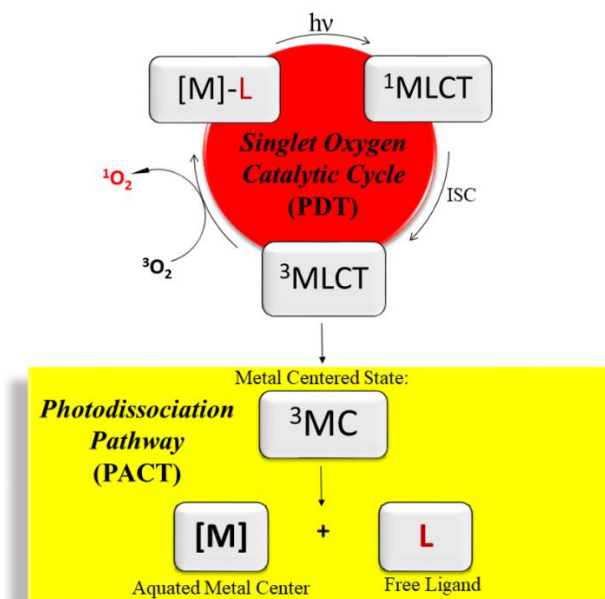


Figure 1.1. Structures of several early chemotherapies that were developed in the last century and still in use today. Methotrexate is a metabolism inhibitor while most Pt-based chemotherapies kill cancer cells via interactions with DNA.

One of the greatest challenges with developing new chemotherapy treatments is the inherent difficulty in selectively targeting cancer cells. Many treatments take advantage of a cancer cells' unique biological characteristics (such as higher metabolism) but neglect to differentiate between healthy cells that share these characteristics. This typically leads to side effects such as severe nausea, loss of appetite, compromised immune system, and loss of hair. This need to limit off-target effects has driven the development of new targeted therapies.

One promising method of targeted drug delivery involves light induced activation of a drug. This process, called photochemotherapy (PCT), utilizes a specific wavelength of light to elicit a therapeutic effect and only occurs in the immediate area of irradiation allowing for precise spatial delivery of the active drug. PCT can be further classified as two different methods: photoactivated chemotherapy (PACT) or photodynamic chemotherapy (PDT) (Scheme 1.1). PACT is a process that typically produces a stoichiometric amount of active drug upon irradiation while PDT relies on a photosensitizer to produce catalytic amounts of singlet oxygen ($^1\text{O}_2$, a toxic reactive oxygen species) to elicit a toxic effect. Photosensitizers that undergo PACT driven toxicity undergo a physical change, such as ligand loss or isomerization, upon irradiation to yield an active chemotherapy agent and do not require oxygen to function.^{11, 13, 14} As a result, PACT is a potentially useful method to treat some hypoxic tumors. In 2018, Gorostiza and co-workers published a study on a PACT analogue of methotrexate, phototrexate, that was nearly inactive in its relaxed *trans* state while its photoactivated *cis* configuration had efficacy similar to that of methotrexate (Figure 1.2).^{11, 15} Unfortunately, this study has drawbacks. In order to activate the drug, *trans*-phototrexate was irradiated with UV light (375 nm), which has relatively poor tissue penetration making treatment of deep tissue tumors difficult.^{11, 15} Upon activation, the *cis*-phototrexate is relatively unstable and has the ability to revert back to the inactive *trans*-phototrexate, potentially limiting the efficacy of the treatment. Other attempts to develop PACT agents have focused on utilizing metallo drugs that undergo ligand substitution upon irradiation.



Scheme 1.1. Photochemotherapy (PCT) includes PDT and PACT options. The PACT pathway typically results in a structural change of the photosensitizer whether that be ligand loss on a metal complex or isomerization.

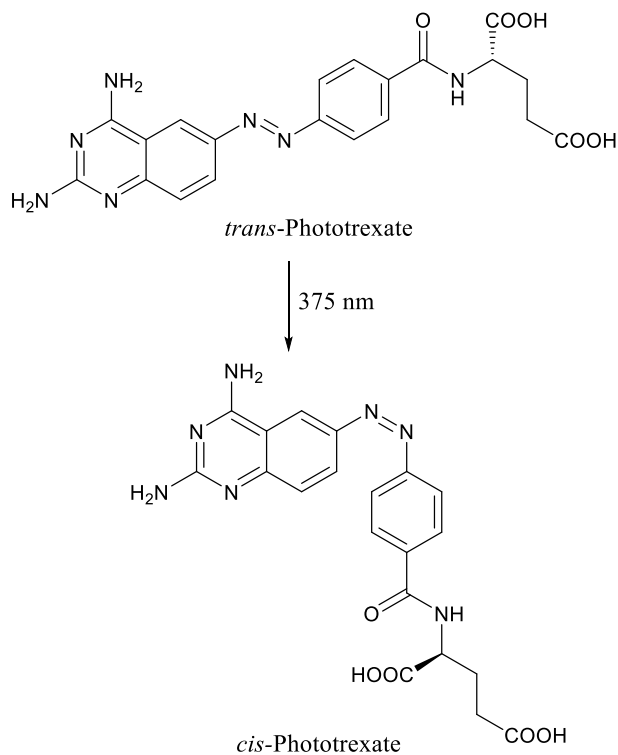


Figure 1.2. Structures of the inactive *trans*-phototrexate, which forms the toxic *cis*-phototrexate upon irradiation with UV light. Adapted from reference 10

Cisplatin and related Pt(II) drugs kill cancer cells via binding to DNA and interrupting cellular transcription; however, they still remain toxic towards healthy cells.¹⁶ This process relies on the ligand substitution and formation of *cis*-[Pt(NH₃)₂(OH)₂]²⁺ from *cis*-[Pt(NH₃)₂Cl₂]. Controlling this substitution with light irradiation can localize the formation and effects of the active drug to a single area, limiting side effects. Ruthenium(II) ammine complexes are well known to undergo photosubstitution upon irradiation and are able to bind to DNA in a fashion similar to that of Pt(II) complexes.¹⁶⁻²² In 2004, Turro et. al published on the complex *cis*-[Ru(bpy)₂(NH₃)₂]²⁺ (bpy = bipyridine) that was able to bind to DNA upon irradiation with efficacy similar to that of cisplatin (Figure 1.3, Turro *Inorg. Chem.* 2004).¹⁶ While this was not the first Ru(II) complex shown to bind to DNA upon irradiation, previously published complexes had used UV light while Turro's study utilized visible light ($\lambda \geq 345$ nm), which can penetrate deeper into tissue.²³⁻²⁵ Turro was then able to build upon this study in a collaboration with Kim Dunbar by developing Ru(II) PACT agents that could not only produce a Ru(II)-aqua adduct that was capable of binding to DNA but would also release the cytotoxic ligand, 5-cyanouracil (5-CNU) (Figure 1.3, Turro, Dunbar *Inorg. Chem.* 2011 & *JACS* 2013).^{26, 27} Those studies demonstrated that it was possible to overcome one of the main limitations of PACT agents: a stoichiometric production of active photoproduct. Further work by Turro and Dunbar produced a Ru(II) complex that was not limited by PACT driven ligand dissociation but was also able to produce singlet oxygen (¹O₂) (PDT) (Figure 1.3, *JACS* 2014).²⁸ This dual pathway complex was toxic in HeLa cells upon irradiation at 466 nm ($EC_{50} = 0.47 \pm 0.02$ μ M, ¹O₂ quantum yield (Φ_{Δ}) = 0.72); however, they found that once the photolabile acetonitrile ligands were substituted for the non-labile bipyridine, singlet oxygen production increased and yielded slightly better toxicity ($EC_{50} = 0.37 \pm 0.06$ μ M, $\Phi_{\Delta} = 0.88(2)$).²⁸

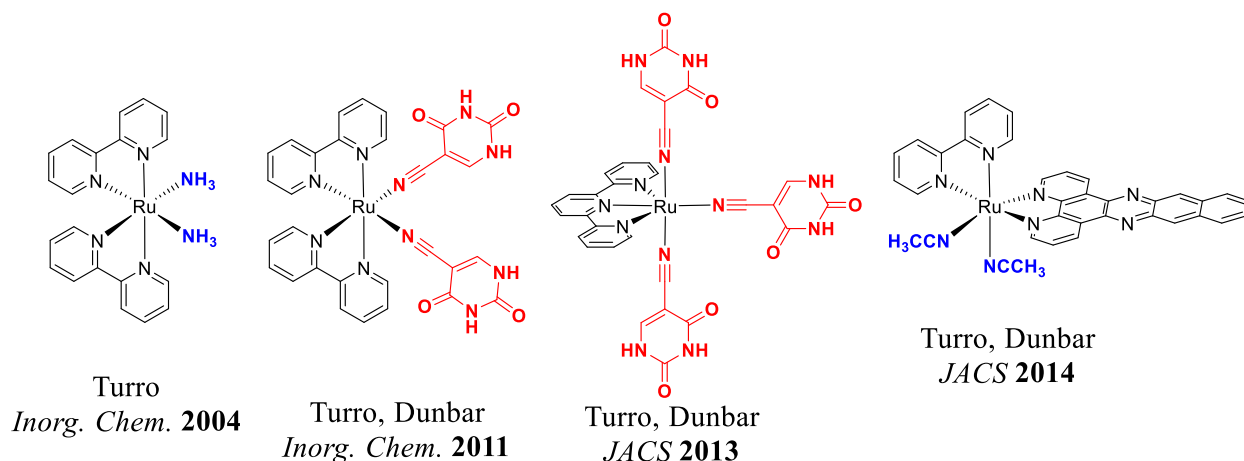


Figure 1.3. Structures of Ru(II) PACT agents studied by Claudia Turro and Kim Dunbar. Ligands highlighted in blue are photolabile while ligands highlighted in red are both photolabile and toxic.

PDT is a method for targeted drug delivery approved by the Food and Drug Administration (FDA). This process utilizes a photosensitizer that is activated after irradiation with a specific wavelength of light and elicits a therapeutic effect via the production of $^1\text{O}_2$.¹³ While Ru(II) complexes have been well documented to photoeject a ligand, they are also efficient producers of singlet oxygen.²⁸⁻³³ $[\text{Ru}(\text{bpy})_3]^{2+}$, for example, is efficient and reliable enough that it is commonly used as a standard for $^1\text{O}_2$ measurement.³⁴ In 2014, Edith Glazer studied two homoleptic Ru(II) polypyridyl complexes that were known $^1\text{O}_2$ generators and found that they were significantly more toxic than cisplatin against Jurkat liver cells ($[\text{Ru}(\text{BPhen})_3]^{2+}$: $\text{EC}_{50} = 0.075 \pm 0.004 \mu\text{M}$, reference chapter 5 for further discussion).³⁵ While significant production of singlet oxygen is beneficial for developing a successful PDT agent, a study by Sherri McFarland demonstrated that other variables may also be impacting toxicity.³⁶ She synthesized and studied the Ru(II) dyads, $[\text{Ru}(\text{bpy})_2(5\text{-PEP})](\text{PF}_6)$ and $[\text{Ru}(\text{bpy})_2(4\text{-PEP})](\text{PF}_6)_2$ (Figure 1.4), and found that, despite being a better producer of singlet oxygen, $[\text{Ru}(\text{bpy})_2(4\text{-PEP})]^{2+}$ was less toxic than $[\text{Ru}(\text{bpy})_2(5\text{-PEP})]^{2+}$ ($\Phi_{\Delta} = 0.87$ in MeCN, $\text{EC}_{50 \text{ light}} = 0.22 \mu\text{M}$ HL60 leukemia cells and $\Phi_{\Delta} = 0.68$, $\text{EC}_{50 \text{ light}} = 0.15 \mu\text{M}$, respectively). $[\text{Ru}(\text{bpy})_2(5\text{-PEP})]^{2+}$ also had

better light toxicity as demonstrated by a phototoxicity index (PI) of 1747 vs 382 for $[\text{Ru}(\text{bpy})_2(4\text{-PEP})]^{2+}$ ($\text{PI} = \text{EC}_{50 \text{ Dark}}/\text{EC}_{50 \text{ Light}}$). She hypothesized that the differences in cellular performance might be attributed to *in vitro* variables such as uptake, subcellular localization, or efflux. McFarland is credited with the development of the only Ru(II) PDT complex currently in human clinical trials.¹⁴

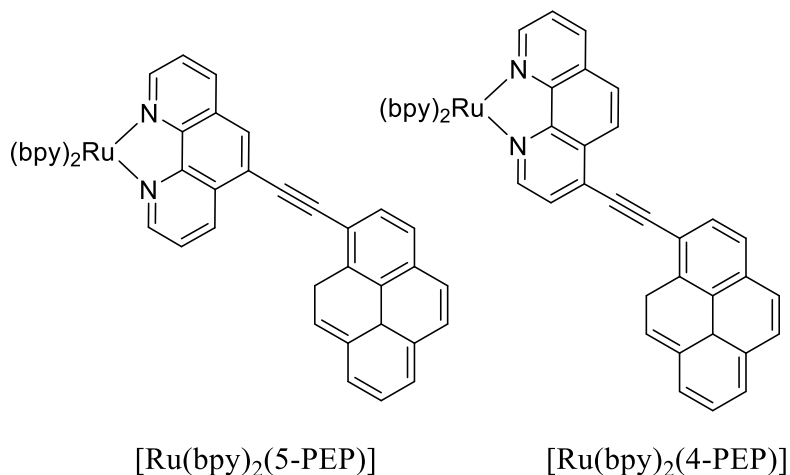


Figure 1.4. Structures of Ru(II) Dyad PDT agents, $[\text{Ru}(\text{bpy})_2(5\text{-PEP})](\text{PF}_6)_2$ and $[\text{Ru}(\text{bpy})_2(4\text{-PEP})](\text{PF}_6)_2$ studied by McFarland. Adapted from reference 35. PF_6 omitted for clarity.

While research has advanced the development of ruthenium anticancer agents, to date, there are only a handful of successful candidates to enter human clinical trials. Only two Ru(III) complexes (NAMI-A and NKP-1339/IT-139/BOLD-100), which are not light activated, have advanced to clinical trials (Figure 1.5).³⁷⁻⁴⁰ NAMI-A, an antimetastatic agent, has since been abandoned after a Phase 2 study did not yield the desired efficacy⁴⁰ while IT-139 (formerly NKP-1339 but currently BOLD-100) has advanced to a Phase 2 study.³⁹ Only one light activated ruthenium compound has advanced in human clinical trials. TLD-1433 is a Ru(II) light-triggered complex being utilized as a PDT agent to treat non-muscle invasive bladder cancer (NMIBC).^{41, 42}

This complex has shown great promise, produces $^1\text{O}_2$ at near quantitative efficiency, and is currently in phase 2 clinical trials.

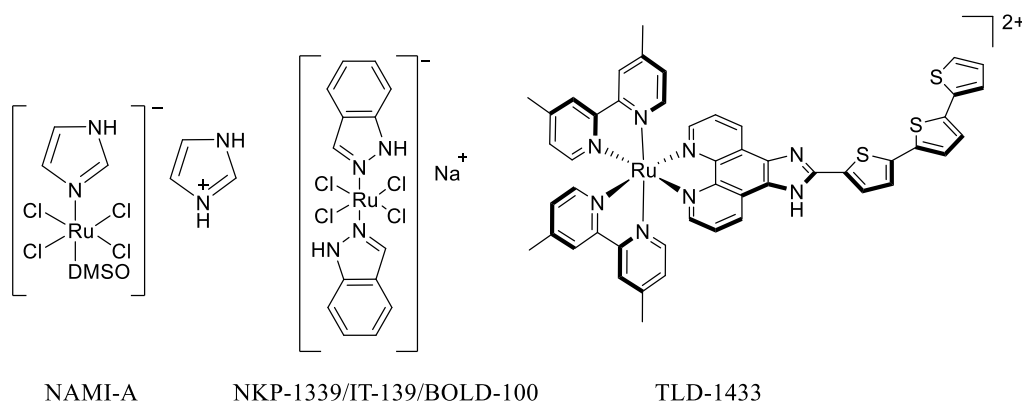


Figure 1.5. Structures of NAMI-A, NKP-1339/IT-139/BOLD-100, and TLD-1433; ruthenium compounds that have entered clinical trials for anticancer treatment.

There is a vast structural diversity of Ru(II) PACT and PDT agents with impressive photophysical properties; however, few have studied the effect of pH responsive ligands. It is of interest to study pH responsive drug candidates as some solid cancer tumors are hypoxic and exhibit decreased extracellular pH (pH_e) relative to normal tissue.^{43, 44} In collaboration with Prof. Jared Paul (Villanova University), the Papish group found that the complex $[(\text{bpy})_2\text{Ru}(6,6'\text{-dhbp})]^{2+}$ (**1**, 6,6'-dhbp = 6,6'-dihydroxybipyridine) had the ability to undergo ligand dissociation when exposed to ambient light for an extended duration. Believing that this may be a good candidate for PACT driven toxicity, a proof of concept study focusing on this complex was published in 2014.⁴⁵ The complex had moderate light toxicity in HeLa cells once irradiated with blue light ($\lambda = 450 \text{ nm}$) ($\text{EC}_{50} = 88(9) \mu\text{M}$). In the study, the photolabile 6,6'-dhbp was replaced with 4,4'-dhbp in order to limit steric bulk near the metal center and reduce photodissociation and yielded a reduction in toxicity ($\text{EC}_{50} = >100 \mu\text{M}$), suggesting photodissociation was necessary for toxicity. This study was expanded in 2017 to include additional potential PACT agents that continued to incorporate the photolabile 6,6'-dhbp ligand.¹ The complexes studied

were of the type $[(N,N')_2Ru(6,6'\text{-dhbp})]Cl_2$ where N,N' would be bipyridine (**1_A**, bpy), phenanthroline (**2_A**, phen), or 2,3-dihydro-[1,4]dioxino-[2,3-f][1,10]phenanthroline (**3_A**, dop) (Figure 1.6). Building upon complex **1_A**, **2_A** incorporates phenanthroline spectator ligands to study the effects of increased aromaticity and thus hydrophobicity. Ru(II) complexes containing phen spectator ligands are also known to eject a photolabile ligand.^{46, 47} The dop ligand (**3_A**) has been previously described as enhancing photodissociation via a twist in the nonplanar six-membered ring containing sp^3 atoms.⁴⁸⁻⁵⁰ Due to 6,6'-dhbp's ability to transition between protonation states, the various species are denoted with the subscript A (**X_A**) for the fully protonated, $[Ru]^{2+}$ complex while the doubly deprotonated species ($[Ru]^0$) is denoted with the subscript B (**X_B**) (Figure 1.6). When in solution, the complexes can readily convert between **X_A** and **X_B** and will be listed without the A or B subscript. All complexes are synthesized as dichloride salts unless stated otherwise.

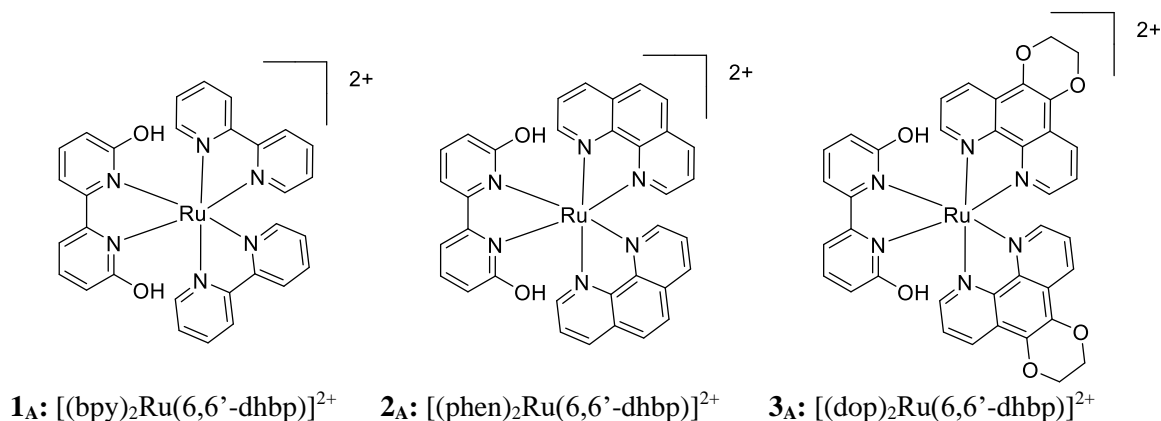


Figure 1.6: Shown are three photoactivated complexes studied in *Inorg. Chem.* **2017**. The structures contain the protic, photolabile ligand 6,6'-dhbp. **X_A** denotes the fully protonated, $[Ru]^{2+}$ complex, while **X_B** denotes the deprotonated, $[Ru]^0$ complex.

All compounds were tested against several cell lines including breast, cervical, and leukemia cancer cell lines; however, the complexes had the best toxicity against breast cancer cell lines (Table 1.1). The cells were incubated with the compound and irradiated with blue light

(450 nm) for one hour. All compounds showed good to moderate toxicity with **3** having the best EC₅₀ of 3.7 μM and highest PI of 120 (Table 1.1). At physiological pH (~7.5), a majority of the species present will be in the deprotonated, **X_B**, form (pK_{A avg} listed in Table 1.2).

Photodissociation quantum yield studies at pH 5.0 and pH 7.5 (majority **X_A** or **X_B**, respectively) were used to determine if the studied complexes were effective PACT agents. All compounds were found to photodissociate better at pH 5.0 vs pH 7.5 (Table 1.2). However, the Φ_{PD} for all compounds were low indicating minimal formation of the proposed toxic aqua species. While still significantly toxic, the mode of action for these complexes did not appear to be through a PACT driven pathway.

Table 1.1. Cell viability data for select cell lines. All EC₅₀'s are reported in μM. For EC₅₀ Light, cells were irradiated with blue light (450 nm) after treatment with the ruthenium compound. PI = EC₅₀ Dark/EC₅₀ Light. *Complete cell viability and uptake data can be found in reference 1.*

Compound	MDA-MB-231 (Breast CSC)			MCF7 (Breast Cancer)			MCF10A (Normal)		
	EC ₅₀ Dark	EC ₅₀ Light	PI	EC ₅₀ Dark	EC ₅₀ Light	PI	EC ₅₀ Dark	EC ₅₀ Light	PI
1	>1000	290(10)	>3.4	>500	>500	~1	>500	210(10)	>2.4
2	280(10)	83(3)	3.4(1)	490(20)	180(10)	2.8(2)	110(10)	13(1)	9(1)
3	190(10)	3.7(2)	52(3)	490(20)	4.1(4)	120(10)	58(1)	29(5)	2.0(3)

Table 1.2. Quantum yield and pK_A data for compounds **1-3**. The compounds exhibited better photodissociation at lower pH. Special Thanks: Schmehl Group, Tulane Univ.

Compound	Formula	Φ _{PD} X _A (pH 5.0)	Φ _{PD} X _B (pH 7.5)	pK _{A avg}
1	[(bpy) ₂ Ru(6,6'-dhbp)] ²⁺	0.0058(5)	0.0012(1)	6.3
2	[(phen) ₂ Ru(6,6'-dhbp)] ²⁺	0.0020(2)	0.000036(1)	6.0(1)
3	[(dop) ₂ Ru(6,6'-dhbp)] ²⁺	0.001(1)	0.00022(3)	5.9(1)

The complexes exhibited good toxicity and light selectivity against breast cancer cell lines despite low Φ_{PD} . This may indicate that the Ru aqua photoproduct may not be the cause of toxicity or the small amount that is being produced, is highly toxic. Recently, in 2018, Dr. Fengrui Qu, formerly of the Papish group, developed a series of complexes to further probe the relationship between Φ_{PD} and toxicity.² A series of analogous complexes were synthesized that replaced 6,6'-dhbp with 6,6'-dimethoxybipyridine (6,6'-dmbp = 6,6'-dimethoxy-2,2'-bipyridine). By replacing the -OH groups with -OMe, the steric bulk near the metal center is increased, allowing for an increase in photodissociation. Only analogues of **2** and **3** were studied (**2**^{OMe} and **3**^{OMe} respectively). These complexes have increased Φ_{PD} over their dhbp analogues; however, cell viability studies showed that they were non-toxic against MDA-MB-231 breast cancer cell lines ($EC_{50} > 100 \mu\text{M}$) (Table 1.3).

Table 1.3. Φ_{PD} was enhanced in complexes that had greater steric bulk near the Ru center but also had decreased toxicity against MDA-MB-231 breast cancer stem cells. *Adapted from reference 46.*

Compound	Structure	$\Phi_{PD} X_A$ (pH 5.0)	EC_{50} (μM) Light
2	$[(\text{phen})_2\text{Ru}(6,6'\text{-dhbp})]\text{Cl}_2$	0.002	83
3	$[(\text{dop})_2\text{Ru}(6,6'\text{-dhbp})]\text{Cl}_2$	0.001	3.7
2 ^{OMe}	$[(\text{phen})_2\text{Ru}(6,6'\text{-dmbp})]\text{Cl}_2$	0.024	>100
3 ^{OMe}	$[(\text{dop})_2\text{Ru}(6,6'\text{-dmbp})]\text{Cl}_2$	0.003	>100

One possible explanation for the complexes' (**1-3**) toxicity despite their low Φ_{PD} would be that a resulting photoproduct was highly toxic. To test this, aquated analogues of **1**, **2**, or **3** were synthesized ($[(\text{OH}_2)_2\text{Ru}(\text{N},\text{N}')_2]^{2+}$ where N,N' = bpy (**1**), phen (**2**), or dop (**3**)). Cells were treated with free 6,6'-dhbp ligand and the aquated Ru(II) complexes. In all cases, both the free ligand and the Ru-aqua adducts were found to be non-toxic ($EC_{50} > 100 \mu\text{M}$) against breast cancer cells. However, this data is not entirely conclusive. The photoproducts (Ru-aqua

complexes and free 6,6'-dhbp) have different physical properties than those of the full complexes and may interact with other biological targets before entering the cells resulting in the lower toxicity. It is speculated that the full complex may behave as a drug delivery system that allows for the release of the toxic photoproduct near its target upon irradiation; however, the ultimate mode of action and final biological target(s) was still unknown.

Much like other metal complexes, it was hypothesized that the complexes affected a biological target within the cell, such as DNA.⁵¹⁻⁵⁴ However, before the ruthenium complex can interact with a molecule like DNA it must first be taken up into the cell. To examine this, the cells were treated with the drugs and the lysate analyzed via inductively coupled plasma mass spectrometry (ICP-MS). Ruthenium is not an element naturally found at a significant concentration within a biological system so any Ru detected within the cell lysate would be attributed to the compound it was treated with.⁵⁵ The cells were treated with a non-lethal dose (10 μ M, chosen to be below dark EC₅₀ values) and analyzed under dark conditions. The treated cells (MDA-MB-231, MCF10A, or MCF7) were washed with new cell media to ensure that any ruthenium detected was attributed to compound that had successfully entered the cell. The uptake was reported as a percentage of ruthenium that was detected in the cell lysate (when compared to the amount the cells were initially dosed with) (Figure 1.7). While the uptake was best for compound **3** at 0.32 %, it is much lower than that of other ruthenium compounds which can have an uptake as high as 70 %.⁵⁶ No identifiable pattern was discovered that could correlate uptake to toxicity. If the complexes were behaving as a delivery system that could deliver toxic photoproducts, one would expect to see significantly higher uptake.

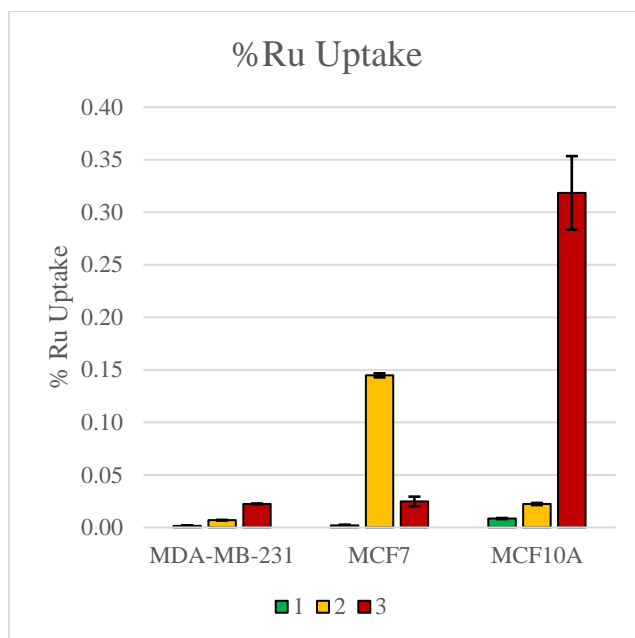


Figure 1.7: Ru uptake as measured by ICP-MS for cells treated with **1-3** (10 μ M) in the dark. Cells were treated with the X_A form of the drug which converts to X_B *in vivo*. Figure adapted from reference 1.

1.3 Summary of Dissertation

While the study yielded interesting results, many of the hypotheses at the onset of the study were now in question and needed re-evaluation. Much of my time in the Papish group has been focused on investigating some of the issues and questions that arose as a result of our initial findings.

1. How are these complexes taken up into the cells?

ICP-MS detected only a small percentage of Ru within cell lysate samples treated with **1-3**, indicating low uptake. While the highest uptake was reported for complex **3**, it was reported in the non-cancerous cell line. Of the cancerous cell lines, compound **2** had the highest uptake in MCF7 but had poor light toxicity ($EC_{50} = 180 \mu$ M). Measuring uptake by ICP-MS is still a viable method; however, there are quicker and more inexpensive methods to probe uptake.

Fluorescence microscopy is a method that has been used with similar ruthenium complexes to determine subcellular localization while flow cytometry is used to determine how many cells within a sample contain drug.⁵⁷⁻⁶⁰ Further understanding of the complexes' hydrophobicity can give insight on the likelihood that a compound will enter the cell via passive diffusion across a lipid bilayer.⁶¹ These studies may help to explain or support the ICP-MS data.

In chapter 2, I will discuss the efforts to further study the mode of uptake for these complexes via fluorescence imaging, flow cytometry, and distribution coefficient ($\text{Log}(D_{o/w})$), as well as determination of potential active transport uptake and efflux mechanisms.

Fluorescence imaging and flow cytometry are two methods that collaborators in the Kim Group can perform within the Department of Chemical and Biological Engineering at The University of Alabama. Distribution coefficient ($\text{Log}(D_{o/w})$) studies are a way to probe the overall hydrophobicity of the complexes at various pH values. $\text{Log}(D_{o/w})$ is used for these complexes as opposed to partition coefficient ($\text{Log } P$) as $\text{Log}(D_{o/w})$ is used for compounds that are sensitive to pH changes. This could be a simple, yet useful method of probing the likelihood of passive transport into the cell. Alternatively, metabolic inhibition studies can aid in determining if the main mode of uptake is an active transport mechanism and if the complex is actively being removed (efflux) from the cell. Work contributing to this study was published in *Journal of Inorganic Biochemistry* in early 2020.⁶²

2. *Can we develop more effective PACT agents that can deliver multiple photoproducts upon irradiation?*

The studied complexes (**1-3**) have higher Φ_{PD} in an acidic environment (\mathbf{X}_A) as opposed to a more basic environment (\mathbf{X}_B); however, the overall Φ_{PD} for all complexes was much lower than anticipated. In fact, at physiological pH (~7.4), the complexes would be at their lowest rates of

photodissociation and unable to produce significant quantities of photoproducts. The photoproducts themselves were non-toxic when tested independently against the breast cancer cell lines (it is possible that the undissociated complex may behave as a delivery mechanism; however, it is unlikely that this is the case as no evidence has been found to support this).

In chapter 3, I will discuss my efforts to synthesize ruthenium PACT agents that could eject a ligand with known toxicity as well as a potentially toxic ruthenium-aqua adduct. 5-Fluorouracil (5-FU) and 5-cyanouracil (5-CNU) were utilized for this project. 5-FU has shown to have independent toxicity against cancer and 5-CNU, a close structural analogue, has been successfully incorporated into potential PACT agents and elicits some toxicity as well as shown independent toxicity.^{7, 26, 27, 63-65} Alongside 5-FU or 5-CNU, these compounds will also incorporate the protic ligand 6,6'-dhbp to determine what effects pH may have on the toxicity of these complexes. These compounds were initially designed to deliver multiple toxic photoproducts upon irradiation; however, synthesis for these complexes proved difficult and yielded a new, unintended product.

3. *How are the complexes toxic if not through a PACT driven pathway?*

Both the *Inorg. Chem.*¹ and *Dalton Trans.*² studies by the Papish group have shown that complexes **1-3** are not effective PACT agents. One aspect of a successful PACT agent is a *direct* correlation between Φ_{PD} and toxicity. While compounds **1-3** do photodissociate, they exhibit an *inverse* relationship with Φ_{PD} and toxicity. This relationship is more indicative of photodynamic therapy (PDT) agents capable of producing 1O_2 .

In chapter 4, I will discuss how our collaborators and I sought to determine if the production of the toxic ROS, singlet oxygen, was the primary mode of action for complexes **1-3**. What roles pH has on the production of singlet oxygen is also investigated. 1O_2 has a short lifetime making

direct detection difficult without the use of specialized equipment. Probes that produce a detectable species once they react with singlet oxygen are a commonly utilized method. I explored several qualitative methods of indirect detection that utilized UV-Vis, fluorescent, and electron paramagnetic resonance (EPR) probes. Meanwhile, our collaborators investigated singlet oxygen quantum yields (Φ_{Δ}) via time-resolved near infrared (IR) spectroscopy (TR-NIR), a quantitative direct detection method. Both myself and our collaborators also sought to study singlet oxygen production as a function of pH. Work on this study has contributed to a recently submitted publication to *Inorganic Chemistry*.

4. *By understanding which characteristics have the biggest influence on toxicity, can we develop even more toxic and light selective complexes?*

Complexes **1-3** did exhibit good toxicity towards breast cancer cell lines with decent light selectivity (best performer: **3** in MCF7 cell line $IC_{50} = 4.1(4) \mu M$, $PI = 120(10)$). These values, unfortunately, are still not among the top performers currently in the literature.⁶⁶ Other ruthenium anticancer complexes capable of selectively ejecting a ligand have significantly higher phototoxicity indexes and toxicity.^{26, 67, 68} Building upon studies that investigated uptake, hydrophobicity, and potential modes of action for complexes **1-3** has given insight into what properties have the greatest influence on toxicity. This has allowed for the rational and evidence-based design of new complexes to further expand our compound library.

In chapter 5, I will discuss the study of new complexes which continue to incorporate 6,6'-dhbp and the spectator ligands, bathophenanthrolinedisulphonic acid (BPS) and bathophenanthroline (BPhen, sometimes referred to as DIP in literature). Throughout these studies, it had been found that the incorporation of these ligands (BPhen in particular) may allow for the proper physical characteristics needed to generate a sufficiently toxic and light selective

complex. While this project is currently underway, I have successfully developed and synthesized several complexes containing the BPS and BPhen ligands that have been tested in cells with impressive results. This may be due to an increased production of singlet oxygen which is currently being investigated.

In chapter 6, the crystal structure of $[\text{Cu}(\text{ClO}_4)(1,4,7,10\text{-tetraazacyclododecane})](\text{ClO}_4)$ is reported.⁶⁹ Copper–cyclen complexes have been studied extensively for their ability to perform catalytic DNA cleavage and peptide hydrolysis.⁷⁰⁻⁷² This is a unique crystal structure in which the Cu(II) ion exhibits a square-pyramidal geometry and is coordinated by the four N atoms of the neutral 1,4,7,10-tetraazacyclododecane (cyclen) ligand and an O atom from one perchlorate anion, with the second perchlorate ion hydrogen-bonded to one of the amine N atoms of the cyclen ligand. The complex cations of two asymmetric units hydrogen-bond across an inversion center, which is clearly visible when viewed along the *a* axis, creating a dimer. This work was published in *Acta Crystallography* in 2017.

References

- [1] Qu, F., Park, S., Martinez, K., Gray, J. L., Thowfeik, F. S., Lundeen, J. A., Kuhn, A. E., Charboneau, D. J., Gerlach, D. L., Lockart, M. M., Law, J. A., Jernigan, K. L., Chambers, N., Zeller, M., Piro, N. A., Kassel, W. S., Schmehl, R. H., Paul, J. J., Merino, E. J., Kim, Y., and Papish, E. T. (2017) Ruthenium Complexes are pH-Activated Metallo Prodrugs (pHAMPs) with Light-Triggered Selective Toxicity Toward Cancer Cells, *Inorg. Chem.* *56*, 7519-7532.
- [2] Qu, F., Martinez, K., Arcidiacono, A. M., Park, S., Zeller, M., Schmehl, R. H., Paul, J. J., Kim, Y., and Papish, E. T. (2018) Sterically demanding methoxy and methyl groups in ruthenium complexes lead to enhanced quantum yields for blue light triggered photodissociation, *Dalton Trans.* *47*, 15685-15693.
- [3] Early History of Cancer, In *The History of Cancer*. <https://www.cancer.org/content/dam/CRC/PDF/Public/6055.00.pdf> (Accessed November 5, 2020). The American Cancer Society.
- [4] (2020) Cancer Facts & Figures 2020, American Cancer Society.
- [5] Thiersch, J. B. (1949) Bone-marrow changes in man after treatment with aminopterin, amethopterin, and aminoanfol; with special reference to megaloblastosis and tumor remission, *Cancer* *2*, 877-883.
- [6] Meyer, L. M., Miller, F. R., Rowen, M. J., Bock, G., and Rutzky, J. (1950) Treatment of acute leukemia with amethopterin (4-amino, 10-methyl pteroyl glutamic acid), *Acta Haematol* *4*, 157-167.
- [7] Sohn, K. J., Smirnakis, F., Moskovitz, D. N., Novakovic, P., Yates, Z., Lucock, M., Croxford, R., and Kim, Y. I. (2004) Effects of folylpolyglutamate synthetase modulation on chemosensitivity of colon cancer cells to 5-fluorouracil and methotrexate, *Gut* *53*, 1825-1831.
- [8] Ferris, R. L., Blumenschein, G., Jr., Fayette, J., Guigay, J., Colevas, A. D., Licitra, L., Harrington, K., Kasper, S., Vokes, E. E., Even, C., Worden, F., Saba, N. F., Iglesias, D. L. C., Haddad, R., Rordorf, T., Kiyota, N., Tahara, M., Monga, M., Lynch, M., Geese, W. J., Kopit, J., Shaw, J. W., and Gillison, M. L. (2016) Nivolumab for Recurrent Squamous-Cell Carcinoma of the Head and Neck, *N Engl J Med* *375*, 1856-1867.

- [9] Cleare, M. J., Hoeschele, J. D., Rosenberg, B., and Van Camp, L. L. (1973) Platinum coordination compounds, p 23 pp., Research Corp.
- [10] Guo, Z., and Sadler, P. J. (1999) Metals in medicine, *Angew. Chem., Int. Ed.* 38, 1512-1531.
- [11] Matera, C., Gomila, A. M. J., Camarero, N., Libergoli, M., Soler, C., and Gorostiza, P. (2018) Photoswitchable Antimetabolite for Targeted Photoactivated Chemotherapy, *J. Am. Chem. Soc.* 140, 15764-15773.
- [12] Ardizzoni, A., Boni, L., Tiseo, M., Fossella, F. V., Schiller, J. H., Paesmans, M., Radosavljevic, D., Paccagnella, A., Zatloukal, P., Mazzanti, P., Bisset, D., and Rosell, R. (2007) Cisplatin- versus carboplatin-based chemotherapy in first-line treatment of advanced non-small-cell lung cancer: an individual patient data meta-analysis, *J. Natl. Cancer Inst.* 99, 847-857.
- [13] Dolmans, D. E. J. G. J., Fukumura, D., and Jain, R. K. (2003) TIMELINE: Photodynamic therapy for cancer, *Nat. Rev. Cancer* 3, 380-387.
- [14] Monroe, S., Colon, K. L., Yin, H., Roque, J., Konda, P., Gujar, S., Thummel, R. P., Lilje, L., Cameron, C. G., and McFarland, S. A. (2019) Transition Metal Complexes and Photodynamic Therapy from a Tumor-Centered Approach: Challenges, Opportunities, and Highlights from the Development of TLD1433, *Chem. Rev. (Washington, DC, U. S.)* 119, 797-828.
- [15] Mulatihan, D., Guo, T., and Zhao, Y. (2020) Azobenzene Photoswitch for Isomerization-Dependent Cancer Therapy via Azo-Combretastatin A4 and Phototrexate, *Photochem. Photobiol.*, Ahead of Print.
- [16] Singh, T. N., and Turro, C. (2004) Photoinitiated DNA Binding by cis-[Ru(bpy)₂(NH₃)₂]²⁺, *Inorg. Chem.* 43, 7260-7262.
- [17] Ford, P. C. (1970) Properties and reactions of ruthenium(II) amine complexes, *Coord. Chem. Rev.* 5, 75-99.
- [18] Ford, P. C. (1982) The ligand field photosubstitution reactions of d₆ hexacoordinate metal complexes, *Coord. Chem. Rev.* 44, 61-82.
- [19] Ford, P. C., Wink, D., and Dibeneditto, J. (1983) Mechanistic aspects of the photosubstitution and photoisomerization reactions of d₆ metal complexes, *Prog. Inorg. Chem.* 30, 213-271.
- [20] Tfouni, E. (2000) Photochemical reactions of ammine-ruthenium(II) complexes, *Coord. Chem. Rev.* 196, 281-305.

- [21] Collins, J. G., Sleeman, A. D., Aldrich-Wright, J. R., Greguric, I., and Hambley, T. W. (1998) A ^1H NMR Study of the DNA Binding of Ruthenium(II) Polypyridyl Complexes, *Inorg. Chem.* *37*, 3133-3141.
- [22] Uma Maheswari, P., and Palaniandavar, M. (2004) DNA binding and cleavage properties of certain tetrammine ruthenium(II) complexes of modified 1,10-phenanthrolines - effect of hydrogen-bonding on DNA-binding affinity, *J. Inorg. Biochem.* *98*, 219-230.
- [23] Harmon, H. L., and Morrison, H. (1995) Anaerobic Photoinduced N7-Binding of cis-Dichlorobis(1,10-phenanthroline)rhodium(III) Chloride to 2'-Deoxyguanosine: A One-Electron-Transfer Chain Process, *Inorg. Chem.* *34*, 4937-4938.
- [24] Morrison, H., and Harmon, H. (2000) "Hot spots" associated with the photoinduced binding of cis-dichloro bis(1,10 phenanthroline)rhodium(III) chloride to HIV-1 and c-raf DNA, *Photochem. Photobiol.* *72*, 731-738.
- [25] Mahnken, R. E., Billadeau, M. A., Nikonowicz, E. P., and Morrison, H. (1992) Development of photo cis-platinum reagents. Reaction of cis-dichlorobis(1,10-phenanthroline)rhodium(III) with calf thymus DNA, nucleotides and nucleosides, *J. Am. Chem. Soc.* *114*, 9253-9265.
- [26] Garner, R. N., Gallucci, J. C., Dunbar, K. R., and Turro, C. (2011) $[\text{Ru}(\text{bpy})_2(5\text{-cyanouracil})_2]^{2+}$ as a Potential Light-Activated Dual-Action Therapeutic Agent, *Inorg. Chem.* *50*, 9213-9215.
- [27] Sgambellone, M. A., David, A., Garner, R. N., Dunbar, K. R., and Turro, C. (2013) Cellular Toxicity Induced by the Photorelease of a Caged Bioactive Molecule: Design of a Potential Dual-Action Ru(II) Complex, *J. Am. Chem. Soc.* *135*, 11274-11282.
- [28] Albani, B. A., Pena, B., Leed, N. A., de Paula, N. A. B. G., Pavani, C., Baptista, M. S., Dunbar, K. R., and Turro, C. (2014) Marked Improvement in Photoinduced Cell Death by a New Tris-heteroleptic Complex with Dual Action: Singlet Oxygen Sensitization and Ligand Dissociation, *J. Am. Chem. Soc.* *136*, 17095-17101.
- [29] Sainuddin, T., McCain, J., Pinto, M., Yin, H., Gibson, J., Hetu, M., and McFarland, S. A. (2016) Organometallic Ru(II) Photosensitizers Derived from π -Expansive Cyclometalating Ligands: Surprising Theranostic PDT Effects, *Inorg. Chem.* *55*, 83-95.
- [30] Loftus, L. M., White, J. K., Albani, B. A., Kohler, L., Kodanko, J. J., Thummel, R. P., Dunbar, K. R., and Turro, C. (2016) New Ru(II) Complex for Dual Activity: Photoinduced Ligand Release and $^1\text{O}_2$ Production, *Chem. Eur. J.* *22*, 3704-3708.
- [31] Tabrizi, L., and Chiniforoshan, H. (2016) New Ru(II) pincer complexes: synthesis, characterization and biological evaluation for photodynamic therapy, *Dalton Trans.* *45*, 18333-18345.

- [32] Ping, J.-T., Peng, H.-S., Qin, J., Wang, Y.-Q., Chen, G.-X., Song, M., Ping, J.-T., and You, F.-T. (2018) A fluorescent nanoprobe for real-time monitoring of intracellular singlet oxygen during photodynamic therapy, *Mikrochim Acta* 185, 269.
- [33] Toupin, N. P., Nadella, S., Steinke, S. J., Turro, C., and Kodanko, J. J. (2020) Dual-Action Ru(II) Complexes with Bulky π -Expansive Ligands: Phototoxicity without DNA Intercalation, *Inorg. Chem.* 59, 3919-3933.
- [34] Lion, Y., Delmelle, M., and Van de Vorst, A. (1976) New method of detecting singlet oxygen production, *Nature (London)* 263, 442-443.
- [35] Dickerson, M., Sun, Y., Howerton, B., and Glazer, E. C. (2014) Modifying Charge and Hydrophilicity of Simple Ru(II) Polypyridyl Complexes Radically Alters Biological Activities: Old Complexes, Surprising New Tricks, *Inorg. Chem.* 53, 10370-10377.
- [36] Lincoln, R., Kohler, L., Monro, S., Yin, H., Stephenson, M., Zong, R., Chouai, A., Dorsey, C., Hennigar, R., Thummel, R. P., and McFarland, S. A. (2013) Exploitation of Long-Lived ^3IL Excited States for Metal-Organic Photodynamic Therapy: Verification in a Metastatic Melanoma Model, *J. Am. Chem. Soc.* 135, 17161-17175.
- [37] Alessio, E. (2017) Thirty Years of the Drug Candidate NAMI-A and the Myths in the Field of Ruthenium Anticancer Compounds: A Personal Perspective, *Eur. J. Inorg. Chem.* 2017, 1549-1560.
- [38] Trondl, R., Heffeter, P., Kowol, C. R., Jakupec, M. A., Berger, W., and Keppler, B. K. (2014) NKP-1339, the first ruthenium-based anticancer drug on the edge to clinical application, *Chem. Sci.* 5, 2925-2932.
- [39] Leijen, S., Burgers, S. A., Baas, P., Pluim, D., Tibben, M., van Werkhoven, E., Alessio, E., Sava, G., Beijnen, J. H., and Schellens, J. H. M. (2015) Phase I/II study with ruthenium compound NAMI-A and gemcitabine in patients with non-small cell lung cancer after first line therapy, *Invest. New Drugs* 33, 201-214.
- [40] Burris, H. A., Bakewell, S., Bendell, J. C., Infante, J., Jones, S. F., Spigel, D. R., Weiss, G. J., Ramanathan, R. K., Ogden, A., and Von Hoff, D. (2016) Safety and activity of IT-139, a ruthenium-based compound, in patients with advanced solid tumours: a first-in-human, open-label, dose-escalation phase I study with expansion cohort, *ESMO Open* 1., e000154.
- [41] Monro, S., Colón, K. L., Yin, H., Roque, J., Konda, P., Gujar, S., Thummel, R. P., Lilge, L., Cameron, C. G., and McFarland, S. A. (2019) Transition Metal Complexes and Photodynamic Therapy from a Tumor-Centered Approach: Challenges, Opportunities, and Highlights from the Development of TLD1433, *Chem. Rev.* 119, 797-828.

- [42] McFarland, S. A., Mandel, A., Dumoulin-White, R., and Gasser, G. (2020) Metal-based photosensitizers for photodynamic therapy: the future of multimodal oncology?, *Curr. Opin. Chem. Biol.* 56, 23-27.
- [43] Denny, W. A. (2001) Prodrug strategies in cancer therapy, *Eur. J. Med. Chem.* 36, 577-595.
- [44] Stubbs, M., McSheehy, P. M., Griffiths, J. R., and Bashford, C. L. (2000) Causes and consequences of tumour acidity and implications for treatment, *Mol. Med. Today* 6, 15-19.
- [45] Hufziger, K. T., Thowfeik, F. S., Charboneau, D. J., Nieto, I., Dougherty, W. G., Kassel, W. S., Dudley, T. J., Merino, E. J., Papish, E. T., and Paul, J. J. (2014) Ruthenium dihydroxybipyridine complexes are tumor activated prodrugs due to low pH and blue light induced ligand release, *J. Inorg. Biochem.* 130, 103-111.
- [46] Laemmel, A.-C., Collin, J.-P., and Sauvage, J.-P. (1999) Efficient and selective photochemical labilization of a given bidentate ligand in mixed ruthenium(II) complexes of the Ru(phen)₂L²⁺ and Ru(bipy)₂L²⁺ family (L = sterically hindering chelate), *Eur. J. Inorg. Chem.*, 383-386.
- [47] Baranoff, E., Collin, J.-P., Furusho, Y., Laemmel, A.-C., and Sauvage, J.-P. (2000) A photochromic system based on photochemical or thermal chelate exchange on Ru(phen)₂L²⁺ (L = diimine or dinitrile ligand), *Chem. Commun. (Cambridge)*, 1935-1936.
- [48] Hidayatullah, A. N., Wachter, E., Heidary, D. K., Parkin, S., and Glazer, E. C. (2014) Photoactive Ru(II) Complexes With Dioxinophenanthroline Ligands Are Potent Cytotoxic Agents, *Inorg. Chem.* 53, 10030-10032.
- [49] Wachter, E., Heidary, D. K., Howerton, B. S., Parkin, S., and Glazer, E. C. (2012) Light-activated ruthenium complexes photobind DNA and are cytotoxic in the photodynamic therapy window, *Chem. Commun. (Cambridge, U. K.)* 48, 9649-9651.
- [50] Howerton, B. S., Heidary, D. K., and Glazer, E. C. (2012) Strained ruthenium complexes are potent light-activated anticancer agents, *J. Am. Chem. Soc.* 134, 8324-8327.
- [51] Routier, S., Joanny, V., Zaparucha, A., Vezin, H., Catteau, J.-P., Bernier, J.-L., and Bailly, C. (1998) Synthesis of metal complexes of 2,9-bis(2-hydroxyphenyl)-1,10-phenanthroline and their DNA binding and cleaving activities, *J. Chem. Soc., Perkin Trans. 2*, 863-868.
- [52] Novakova, O., Kasparkova, J., Bursova, V., Hofr, C., Vojtiskova, M., Chen, H., Sadler, P. J., and Brabec, V. (2005) Conformation of DNA Modified by Monofunctional Ru(II) Arene Complexes: Recognition by DNA Binding Proteins and Repair. Relationship to Cytotoxicity, *Chem. Biol.* 12, 121-129.

- [53] Magennis, S. W., Habtemariam, A., Novakova, O., Henry, J. B., Meier, S., Parsons, S., Oswald, I. D. H., Brabec, V., and Sadler, P. J. (2007) Dual Triggering of DNA Binding and Fluorescence via Photoactivation of a Dinuclear Ruthenium(II) Arene Complex, *Inorg. Chem.* *46*, 5059-5068.
- [54] Ganeshpandian, M., Loganathan, R., Suresh, E., Riyasdeen, A., Akbarsha, M. A., and Palaniandavar, M. (2014) New ruthenium(II) arene complexes of anthracenyl-appended diazacycloalkanes: effect of ligand intercalation and hydrophobicity on DNA and protein binding and cleavage and cytotoxicity, *Dalton Trans.* *43*, 1203-1219.
- [55] Iyer, S. (2009) Atoms & Life, In *Ask a Biologist*, Elements Found in the Human Body, Arizona State University.
- [56] Kalaivani, P., Prabhakaran, R., Poornima, P., Dallemer, F., Vijayalakshmi, K., Padma, V. V., and Natarajan, K. (2012) Versatile coordination behavior of salicylaldehydethiosemicarbazone in ruthenium(II) carbonyl complexes: synthesis, spectral, x-ray, electrochemistry, DNA binding, cytotoxicity, and cellular uptake studies, *Organometallics* *31*, 8323-8332.
- [57] Puckett, C. A., and Barton, J. K. (2007) Methods to Explore Cellular Uptake of Ruthenium Complexes, *J. Am. Chem. Soc.* *129*, 46-47.
- [58] Puckett, C. A., and Barton, J. K. (2008) Mechanism of Cellular Uptake of a Ruthenium Polypyridyl Complex, *Biochemistry* *47*, 11711-11716.
- [59] Banks, W. A. (2009) Characteristics of compounds that cross the blood-brain barrier, *BMC Neurol.* *9*, S3.
- [60] Svensson, F. R., Matson, M., Li, M., and Lincoln, P. (2010) Lipophilic ruthenium complexes with tuned cell membrane affinity and photoactivated uptake, *Biophys. Chem.* *149*, 102-106.
- [61] Zhang, J. X., Wong, K.-L., Wong, W.-K., Mak, N.-K., Kwong, D. W. J., and Tam, H.-L. (2011) Two-photon induced luminescence, singlet oxygen generation, cellular uptake and photocytotoxic properties of amphiphilic Ru(II) polypyridyl-porphyrin conjugates as potential bifunctional photodynamic therapeutic agents, *Org. Biomol. Chem.* *9*, 6004-6010.
- [62] Park, S., Gray, J. L., Altman, S. D., Hairston, A. R., Beswick, B. T., Kim, Y., and Papish, E. T. (2020) Cellular uptake of protic ruthenium complexes is influenced by pH dependent passive diffusion and energy dependent efflux, *J. Inorg. Biochem.* *203*, 110922.
- [63] Lenz, H. J., Leichman, C. G., Danenberg, K. D., Danenberg, P. V., Groshen, S., Cohen, H., Laine, L., Crookes, P., Silberman, H., Baranda, J., Garcia, Y., Li, J., and Leichman, L. (1996) Thymidylate synthase mRNA level in adenocarcinoma of the stomach: a predictor for primary tumor response and overall survival, *J. Clin. Oncol.* *14*, 176-182.

- [64] Schultz, R. M., Patel, V. F., Worzalla, J. F., and Shih, C. (1999) Role of thymidylate synthase in the antitumor activity of the multitargeted antifolate, LY231514, *Anticancer Res.* *19*, 437-443.
- [65] Gentry, G. A., Morse, P. A., Jr., and Dorsett, M. T. (1971) In vivo inhibition of pyrimidine catabolism by 5-cyanouracil, *Cancer Res.* *31*, 909-912.
- [66] Roque, J. A., Barrett, P. C., Cole, H. D., Lifshits, L. M., Shi, G., Monro, S., von Dohlen, D., Kim, S., Russo, N., Deep, G., Cameron, C. G., Alberto, M. E., and McFarland, S. A. (2020) Breaking the barrier: an osmium photosensitizer with unprecedented hypoxic phototoxicity for real world photodynamic therapy, *Chem. Sci.*, Ahead of Print.
- [67] Knoll, J. D., Albani, B. A., and Turro, C. (2015) New Ru(II) Complexes for Dual Photoreactivity: Ligand Exchange and $^1\text{O}_2$ Generation, *Acc. Chem. Res.* *48*, 2280-2287.
- [68] Albani, B. A., Durr, C. B., and Turro, C. (2013) Selective Photoinduced Ligand Exchange in a New Tris-Heteroleptic Ru(II) Complex, *J. Phys. Chem. A* *117*, 13885-13892.
- [69] Gray, J. L., Gerlach, D. L., and Papish, E. T. (2017) Crystal structure of (perchlorato- κO)(1,4,7,10-tetraazacyclododecane- κ4N)copper(II) perchlorate, *Acta Crystallogr., Sect. E: Crystallogr. Commun.* *73*, 31-34.
- [70] Zhang, X., Liu, X., Phillips, D. L., and Zhao, C. (2016) Mechanistic Insights Into the Factors That Influence the DNA Nuclease Activity of Mononuclear Facial Copper Complexes Containing Hetero-Substituted Cyclens, *ACS Catal.* *6*, 248-257.
- [71] Li, S., Chen, J.-X., Xiang, Q.-X., Zhang, L.-Q., Zhou, C.-H., Xie, J.-Q., Yu, L., and Li, F.-Z. (2014) The synthesis and activities of novel mononuclear or dinuclear cyclen complexes bearing azole pendants as antibacterial and antifungal agents, *Eur. J. Med. Chem.* *84*, 677-686.
- [72] Kruppa, M., Frank, D., Leffler-Schuster, H., and König, B. (2006) Screening of metal complex–amino acid side chain interactions by potentiometric titration, *Inorganica Chimica Acta* *359*, 1159-1168.

CHAPTER 2

CELLULAR UPTAKE OF PROTIC RUTHENIUM COMPLEXES IS INFLUENCED BY pH DEPENDENT PASSIVE DIFFUSION AND ENERGY DEPENDENT EFFLUX

Adapted From: Park, Seungjo*; Gray, Jessica L.*; Altman, Sarah D.; Hairston, Angela R.; Kim, Yonghyun; Papish, Elizabeth T., *J. Inorg. Biochem.*, **2020**, 203, 110922

** These authors contributed equally.*

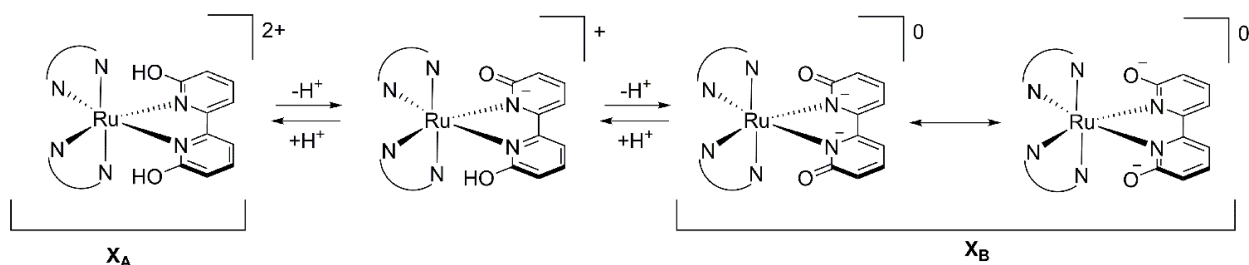
2.1 Abstract

The lipophilic versus hydrophilic properties of three protic ruthenium compounds were studied as a function of pH. Specifically, I measured $\log(D_{o/w})$ values for $[(N,N)_2Ru(6,6'$ -dhbp)]Cl₂ complexes (where N,N = bpy (**1**), phen (**2**), dop (**3**) and 6,6'-dhbp is the diprotic dihydroxybipyridine ligand) from pH 4.0 to 8.0. This study demonstrates that as the ligand is deprotonated at higher pH values the resulting neutral charge on the complex improves its lipophilic properties. Thus, improved uptake by passive diffusion is expected with protic ligands on Ru(II). Furthermore, cellular studies have demonstrated that passive diffusion is the dominant pathway for cellular uptake. However, metabolic inhibition has also shown that energy dependent efflux reduces the amount of the ruthenium complex (as measured by mean fluorescence intensity) in the cells. These compounds have been shown by fluorescence microscopy to accumulate in the nuclei of cancer cells (MCF7, MDA-MB-231, and HeLa). Taken together, this data shows that uptake is required for toxicity, but uptake alone is not sufficient. The greatest light activated toxicity appears to occur in breast cancer cell lines with relatively moderate uptake (MCF7 and MDA-MB-231) rather than the cell line with the greatest uptake of complex **3** (normal breast cell line MCF-10A).

2.2 Introduction

The anti-proliferative properties of certain ruthenium complexes are known to depend on their uptake into cells. Several mechanisms are possible for cellular uptake including energy independent processes such as passive diffusion and facilitated diffusion.²⁻⁴ Energy dependent uptake and efflux of drugs can also occur, and these processes are termed active transport.²⁻⁴ For many ruthenium complexes, both active transport and passive diffusion both occur although the relative amount of each process can vary depending on drug concentration (which influences passive diffusion) and the gene expression of the cell line (which can up regulate pumps and proteins for active transport).⁵ This project focused on studying how the charge of protic ruthenium complexes can influence their passive diffusion. Passive diffusion is difficult to directly measure, but it can be estimated based on the distribution coefficient which quantifies how the ionizable metal complex distributes between octanol and water.⁶⁻¹¹ One key innovation in this project is in determining how distribution coefficients for protic ruthenium complexes vary as a function of pH. While pH dependent distribution coefficients are well established for protic organic drugs,^{6, 8, 12} very few papers have studied this phenomenon with protic metallodrugs.¹³ In 2017, a series of light activated ruthenium complexes was reported, $[(N,N)_2Ru(6,6'\text{-dhbp})]^{2+}$, wherein (N,N) is varied from 2,2'-bipyridine (bpy) (in **1_A**) to 1,10-phenanthroline (phen) (in **2_A**) to 2,3-dihydro-[1,4]dioxino[2,3-f][1,10]phenanthroline (dop) (in **3_A**) (Figure 1.6).^{1, 14, 15} The protic ligand, 6,6'-dihydroxy-2,2'-bipyridine (6,6'-dhbp), provides a means of changing the complex charge with pH. As shown in Scheme 2.1, at low pH the complexes are in their dicationic form (**X_A**) where the subscript A indicates the acidic form is present (Scheme 2.1). Importantly, deprotonation events change the charge of the metal complex and the neutral form of the complex is achieved at elevated pH values (Scheme 2.1, **X_B** with

subscript B for basic form). Thus, for complex **1** the known pK_a values in Table 2.1 indicate that the dicationic species **1_A** predominates at pH 5, but at physiological pH values (pH = 7.5) the neutral species **1_B** predominates. Although the pK_a values are slightly different for **2** and **3**, a similar trend applies, and at physiological pH values both complexes are mostly deprotonated and present as the neutral species, **2_B** and **3_B**. Complexes **1-3** were synthesized as the dicationic acidic forms (**1_A-3_A**, isolated as the dichloride salt), but they are readily deprotonated in cell media at pH 7.4. These complexes show light activated toxicity with the best toxicity being observed for complex **3** in breast cancer cells (Table 2.2 shows an excerpt of previously reported data¹).¹ This toxicity was originally attributed to light triggered ligand loss (photodissociation), but more recent studies suggest the mechanism may be more complicated and appears that singlet oxygen production (rather than photodissociation) is responsible for the observed phototoxicity of **3**.¹⁶ Further work on this topic is in progress and is discussed in subsequent chapters. Despite a complex mechanism for toxicity, having a protic ligand offers advantages by allowing for comparison of OH bearing complexes to their OMe analogs.^{1, 16} The methoxy substituted ligands (e.g. 6,6'-dimethoxy-2,2'-bipyridine = 6,6'-dmbp) led to ruthenium complexes (e.g. $[(\text{dop})_2\text{Ru}(6,6'\text{-dmbp})]^{2+}$) that were non-toxic (in both light and dark conditions).¹⁶



Scheme 2.1. Protonation/deprotonation pathway for complexes **1**, **2**, and **3**.

Table 2.1. Thermodynamic Acidity Data for Compounds **1**, **2**, and **3**^a

Compound	Structure	p <i>K</i> _{a1}	p <i>K</i> _{a2}	p <i>K</i> _{a avg}
1_A	[(bpy) ₂ Ru(6,6'-dhbp)] ²⁺	5.26	7.27	6.3
2_A	[(phen) ₂ Ru(6,6'-dhbp)] ²⁺	5.2(2)	6.8(2)	6.0(1)
3_A	[(dop) ₂ Ru(6,6'-dhbp)] ²⁺	5.0(2)	6.8(2)	5.9(1)

^aThe p*K*_a data has been previously reported.^{1, 17} Standard deviation shown in parenthesis.

In this work, log(*D*_{o/w}) is measured as a function of pH and what this data implies for the mechanism of cellular uptake is discussed. Distribution coefficient (*D*) is used rather than *P* (partition coefficient which is frequently used for aprotic compounds⁹) because *D* is more appropriate for ionizable compounds. *D*_{o/w} refers to the concentration of all ruthenium species in octanol divided by the concentration of all ruthenium species in water. Log(*D*_{o/w}) gives a rough estimate of drug uptake by passive diffusion. Lipophilic complexes display positive Log(*D*_{o/w}) values that are ideally between 2 and 6 for good cellular uptake with sufficient water solubility for drug administration.^{7, 17-19} While prior work discussed Log(*D*_{o/w}) values at pH 7.4, this work is the first example of measuring the distribution coefficient as a function of pH for a protic metallo-prodrug. Therefore, these results can elucidate how uptake by passive diffusion will vary in different pH environments. It is well-established that cancer cells and hypoxic tumors can acidify their surroundings due to metabolic abnormalities including an overreliance on fermentation.²⁰⁻²² This is known as the aerobic glycolysis or the Warburg effect. This leads to the expectation that uptake by passive diffusion may vary as a function of extracellular pH. Herein, evidence is presented to suggest that the mechanism of uptake for **1-3** involves a combination of passive diffusion and active transport including predominantly efflux.

Table 2.2 Cell Viability Data for Treatment with **1-3** in the Dark and upon Irradiation for One Hour with Blue Light (450 nm)^a

MDA-MD-231 (breast CSC)				MCF7 (breast cancer)		
Compound	EC ₅₀ dark	EC ₅₀ light	PI ^b	EC ₅₀ dark	EC ₅₀ light	PI
1	>1000	290(10)	>3.4	>500	>500	~1
2	280(10)	83(3)	3.4(1)	490(20)	180(10)	2.8(2)
3	190(10)	3.7(2)	52(3)	490(20)	4.1(4)	120(10)

MCF10A (normal)				vs HeLa (cervical cancer)		
Compound	EC ₅₀ dark	EC ₅₀ light	PI ^b	EC ₅₀ dark ^c	EC ₅₀ light ^c	PI
1	>500	210(10)	>2.4	148	202	0.73
2	110(10)	13(1)	9(1)	1440	383	3.8
3	58(1)	29(5)	2.0(3)	730	120	6

^aIC₅₀ values are in μM and were previously reported.¹

^bThe phototoxicity index (PI) is the ratio of IC₅₀ in the dark to IC₅₀ in the light.

^cThe ESD's for HeLa EC₅₀'s are $\pm 0.01 \mu\text{M}$

2.3 Results and Discussion

2.3.1 Interpreting $\text{Log}(D_{o/w})$ values in terms of the pK_a values and the lipophilicity of each species.

The $\text{Log}(D_{o/w})$ values are measured across a pH range of 4.00-8.00 in acetate or phosphate buffer (Table 2.3 and Figures 2.1-2.3). This range of pH values allowed me to quantify the lipophilicity of the acidic form (**X_A**) at low pH and the basic form (**X_B**) at high pH. Across the pH range, compound **3** generally had the highest $\text{Log}(D_{o/w})$ values followed by compounds **2** and **1**. For complex **1**, Figure 2.1 shows the $\text{Log}(D_{o/w})$ values as a function of pH as blue diamonds. The mole fractions of **1_A** (in yellow), the monoprotic form of **1** (in green), and **1_B** were calculated based upon the pK_a values and superimposed on this plot.²³ Each observed $\text{Log}(D_{o/w})$ value was assumed to arise from a weighted average of the $\text{Log}(D_{o/w})$ values for each protonation state and the mole fraction of that protonation state. This allowed for the calculation

of a predicted $\text{Log}(D_{o/w})$ value at each pH value based upon the generated line of best fit. The results of this analysis are shown in Table 2.4. The $\text{Log}(D_{o/w})$ values for \mathbf{X}_A and \mathbf{X}_B are known more precisely than for the monoprotic species. At low pH, the observed $\text{Log}(D_{o/w})$ arises from mostly \mathbf{X}_A in solution and at high pH the $\text{Log}(D_{o/w})$ arises from mostly \mathbf{X}_B in solution. However, even at intermediate pH values (e.g. pH 6.0 to 6.6 for **1**) where ~80-83 % of the monoprotic species is present, there is still a significant amount of $\mathbf{1}_A$ and $\mathbf{1}_B$ at these pH values. Thus, the value obtained for $\text{Log}(D_{o/w})$ for the monoprotic species is highly dependent on what value is assigned to $\mathbf{1}_A$ and $\mathbf{1}_B$ based upon the high and low pH data.

Table 2.3. $\text{Log}(D_{o/w})$ Values for Compounds **1**, **2**, and **3**^a

		1	2	3
	pH	$\text{Log}(D_{o/w})$	$\text{Log}(D_{o/w})$	$\text{Log}(D_{o/w})$
0.1M Acetate Buffer	4.00	0.04(3)	0.17(1)	0.83(2)
	5.00	0.11(2)	0.68(6)	1.33(2)
	5.25	-	-	1.37(3)
0.1M Phosphate Buffer	5.80	-	1.3(1)	-
	6.00	0.57(2)	1.0(1)	1.45(1)
	6.60	1.10(2)	-	-
	6.70	-	1.4(2)	-
	7.00	1.18(1)	1.5(1)	1.62(4)
	7.40	1.36(1)	1.63(5)	1.81(5)
	8.00	1.39(2)	1.7(2)	2.10(6)

^aAll $\text{Log}(D_{o/w})$ values were measured in quadruplicate.

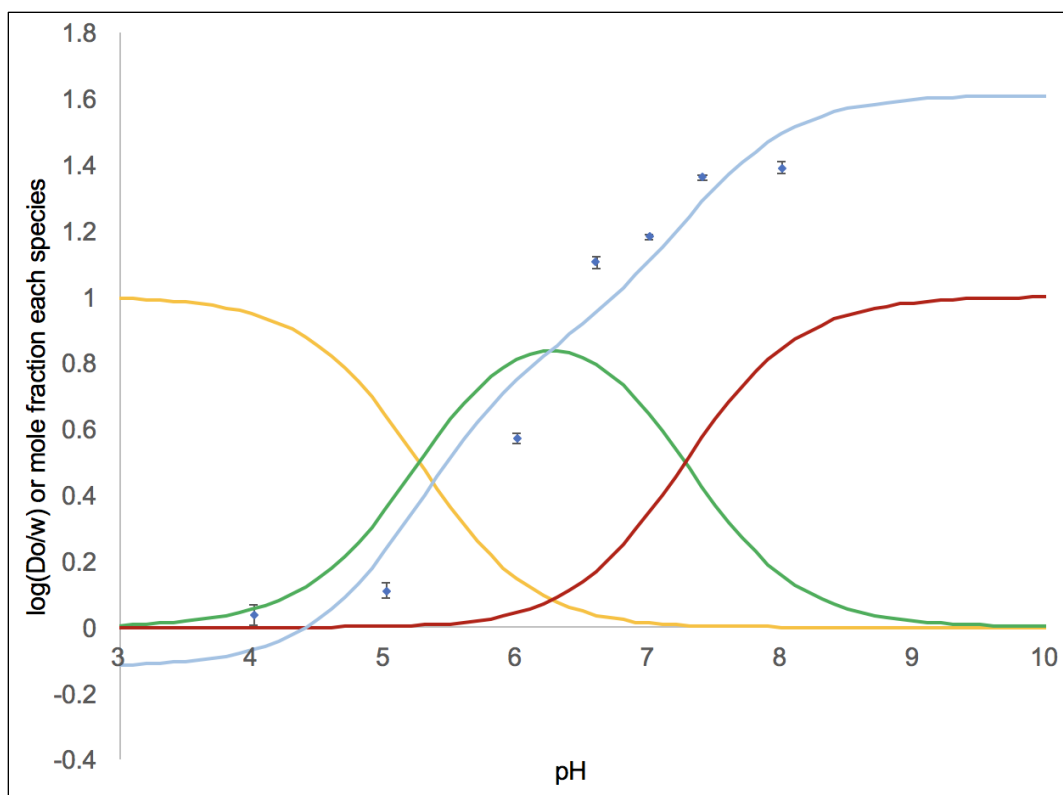


Figure 2.1. Log($D_{o/w}$) as a function of pH data for **1** is shown by the blue diamonds with error bars. The pK_a values were used to calculate the proportion of the diprotic acid **1_A** (shown in yellow), the monoprotic species (in green), and the conjugate base **1_B** (in red). The curve fit in light blue shows that predicted Log($D_{o/w}$) values of -0.1 for **1_A**, 0.9 for the monoprotic species, and 1.6 for **1_B** produce a satisfactory fit. To generate the fit, the Log($D_{o/w}$) values for these species were empirically varied until the predicted Log($D_{o/w}$) (as a weighted average considering the proportion of each species and its Log($D_{o/w}$) value) closely matched the observed Log($D_{o/w}$) at each pH.

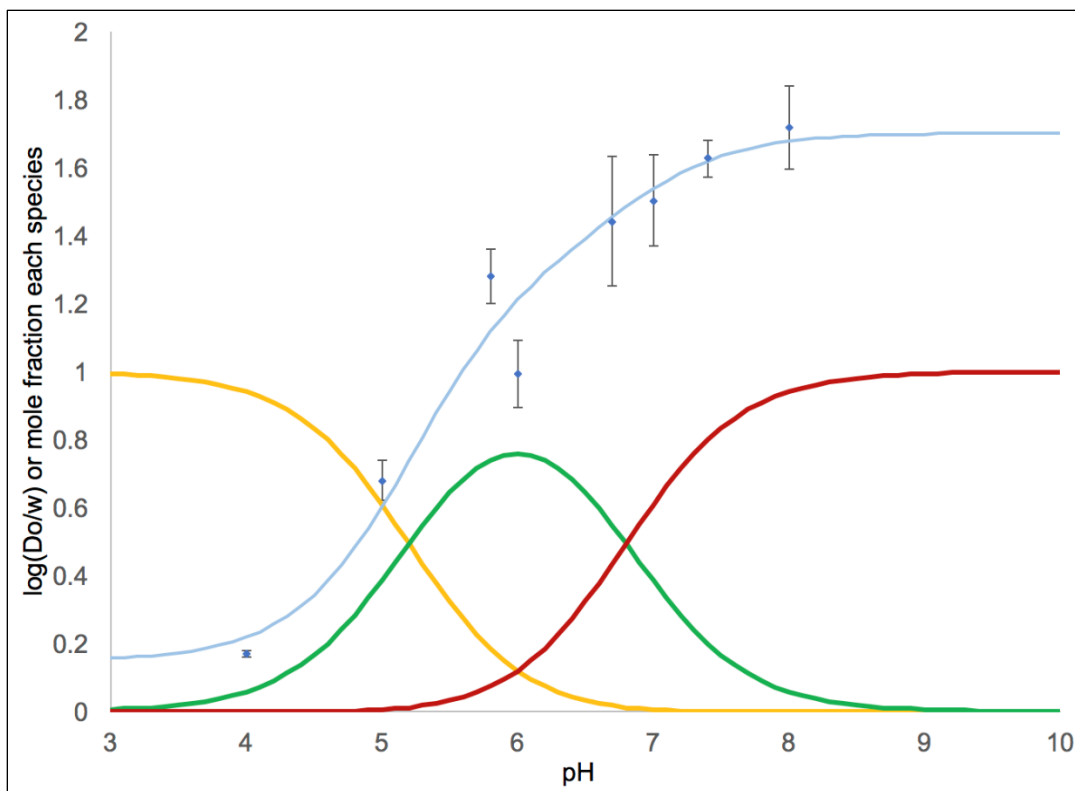


Figure 2.2. $\text{Log}(D_{o/w})$ as a function of pH data for **2** is shown by the blue diamonds with error bars. The $\text{p}K_a$ values were used to calculate the proportion of the diprotic acid **2_A** (shown in yellow), the monoprotic species (in green), and the conjugate base **2_B** (in red). The curve fit in light blue shows that predicted $\text{Log}(D_{o/w})$ values of 0.2 for **2_A**, 1.3 for the monoprotic species, and 1.7 for **2_B** produce a satisfactory fit. To generate the fit, the $\text{Log}(D_{o/w})$ values for these species were empirically varied until the predicted $\text{Log}(D_{o/w})$ (as a weighted average considering the proportion of each species and its $\text{Log}(D_{o/w})$ value) closely matched the observed $\text{Log}(D_{o/w})$ at each pH.

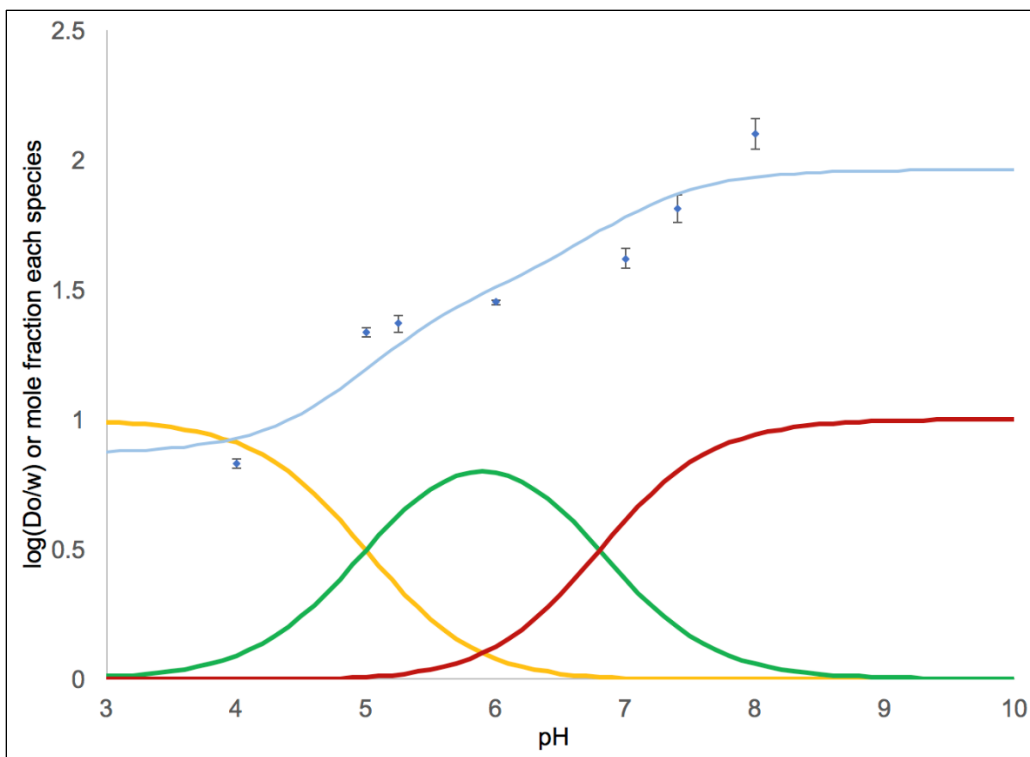


Figure 2.3. $\text{Log}(D_{o/w})$ as a function of pH data for **3** is shown by the blue diamonds with error bars. The $\text{p}K_a$ values were used to calculate the proportion of the diprotic acid **3_A** (shown in yellow), the monoprotic species (in green), and the conjugate base **3_B** (in red). The curve fit in light blue shows that predicted $\text{Log}(D_{o/w})$ values of 0.9 for **3_A**, 1.5 for the monoprotic species, and 2.0 for **3_B** produce a satisfactory fit. To generate the fit, the $\text{Log}(D_{o/w})$ values for these species were empirically varied until the predicted $\text{Log}(D_{o/w})$ (as a weighted average considering the proportion of each species and its $\text{Log}(D_{o/w})$ value) closely matched the observed $\text{Log}(D_{o/w})$ at each pH.

Table 2.4. Estimated $\text{Log}(D_{o/w})$ Values for Protonation States of **1**, **2**, and **3**^a

	1	2	3
	$\text{Log}(D_{o/w})$	$\text{Log}(D_{o/w})$	$\text{Log}(D_{o/w})$
Acidic Form (X_A)	-0.1	0.2	0.9
Monoprotic Acid	0.9	1.3	1.5
Basic Form (X_B)	1.6	1.7	2.0

^aEstimated $\text{Log}(D_{o/w})$ values are determined from the best fit in Figures 2.1-2.3. The errors in these values are hard to quantify but can be considered +/- 0.2.

Examining this data more closely (Tables 2.3 and 2.4, Figures 2.1-2.3), at physiological pH (7.4) the mole fractions of **1_B**, the monoprotic species, and **1_A** are ~0.57, 0.42 and 0.003, respectively. This leads to the observed Log($D_{o/w}$) of 1.36(1) at pH 7.4, where the major species is **1_B**. For **2**, lower pK_a values (Table 2.1) lead to mole fractions for **2_B**, the monoprotic species, and **2_A** of ~0.80, 0.20 and 0.001, respectively, and the observed Log($D_{o/w}$) is 1.63(1) at pH 7.4. Here the increased acidity allowed the lipophilicity of **2_B** to dominate, even though the Log($D_{o/w}$) values for **1_B** and **2_B** are similar. Finally, for **3**, the pK_a values and the fraction of each species at pH 7.4 (~0.8, 0.2, and 8×10^{-4} , respectively) are similar to that seen for **2**. Therefore, the lipophilicity increases from **2** to **3** (Log($D_{o/w}$) is 1.81(5) at pH 7.4 for **3**) is due to the structure of **3** including more aliphatic rings rather than the pK_a values, which are similar.

Comparing the acidic forms (**X_A**) to the basic forms (**X_B**), doubly deprotonating the ligand and forming a neutral species allows the Log($D_{o/w}$) values to increase by ~1.7 (for **1**) to ~1.1 (for **3**) orders of magnitude. Similarly, [(phen)₂Ru(6,6'-dmbp)]²⁺ and [(dop)₂Ru(6,6'-dmbp)]²⁺ were synthesized (where 6,6'-dmbp = 6,6'-dimethoxy-2,2'-bipyridine), are aprotic, and displayed negative Log($D_{o/w}$) values of -1.3(2) and -1.1(1), respectively.¹⁶ The increased hydrophilicity can be attributed to the 2+ charge on each complex that results from using the 6,6'-dmbp ligand in place of 6,6'-dhbp. A lack of toxicity (in the dark and the light) for these compounds was attributed primarily to both unfavorable hydrophobicity and secondarily to mechanistic differences in light activation.¹⁶

2.3.2 Variations in the pH External (pH_e) of the Cell Lines Studied and Implications for the Mechanism of Cellular Uptake.

At this stage, it is hypothesized that variations in the external pH (pH_e) could lead to differences in ruthenium complex uptake by passive diffusion, and one would expect a lower pH_e

would lead to less uptake. Therefore, the Kim group measured the decrease in pH_e over 48 h without changing the media in one non-cancerous (normal) breast epithelial cell line (MCF10A), two breast cancer cell lines (MCF7 and MDA-MB-231), and in one cervical cancer cell line (HeLa) (Table 2.5). The results showed that HeLa cells acidified their surroundings more than the breast cell lines. While HeLa had relatively low uptake as expected, the correlation between $\Delta(\text{pH}_e)$ and cellular uptake of complex **3** as measured by mean fluorescence intensity (MFI) was not consistent across all cell lines (Table 2.5). This suggests that passive diffusion may not be the only factor. The observed uptake appears to be related to both uptake by passive diffusion and efflux (by active transport) as described below. Furthermore, during most experiments (e.g. those leading to MFI and IC_{50} data in Table 2.5), the media was changed regularly, which prevented a significant pH_e drop. Thus, although certain cell lines do acidify the surroundings more than the others, the media supplied results in a similar pH_e observed in practice from cell line to cell line.

Table 2.5. The Change in pH_e over 48 h in Various Cell Lines and Uptake of Complex **3**.

Cell Line	$\Delta(\text{pH}_e)$ over 48 h ^a	MFI ^b	EC_{50} Dark for 3 ^c	EC_{50} Light for 3 ^c
MCF10A	-0.32 ± 0.01	1189 ± 654	58	29
MDA-MD-231	-0.49 ± 0.09	181 ± 84	190	3.7
MCF7	-0.12 ± 0.03	596 ± 206	490	4.1
HeLa	-0.88 ± 0.07	322 ± 134	730	120

^aThe external pH was monitored for 48 h without changing the media. Each result is the average of five experiments.

^bMean fluorescence intensity (MFI) is proportional to uptake of **3**. All cell lines were treated with 50 μM of **3** in the dark. These experiments were under typical conditions which included changing the media regularly.

^c EC_{50} values were reported previously and are shown in μM .¹

2.3.3 Cellular uptake and efflux mechanism for complex **3**.

It is hypothesized that the specific cytotoxicity of complex **3** could be related to its cellular uptake. To test this hypothesis, the Kim group treated cells with various concentrations

of complex **3** and measured the uptake by utilizing the inherent fluorescence of the Ru complex. Herein, the Kim Group measured MFI by flow cytometry to provide a qualitative measure of uptake; and while this information is not quantitative and it has limitations (see Materials and Methods section), it can provide a useful means of comparing uptake in different cell lines and under different conditions. As such, it has been used by other researchers to determine the mechanism of ruthenium drug uptake in cells.^{3, 4, 24} In all cell lines at 50 μM of complex **3**, two distinct populations are observed (Figure 2.4). All cancer cells (i.e., all except MCF10A) showed higher uptake of complex **3** in the shrunk cell population (Figure 2.4). Cell shrinkage appears to be a result of the uptake of complex **3** in cancer cells.

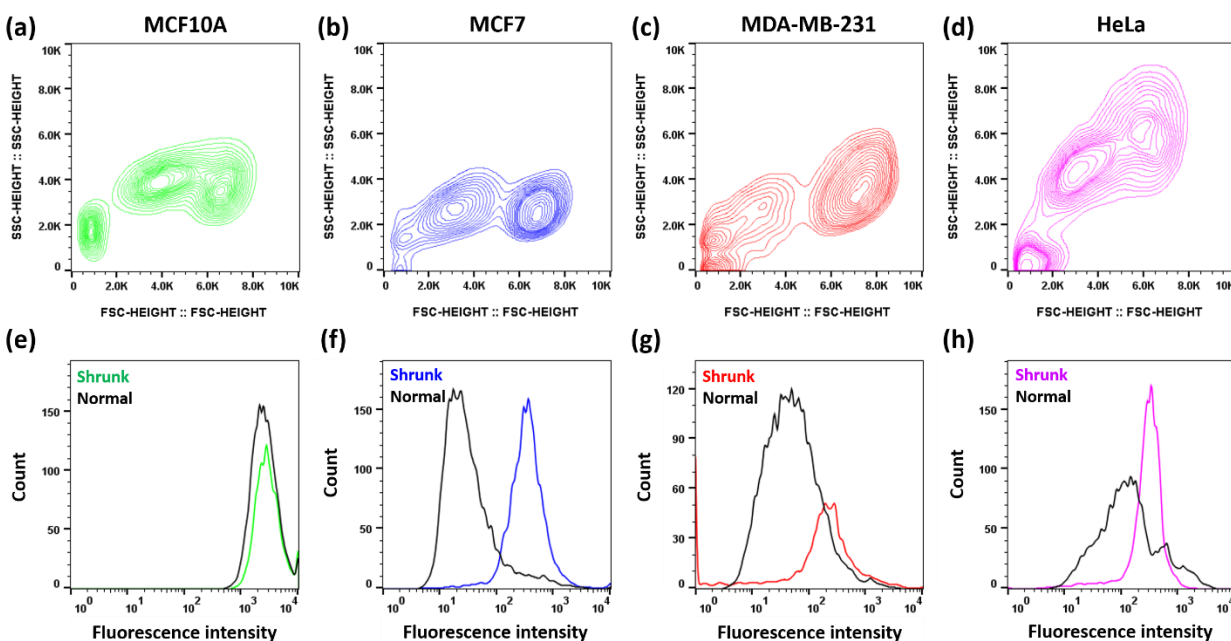


Figure 2.4. MCF10A, MCF7, MDA-MB-231, and HeLa cells were administered with 50 μM of **3_A** and were studied by flow cytometry. (a – d) Flow cytometry contour plots of cell size and granularity were detected using forward scatter (FSC) and side scatter (SSC), respectively. Cell debris was detected at bottom left corner for all cell lines ($\leq 2.0\text{K}$ SSC, $\leq 2.0\text{K}$ FSC). The population on the left indicates cells with smaller sizes, i.e., shrunk cells (FSC 2.0K-4.0K), whereas the population on the right indicates cells with normal sizes (FSC $\geq 5.0\text{K}$). (e – h) Flow cytometry histogram analysis shows fluorescence intensity which is proportional to the Ru concentration. Shrunk and normal cells correspond to the same populations from a-d.

The uptake of complex **3** was measured by mean fluorescence intensity (MFI) as a function of the concentration for the shrunk population using flow cytometry (Figure 2.5). In all samples, the MFI is directly proportional to external Ru concentration. This implies that the dominant mechanism of Ru uptake was via passive diffusion. Interestingly, a higher uptake of complex **3** with the non-cancerous cell line MCF10A versus the other cell lines is observed, which may explain why a relatively high dark toxicity was observed for **3** versus MCF10A ($IC_{50} = 58 \mu\text{M}$).

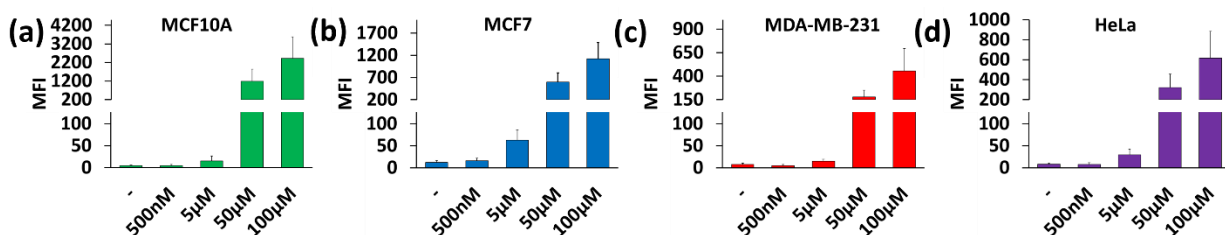


Figure 2.5. Cellular uptake of **3_A** as a function of concentration (x axis) is proportional to the mean fluorescence intensity (MFI) \pm SD (y axis). Cells were treated with 0 – 100 μM of **3_A** in the dark. (a) MCF10A. (b) MCF7. (c) MDA-MB-231. (d) HeLa. The no drug control (-) shows the inherent fluorescence for the cells in the absence of **3_A**.

Furthermore, to determine if light enhances uptake, the Kim group measured drug uptake both in the dark and under blue-light irradiation conditions (Figure 2.6). No increase in uptake upon light irradiation was observed. In all cell lines except MCF10A, light irradiation caused an apparent decrease in uptake, which can better be interpreted as light leading to cell death in these cells with sufficient uptake; thus, only the cells with low uptake survive and are observed. Further experiments to probe photoactivated uptake are discussed below.

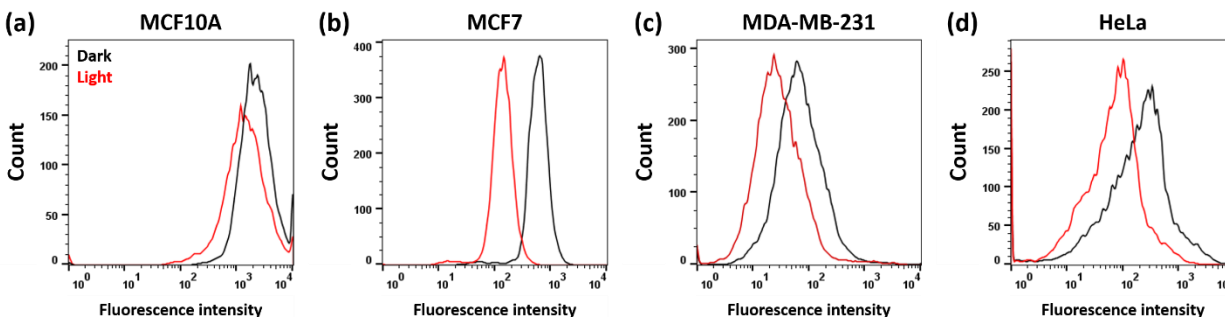


Figure 2.6. Representative flow cytometry analysis of the influence of light on cellular uptake of 50 μM of **3A**. Fluorescence intensity is proportional to the Ru concentration in cells. (a) MCF10A. (b) MCF7. (c) MDA-MB-231. (d) HeLa. This data suggests that light does not cause increased uptake.

Others have used metabolic inhibitors such as deoxyglucose and oligomycin to determine whether uptake and efflux is energy dependent or independent.^{3, 4} The Kim group tested the impact of deoxyglucose and oligomycin on cellular uptake of **3** in a variety of cell lines (Figure 2.7). When ATP production was inhibited, a significantly higher MFI is observed in all cancer cell lines (i.e., all cell lines except MCF10A). Since this shows a higher uptake of **3** with metabolic inhibition, this ruled out the possibility of energy-dependent active transport of the complex into the cells. On the contrary, this suggests that there may be an energy-dependent efflux of the compounds out of the cancer cells in normal cell culture conditions. This is not surprising as the high activity of efflux pumps is a known characteristic of cancer cells and have been previously attributed to their drug resistance.²

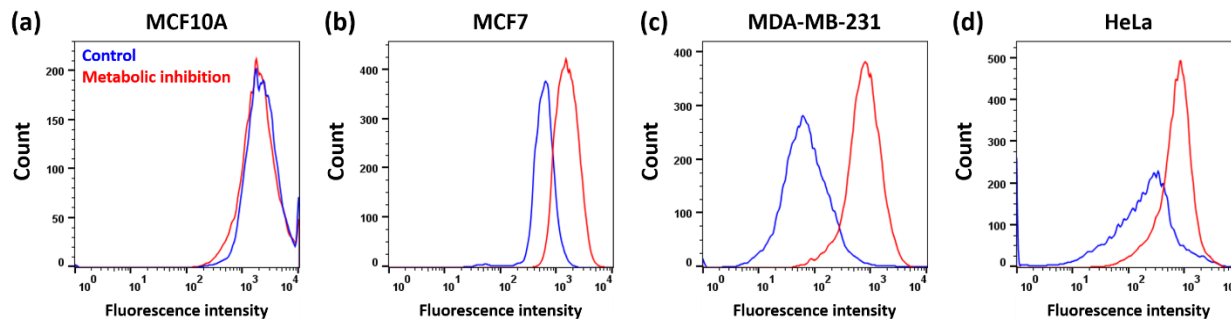


Figure 2.7. Representative flow cytometry analysis of cellular uptake of 50 μM of **3_A** as measured by MFI in the dark under normal metabolism (control in blue) and under metabolic inhibition conditions (with deoxyglucose and oligomycin in red). (a) MCF10A. (b) MCF7. (c) MDA-MB-231. (d) HeLa. Fluorescence intensity is proportional to the Ru concentration in cells.

2.3.4 Subcellular localization of the ruthenium complex **3**.

Despite the relatively low uptake of complex **3** in MDA-MB-231 and MCF7 (as compared to MCF10A), complex **3** showed a promising light-dependent cytotoxicity in these breast cancer cell lines.¹ Many cytotoxic ruthenium complexes have been shown to localize in the nucleus of cells and bind to DNA.^{5, 25, 26} Thus, the Kim group studied the localization of **3** by using fluorescence microscopy after its uptake in three cancer cell lines, MDA-MB-231, MCF7, and HeLa (Figure 2.8). Cellular uptake was visualized in the dark and upon irradiation with blue light to determine if light influences subcellular localization. The normal cells, MCF10A, were also treated with complex **3** in the dark and visualized (Figure 2A.7). Interestingly, the Ru complex was localized in the nucleus after the treatment with **3** in the dark in all four cell lines. Light irradiation did not increase the amount of complex **3** in the cells, and this result suggests either that photoactivated uptake is not occurring or that the laser light used for the fluorescence imaging in the “dark” experiments in Figure 2.8 is sufficient to cause photoactivated uptake. In prior work,¹ uptake was measured in the dark by ICP-MS, and this suggests that photoactivated

uptake is not the major route of entry for complex 3 from the combined data.²⁵ Interestingly, nuclear localization occurred despite low up-take in several cell lines (Table 2.5). This suggests that the mode of action for light induced activity may involve either direct binding of the Ru complexes to DNA or the ability of these complexes to generate reactive oxygen species (ROS) in proximity to DNA upon light irradiation.

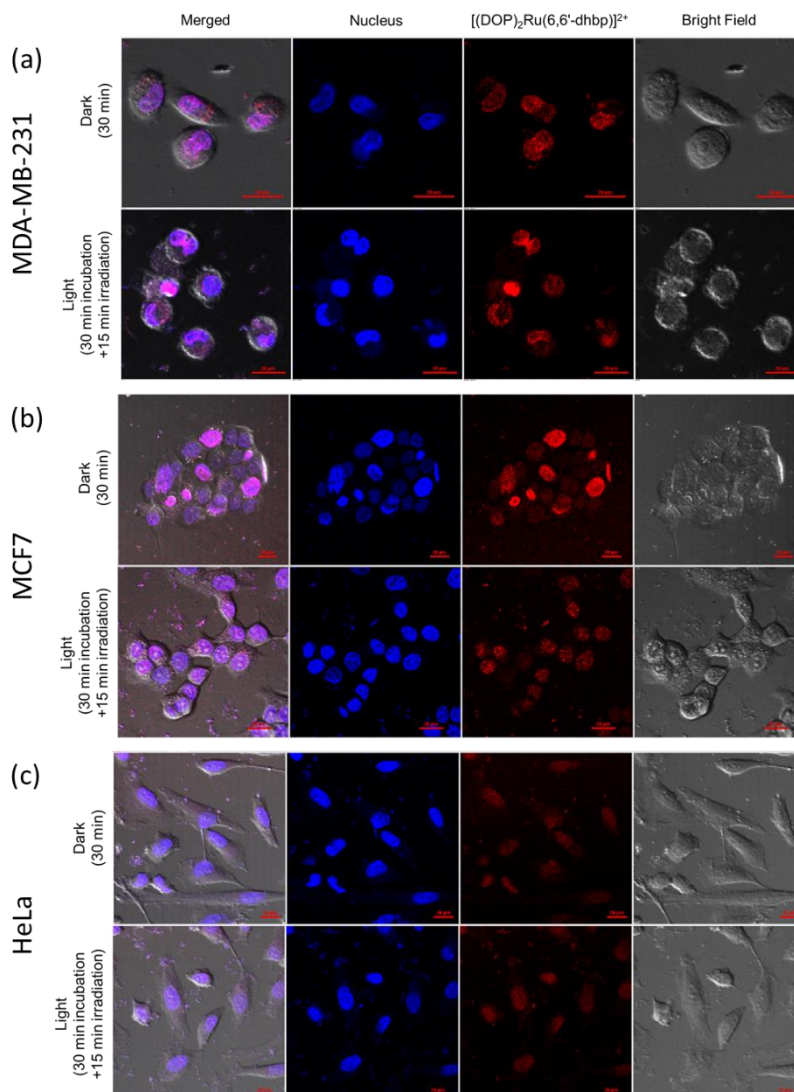


Figure 2.8. Localization of complex 3_A after treatment in the dark and in the blue light. (a) MDA-MB-231. (b) MCF7. (c) MCF10A. Ru complex (TRITC; red), nuclei (Hoechst 33342; blue). Scale bar: 20 μm.

2.4 Conclusion

The observed uptake of the most toxic light activated complex, **3**, results from a combination of uptake by passive diffusion and energy dependent efflux. Uptake by passive diffusion is more favorable for **3** vs. **1** or **2** due increased hydrophobicity for **3** and higher $\log(D_{o/w})$ values at each pH studied. Furthermore, a comparison of $[(\text{dop})_2\text{Ru}(6,6'\text{-dmbp})]^{2+}$ to **3** $[(\text{dop})_2\text{Ru}(6,6'\text{-dhbp})]^{2+}$ shows that the presence of the protic 6,6'-dhbp ligand increases the hydrophobicity by nearly 3 $\log(D_{o/w})$ units (-1.1(1) to 1.81(5), respectively, at pH 7.4). For compounds **1**, **2**, and **3**, going from the acidic form ($\mathbf{X_A}$) to the basic form ($\mathbf{X_B}$) increases the $\log(D_{o/w})$ values by 1.1 (for **3**) to 1.7 (for **1**). Thus, cellular $\Delta(\text{pH}_e)$ was measured (without changing the media for 48 h) and may be expected to influence uptake by passive diffusion in scenarios where pH_e is not tightly controlled (e.g. hypoxic solid tumors). For example, externally acidic cancerous cells displaying the Warburg phenotype are expected to display less uptake of protic metallodrugs; this prediction was born out for HeLa cells with acidification of the surrounding and relatively low uptake (Table 2.5). However, in practice frequently changing the media for cultured cancer cells prevents a significant change in pH_e and thus the Warburg phenotype was not well correlated with decreased uptake in all cell lines that were studied.

By investigating the influence of metabolic inhibition, it is observed that MDA-MB-231 cells show the greatest increase in Ru uptake when ATP production is inhibited. This suggests that this cell line has more efflux pumps that under normal metabolic conditions pump out complex **3** to counteract passive diffusion into the cell. This results in the lowest concentration of **3** in the MDA-MB-231 cells by MFI. In contrast, the cell line MCF10A shows no difference in the concentration of **3** in cells with and without metabolic inhibition. This shows a lack of efflux pumps for this normal cell line, and passive diffusion into the cells without efflux leads to a

higher concentration of **3** in these cells (Table 2.5). The remaining cell lines (MCF7 and HeLa) are intermediate in showing some efflux out of the cells and thus intermediate uptake by MFI values. Subcellular localization studies show that **3** goes readily to the nucleus in the dark in each cancerous cell line. The highest net uptake of **3** appears to lead to the highest dark toxicity in MCF10A. However, the data does not suggest an explanation for why greater light activated toxicity is seen in certain cell lines (MDA-MB-231 and MCF7). Most likely, this relates to the inherent vulnerability of these cell lines to generated ROS rather than simply being correlated with uptake alone. Good uptake is required for toxicity and this chapter has explored the factors (passive diffusion and efflux) that influence uptake, but uptake alone is not sufficient for light driven toxicity.

2.5 Materials and Methods

2.5.1 Materials and Instrumentation

1-Octanol (99.99 %) was purchased from Acros Organics and used without further purification. Compounds **1-3** were synthesized using published methods without modification.¹
¹⁴ Buffer solutions for Log($D_{o/w}$) measurements were prepared fresh at 0.1M acetate (pH 4.00-5.25) or 0.1M phosphate (pH 5.8-8.0). UV-Visible spectra were collected on a Perkin Elmer Lambda 35 spectrometer and measured in the range of 300-700 nm.

2.5.2 Log($D_{o/w}$) as a function of pH Measurements

Octanol and buffer at a given pH were mixed in a 1:1 ratio and stirred for 24 h before use to ensure the solutions were saturated with the corresponding solution. The procedure used to measure Log($D_{o/w}$) as a function of pH was a modified “shake flask” method that was deemed acceptable for use by measuring the Log($D_{o/w}$) at pH 7.4 of 5-fluorouracil and comparing those

results to reported literature values.²⁷ These experiments were carried out under dark conditions to protect the compounds from light exposure.^{1, 27-29} As a general procedure, the ruthenium compound of interest (200 μ M) was first dissolved in *n*-octanol saturated with buffer. A portion of this solution (5 mL) was then mixed with an equal volume of buffer saturated with *n*-octanol and gently stirred for 24 h at ambient temperature while avoiding light exposure. Afterwards, an aliquot was removed from the aqueous phase, filtered, and the absorbance was measured via UV-Vis spectroscopy to determine the concentration in the aqueous phase. Typical procedures call for centrifugation of the solution;^{30, 31} however, due to the light-sensitive nature of the analyzed complexes, the samples were filtered while being prepared in a dark room. A small amount of white precipitate was observed in the octanol phase which was believed to be insoluble buffer salts and not the compounds of interest which are deeply colored. From this data, the concentration of the compound in the organic phase was calculated and used to establish a $\text{Log}(D_{o/w})$ value (Eq. 2.1). All measurements were done in quadruplicate at a given pH value with the average $\text{Log}(D_{o/w})$ reported.

$$\text{Eq. 2.1 } \log(D_{o/w}) = \log([Ru]_{org}/[Ru]_{Aq})$$

2.5.3 Analysis of $\text{Log}(D_{o/w})$ Data and Fraction of Species

*Fraction of Species*²³

For compounds **1-3**, the mole fraction of each species at any given pH was calculated using equations 2.2-2.4²³ and previously published pK_a values (Table 2.1).¹ The data was then plotted in Excel.

$$\text{Eq. 2.2} \quad f_{H_2A} = \frac{[H^+]^2}{[H^+]^2 + K_{a1}[H^+] + K_{a1}K_{a2}}$$

$$\text{Eq. 2.3} \quad f_{HA^-} = \frac{K_{a1}[H^+]}{[H^+]^2 + K_{a1}[H^+] + K_{a1}K_{a2}}$$

$$\text{Eq. 2.4} \quad f_{A^{2-}} = \frac{K_{a1}K_{a2}}{[H^+]^2 + K_{a1}[H^+] + K_{a1}K_{a2}}$$

Determining $\text{Log}(D_{o/w})$ Fit for **1-3**

To generate the fit, the $\text{Log}(D_{o/w})$ values for these species were empirically varied until the predicted $\text{Log}(D_{o/w})$ (as a weighted average considering the proportion of each species and its $\text{Log}(D_{o/w})$ value, see Eq. 2.5) closely matched the observed $\text{Log}(D_{o/w})$ at each pH. For complexes **1-3**, the calculated fraction of species (Eq's 2.2-2.4) and empirically determined $\text{Log}(D_{o/w})$ values for $[\text{Ru}]^{2+}$, $[\text{Ru}]^+$, and $[\text{Ru}]^0$ (Table 2.4) were used to determine the predicted $\text{Log}(D_{o/w})$ value at a given pH (Eq. 2.5). The predicted $\text{Log}(D_{o/w})$ for each species (Table 2.4) were varied until optimal residual sum of squares values were reached (Table 2.6). Residual plots can be found in the appendix (Figures 2A.1-2A.3).

Table 2.6 Residual sum of squares for complexes **1-3** as determined from the measured $\text{Log}(D_{o/w})$ data and predicted $\text{Log}(D_{o/w})$ values

	Complex		
	1	2	3
Residual Sum of Squares	-0.102	0.0394	0.0942

Eq. 2.5 Predicted $\text{Log}(D_{o/w})$

$$= \left(f_{H_2A} \times \text{Log}(D_{o/w})_{[\text{Ru}]^{2+}} \right) + \left(f_{HA^-} \times \text{Log}(D_{o/w})_{[\text{Ru}]^+} \right) \\ + \left(f_{A^{2-}} \times \text{Log}(D_{o/w})_{[\text{Ru}]^0} \right)$$

2.5.4 Cell Culture-Kim Group

HeLa, MCF7, MDA-MB-231, and MCF10A cell lines were purchased from ATCC. HeLa, MCF7, and MDA-MB-231 were grown with DMEM (Gibco, 21063-029) supplemented with 10 % FBS (Gibco, 26140079). MCF10A was grown with MEGM (Lonza Walkersville CC4136). All cells were grown in humidified incubators at 37°C with 5 % CO₂.

2.3.5 pH External of Various Cell Lines-Kim Group

Cells (3×10^5) were seeded in a 6 well plate and incubated for overnight to let them adhere to the plate. Media was replaced once, and the pH was measured over 48 h using a Mettler Toledo pH meter.

2.5.6 Measuring Uptake of the Ru Complex 3 at Varying Concentrations by Flow Cytometry-Kim Group

Cells were treated with 500 nM, 5 μM, 50 μM, and 100 μM of complex **3** in a dark room and incubated for 1 h at 37 °C. After incubation, cells were washed with phosphate buffered saline (PBS) and then irradiated by blue light (Philips, goLITE) for 30 min at 37 °C. Uptake of Ru was detected in FL4 channel using Bio-Rad S3e sorter and measured by mean fluorescent intensity (MFI). There is precedence in the literature for measuring uptake of ruthenium complexes by MFI using flow cytometry.^{3, 4, 24} It is noted that there are limitations to using MFI to determine uptake. Here, the inherent luminescence of the ruthenium complexes is observed, and this luminescence is sensitive to the local environment. It cannot rule out the possibility that certain biological molecules may quench the excited state for the ruthenium complexes, and this may produce less MFI in certain cellular environments.

2.5.6 Measuring Uptake of the Ru Complex 3 Under Metabolic Inhibition-Kim Group

Uptake of complex **3** was analyzed during inhibition of metabolic activity following a procedure from the Barton group.⁴ Briefly, cells were treated with 50 mM of 2-deoxy-D-glucose (Acros Organics, 111980010) and 5 μ M of oligomycin A (Tocris Bioscience, 4110/5) in PBS for 1 h at 37°C with 5 % CO₂ and washed with phosphate-buffered saline (PBS). After the inhibition, cells were treated with various concentrations of **3** in PBS for the metabolic activity inhibition samples and media for the control samples. Then, the uptake of the Ru compound was analyzed by flow cytometry.

2.5.7. Immunofluorescence Imaging of Ru Localization-Kim Group

Cells were seeded in a chamber slide (Greiner Bio-One, 543079) and incubated overnight at 37°C and analyzed for stable attachment. nuclei were stained using Hoechst 33342 (Invitrogen, H1399) 5 μ M of complex **3** was added to cells in the dark room for 30 min. After incubation, the cells were irradiated by blue light to activate the complex for 15 min. All images were acquired within 5 min after incubation and irradiation, using Nikon C2+ confocal microscope. Cells were counted using Bio-Rad's T20 automated cell counter.

2.6 Acknowledgements

This work was supported by the National Science Foundation EPSCoR Track 2 Grant (OIA-1539035), the Undergraduate Creativity and Research Academy (UCRA) at UA, the Research Grants Committee (RGC) at UA, and the Alabama Commission on Higher Education Fellowship (to Seungjo Park). We thank the NSF REU (CHE 1358971) program for full support to Angela Hairston and partial support to Sarah Altman. We also acknowledge support from NIH (R15-GM132803-01).

References

- [1] Qu, F., Park, S., Martinez, K., Gray, J. L., Thowfeik, F. S., Lundeen, J. A., Kuhn, A. E., Charboneau, D. J., Gerlach, D. L., Lockart, M. M., Law, J. A., Jernigan, K. L., Chambers, N., Zeller, M., Piro, N. A., Kassel, W. S., Schmehl, R. H., Paul, J. J., Merino, E. J., Kim, Y., and Papish, E. T. (2017) Ruthenium Complexes are pH-Activated Metallo Prodrugs (pHAMPs) with Light-Triggered Selective Toxicity Toward Cancer Cells, *Inorg. Chem.* *56*, 7519-7532.
- [2] Spreckelmeyer, S., van der Zee, M., Bertrand, B., Bodio, E., Sturup, S., and Casini, A. (2018) Relevance of copper and organic cation transporters in the activity and transport mechanisms of an anticancer cyclometallated gold(III) compound in comparison to cisplatin, *Front. Chem. (Lausanne, Switz.)* *6*, 377/371-377/315.
- [3] Puckett, C. A., and Barton, J. K. (2007) Methods to Explore Cellular Uptake of Ruthenium Complexes, *J. Am. Chem. Soc.* *129*, 46-47.
- [4] Puckett, C. A., and Barton, J. K. (2008) Mechanism of Cellular Uptake of a Ruthenium Polypyridyl Complex, *Biochemistry* *47*, 11711-11716.
- [5] Klajner, M., Licon, C., Fetzer, L., Hebraud, P., Mellitzer, G., Pfeffer, M., Harlepp, S., and Gaidon, C. (2014) Subcellular localization and transport kinetics of ruthenium organometallic anticancer compounds in living cells: a dose-dependent role for amino acid and iron transporters, *Inorg. Chem.* *53*, 5150-5158.
- [6] Mehling, T., Kloss, L., Ingram, T., and Smirnova, I. (2013) Partition Coefficients of Ionizable Solutes in Mixed Nonionic/Ionic Micellar Systems, *Langmuir* *29*, 1035-1044.
- [7] Tardito, S., Bassanetti, I., Bignardi, C., Elviri, L., Tegoni, M., Mucchino, C., Bussolati, O., Franchi-Gazzola, R., and Marchio, L. (2011) Copper Binding Agents Acting as Copper Ionophores Lead to Caspase Inhibition and Paraptotic Cell Death in Human Cancer Cells, *J. Am. Chem. Soc.* *133*, 6235-6242.
- [8] Ingram, T., Richter, U., Mehling, T., and Smirnova, I. (2011) Modelling of pH dependent n-octanol/water partition coefficients of ionizable pharmaceuticals, *Fluid Phase Equilib.* *305*, 197-203.
- [9] Mannhold, R., Poda, G. I., Ostermann, C., and Tetko, I. V. (2009) Calculation of molecular lipophilicity: state-of-the-art and comparison of logP methods on more than 96,000 compounds, *J. Pharm. Sci.* *98*, 861-893.

- [10] Fetzer, L., Boff, B., Ali, M., Meng, X., Collin, J.-P., Sirlin, C., Gaiddon, C., and Pfeffer, M. (2011) Library of second-generation cycloruthenated compounds and evaluation of their biological properties as potential anticancer drugs: Passing the nanomolar barrier, *Dalton Trans.* *40*, 8869-8878.
- [11] Huang, H., Zhang, P., Chen, H., Ji, L., and Chao, H. (2015) Comparison Between Polypyridyl and Cyclometalated Ruthenium(II) Complexes: Anticancer Activities Against 2D and 3D Cancer Models, *Chem. - Eur. J.* *21*, 715-725.
- [12] Yoshida, F., and Topliss, J. G. (2000) QSAR Model for Drug Human Oral Bioavailability, *J. Med. Chem.* *43*, 2575-2585.
- [13] Ochsenkuehn-Petropoulou, M. T., and Tsopelas, F. N. (2004) Separation of organoselenium compounds and their electrochemical detection, *Anal. Bioanal. Chem.* *379*, 770-776.
- [14] Hufziger, K. T., Thowfeik, F. S., Charboneau, D. J., Nieto, I., Dougherty, W. G., Kassel, W. S., Dudley, T. J., Merino, E. J., Papish, E. T., and Paul, J. J. (2014) Ruthenium dihydroxybipyridine complexes are tumor activated prodrugs due to low pH and blue light induced ligand release, *J. Inorg. Biochem.* *130*, 103-111.
- [15] Papish, E. T., and Nieto, I. (2014) Patent Application filed with the US Patent Office.
- [16] Qu, F., Martinez, K., Arcidiacono, A. M., Park, S., Zeller, M., Schmehl, R. H., Paul, J. J., Kim, Y., and Papish, E. T. (2018) Sterically demanding methoxy and methyl groups in ruthenium complexes lead to enhanced quantum yields for blue light triggered photodissociation, *Dalton Trans.* *47*, 15685-15693.
- [17] Zeng, L., Chen, Y., Huang, H., Wang, J., Zhao, D., Ji, L., and Chao, H. (2015) Cyclometalated Ruthenium(II) Anthraquinone Complexes Exhibit Strong Anticancer Activity in Hypoxic Tumor Cells, *Chem. - Eur. J.* *21*, 15308-15319.
- [18] Chow, M. J., Babak, M. V., Wong, D. Y. Q., Pastorin, G., Gaiddon, C., and Ang, W. H. (2016) Structural Determinants of p53-Independence in Anticancer Ruthenium-Arene Schiff-Base Complexes, *Mol. Pharmaceutics* *13*, 2543-2554.
- [19] Tabrizi, L., and Chiniforoshan, H. (2016) New RuII pincer complexes: synthesis, characterization and biological evaluation for photodynamic therapy, *Dalton Trans.* *45*, 18333-18345.
- [20] Cardone, R. A., Casavola, V., and Reshkin, S. J. (2005) The role of disturbed pH dynamics and the Na⁺/H⁺ exchanger in metastasis, *Nat. Rev. Cancer* *5*, 786-795.
- [21] Gatenby, R. A., and Gillies, R. J. (2004) Why do cancers have high aerobic glycolysis?, *Nat. Rev. Cancer* *4*, 891-899.

- [22] Seyfried, T. N., Flores, R. E., Poff, A. M., and D'Agostino, D. P. (2014) Cancer as a metabolic disease: implications for novel therapeutics, *Carcinogenesis* 35, 515-527.
- [23] McCord, P. Fraction of Species, <https://ch301.cm.utexas.edu/help/ch302/ab/fracspeced.pdf>, Accessed January 10, 2019.
- [24] Li, X., Heimann, K., Dinh, X. T., Keene, F. R., and Collins, J. G. (2016) Biological processing of dinuclear ruthenium complexes in eukaryotic cells, *Mol. BioSyst.* 12, 3032-3045.
- [25] Svensson, F. R., Matson, M., Li, M., and Lincoln, P. (2010) Lipophilic ruthenium complexes with tuned cell membrane affinity and photoactivated uptake, *Biophys. Chem.* 149, 102-106.
- [26] Li, F., Collins, J. G., and Keene, F. R. (2015) Ruthenium complexes as antimicrobial agents, *Chem. Soc. Rev.* 44, 2529-2542.
- [27] El Maghraby, G. M. M., Williams, A. C., and Barry, B. W. (2005) Drug interaction and location in liposomes: correlation with polar surface areas, *Int. J. Pharm.* 292, 179-185.
- [28] Ghosh, G., Colon, K. L., Fuller, A., Sainuddin, T., Bradner, E., McCain, J., Monroe, S. M. A., Yin, H., Hetu, M. W., Cameron, C. G., and McFarland, S. A. (2018) Cyclometalated Ruthenium(II) Complexes Derived from α -Oligothiophenes as Highly Selective Cytotoxic or Photocytotoxic Agents, *Inorg. Chem.* 57, 7694-7712.
- [29] Morris, M. E. (2012) Drug Metabolism and Pharmacokinetics Quick Guide, *Clin. Pharmacol. Ther.* (N. Y., NY, U. S.) 91, 767-768.
- [30] Chang, S. W., Lewis, A. R., Prosser, K. E., Thompson, J. R., Gladkikh, M., Bally, M. B., Warren, J. J., and Walsby, C. J. (2016) CF3 Derivatives of the Anticancer Ru(III) Complexes KP1019, NKP-1339, and Their Imidazole and Pyridine Analogues Show Enhanced Lipophilicity, Albumin Interactions, and Cytotoxicity, *Inorg. Chem.* 55, 4850-4863.
- [31] Fang, L., Gou, S., Zhao, J., Sun, Y., and Cheng, L. (2013) Platinum(II) complexes with N-monoalkyl 1R,2R-diaminocyclohexane derivatives as carrier ligands and 3-hydroxycyclobutane-1,1-dicarboxylate as a leaving group: Potent cytotoxicity and DNA binding ability, *Eur. J. Med. Chem.* 69, 842-847.
- [32] (2020) OriginPro, Version 2020, OriginLab Corporation, Northampton, MA, USA.

2A. Appendix

2A.1 Residual analysis of $\text{Log}(D_{o/w})$ for 1-3

Residual plots were generated in OriginPro 2020 software.³²

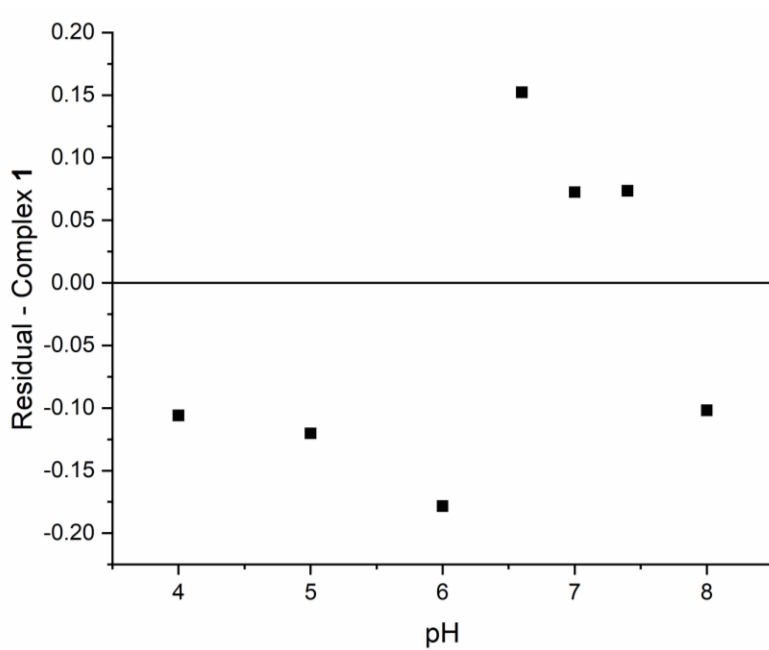


Figure 2A.1. Plotted $\text{Log}(D_{o/w})$ residuals for complex 1

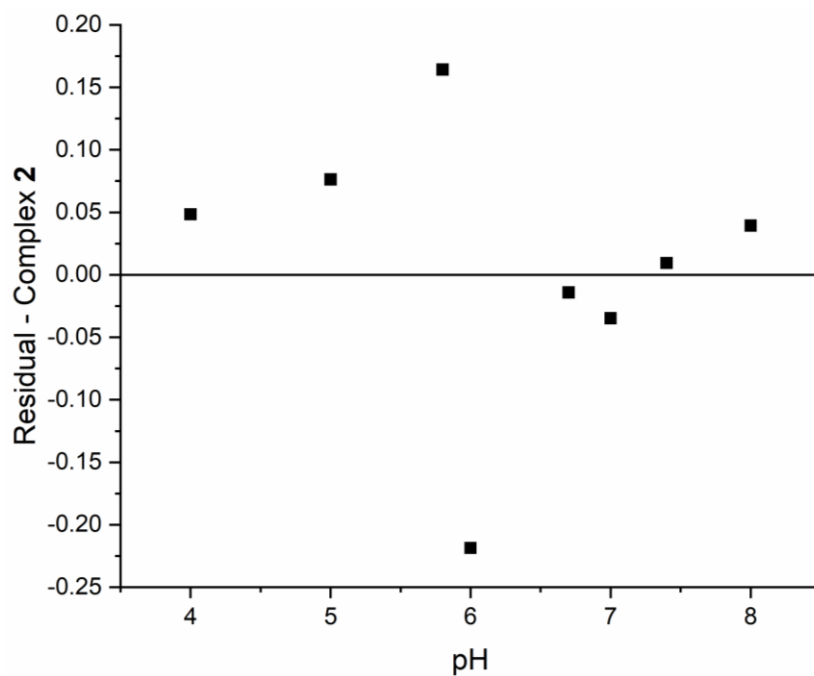


Figure 2A.2. Plotted $\text{Log}(D_{o/w})$ residuals for complex 2

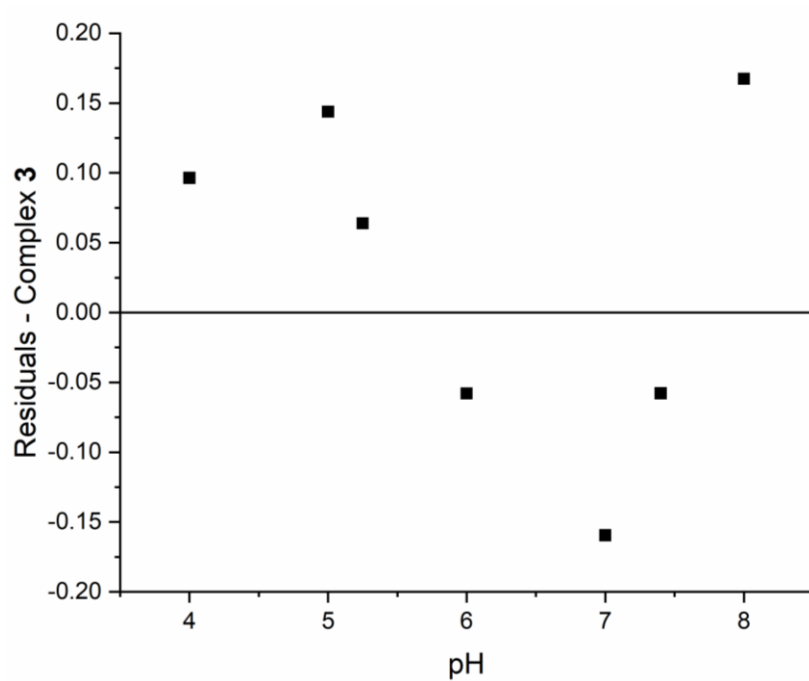


Figure 2A.3. Plotted $\text{Log}(D_{o/w})$ residuals for complex 3

2A.2 Molar absorptivity

As a general procedure, buffer was mixed in a 1:1 ratio with 1-octanol and stirred for 24 h before use to ensure the buffer was saturated with octanol before use. The “line of best fit” method was used to calculate the necessary molar absorptivity values.

Seven sample solutions ranging from 10-70 μM of the analyte in pre-saturated buffer solution were used for analysis. An aliquot of the sample solution was measured via UV-Vis (300-700 nm for ruthenium complexes and 200-500 nm for 5-fluorouracil (5-FU)). The absorbance at λ_{max} was plotted vs. the concentration (M) of the sample. The molar absorptivity was found by calculating the slope of the line of best fit with the y-int=0. Reported molar absorptivity values (ϵ) are listed in units of $\text{Lmol}^{-1}\text{cm}^{-1}$.

Sample spectra for complex **1** at pH 6.00 are shown along with all molar absorptivity values (ϵ).

2A.2.1 Ruthenium Complexes

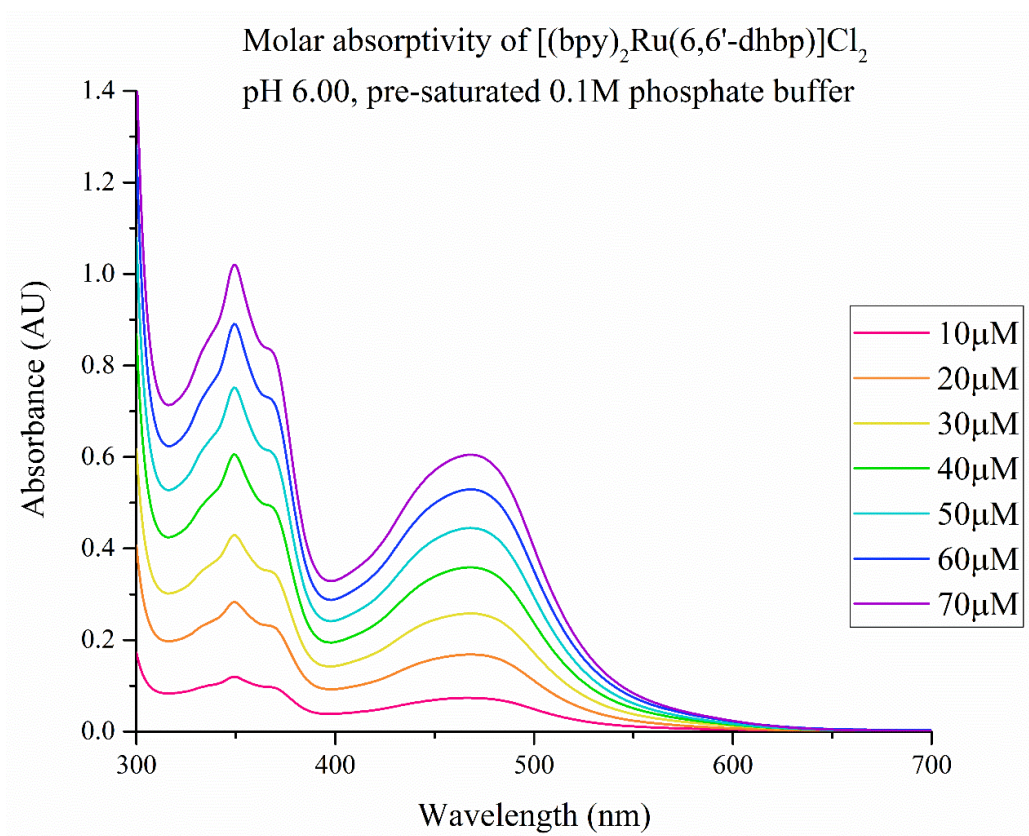


Figure 2A.4. Complex 1 at pH 6.00 in pre-saturated 0.1 M phosphate buffer

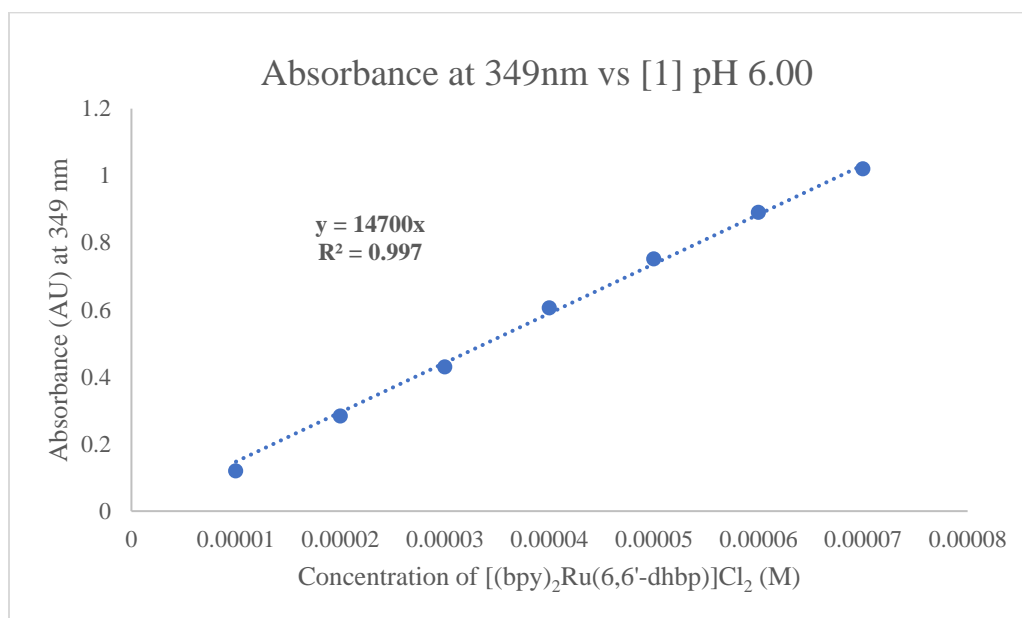


Figure 2A.5. Complex 1 at pH 6.00 in pre-saturated 0.1 M phosphate buffer-Molar absorptivity plot

Table 2A.1. Molar absorptivity data for complexes 1, 2, and 3 at various pH values.

	pH	1 [(bpy) ₂ Ru(dhbp)]Cl ₂		2 [(phen) ₂ Ru(dhbp)]Cl ₂		3 [(dop) ₂ Ru(dhbp)]Cl ₂	
		nm	ε ^a	nm	ε ^a	nm	ε ^a
0.1 M Acetate Buffer	4.00	348	16100	455	11100	347	18900
	5.00	348	16400	348	11500	347	21200
	5.25	-	-	-	-	348	12200
0.1 M Phosphate Buffer	5.80	-	-	457	12400	-	-
	6.00	349	14700	457	7910	350	15000
	6.60	356	10300	463	11300	342	7000
	6.70	-	-	463	8610	-	-
	7.00	358	13900	360	12800	341	13500
	7.40	358	16000	450	10900	341	13000
	8.00	359	17000	378	8610	341	15200

$${}^a\epsilon = \text{Lmol}^{-1}\text{cm}^{-1}$$

2A.2.2 Molar absorptivity of 5-Fluorouracil (5-FU)

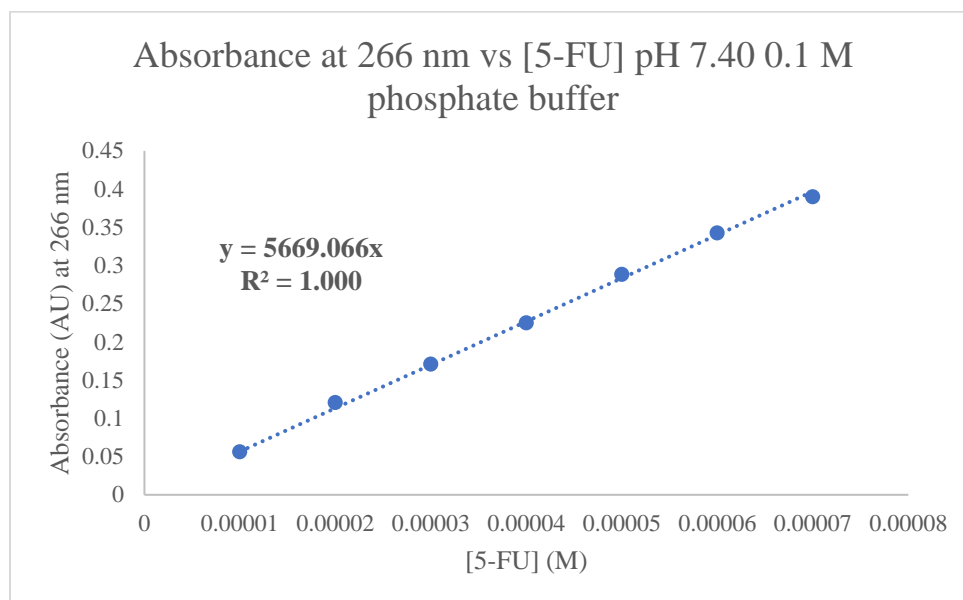


Figure 2A.6. 5-FU at pH 7.40 in pre-saturated 0.1 M phosphate buffer-Molar absorptivity plot.

2A.3. $\text{Log}(D_{o/w})$ Measurements

$\text{Log}(D_{o/w})$ for 5-fluorouracil: method verification

5-fluorouracil was first dissolved in *n*-octanol saturated with pH 7.40 buffer (0.1M phosphate) to a final concentration of 142.8 μM . 5 mL of this solution was then mixed with an equal volume of buffer saturated with *n*-octanol and gently stirred for 24 h at ambient temperature. Afterwards, an aliquot was removed from the aqueous phase, filtered, and the absorbance was measured via UV-Vis spectroscopy from 200-500nm to determine the concentration in the aqueous phase. From this data, the concentration of the compound in the organic phase was calculated and used to establish a $\text{Log}(D_{o/w})$ value (Eq. 2.1). Measurements were repeated in triplicate. The measured $\text{log}(D_{o/w})$ was found to be within 0.3 of reported values (reference [24] value: -0.824), validating the method used.

Table 2A.2. $\text{Log}(D_{o/w})$ data for 5-FU at pH 7.40

$\text{Log}(D_{o/w})$ Replicate	$\text{Log}(D_{o/w})$
1	-0.499
2	-0.767
3	-0.659
Average $\text{Log}(D_{o/w})$	-0.642
Standard Deviation	0.135

$\text{Log}(D_{o/w})$ for ruthenium compounds 1, 2, and 3

As a general procedure, the ruthenium compound of interest (200 μM) was first dissolved in *n*-octanol saturated with buffer. Five milliliters of this solution was then mixed with an equal volume of buffer saturated with *n*-octanol and gently stirred for 24 h at ambient temperature while avoiding light exposure. Afterwards, an aliquot was removed from the aqueous phase, filtered, and the absorbance was measured via UV-Vis spectroscopy from 300-700 nm to determine the concentration in the aqueous phase. From this data, the concentration of the compound in the organic phase was calculated and used to establish a $\text{Log}(D_{o/w})$ value (Eq. 2.1).

All measurements were repeated three or more times. 0.1 M acetate buffer was used for pH 4.00-5.25, while 0.1 M phosphate buffer was used for pH 5.80-8.00.

Log(D_{o/w}) values for [(bpy)₂Ru(6,6'-dhbp)]Cl₂

Table 2A.3. Log(D_{o/w}) data for [(bpy)₂Ru(6,6'-dhbp)]Cl₂ (**1**) at various pH values

Log(D _{o/w}) Replicate	pH						
	4.00	5.00	6.00	6.60	7.00	7.40	8.00
1	0.048	0.146	0.568	1.117	1.181	1.353	1.410
2	0.010	0.092	0.549	1.116	1.173	1.349	1.398
3	0.016	0.101	0.574	1.103	1.187	1.356	1.384
4	0.072	0.116	0.585	1.080	1.181	1.372	1.371
Average Log(D _{o/w})	0.037	0.114	0.569	1.104	1.181	1.357	1.391
Standard Deviation	0.029	0.024	0.015	0.017	0.006	0.010	0.017

Log(D_{o/w}) values for [(phen)₂Ru(6,6'-dhbp)]Cl₂

Table 2A.4. Log(D_{o/w}) data for [(phen)₂Ru(6,6'-dhbp)]Cl₂ (**2**) at various pH values

Log(D _{o/w}) Replicate	pH							
	4.00	5.00	5.80	6.00	6.70	7.00	7.40	8.00
1	0.153	0.640	1.368	1.105	1.648	1.674	1.686	1.768
2	0.161	0.746	1.244	0.921	1.279	1.416	1.629	1.860
3	0.175	0.647	1.214	1.043	1.400	1.539	1.556	1.650
4	0.174	-	1.276	0.896	-	1.380	1.639	1.584
Average Log(D _{o/w})	0.166	0.678	1.275	0.991	1.442	1.502	1.627	1.715
Standard Deviation	0.011	0.059	0.067	0.099	0.188	0.133	0.054	0.123

Log(D_{o/w}) values for [(dop)₂Ru(6,6'-dhbp)]Cl₂

Table 2A.5. Log(D_{o/w}) data for [(dop)₂Ru(6,6'-dhbp)]Cl₂ (**3**) at various pH values

Log(D _{o/w}) Replicate	pH						
	4.00	5.00	5.25	6.00	7.00	7.40	8.00
1	0.849	1.311	1.405	1.449	1.643	1.815	2.078
2	0.830	1.347	1.349	1.439	1.595	1.752	2.157
3	0.806	1.333	1.381	1.459	1.581	1.791	2.028
4	0.839	1.349	1.335	1.451	1.658	1.878	2.144
Average Log(D _{o/w})	0.831	1.335	1.367	1.450	1.619	1.809	2.102
Standard Deviation	0.018	0.017	0.032	0.008	0.037	0.053	0.060

2A.4. Uptake of 3_A in Normal Cells

Uptake of 3_A was measured in normal breast cells (MCF10A) as a point of comparison to cancerous breast cell lines. Like other cell lines tested, compound 3 localizes within the nucleus of MCF10A cells.

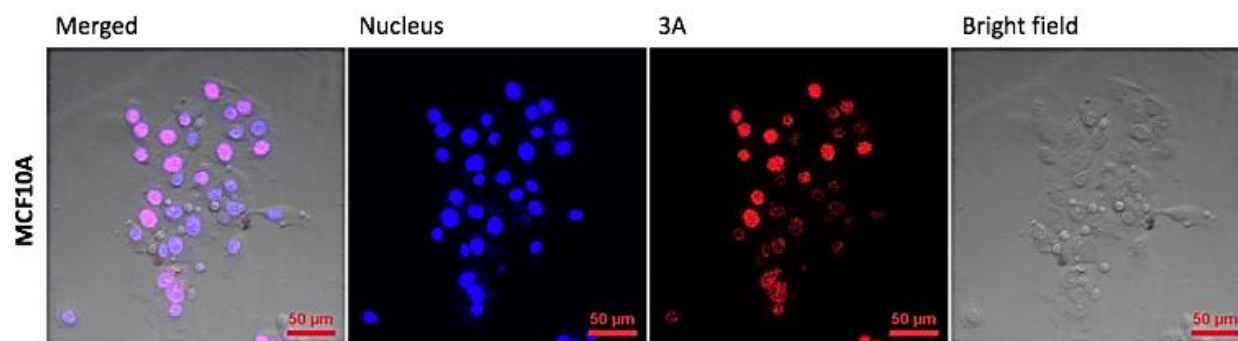


Figure 2A.7. Localization of complex 3_A ($5 \mu\text{M}$) in MCF10A after treatment in the dark for 30 min. Ru complex (TRITC; red), nuclei (Hoechst 33342; blue). Scale bar: $50 \mu\text{m}$.

CHAPTER 3

EFFORTS TOWARDS INCORPORATING A CYTOTOXIC LIGAND INTO RUTHENIUM COMPLEXES

3.1 Abstract

Photochemotherapy (PCT) is an advantageous method to treat cancer as it allows for precise spatial delivery of a drug to reduce off target side effects. Photoactivated chemotherapy (PACT) is a form of PCT which typically relies on light-induced ligand dissociation to generate toxic species where the metal fragment and/or the free ligand may be toxic. The ligands 5-fluorouracil (5-FU) and 5-cyanouracil (5-CNU) are two potential ligands that, on their own, have shown toxic effects towards cancer cells and may be utilized in a PACT system.

The efforts to synthesize a complex of the type $[(\text{Ru}(\text{bpy})_2)_n(5\text{-FU})](\text{ClO}_4)_n$ (bpy = bipyridine) ($n=1$ or 2) that can be activated by light allowing for precise spatial delivery of multiple active drugs are described herein. Evidence has supported the synthesis of $[(\text{Ru}(\text{bpy})_2)_2(5\text{-FU})]^{2+}$ (**5**); however, the structure of 5-FU allows for the synthesis of multiple isomers, making isolation of a single pure product for cellular testing difficult.

A complex incorporating 5-CNU, 2,2':6',2''-terpyridine (tpy), and 6,6'-dihydroxy-2,2'-bipyridine (6,6'-dhbp) ligands was designed in hopes that it may also act as a photoactivated prodrug. Synthesis of $[(\text{tpy})\text{Ru}(6,6'\text{-dhbp})(5\text{-CNU})]^{2+}$ (**6**) yielded what appears to be a mixture of products as seen by ^1H NMR analysis. XRD and IR data have shown the synthesis of a ruthenium complex containing a novel tridentate ligand formed from the intermolecular reaction

of 5-CNU and 6,6'-dhbp, resulting in the complex $[(\text{tpy})\text{Ru}(\text{dhbp-CNU})]^{2+}$ (**7**), which is not likely to be toxic through a PACT driven mechanism.

3.2 Introduction

As of late, research within the Papish group and others has focused on the development of ruthenium-based complexes as potential anticancer therapies.¹⁻¹⁶ Some of these complexes are capable of killing cancer cells only upon irradiation, allowing for precise spatial and temporal delivery of the drug. This method of targeted therapy is more commonly referred to as PCT. PCT includes both PDT and PACT (Scheme 1.1).¹⁶ However, unlike PDT, PACT agents do not require oxygen for toxicity giving them a functional advantage in low-oxygen environments, such as hypoxic tumors. PACT with metal complexes typically relies on light-induced ligand dissociation to generate toxic species where the metal fragment and/or the free ligand may be toxic.¹⁷⁻¹⁹ Both PACT allows for precise drug delivery by exhibiting therapeutic effects only at the site of irradiation-minimizing off target effects.

In 2017, the Papish group documented a series of light-activated ruthenium complexes that were designed as PACT agents and contained the protic ligand, 6,6'-dhbp (Figure 1.6).²⁰ The complexes were only able to photodissociate to a small degree but still had significant toxicity. This may be due to the complexes behaving as a drug delivery system for the highly toxic photoproducts. Tests were conducted to identify the toxic photoproduct (either the ruthenium aqua adduct or free 6,6'-dhbp ligand); however, the results proved to be inconclusive as the physical properties of the individual photoproducts varies widely from the complete complex and most likely behaves differently in a cellular environment. As such these complexes may behave as potent drug delivery systems capable of precisely delivering a ligand that is known to have anticancer activity.

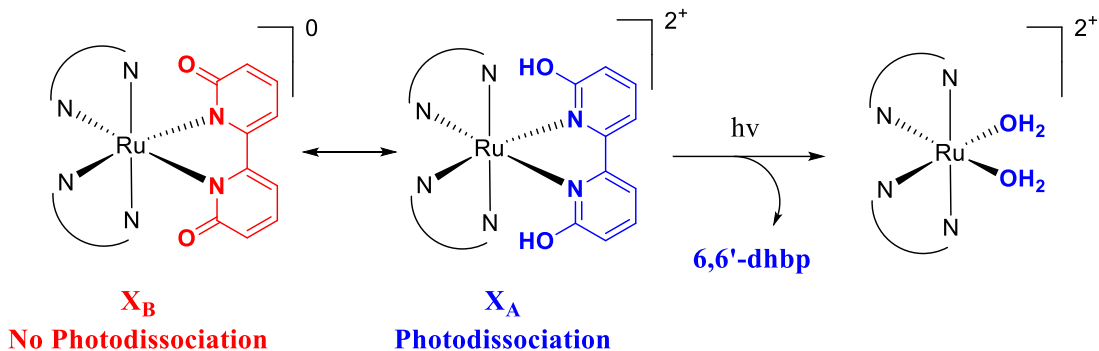


Figure 3.1 General reaction scheme of the light activated ruthenium anticancer prodrug with the aqua adduct photoproduct capable of binding to biological targets. \mathbf{X}_A denotes the acidic form of the drug, while \mathbf{X}_B denotes the basic form. The compound should readily undergo photodissociation as \mathbf{X}_A .

5-Fluorouracil is an anticancer agent that is currently in use today (Figure 3.2). It was first described as a “tumor inhibitory compound” in 1957 by Scheiner and coworkers.²¹ 5-FU behaves as a “suicide inhibitor”, allowing for irreversible binding to its target enzyme.²² Unfortunately, there are many deleterious side-effects associated with 5-FU due to a narrow therapeutic window.^{23, 24} Many of its symptoms include gastrointestinal complications, cardiotoxicity, psychosis, mania, and even death. It is hypothesized that the therapeutic window of 5-FU could be improved by synthesizing a ruthenium complex of the type $[(\text{Ru}(\text{N},\text{N}')_2)_n(5\text{-FU})]^{n+}$, where N,N' is a bidentate N-donor ligand, allowing for precise drug delivery through light activated dissociation, delivering multiple anticancer agents per dose. Due to the multiple coordination sites on 5-FU, the final complex could be a monomer $[(\text{Ru}(\text{N},\text{N}')_2)(5\text{-FU})]^{+}$ (**4**) or a dimer $[(\text{Ru}(\text{N},\text{N}')_2)_2(5\text{-FU})]^{2+}$ (**5**) (Figure 3.2).

Another potential anticancer target is a ruthenium complex that incorporates 5-cyanouracil (5-CNU) which has shown to inhibit cellular functions *in vivo*.^{25, 26} Previous studies by Turro and co-workers investigated *cis*- $[\text{Ru}(\text{bpy})_2(5\text{-CNU})_2]^{2+}$ and $[(\text{tpy})\text{Ru}(5\text{-CNU})_3]^{2+}$ complexes (Figure 3.3). These compounds were able to release two 5-CNU ligands and a

potentially active ruthenium photoproduct that could covalently bind to DNA.^{27, 28} This concept, as well as the use of the pH sensitive ligand, 6,6'-dhbp, has been utilized to design the complex, $[(\text{tpy})\text{Ru}(6,6'\text{-dhbp})(5\text{-CNU})]^{2+}$ (**6**). The design of the complex was also influenced by previous work in the Papish group on water oxidation (Figure 3.3).²⁹ The complex may be able to act as an anticancer prodrug that can be activated under specific light conditions. Reported here are the efforts towards the design and synthesis of ruthenium PACT agents that incorporate 5-FU and 5-CNU.

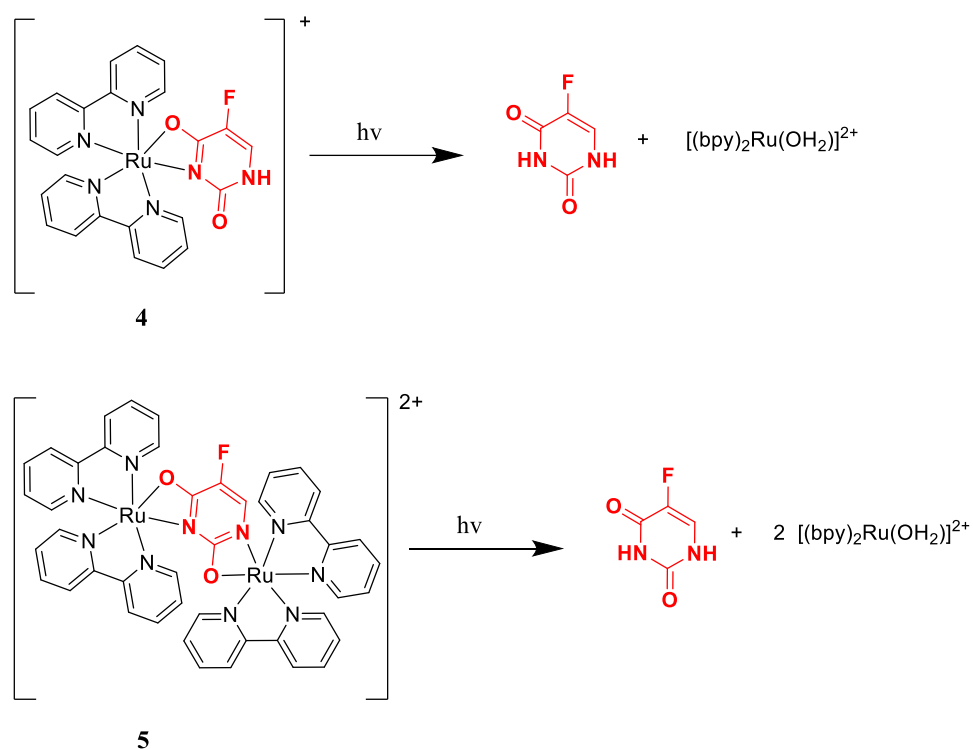


Figure 3.2. Proposed mechanism for the delivery of a $[(\text{Ru}(\text{bpy})_2)_n(5\text{-FU})]^{n+}$ complex that can deliver multiple anticancer agents per dose. 5-FU is highlighted in red. Top: Photoreaction with compound **4**. Bottom: Photoreaction with compound **5**.

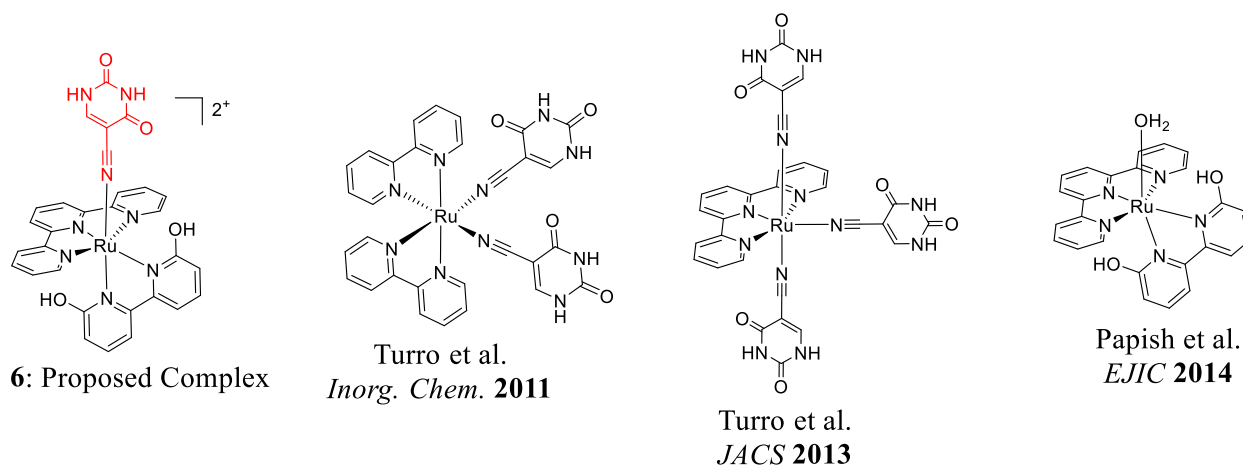


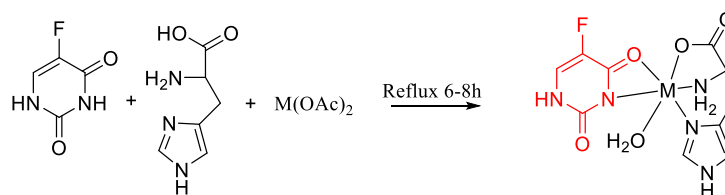
Figure 3.3. (left) Structure of **6** with 5-CNU drawn in red. The structure of the proposed complex was influenced by previously reported complexes from Turro et al. and Papish et al.

3.3 Results and Discussion

3.3.1 Incorporating 5-Fluorouracil

Initial synthesis attempts focused on a modified procedure from Shobana *et al.* (Scheme 3.1).³⁰ Data collected from this initial set of reaction conditions show that multiple products were formed as seen in the ¹⁹F NMR (Figure 3.4) and MALDI-TOF mass spectrum (Figure 3.6).

Unfortunately, the exact identity of these products is still unknown. Attempts to isolate a crystal suitable for single crystal XRD were unsuccessful. If in the form of **4** and 5-FU behaves as a bidentate N,O donor ligand, there are 3 possible isomers (Figure 3.5).



Scheme 3.1. Proposed scheme adapted from Shobana *et al.* (ref. 30) where M is either Ni(II), Zn(II), or Cu(II).

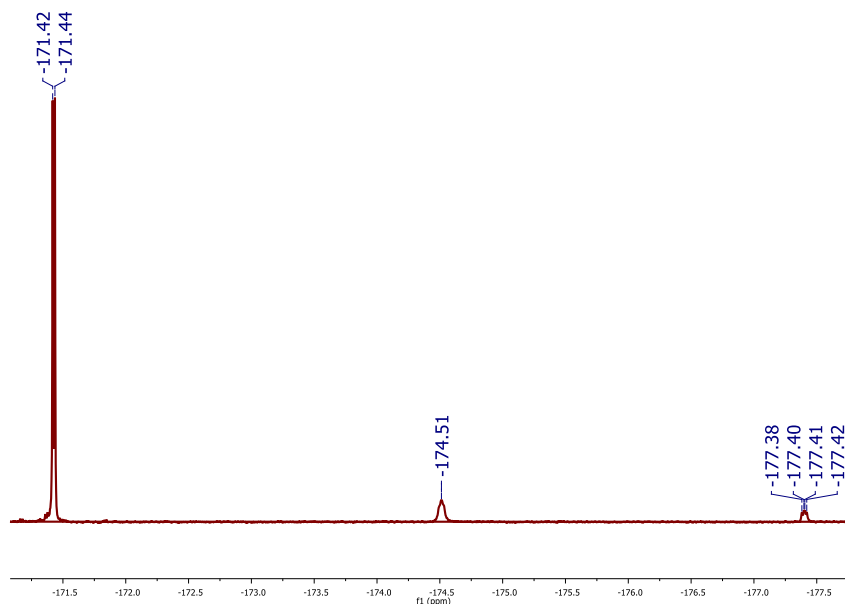


Figure 3.4. ^{19}F NMR spectrum in DMSO of reaction conditions 1 showing a large starting material peak at -171 ppm and two unidentified peaks at -174.5ppm and -177.4 respectively.

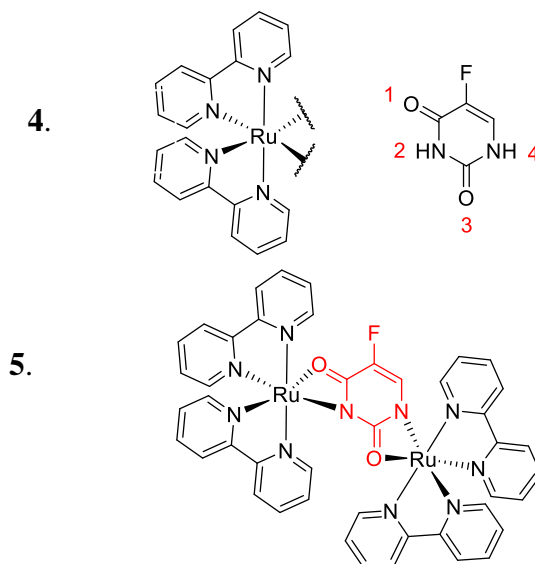


Figure 3.5. (Left) The two predicted products, 4 and 5. Complex 4 could possibly bind to 5-FU at the 1-2, 2-3, or 3-4 positions at on the ligand for a potential of 3 different isomers.

These reactions appear to show a large amount of unreacted 5-FU (-171 ppm in ^{19}F NMR) leading to the conclusion that these reaction conditions are not very productive. No color change or change in NMR spectrum was observed when the sample was exposed to several days

of ambient light suggesting that the product was light stable. Matrix-assisted laser desorption/ionization time of flight (MALDI-ToF) mass spectrometry shows peaks that correlates to a monomeric species. However, peaks around the 1000 m/z region (where m/z = mass to charge ratio) suggest the presence of a larger $[C_{44}H_{33}N_{10}O_2FRu_2Cl]^+$ ($[M]^+$) species (Figure 3.6).

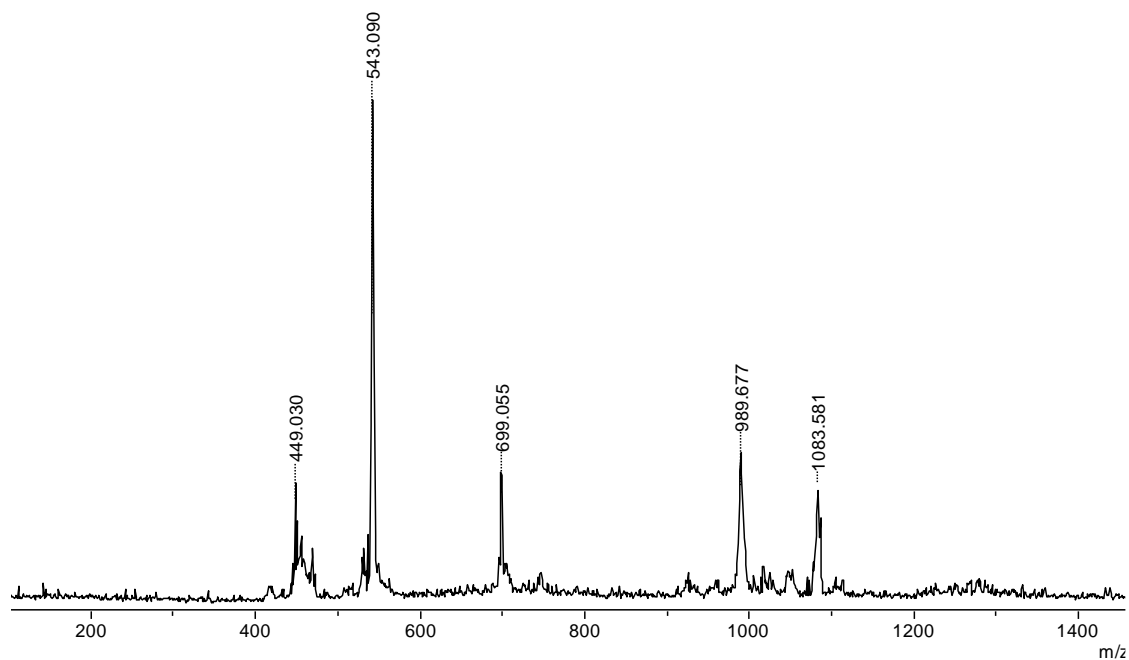
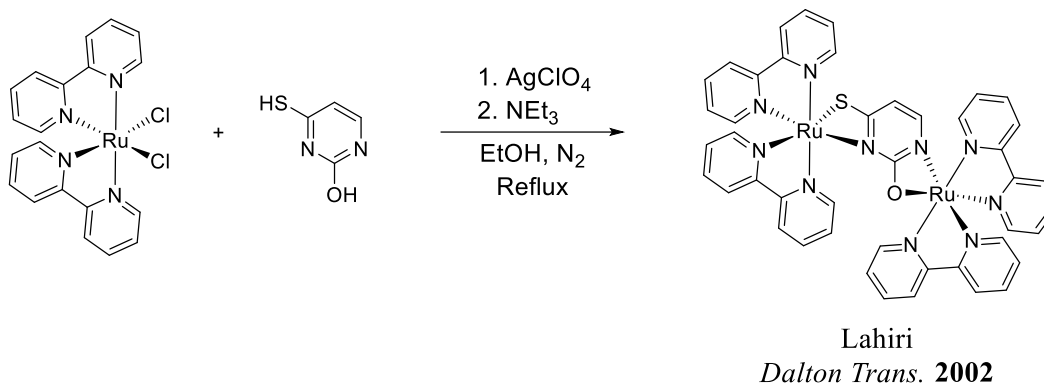


Figure 3.6. MALDI-ToF mass spectrum. $[Ru(bpy)_2(5-FU)]^+$ has a calculated m/z of 543.

An alternative synthetic route was modified from work published by Lahiri and co-workers who synthesized a di-nuclear bis(bipyridine)ruthenium(II) complex containing thiouracil (Scheme 3.2).³¹ Upon running this reaction with 5-FU, a small amount of solid appeared to precipitate. Only excess starting material (5-FU) was found in solution; however, a ^{19}F NMR spectrum in DMSO- $[d_6]$ of the precipitate showed five different peaks, only one of which was identified as starting material (Figure 3.7). This indicates the formation of multiple products containing 5-FU. The peak at -174 ppm appears consistently through all experiments, suggesting

that this may correlate to the favored product. The remaining peaks may be attributed to the three monomer conformations as well as unreacted, deprotonated 5-FU.



Scheme 3.2 Synthesis of $[(\text{Ru}(\text{bpy})_2(\text{thiouracil}))(\text{ClO}_4)_2]$ described by Lahiri and co-workers. (Adapted from reference 31). Their complex is similar in structure to complex **5**.

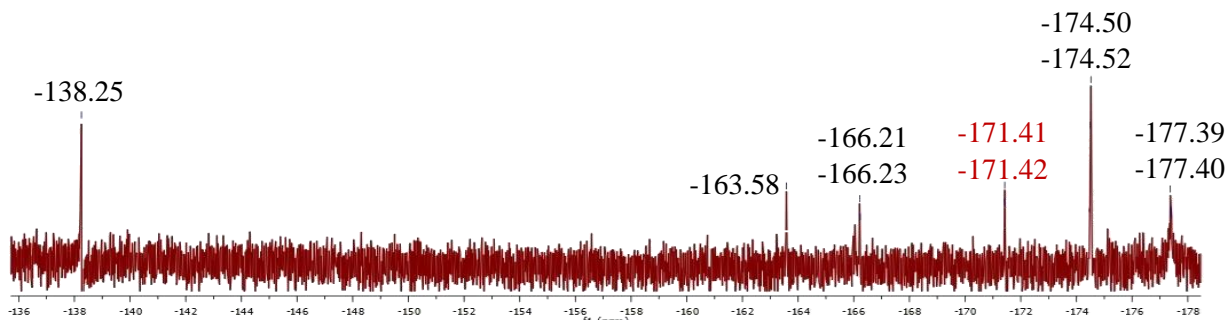
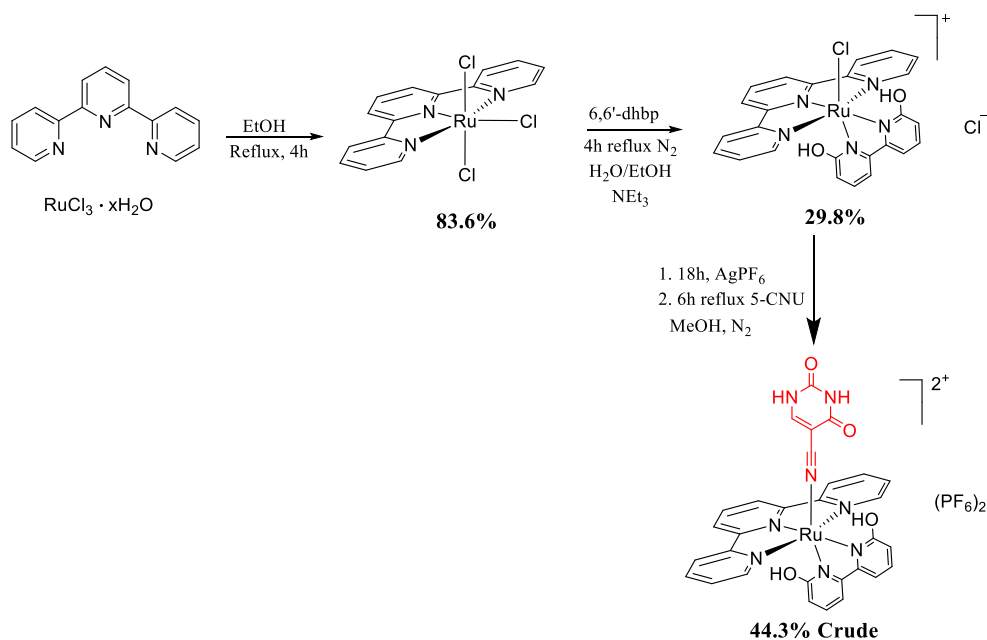


Figure 3.7. ^{19}F NMR spectrum in $\text{DMSO}-[d_6]$ of the solid recovered from Lahiri conditions. Starting material is present at -171.41 & -171.42 . All shifts are in ppm.

3.3.2 Incorporating 5-Cyanouracil

While 5-FU is a known chemotherapy agent, it has not been highly documented in systems that utilize PACT driven toxicity. Turro and co-workers have successfully shown that ruthenium complexes incorporating 5-CNU can yield a light activated complex capable of ejecting 5-CNU upon irradiation. A ruthenium complex that incorporate 5-CNU as well as 6,6'-dhbp is proposed in hopes of developing a complex capable of PACT driven toxicity. Synthesis of the target complex, **6** ($[(\text{tpy})\text{Ru}(6,6'\text{-dhbp})(5\text{-CNU})]^{2+}$), requires the synthesis of several

intermediate complexes; however, all are synthesized with minimum modifications to reported methods (Scheme 3.3).^{27-29, 32} An excess of RuCl₃ is used in the synthesis of Ru(tpy)Cl₃ to avoid generating [Ru(tpy)₂]²⁺. Regardless, this side product is usually generated in small quantities but can be washed out with warm EtOH. The complex, [(tpy)RuCl(6,6'-dhbp)]Cl was synthesized with no change to the literature procedure.³²



Scheme 3.3. Proposed synthesis route for **6** as a PF₆ salt with highest achieved yields for each complex.

Attempts to synthesize **6** have been modified from previously reported syntheses of ruthenium-based 5-CNU complexes.^{27, 28} The ¹H NMR spectrum of the isolated sample in MeOD-[d₄] shows two singlets at 7.89 ppm and 8.63 ppm integrating for 1 and 0.3 hydrogens, respectively (Figure 3.7). These signals likely correspond to the sp² hydrogen of 5-CNU (free 5-CNU in MeOD-[d₄] resonates at 6.65 ppm (s, 1H)); however, these peaks also indicate multiple products with a bound 5-CNU. This is further supported by the XRD data. XRD analysis of an

orange crystal shows a reaction had occurred between the 6,6'-dhbp and 5-CNU ligands, forming a new tridentate ligand (Figure 3.9).^{33, 34} The resolved crystal structure is of low resolution and considered unsuitable for publication due in part to a high R-factor (residual factor or reliability factor) of 23.2 %. The R-factor is a measure of the agreement between the crystallographic model and experimental X-ray diffraction data, and smaller molecules such as these should have R-factors of ≤ 5 % to be of publishable quality.³⁵ As a result, accurate bond length and angle data cannot be measured from this data set; however, it does provide general connectivity information. IR data does not indicate the presence of a nitrile (Figure 3.10). If the desired product was synthesized, it is most likely a minor product compared to the isolated complex, **7**. ESI-MS data on the isolated sample further supported the formation of **7** (Figure 3.11).

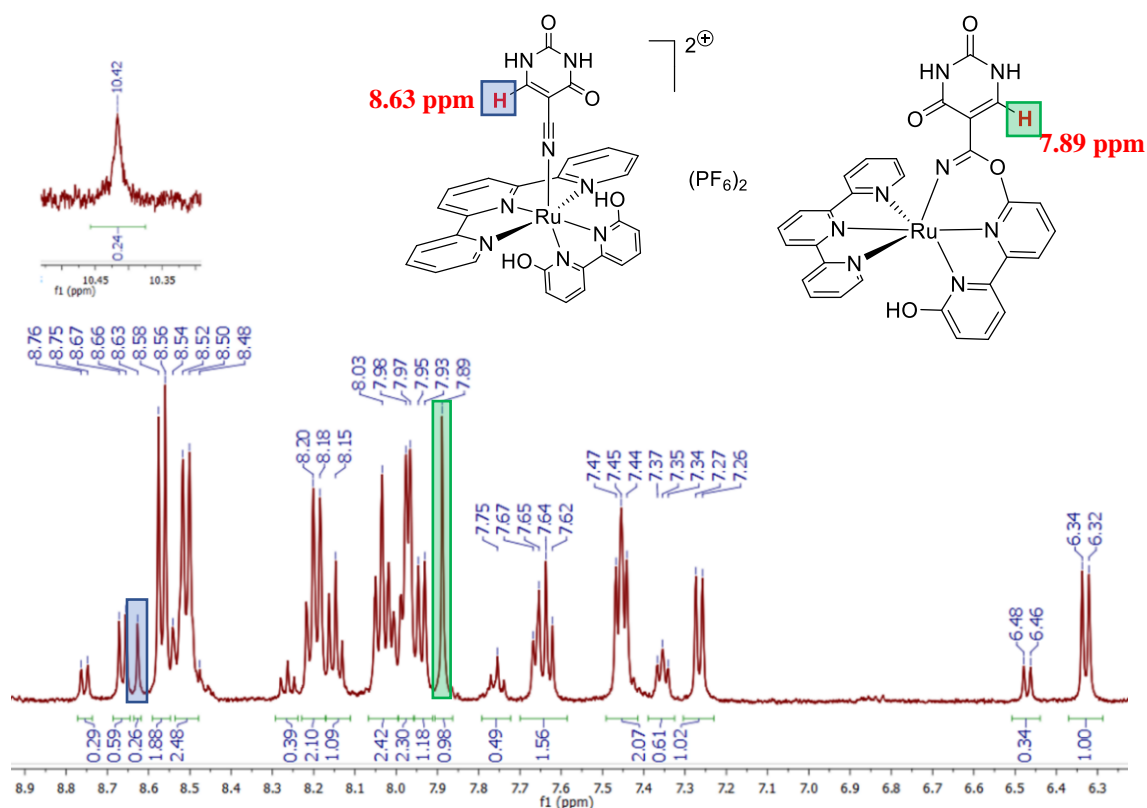


Figure 3.8. ^1H NMR spectrum of the isolated product mixture in $\text{MeOD-}[d_4]$. The two highlighted singlets (blue and green boxes) correspond to the sp^2 hydrogen on 5-CNU. These two singlets indicate the presence of at least two different complexes containing 5-CNU. Insert: Structures of complexes **6** (left) and **7** (right).

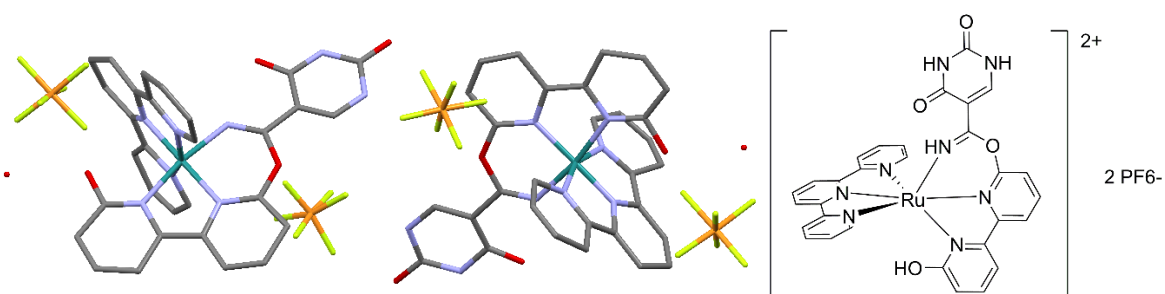


Figure 3.9. (Left) Low resolution crystal structure of **7** as the PF_6 salt. The solved structure has a high R-factor of 23.2 % preventing accurate measurement of bond lengths and angles. The XRD data can still provide preliminary connectivity data. (Right) Chemdraw structure of the isolated complex.

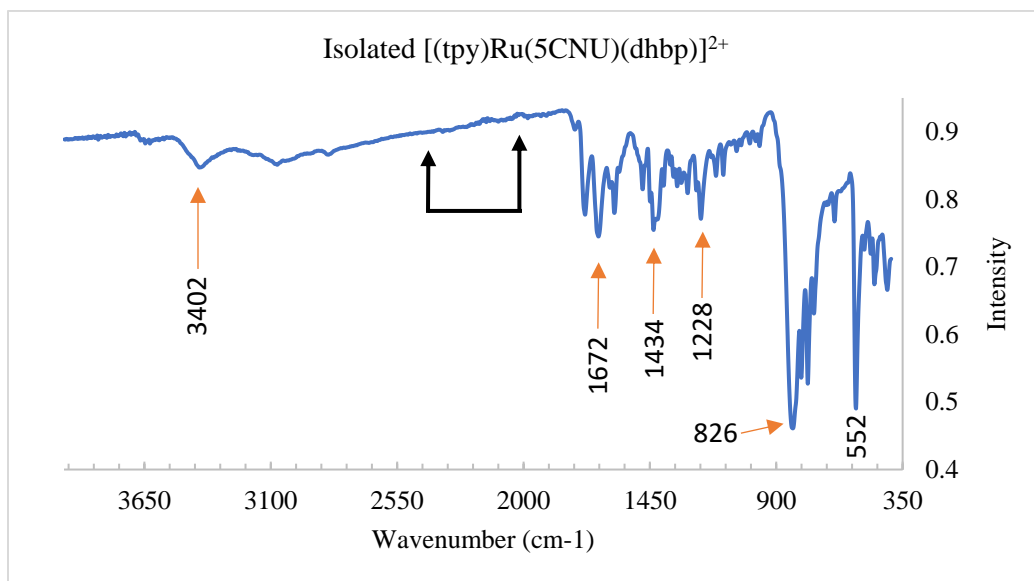


Figure 3.10. IR spectrum of the isolated product mixture. Black arrows indicate the region where nitrile signals are typically found ($2400\text{-}2000\text{ cm}^{-1}$). One would expect a noticeable nitrile if complex **6** was the major product formed in the reaction; however, none is observed.

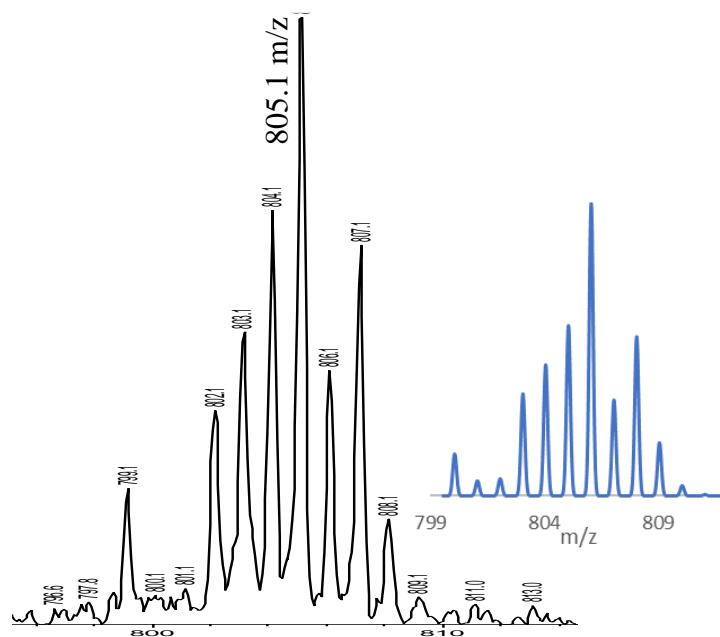


Figure 3.11. ESI-MS (positive mode, $[M]^+$) data of **7** with the recorded spectrum and simulated spectrum (blue, inset).

The connectivity data gathered from the XRD analysis of complex **7** allowed for the rough assignment of hydrogens within the ^1H NMR spectrum (Figure 3.12). Throughout the spectrum, many peaks integrate in a 3:1 ratio. The new complex, **7**, is most likely the major product as it was the only one isolated for XRD analysis. This assumption allowed for assignment of NMR peaks to their respective complexes. Assignment to individual ligands was also possible due to the symmetry of the tpy ligand. Hydrogens on the tpy ligand will integrate at a 2:1 ratio compared to hydrogens on the dhbp ligand. While a “best guess” assignment can be given to many of the peaks in the ^1H NMR spectrum, further specific assignment will require analysis via 2D NMR techniques. Full characterization of this complex (which includes 2D NMR analysis, high-resolution mass spectrometry, and elemental analysis) will be completed once a pure sample is obtained.

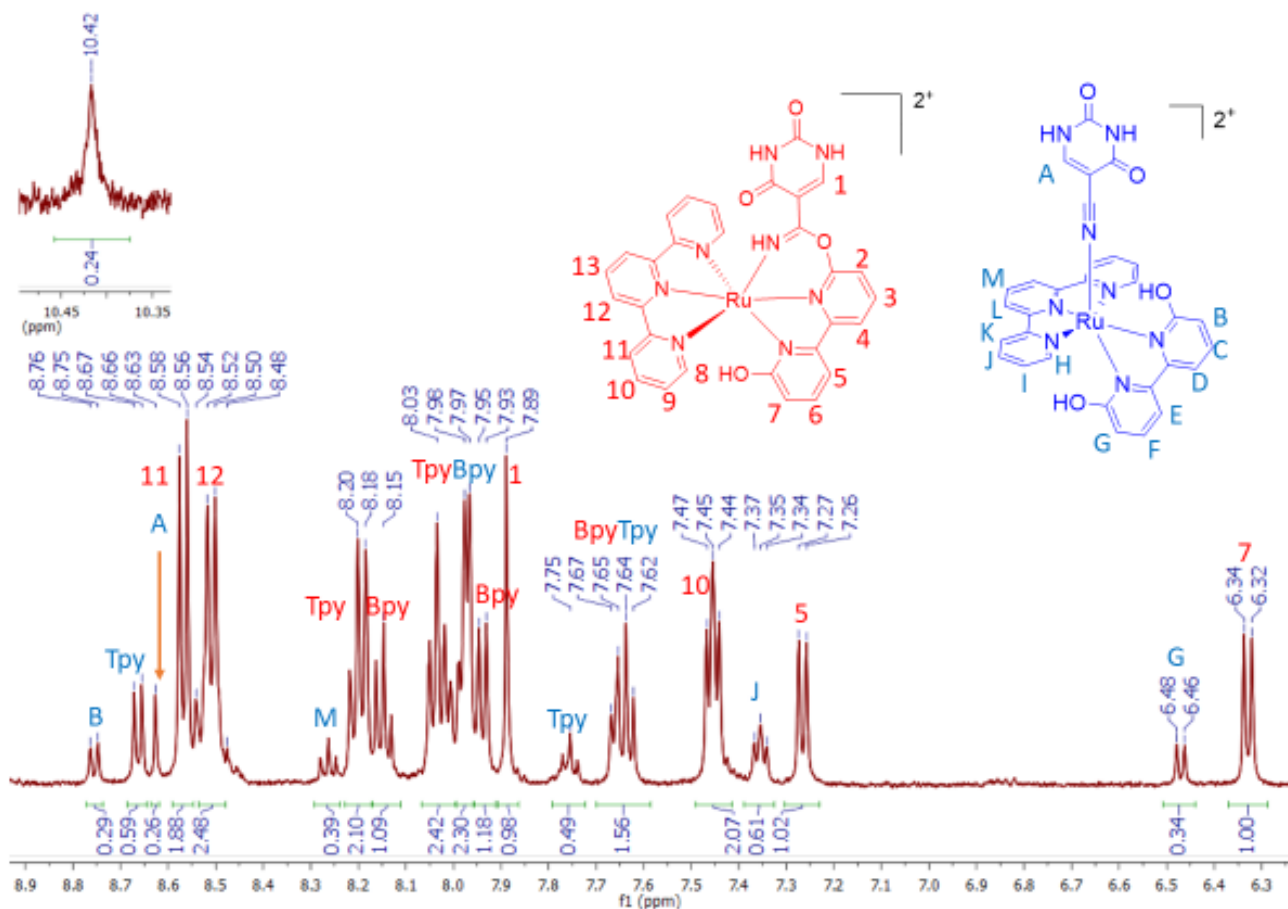


Figure 3.12. ^1H NMR spectrum of crude product mixture in $\text{DMSO-}[d_6]$. Peaks corresponding to the original desired product, **6** are labeled in blue while peaks for the novel complex, **7**, are assigned in red. Integrations show that the products exist in a 3:1 mixture (**7**:**6**). Further assignments of specific hydrogens will require analysis with 2D NMR techniques.

3.4 Conclusion

3.4.1 Incorporating 5-Fluorouracil

Although both synthetic techniques appear to produce a $[(\text{Ru}(\text{N},\text{N}')_2)_n(5\text{-FU})]^{n+}$ complex, as shown in ^{19}F NMR analysis, the Lahiri approach appears to yield more favorable results.

Reaction conditions still need to be improved in order to yield a single pure product. The compounds appear to have the ability to crystallize; however, no crystals viable for single crystal XRD have been produced. MALDI-TOF mass spectrometry has yielded MS data that supports

the production complex **4**; however, many peaks in the spectrum still require identification, and there appears to be a mixture of products. Reaction conditions still need to be modified in order to produce larger quantities of pure product.

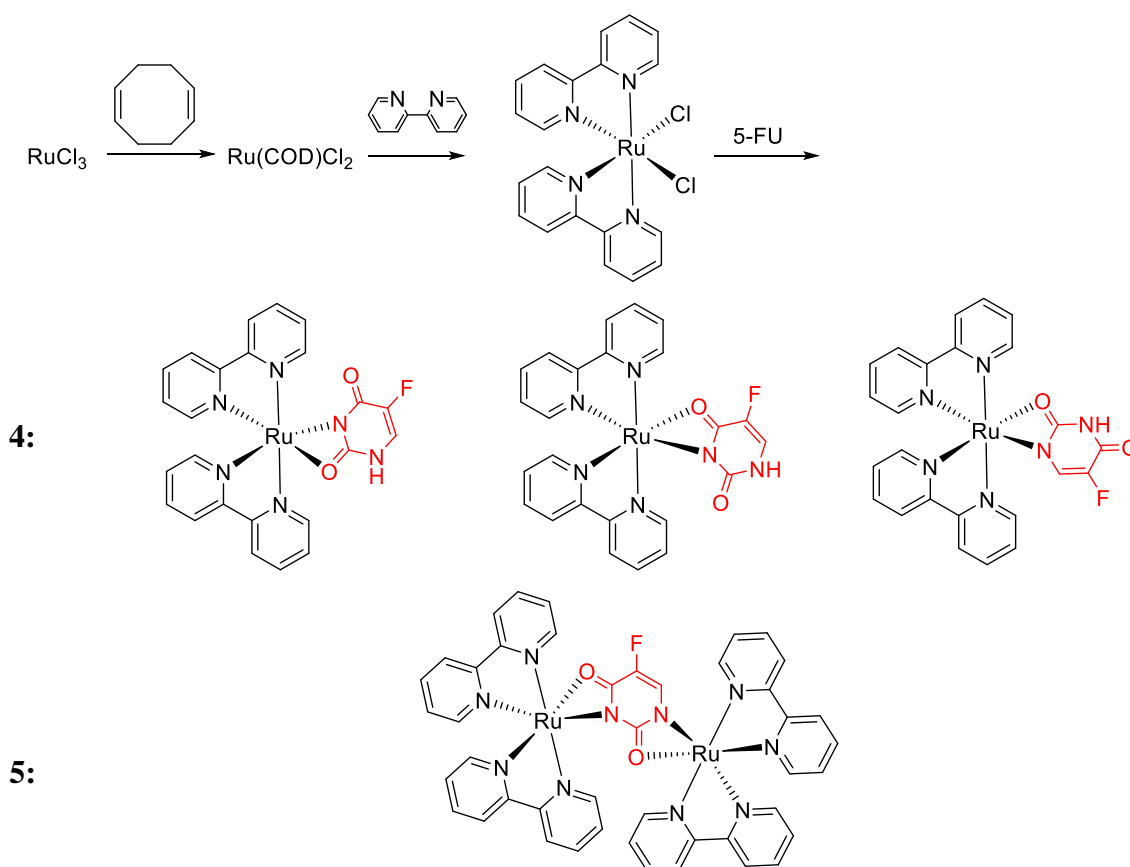
3.4.2 Incorporating 5-Cyanouracil

Efforts to synthesize **6** have yielded what appears to be a mixture of products, including the new complex, **7** ($[(\text{tpy})\text{Ru}(\text{dhbp-CNU})]^{2+}$). ^1H NMR spectrum of the isolated sample in MeOD- $[\text{d}_4]$ shows two singlets at 7.89 ppm and 8.63 ppm integrating for 1 and 0.3 hydrogens, respectively. These signals likely correspond to the sp^2 hydrogen of 5-CNU (free 5-CNU in MeOD- $[\text{d}_4]$ 6.65 ppm (s,1H)); however, they also indicate multiple products with a bound 5-CNU. XRD data of isolated crystals show a reaction had occurred between the 6,6'-dhbp and 5-CNU ligands, forming a new tridentate ligand. For this new, dhbp-CNU complex to function as a PACT agent, a tridentate ligand will now need to photodissociate - a much more difficult task than the photodissociation of a monodentate ligand, making PACT driven toxicity unlikely. Synthesis of **6** may be possible with the addition of protecting groups on the hydroxyl groups of 6,6'-dhbp; however, once the protecting groups are removed, the dhbp-CNU complex may still form in solution. If either the desired complex **6** or isolated complex **7** were to be tested in cells, they would need further characterization and purification. It is likely possible to directly synthesize complex **7** by increasing the reaction time and/or adding an advantageous amount of base to solution to encourage the dhbp ligand to react with the 5-CNU ligand. The $[(\text{tpy})\text{Ru}(\text{dhbp-CNU})]^{2+}$ (**7**) complex may yet be toxic to cells; however, a pure sample is required for testing (and full characterization) and the likelihood of PACT driven toxicity is low.

3.5 Materials and Methods

3.5.1 Synthesis of ruthenium 5-FU complexes (**4** and **5**)

The synthesis of $(\text{Ru}(\text{COD})\text{Cl}_2)$ and $(\text{bpy})_2\text{RuCl}_2$ (Scheme 3.4) were carried out without modification to literature.^{13, 36} The attempted syntheses of **4** was carried out according to modified literature procedures.^{30, 31} All syntheses of the final complex were carried out under low light conditions.



Scheme 3.4. Synthesis scheme for ruthenium 5-FU complex. Since 5-FU has multiple coordination sites, there is the potential for multiple products to be formed.

*Shobana Approach*³⁰

Ru(bpy)₂Cl₂ (66.3 mg, 0.137 mmol) and 5-FU (18.5 mg, 0.142 mmol) were separately mixed in 10 mL methanol. While stirring, the Ru(bpy)₂Cl₂ was added slowly to the 5-FU solution. The reaction was refluxed for 18 h before removing the solvent under vacuum. Analysis showed that most of the species present were unreacted starting material. No product yield was calculated. ¹⁹F NMR (360 MHz, DMSO-[d₆]): δ -171.43 (d, 1H), -174.51 (d, 1H), -177.40 (d, 1H). MALDI-ToF MS [C₂₄H₁₈N₆O₂FRu]⁺: 543 m/z (Calculated m/z = 543.1)

*Lahiri Approach*³¹

Under inert atmosphere, Ru(bpy)₂Cl₂ (100.4 mg, 0.2074 mmol) and AgClO₄ (91 mg, 0.44 mmol) were refluxed in ethanol for 1 hour, upon which a gray-white precipitate was observed. Upon vacuum filtration, the orange-red filtrate was collected and transferred to another flask and the gray-white residue was discarded. Separately, 5-FU (13.5 mg, 0.103 mmol) and triethylamine (20.17 mg, 0.1975 mmol) were mixed in 2 mL ethanol. The 5-FU solution was slowly added to the [Ru(bpy)₂(OH₂)₂](ClO₄)₂ filtrate and refluxed for a total of 14 h. The reaction solution was then allowed to cool to room temperature whereupon a small amount of solid precipitation was observed. The solution was moved to the freezer for 1 h to facilitate further precipitation. No extra precipitation was observed, and the solution was filtered to yield a very dark flaky residue and a red-purple filtrate. The residue (23 mg) was recovered before attempting to recrystallize in a minimum amount of 1:3 acetonitrile-benzene solution. ¹⁹F NMR (360 MHz, DMSO-[d₆]): δ -138.25 (d, 1H), -136.58 (d, 1H), -166.22 (d, 1H), -171.43 (d, 1H), -174.51 (d, 1H), -177.40 (d, 1H). ESI MS [C₄₄H₃₃N₁₀O₂FRu₂Cl]⁺: 991.1 m/z (Calculated m/z = 991.1)

3.5.2 Synthesis of ruthenium 5-CNU complexes (**6** and **7**)

Synthesis of $(tpy)RuCl_3$ ³⁷

217.3 mg (0.89 mmol) of 2,2':6,2-terpyridine and 476.1 mg (1.8 mmol) of $RuCl_3 \cdot 3H_2O$ were added to a flask followed by 37 mL 100 % ethanol. The resulting dark solution was heated to reflux (95°-100°) for 5.5 hours then filtered hot via Büchner funnel. The dark solid was washed with warm EtOH (3 x 10 mL) followed by water (3 x 10 mL) and ethyl ether (3 x 10 mL) and dried via oil pump vacuum overnight. Recovered 328.9 mg (83.6 % yield). MALDI-ToF $[C_{15}H_{11}N_3Cl_2Ru]^+$: 404.9 m/z (Calculated m/z = 404.9)

Synthesis of $[(tpy)RuCl(6,6'-dhbp)]Cl$ ³²

$[(tpy)RuCl(6,6'-dhbp)]Cl$ was synthesized without modification to literature procedures. 30 % yield. ¹H NMR (360 MHz, CD₃OD): δ 6.21 (d, 1H), 7.26 (d, 1H), 7.28 (t, 2H), 7.51 (t, 1H), 7.89 (d, 1H), 7.91 (t, 2H), 7.97 (d, 2H), 8.04 (t, 1H), 8.13 (t, 1H), 8.19 (d, 1H), 8.45 (d, 2H), 8.50 (d, 2H), 12.00 (s, 1H). ESI-MS $[C_{25}H_{19}N_5O_2RuCl]^{++}$ m/z = 558.0 (Calculated m/z = 558.0).

Synthesis of $[(tpy)Ru(6,6'-dhbp)(5-CNU)](PF_6)_2$ (**6**)

Complex **6** has been synthesized according to modified literature procedures.^{27, 28} $[(tpy)RuCl(6,6'-dhbp)]Cl$ (67.0 mg, 0.11 mmol) and $AgPF_6$ (58 mg, 0.23 mmol) were added to a flask in the glovebox followed by 10 mL MeOH and left to stir for 18 h before filtration. 5-cyanouracil (54.7 mg, 0.399 mmol) was then added to the filtrate and the solution refluxed under dark conditions for 8 h. Once cool, the MeOH was removed via rotary evaporation and the resulting solid was re-dissolved in boiling H₂O (5-10 mL) followed by an addition of saturated $NH_4PF_6(aq)$ solution (5 mL) to crash out the solid product. The solution was then filtered and the solid washed with cold water (3 x 5 mL) and ethyl ether (3 x 5 mL) and left under vacuum to

dry. 47.6 mg of impure solid, as shown by NMR, has been recovered resulting in a 44.3% crude yield. ESI-MS $[\text{C}_{30}\text{H}_{22}\text{N}_8\text{O}_4\text{RuPF}_6]^+$ $m/z = 805.0$ (Calculated $m/z = 805.0$). X-ray quality crystals were grown via vapor diffusion of ethyl ether into a saturated methanol solution at 10°C. Red orange crystals were observed after 3 days and were suitable for a low-resolution structure determination but did not yield a publication quality crystal structure. The structure was identified as complex **7**.

References

- [1] Morris, R. E., Aird, R. E., Murdoch, P. d. S., Chen, H., Cummings, J., Hughes, N. D., Parsons, S., Parkin, A., Boyd, G., Jodrell, D. I., and Sadler, P. J. (2001) Inhibition of Cancer Cell Growth by Ruthenium(II) Arene Complexes, *J. Med. Chem.* *44*, 3616-3621.
- [2] Aird, R. E., Cummings, J., Ritchie, A. A., Muir, M., Morris, R. E., Chen, H., Sadler, P. J., and Jodrell, D. I. (2002) In vitro and in vivo activity and cross resistance profiles of novel ruthenium (II) organometallic arene complexes in human ovarian cancer, *Br. J. Cancer* *86*, 1652-1657.
- [3] Zhang, C. X., and Lippard, S. J. (2003) New metal complexes as potential therapeutics, *Curr. Opin. Chem. Biol.* *7*, 481-489.
- [4] Sava, G., Zorzet, S., Turrin, C., Vita, F., Soranzo, M., Zabucchi, G., Cocchietto, M., Bergamo, A., DiGiovine, S., Pezzoni, G., Sartor, L., and Garbisa, S. (2003) Dual Action of NAMI-A in Inhibition of Solid Tumor Metastasis: Selective Targeting of Metastatic Cells and Binding to Collagen, *Clin. Cancer Res.* *9*, 1898-1905.
- [5] Collin, J.-P., Jouvenot, D., Koizumi, M., and Sauvage, J.-P. (2005) Light-Driven Expulsion of the Sterically Hinderig Ligand L in Tris-diimine Ruthenium(II) Complexes of the Ru(phen)₂(L)²⁺ Family: A Pronounced Ring Effect, *Inorg. Chem.* *44*, 4693-4698.
- [6] Novakova, O., Kasparkova, J., Bursova, V., Hofr, C., Vojtiskova, M., Chen, H., Sadler, P. J., and Brabec, V. (2005) Conformation of DNA Modified by Monofunctional Ru(II) Arene Complexes: Recognition by DNA Binding Proteins and Repair. Relationship to Cytotoxicity, *Chem. Biol.* *12*, 121-129.
- [7] Magennis, S. W., Habtemariam, A., Novakova, O., Henry, J. B., Meier, S., Parsons, S., Oswald, I. D. H., Brabec, V., and Sadler, P. J. (2007) Dual Triggering of DNA Binding and Fluorescence via Photoactivation of a Dinuclear Ruthenium(II) Arene Complex, *Inorg. Chem.* *46*, 5059-5068.
- [8] Betanzos-Lara, S., Salassa, L., Habtemariam, A., Novakova, O., Pizarro, A. M., Clarkson, G. J., Liskova, B., Brabec, V., and Sadler, P. J. (2012) Photoactivatable Organometallic Pyridyl Ruthenium(II) Arene Complexes, *Organometallics* *31*, 3466-3479.
- [9] Ragazzon, G., Bratsos, I., Alessio, E., Salassa, L., Habtemariam, A., McQuitty, R. J., Clarkson, G. J., and Sadler, P. J. (2012) Design of photoactivatable metallodrugs:

Selective and rapid light-induced ligand dissociation from half-sandwich [Ru([9]aneS3)(N-N')(py)]²⁺ complexes, *Inorg. Chim. Acta* 393, 230-238.

- [10] Aitken, J. B., Antony, S., Weekley, C. M., Lai, B., Spiccia, L., and Harris, H. H. (2012) Distinct cellular fates for KP1019 and NAMI-A determined by X-ray fluorescence imaging of single cells, *Metallomics* 4, 1051-1056.
- [11] Su, W., Zhou, Q., Huang, Y., Huang, Q., Huo, L., Xiao, Q., Huang, S., Huang, C., Chen, R., Qian, Q., Liu, L., and Li, P. (2013) Synthesis, crystal and electronic structure, anticancer activity of ruthenium(II) arene complexes with thiosemicarbazones, *Appl. Organomet. Chem.* 27, 307-312.
- [12] Stevens, S. K., Strehle, A. P., Miller, R. L., Gammons, S. H., Hoffman, K. J., McCarty, J. T., Miller, M. E., Stultz, L. K., and Hanson, P. K. (2013) The anticancer ruthenium complex KP1019 induces DNA damage, leading to cell cycle delay and cell death in *Saccharomyces cerevisiae*, *Mol. Pharmacol.* 83, 225-234.
- [13] Hufziger, K. T., Thowfeik, F. S., Charboneau, D. J., Nieto, I., Dougherty, W. G., Kassel, W. S., Dudley, T. J., Merino, E. J., Papish, E. T., and Paul, J. J. (2014) Ruthenium dihydroxybipyridine complexes are tumor activated prodrugs due to low pH and blue light induced ligand release, *J. Inorg. Biochem.* 130, 103-111.
- [14] Chen, Y., Lei, W., Jiang, G., Hou, Y., Li, C., Zhang, B., Zhou, Q., and Wang, X. (2014) Fusion of photodynamic therapy and photoactivated chemotherapy: a novel Ru(II) arene complex with dual activities of photobinding and photocleavage toward DNA, *Dalton Trans.* 43, 15375-15384.
- [15] Ganeshpandian, M., Loganathan, R., Suresh, E., Riyasdeen, A., Akbarsha, M. A., and Palaniandavar, M. (2014) New ruthenium(II) arene complexes of anthracenyl-appended diazacycloalkanes: effect of ligand intercalation and hydrophobicity on DNA and protein binding and cleavage and cytotoxicity, *Dalton Trans.* 43, 1203-1219.
- [16] White, J. K., Schmehl, R. H., and Turro, C. (2017) An overview of photosubstitution reactions of Ru(II) imine complexes and their application in photobiology and photodynamic therapy, *Inorg. Chim. Acta* 454, 7-20.
- [17] Knoll, J. D., Albani, B. A., and Turro, C. (2015) New Ru(II) Complexes for Dual Photoreactivity: Ligand Exchange and ¹O₂ Generation, *Acc. Chem. Res.* 48, 2280-2287.
- [18] Huisman, M., White, J. K., Lewalski, V. G., Podgorski, I., Turro, C., and Kodanko, J. J. (2016) Caging the uncageable: using metal complex release for photochemical control over irreversible inhibition, *Chem. Commun. (Cambridge, U. K.)* 52, 12590-12593.
- [19] Loftus, L. M., White, J. K., Albani, B. A., Kohler, L., Kodanko, J. J., Thummel, R. P., Dunbar, K. R., and Turro, C. (2016) New Ru(II) Complex for Dual Activity: Photoinduced Ligand Release and ¹O₂ Production, *Chem. - Eur. J.* 22, 3704-3708.

- [20] Qu, F., Park, S., Martinez, K., Gray, J. L., Thowfeik, F. S., Lundeen, J. A., Kuhn, A. E., Charboneau, D. J., Gerlach, D. L., Lockart, M. M., Law, J. A., Jernigan, K. L., Chambers, N., Zeller, M., Piro, N. A., Kassel, W. S., Schmehl, R. H., Paul, J. J., Merino, E. J., Kim, Y., and Papish, E. T. (2017) Ruthenium Complexes are pH-Activated Metallo Prodrugs (pHAMPs) with Light-Triggered Selective Toxicity Toward Cancer Cells, *Inorg. Chem.* *56*, 7519-7532.
- [21] Heidelberger, C., Chaudhuri, N. K., Danneberg, P., Mooren, D., Griesbach, L., Duschinsky, R., Schnitzer, R. J., Plevin, E., and Scheiner, J. (1957) Fluorinated pyrimidines, a new class of tumor-inhibitory compounds, *Nature (London, U. K.)* *179*, 663-666.
- [22] Peters, G. J., Backus, H. H. J., Freemantle, S., van Triest, B., Codacci-Pisanelli, G., van der Wilt, C. L., Smid, K., Lunec, J., Calvert, A. H., Marsh, S., McLeod, H. L., Bloemena, E., Meijer, S., Jansen, G., van Groeningen, C. J., and Pinedo, H. M. (2002) Induction of thymidylate synthase as a 5-fluorouracil resistance mechanism, *Biochim. Biophys. Acta, Mol. Basis Dis.* *1587*, 194-205.
- [23] Ha, J. H., Hwang, D.-Y., Yu, J., Park, D.-H., and Ryu, S.-H. (2011) Onset of manic episode during chemotherapy with 5-Fluorouracil, *Psychiatry Invest.* *8*, 71-73.
- [24] Latchman, J., Guastella, A., and Toftagen, C. (2014) 5-Fluorouracil toxicity and dihydropyrimidine dehydrogenase enzyme: implications for practice, *Clin. J. Oncol. Nurs.* *18*, 581-585.
- [25] Gentry, G. A., Morse, P. A., Jr., and Dorsett, M. T. (1971) In vivo inhibition of pyrimidine catabolism by 5-cyanouracil, *Cancer Res.* *31*, 909-912.
- [26] Porter, D. J. T., Chestnut, W. G., Merrill, B. M., and Spector, T. (1992) Mechanism-based inactivation of dihydropyrimidine dehydrogenase by 5-ethynyluracil, *J. Biol. Chem.* *267*, 5236-5242.
- [27] Garner, R. N., Gallucci, J. C., Dunbar, K. R., and Turro, C. (2011) $[\text{Ru}(\text{bpy})_2(5\text{-cyanouracil})_2]^{2+}$ as a Potential Light-Activated Dual-Action Therapeutic Agent, *Inorg. Chem.* *50*, 9213-9215.
- [28] Sgambellone, M. A., David, A., Garner, R. N., Dunbar, K. R., and Turro, C. (2013) Cellular Toxicity Induced by the Photorelease of a Caged Bioactive Molecule: Design of a Potential Dual-Action Ru(II) Complex, *J. Am. Chem. Soc.* *135*, 11274-11282.
- [29] Marelius, D. C., Bhagan, S., Charboneau, D. J., Schroeder, K. M., Kamdar, J. M., McGettigan, A. R., Freeman, B. J., Moore, C. E., Rheingold, A. L., Cooksy, A. L., Smith, D. K., Paul, J. J., Papish, E. T., and Grotjahn, D. B. (2014) How Do Proximal Hydroxy or Methoxy Groups on the Bidentate Ligand Affect [(2,2';6',2''-Terpyridine)Ru(N,N)X] Water-Oxidation Catalysts? Synthesis, Characterization, and Reactivity at Acidic and Near-Neutral pH, *Eur. J. Inorg. Chem.* *2014*, 676-689.

- [30] Shobana, S., Dharmaraja, J., and Selvaraj, S. (2013) Mixed ligand complexation of some transition metal ions in solution and solid state: spectral characterization, antimicrobial, antioxidant, DNA cleavage activities and molecular modeling, *Spectrochim. Acta A Mol. Biomol. Spectrosc.* 107, 117-132.
- [31] Chakraborty, S., Laye, R. H., Munshi, P., Paul, R. L., Ward, M. D., and Kumar Lahiri, G. (2002) Dinuclear bis(bipyridine)ruthenium(II) complexes $[(bpy)_2RuII\{L\}_2-RuII(bpy)_2]^{2+}$ incorporating thiouracil-based dianionic asymmetric bridging ligands: synthesis, structure, redox and spectroelectrochemical properties, *J. Chem. Soc., Dalton Trans.*, 2348-2353.
- [32] Duan, L., Manbeck, G. F., Kowalczyk, M., Szalda, D. J., Muckerman, J. T., Himeda, Y., and Fujita, E. (2016) Noninnocent Proton-Responsive Ligand Facilitates Reductive Deprotonation and Hinders CO₂ Reduction Catalysis in $[Ru(tpy)(6DHBP)(NCCH_3)]^{2+}$ (6DHBP = 6,6'-(OH)₂bpy), *Inorg. Chem.* 55, 4582-4594.
- [33] Nakajima, N., and Ubukata, M. (2005) Imidates, *Sci. Synth.* 22, 343-360.
- [34] Houben, J. (1926) Nucleus condensation of phenols and phenol ethers with nitriles to phenol and phenol ether ketimides and ketones. I, *Ber. Dtsch. Chem. Ges. B* 59B, 2878-2891.
- [35] (2017) R factor, Online Dictionary of Crystallography. https://dictionary.iucr.org/R_factor (Accessed: 6 December 2020).
- [36] Saitou, R., Chung, K.-G., Nishimura, H., Sakai, T., Komiya, S., Noda, N., and Nishiguchi, M. (2012) Method for producing ruthenium compound, US20120101290A1.
- [37] Choudhuri, M. M. R., Behzad, M., Al-Noaimi, M., Yap, G. P. A., Kaim, W., Sarkar, B., and Crutchley, R. J. (2015) Variable Noninnocence of Substituted Azobis(phenylcyanamido)diruthenium Complexes, *Inorg. Chem.* 54, 1508-1517.

CHAPTER 4

INVESTIGATING MODE OF ACTION FOR RUTHENIUM COMPLEXES: MEASURING SINGLET OXYGEN PRODUCTION AND LUMINESCENT PROPERTIES

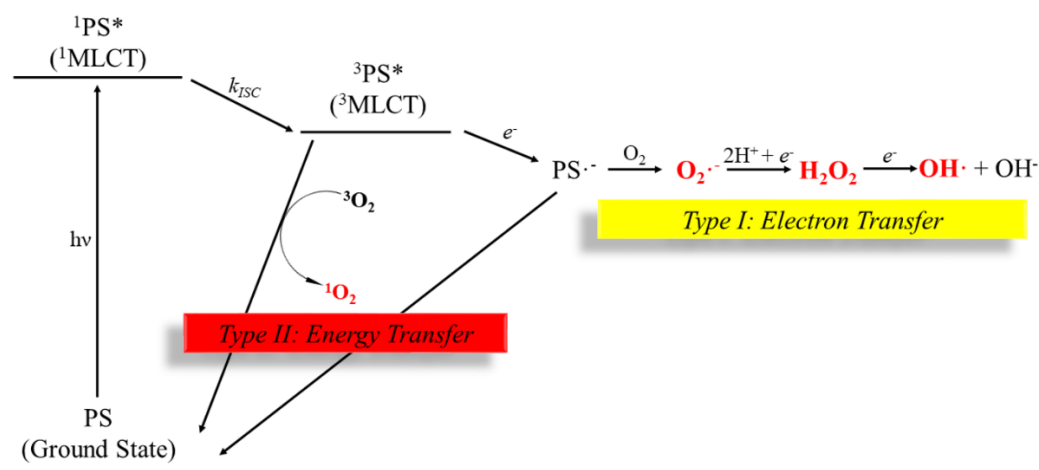
4.1 Abstract

Singlet oxygen is considered a highly toxic ROS that can be produced in catalytic amounts by a photosensitizer upon irradiation. This process is known as photodynamic therapy (PDT) and is an FDA-approved treatment that can be utilized for the selective treatment of cancer. This chapter investigates how compounds of the type $[(N,N')_2Ru(6,6'$ -dihydroxybipyridine)]²⁺ (where N,N' = bpy, phen, or dop) are able to kill cancer cells via a PDT pathway. These compounds are also capable of photodissociation; however, once deprotonated (as they would be at physiological pH) they favor a pathway that is dominated by the production of singlet oxygen. All the tested complexes have higher singlet oxygen quantum yields (Φ_{Δ}) once deprotonated (\mathbf{X}_B) than when fully protonated (\mathbf{X}_A). Complex **2** ($[(phen)_2Ru(6,6'$ -dhbp)]) has the highest measured Φ_{Δ} 's at 0.87(9) in its deprotonated (\mathbf{X}_B) form and 0.048(2) for its protonated (\mathbf{X}_A) form. Computational work and preliminary luminescent studies on complexes **2** and **3** ($[(dop)_2Ru(6,6'$ -dhbp)]) show ³MLCT excited states which are lower in relative energy when fully deprotonated than when they are fully protonated (**2_A** and **3_A**, respectively). A new complex, $[(dop)_2Ru(4,4'$ -dhbp)]Cl₂ (**8_A**), has also been synthesized and studied with the aim of producing a compound that could be a highly efficient producer of ¹O₂. Preliminary data shows

that this complex is capable of singlet oxygen production at higher rates than **1-3** in acetonitrile; however, further work is needed to complete the study.

4.2 Introduction

As discussed in chapter one, there is a significant need to develop new therapies capable of selectively targeting cancer cells. Photochemotherapy (PCT) is a treatment method which utilizes irradiation to elicit a therapeutic effect and only occurs in the immediate area of irradiation allowing for precise spatial delivery of the active drug.¹ PCT can be further classified as PDT or PACT. While PACT agents are typically consumed in the reaction, PDT agents can produce a catalytic amount of photoproduct upon irradiation, typically singlet oxygen ($^1\text{O}_2$, a toxic reactive oxygen species (ROS)) (Scheme 4.1). Ruthenium(II) complexes have been extensively studied as potential PACT or PDT anticancer agents due to their ability to bind to DNA similar to Pt-based drugs and their propensity to undergo light-induced ligand substitution and/or $^1\text{O}_2$ production.²⁻⁸



Scheme 4.1: Formation by ROS by Type I (yellow, various ROS) and Type II (red, $^1\text{O}_2$) processes

In 2013, Sherri McFarland published on a series of Ru(II) dyad complexes capable of significant $^1\text{O}_2$ quantum yields (Φ_Δ) and sub-micromolar toxicity towards leukemia cells (Figure 1.4).⁷ These complexes were also light selective as shown by phototoxicity indices (PI's) of over 1700 ($\text{PI} = \text{EC}_{50} \text{ dark}/\text{EC}_{50} \text{ light}$). This work is supported by the development of TLD-1433, which is currently the only light activated Ru(II) PDT agent.⁹ TLD-1433 is a Ru(II) PDT agent in phase 2 clinical trials (Clinicaltrials.gov identifier NCT03945162) developed by McFarland and co-workers to treat non-muscle invasive bladder cancer and produces $^1\text{O}_2$ at near quantitative efficiency (Figure 1.5).^{8, 10} Unfortunately, PDT agents typically require oxygenated environments and, as a result, may underperform PACT agents in hypoxic environments that are associated with some tumors.^{10, 11} Turro and Dunbar published on a Ru(II) complex in *JACS*, 2014 with the potential to overcome this limitation.⁶ Their complex, $[\text{Ru}(\text{bpy})(\text{dppn})(\text{CH}_3\text{CN})_2]^{2+}$ (Figure 1.3), was capable of both PDT and PACT pathways upon irradiation. They also found that structural modifications that increased singlet oxygen production also increased light toxicity. This is consistent with the fact that both PACT and PDT are competing pathways and limiting photodissociation would push favorability towards a PDT-type mode of action. Furthermore, their study confirmed the possibility that both pathways occur simultaneously, leading to multiple modes of toxicity.

Since 2014, the Papish group has published on a series of Ru(II) complexes containing protic bipyridine ligands as potential PACT agents.¹²⁻¹⁵ These complexes (**1-3**, Figure 1.6) showed good light selectivity and toxicity in several breast cancer cell lines; however, they exhibited limited photodissociation that would normally be associated with PACT agents (Tables 1.1 & 1.2). A further study by Fengrui Qu, formerly of the Papish group, developed a series of analogous complexes which replaced 6,6'-dhbp with 6,6'-dimethoxybipyridine (6,6'-dmbp =

6,6'-dimethoxy-2,2'-bipyridine) (Table 1.3, 4.1).¹⁴ Substitution of 6,6'-*dhbp* with 6,6'-*dmbp* (-OH vs -OMe groups at the 6,6' position) introduced more steric bulk near the metal center, increasing photodissociation quantum yields (Φ_{PD}). This structural change rendered the complexes non-toxic ($EC_{50 \text{ light}} > 100 \mu\text{M}$). Only analogues of compounds **2** and **3** were studied ($[(\text{phen})_2\text{Ru}(6,6'\text{-dmbp})]\text{Cl}_2$ (**2^{OMe}**) and $[(\text{dop})_2\text{Ru}(6,6'\text{-dmpb})]\text{Cl}_2$ (**3^{OMe}**), respectively). Increasing photodissociation pushes favorability toward a PACT mechanism over a PDT driven mode of action suggesting that, for complexes **1-3**, a PDT based mode of action is the most probable contributor to toxicity. These complexes; however, may behave similarly to those studied by Turro and Dunbar. Their complex was capable of limited photodissociation with high toxicity (which was determined to be due to $^1\text{O}_2$ production). However, unlike their complexes, study of these complexes will investigate the effects of protic ligands within the system.⁶

Table 4.1. Quantum yield of photodissociation and EC_{50} toxicity data (μM) against MDA-MB-231 breast cancer stem cell line. Complexes with more steric bulk near the metal center (**2^{OMe}** and **3^{OMe}**) had increased rates of photodissociation but are non-toxic. Toxicity and rates of photodissociation appear to be inversely related. *Data adapted from references 13 and 14.*

Compound	pK_a avg	Φ_{PD} for X_A	Φ_{PD} for X_B	$EC_{50 \text{ light}}$ MDA-MB-231
2	6.0(1)	0.0020(2)	0.000036(1)	83(3)
3	5.9(1)	0.001(1)	0.00022(3)	3.7(2)
2^{OMe}	N/A	0.024(6)	N/A	>100
3^{OMe}	N/A	0.0030(2)	N/A	>100

Herein, the efforts to assess singlet oxygen production of these complexes are discussed. Singlet oxygen can be directly measured using near-IR due to weak luminescence at $\sim 1,286 \text{ nm}$. Its short lifetime ($\sim 0.04 \mu\text{s}$ in biological systems) makes it difficult to directly detect without specialized equipment (time-resolved near-IR, for example (TR-NIR)).¹⁶ In the absence of TR-NIR, a trapping molecule is typically used to indirectly determine the presence singlet oxygen by

reacting with $^1\text{O}_2$ to produce a species that can be detected with common spectroscopy techniques. Collaborator Sherri McFarland was able to measure Φ_Δ with TR-NIR while I conducted indirect measurements of $^1\text{O}_2$ production using the trapping molecules 2,2',6,6'-tetramethylpiperidine (TEMP), 1,3-diphenylisobenzofuran (DPBF), and singlet oxygen sensor green (SOSG). When reacted with singlet oxygen, TEMP, DPBF, and SOSG generate products that can be detected via electron paramagnetic resonance (EPR), UV-Vis, and fluorescence respectively. These measurements are carried out in solution allowing for the study of $^1\text{O}_2$ production under various conditions including varied pH and presence (or absence) of oxygen.

2,2,6,6-Tetramethylpiperidine (TEMP) will react with $^1\text{O}_2$ to produce the EPR detectable species, TEMPO (2,2,6,6-tetramethylpiperidin-1-yl)oxidanyl) (Figure 4.1).^{17, 18} Neither TEMP or the ruthenium compounds proposed in this study are EPR active, making the detection of singlet oxygen via TEMPO formation a feasible study.

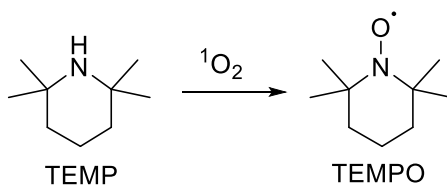


Figure 4.1. Shown is the reaction scheme of TEMP with singlet oxygen to form TEMPO.

An alternative method of detecting $^1\text{O}_2$ utilizes UV-Vis spectroscopy and the probe 1,3-diphenylisobenzofuran (DPBF)¹⁹. The reaction between DPBF and $^1\text{O}_2$ can be characterized by a decrease in absorbance at 411 nm in ethanol (Figure 4.2). This reaction occurs in a 1:1 stoichiometry allowing for precise quantification of $^1\text{O}_2$ generation.

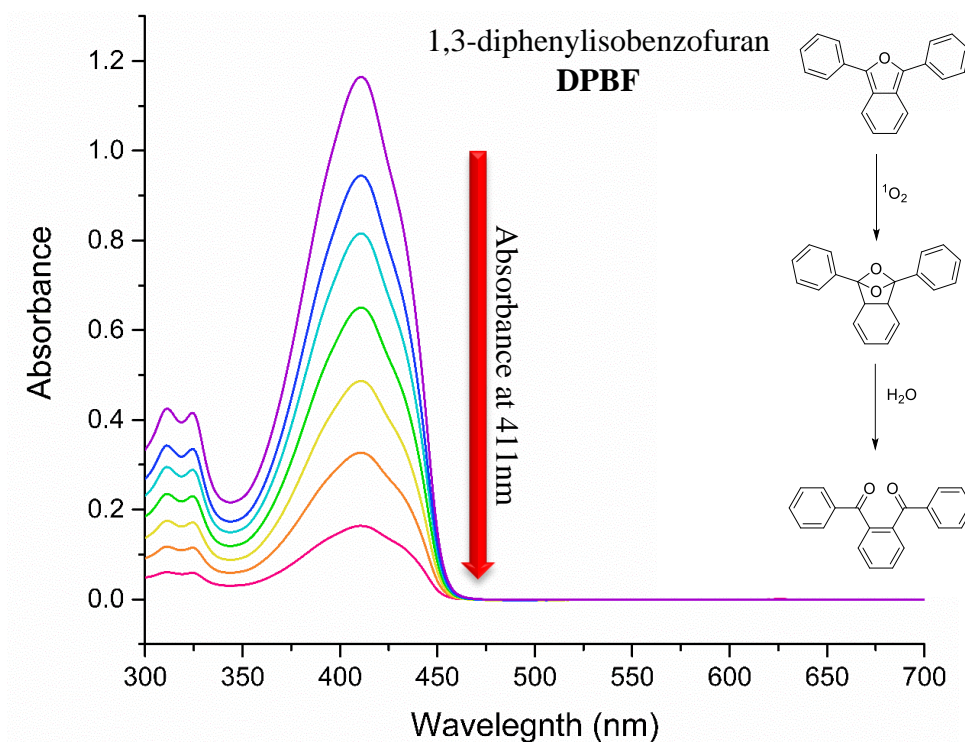


Figure 4.2. Shown is the typical absorption spectra and reaction scheme (insert) of DPBF reacting with $^1\text{O}_2$ resulting in a decrease in absorbance at 411 nm.

The fluorescent probe, singlet oxygen sensor green (SOSG), is a well-known fluorescent probe that is selective for singlet oxygen.²⁰ It is typically used to detect singlet oxygen in solution as well as in cells by producing detectable fluorescence at 525 nm upon excitation at 504 nm. SOSG is typically used for a qualitative measurement of singlet oxygen in cells; however, it is possible to collect quantitative data when compared to a standard in solution.

While all the indirect methods can provide evidence of $^1\text{O}_2$, there is the possibility that the probe molecule may interact with the compound of study. As such, Prof. Sherri McFarland (University of Texas, Arlington) measured the Φ_Δ for compounds **1-3** in both their acidic (\mathbf{X}_A) and basic forms (\mathbf{X}_B). Measurements were performed in deuterated methanol (CD_3OD) and acetonitrile (MeCN) as water quenches the luminescence of $^1\text{O}_2$.

Knowing the mode of action for these complexes can also aid in the design of new compounds with improved performance. I synthesized and studied the complex $[(\text{dop})_2\text{Ru}(4,4'\text{-dhbp})]\text{Cl}_2$ (**8_A**) with this aim in mind. By exchanging 6,6'-dhbp with 4,4'-dhbp, steric bulk near the metal center can be reduced, potentially limiting photodissociation (and thus increase production of $^1\text{O}_2$). Complex **8** continues to include the dop spectator ligand from the most toxic complex, **3**, while also probing the effects of pH by incorporating -OH groups. This chapter discusses the findings from the investigation of $^1\text{O}_2$ production for complexes **1-3** and **8** and further investigates causes for differences in $^1\text{O}_2$ production between the **X_A** and **X_B** form of the drugs.

4.3 Results and Discussion

4.3.1. Detecting $^1\text{O}_2$ with EPR/TEMP

Initial in-house experiments used the EPR/TEMP method of $^1\text{O}_2$ detection. This method utilizes the reaction of TEMP with $^1\text{O}_2$ to form TEMPO, which is detectable by continuous wave (CW) EPR. Both TEMP and compounds **1-3** are EPR silent allowing for the easy detection of the TEMPO product. Initial experiments were run in EtOH and carried out under ambient conditions with final concentrations of 0.5 mM ruthenium compound and 50 mM TEMP. The sample was then irradiated with blue light (450 nm) and measured after various time intervals to monitor the formation of TEMPO (Figure 4.3). Control experiments were carried out under dry and oxygen free (N_2) conditions to observe any change in the spectra. Both experiments produced a triplet TEMPO signal; however, the overall intensity of the air free sample was greatly decreased (the signal present in the oxygen free sample is most likely due to the presence of trace oxygen). For both samples, a large central peak was observed in early scans which decreased in intensity over

time. It was initially thought that this was an intermediate related to a photodissociation mechanism, but control experiments of just the ruthenium complex subsequently ruled this out.

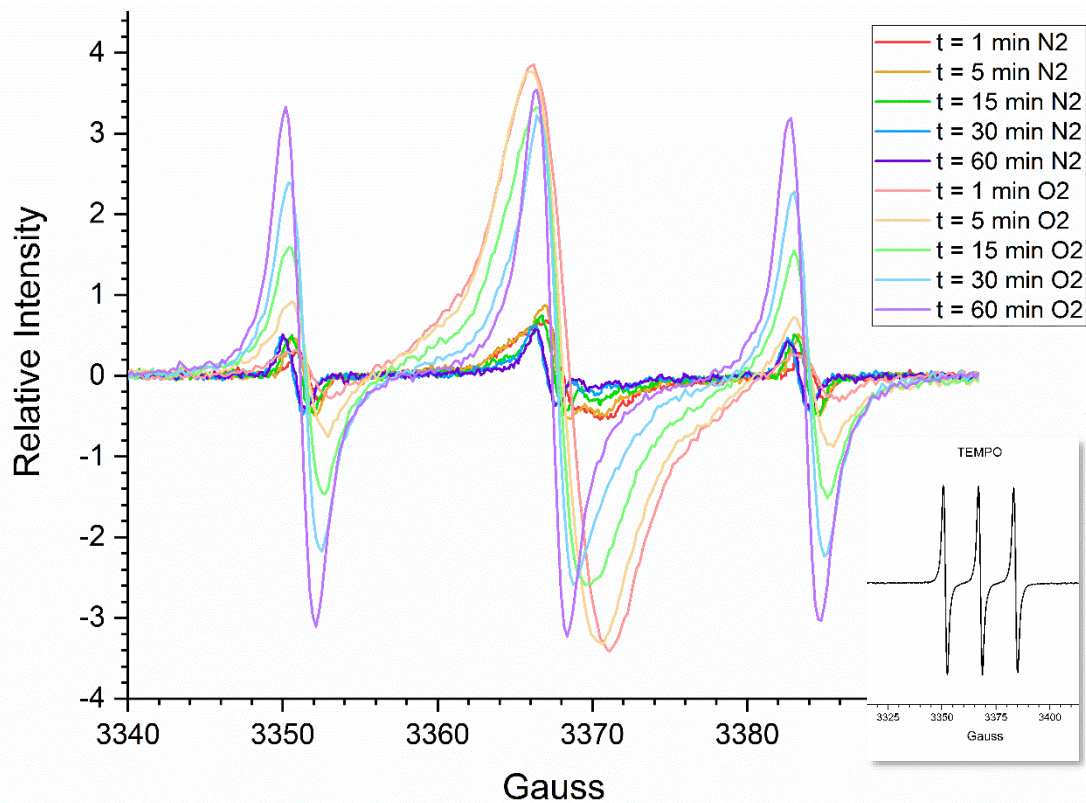


Figure 4.3. CW-EPR scans of 3_A (0.5 mM) and TEMP (50 mM) in ethanol after being irradiated at various time intervals with blue light (450 nm) with the oxygen free experiment (N₂) shown in darker colors and the ambient conditions experiment (O₂) shown in lighter colors. **Insert:** Typical EPR signal of TEMP for comparison.

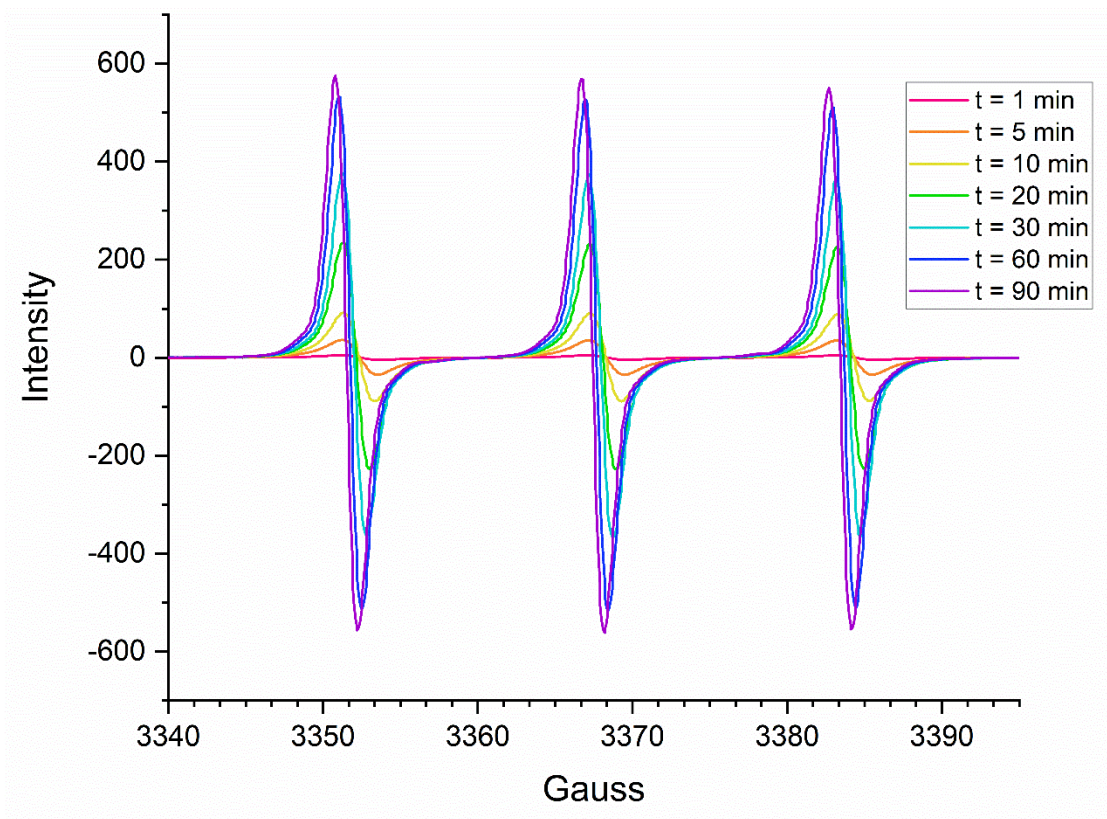


Figure 4.4. $^1\text{O}_2$ (+)-control experiment with $[\text{Ru}(\text{bpy})_3]^{2+}$ under ambient conditions in a toluene/MeOH solution. The sample was irradiated with blue light (450 nm) with CW-EPR scans taken at various time intervals.

The EPR method for detection of singlet oxygen (via detection of TEMPO after oxidation of TEMP) has been researched since the 1970s.¹⁷ Compound **3** was initially chosen for study as it was the most toxic. Initial EPR studies showed promise for $^1\text{O}_2$ production; however, EPR detectable species other than TEMPO are present in solution making $^1\text{O}_2$ generation difficult to quantify. Controls ruled out the possibility that these unidentified species came solely from TEMP or **3_A**, but rather the interaction between the two upon irradiation. Experiments carried out under inert atmosphere also indicated that this was not an oxygen dependent reaction, as the signal intensity should have decreased. Zhang and co-workers had used the same EPR/TEMPO

method with a Ru(II) complex but did not report evidence of any abnormalities within their spectra.¹⁹

Nardi and co-workers have previously studied the effectiveness and scope of the EPR/TEMPO method for singlet oxygen detection.¹⁸ They demonstrated that this method can lead to a significant overestimation of singlet oxygen production as the excited state of the photosensitizer (in this case **3**) can be quenched by TEMP, acting as an electron donor (Figure 4.5). In doing so, Nardi et al. proposed that this would generate the TEMP radical cation which could eventually give rise to an EPR detectable TEMPO signal that was not associated with singlet oxygen production. Nardi's proposed generation of TEMPO still requires the presence of molecular oxygen; and while the experiment was carried out under anaerobic conditions, it may not be 100 % free of molecular oxygen. Compounds **1-3** may still have the potential to produce singlet oxygen; however, the EPR/TEMPO method of detection has proven unreliable and has produced unusual results. In order to determine if this is a biologically relevant reaction, it would be advantageous to run the experiment with a biomolecule that was similar in structure to TEMP, such as proline. If similar results are observed when run with **3** and proline, then this may also be a reaction that occurs within cells.

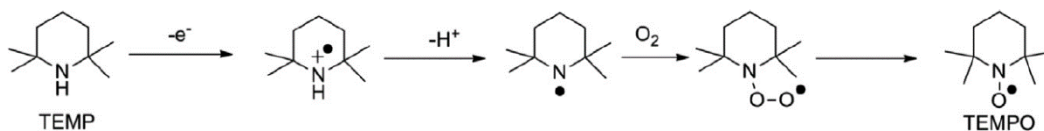


Figure 4.5. Proposed mechanism for the electron transfer oxidation of TEMP to TEMPO in the presence of molecular oxygen. *Figure adapted from reference 18*

4.3.2 Detecting $^1\text{O}_2$ with UV-Vis/DPBF

The 1:1 reaction between DPBF and $^1\text{O}_2$ can be monitored by an observed decrease in absorbance at 411 nm in ethanol.^{19, 21} Under dark conditions, samples in ethanol were prepared under ambient atmosphere with final concentrations of 1 μM **3A** and 100 μM DPBF. The sample was then irradiated with blue light (450 nm) and the absorbance was measured at various time intervals over the course of two hours. A significant decrease in absorbance at 411 nm was observed which was initially believed to be a result of the reaction between DPBF and $^1\text{O}_2$ (Figure 4.6). However, a subsequent control experiment performed in the absence of compound **3A** also resulted in a significant decrease in absorption (Figure 4.7). In the presence of compound **3A**, the absorbance at 411 nm after 10 minutes of irradiation was 82 % less than the absorbance at 0 minutes of irradiation. The control experiment (DPBF only) exhibited a 92 % decrease in absorbance at 411 nm after the same amount of irradiation. This is most likely caused by photobleaching of DPBF by the irradiation source, thus rendering this method ineffective for this system.²¹

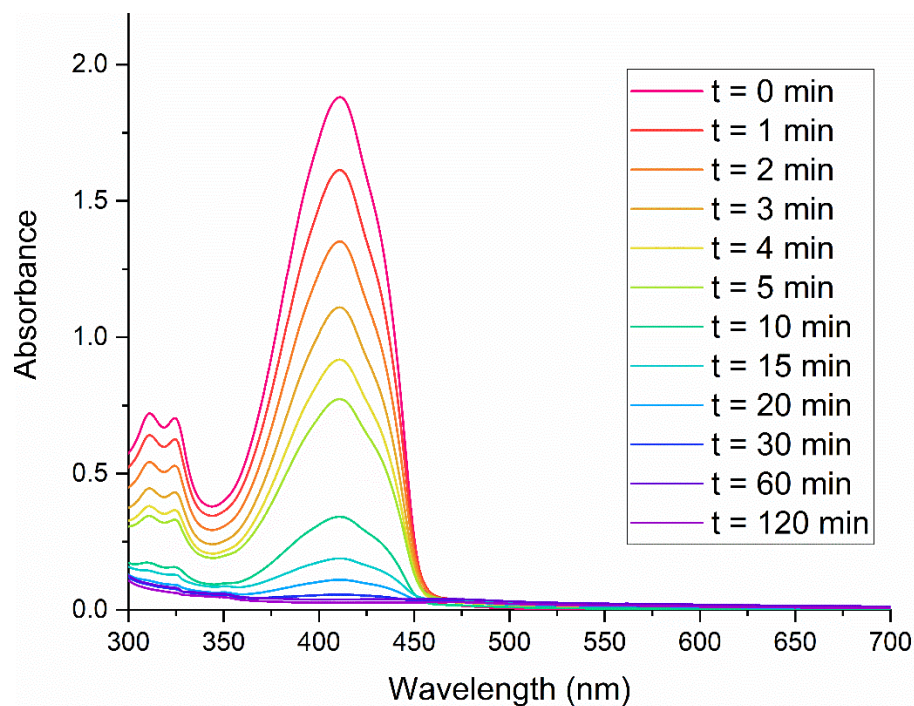


Figure 4.6. UV-Vis data of 3_A (1 μM) and DPBF (100 μM) in ethanol handled under ambient conditions. The sample was irradiated over the course of 2 hours with blue light (450 nm).

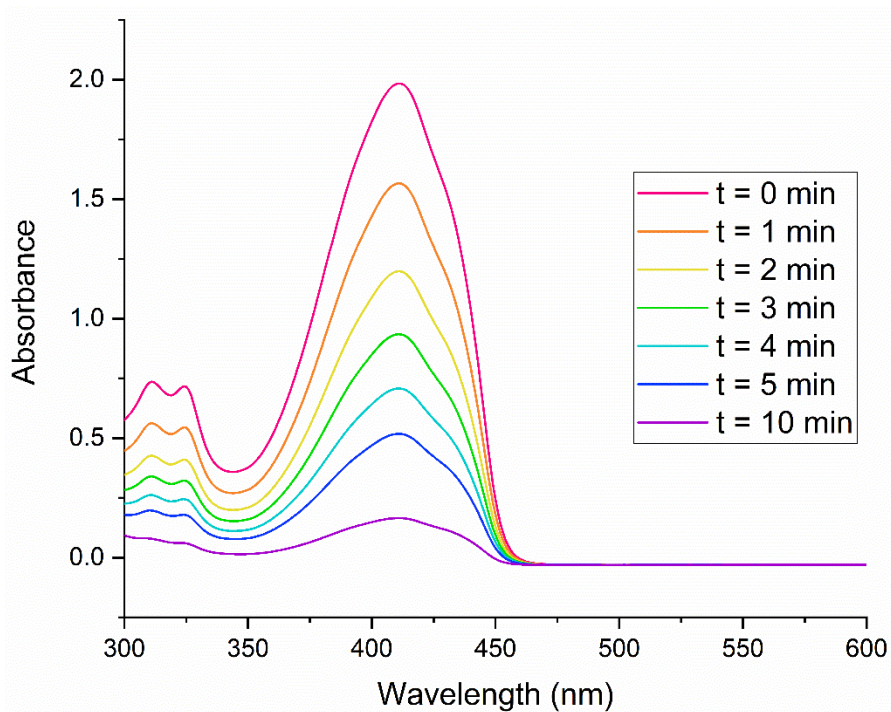


Figure 4.7. UV-Vis data of negative control experiment. DPBF in ethanol (100 μM) was handled under ambient conditions. The sample was irradiated over the course of 10 min with blue light (450 nm).

4.3.3 Detecting $^1\text{O}_2$ with fluorescence/SOSG

The fluorescent probe singlet oxygen sensor green (SOSG) emits weak fluorescence at 525 nm that is significantly amplified upon interacting with singlet oxygen.²² SOSG can be used for detecting $^1\text{O}_2$ in cellular environments and, in this instance, in solution. Unlike other probes used, SOSG can be used in aqueous conditions allowing for a better comparison of $^1\text{O}_2$ production under biological conditions. Initial SOSG studies in-solution utilized compound **2** due to its availability and similar characteristics to compound **3**. $[\text{Ru}(\text{bpy})_3]^{2+}$ was used as a positive control.

The blue light source used in previous experiments was replaced with a white light source (STASUN 200W LED Flood Light, 100-256V, 20000lm) for fluorescence experiments due to equipment failure. The SOSG probe exhibits some inherent fluorescence at 525 nm upon excitation at 504 nm; however, a significant increase in intensity was observed once in the presence of $^1\text{O}_2$ (Figure 4.8). The (+)-control sample containing both SOSG and $[\text{Ru}(\text{bpy})_3]^{2+}$ had intense fluorescence after one minute of irradiation that eventually decayed as opposed to increase over time. The most likely cause is the rapid production of $^1\text{O}_2$ by $[\text{Ru}(\text{bpy})_3]^{2+}$, which then reacted with most, if not all, of the available SOSG in solution. Reducing the concentration of $[\text{Ru}(\text{bpy})_3]^{2+}$ or increasing the concentration of SOSG could rectify this. A control experiment analyzing a solution of only $[\text{Ru}(\text{bpy})_3]^{2+}$ did not increase or decrease in fluorescence over the course of irradiation.

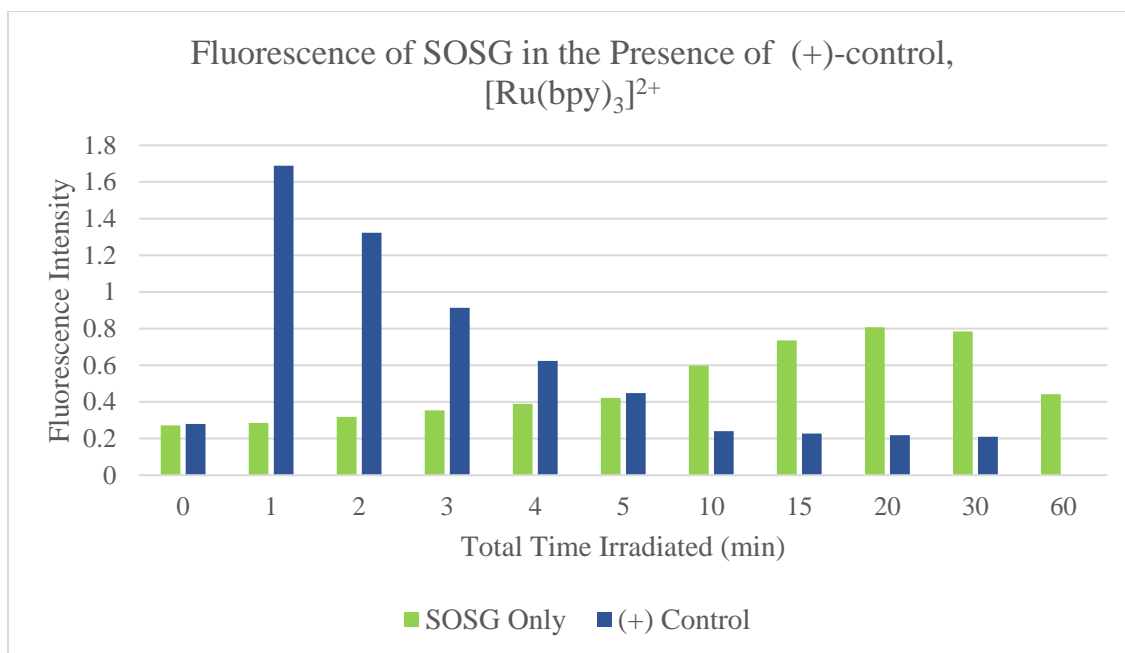


Figure 4.8. Fluorescence intensity at 525 nm of SOSG (1 μM) and $[\text{Ru}(\text{bpy})_3]^{2+}$ + SOSG (10 μM and 1 μM respectively) solutions in 0.1 M pH 8.0 phosphate buffer upon excitation at 504 nm. SOSG exhibits some inherent fluorescence at 525 nm (green) which is greatly increased in the presence of a $^1\text{O}_2$ producing molecule like $[\text{Ru}(\text{bpy})_3]^{2+}$ (blue).

While the control experiment showed good proof of concept data, the actual experiment with compound **2** did not show encouraging results. Upon irradiation with the same light source and conditions, compound **2** appeared to quench the inherent fluorescence of SOSG (Figure 4.9). Compound **2** did show an increased rate of photodissociation (Appendix 4A.1) when irradiated with this new light source; however, it is unknown what interaction with SOSG caused the decrease in fluorescence.

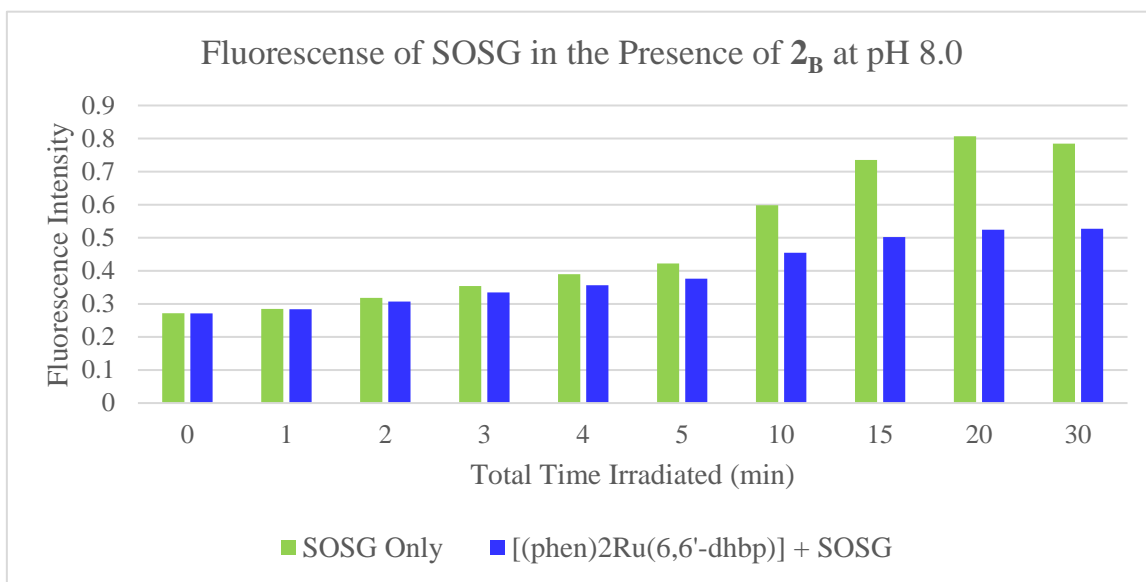


Figure 4.9. Fluorescence intensity at 525 nm of a solution of SOSG only (green, 1 μ M in 0.1 M pH 8.0 phosphate buffer) compared to a solution of **2_B** + SOSG (Blue, 10 μ M and 1 μ M respectively in 0.1 M pH 8.0 phosphate buffer) upon excitation at 504 nm. It was found that compound **2** quenched the inherent fluorescence of SOSG.

4.3.4. Direct Detection of $^1\text{O}_2$ and Singlet Oxygen Quantum Yields-McFarland Group

The quantum yields for $^1\text{O}_2$ formation (Φ_Δ) were determined by the McFarland group for **1-3** using the direct method based on the $^1\text{O}_2$ luminescence at 1268 nm (Table 4.2). Analogous compounds to compounds **2** and **3** which contain a -OMe group in place of an -OH at the 6,6' positions on the dihydroxybipyridine ligand (**2^{OMe}** and **3^{OMe}** respectively, previously studied in reference 14) were also studied as a point of comparison to determine what effects pH and photodissociation had on Φ_Δ . The protic complexes, where applicable, were studied as both their isolated acidic forms (**1_A-3_A**) bearing OH groups and their isolated basic forms for the complexes (**2_B-3_B**). Values for Φ_Δ were 0.048 for **2_A** and **3_A**, but the deprotonated analogs **2_B** and **3_B** gave Φ_Δ values of 0.87 and 0.48, respectively. Quantum yields for $^1\text{O}_2$ are enhanced 10 to 20-fold by deprotonation of the 6,6'-dhbp ligand which generates the corresponding neutral Ru(II) complexes. Thus, for **3_B** (the form present at physiological pH), Φ_Δ is three orders of magnitude greater than

Φ_{PD} . Likewise, for **2_B**, Φ_{Δ} is four orders of magnitude greater than Φ_{PD} . As a point of comparison, the 1O_2 quantum yields for **2^{OMe}** and **3^{OMe}** were calculated to be near 0.01 (Table 4.2) which shows that the change from -OH (in **2_A** and **3_A**) to -OMe groups reduces the quantum yield five-fold. Computational studies of the excited states generated upon irradiation were performed by Dr. Qu and the Webster Group and found that the difference in Φ_{Δ} from **X_B** to **X_A** is due in part to the relative free energy of the 3MC state (Appendix, 4A.3). Studying complexes **2** and **3**, they found that the **X_B** form had a relatively inaccessible 3MC state which would favor a PDT pathway over a photodissociation (PACT) pathway (Figures 4A.3 and 4A.5).

Table 4.2. Comparison of Φ_{Δ} data from complexes **1-3** and analogous compounds, **2^{OMe}** and **3^{OMe}**, in deuterated methanol (CD₃OD).

Compound	Structure	pK _a avg	Φ_{Δ} in CD ₃ OD	
			X _A ^a	X _B ^a
1	[(bpy) ₂ Ru(6,6'-dhbp)] ²⁺	6.3	0.041(2)	0.18(2)
2	[(phen) ₂ Ru(6,6'-dhbp)] ²⁺	6.0(1)	0.048(2)	0.87(9)
3	[(dop) ₂ Ru(6,6'-dhbp)] ²⁺	5.9(1)	0.048(2)	0.48(5)
2^{OMe}	[(phen) ₂ Ru(6,6'-dmbp)] ²⁺	N/A	0.01(1) ^b	N/A
3^{OMe}	[(dop) ₂ Ru(6,6'-dmbp)] ²⁺	N/A	0.01(1) ^b	N/A

^aIsolated **X_A** or **X_B** (in **1-3**) was used in CD₃OD. The aprotic complexes **2^{OMe}** and **3^{OMe}** are included in the **X_A** column because they carry the same charge as **1_A-3_A**

^bPhotodissociation also occurred during these experiments to quantify singlet oxygen, thereby reducing the accuracy of this measurement. Incident photons could have led to either product.

4.3.5. Development of new Protic Ru(II) PDT Complexes

With the data gathered from **1-3** and **2^{OMe}** and **3^{OMe}**, a direct correlation between increasing steric bulk near the metal center and an increase in Φ_{PD} . To limit photodissociation, a complex that removed steric bulk from the metal center by replacing 6,6'-dhbp with 4,4'-dhbp is studied. The complex [(phen)₂Ru(4,4'-dhbp)]Cl₂ had been briefly studied in *Inorganic Chemistry*, 2017 study but had limited toxicity (EC₅₀ > 100 μM in MCF7).¹³ A similar complex,

$[(\text{dop})_2\text{Ru}(4,4'\text{-dhbp})]\text{Cl}_2$ (**8_A**), which incorporates the same spectator ligand (dop) as the most toxic complex, **3**, is reported (Figure 4.11).¹³ X-ray crystallography showed significantly less torsion within the dhbp ligand and shorter Ru-N bond lengths which may lead to better photostability (Figure 4.10, Table 4.3). Initial photodissociation studies were carried out in methanol and monitored via UV-Vis spectroscopy (Figure 4.12). The UV-Vis spectra of **8_A** showed little to no change over the course of irradiation when compared to **3_A** under the same conditions indicating limited (if any) photodissociation. There was a slight change observed in the absorbance spectra of **8_A** over the total course of irradiation ($\Delta\text{Abs}_{\text{max}} = 0.019$ at 498 nm); however, even less change in the absorbance spectra was observed for **8_B** over the same amount of irradiation in methanol ($\Delta\text{Abs}_{\text{max}} = 7.79 \times 10^{-3}$ at 302 nm, Figure 4A.1). The Φ_{Δ} for complex **8** has been measured in both MeCN and CD₃OD (Table 4.3). In CD₃OD, **8_A** and **8_B** have Φ_{Δ} 's similar to that of the standard used, $[\text{Ru}(\text{bpy})_3]^{2+}$ (Φ_{Δ} 's were measured to be 1.13 and 1.03 for **8_A** and **8_B** respectively; however, the absolute Φ_{Δ} of the standard ($[\text{Ru}(\text{bpy})_3](\text{PF}_6)_2$) in CD₃OD is needed). As a general trend, Φ_{Δ} in CD₃OD for complexes **1-3** are higher for their deprotonated **X_B** forms than for their fully protonated **X_A** form. In acetonitrile (MeCN); however, **8** exhibited the opposite trend with **8_A** having a higher Φ_{Δ} than **8_B** (0.37 vs 0.09 respectively). Furthermore, **8_A** had higher Φ_{Δ} 's than **1_A-3_A** in acetonitrile; however, it is yet to be determined how **8_B** compares to **1_B-3_B** in MeCN. As complexes **1-3** will exist primarily as their **X_B** forms at physiological pH, the same is likely for complex **8** (measuring the $\text{p}K_{\text{a}}$ is currently planned for future studies).

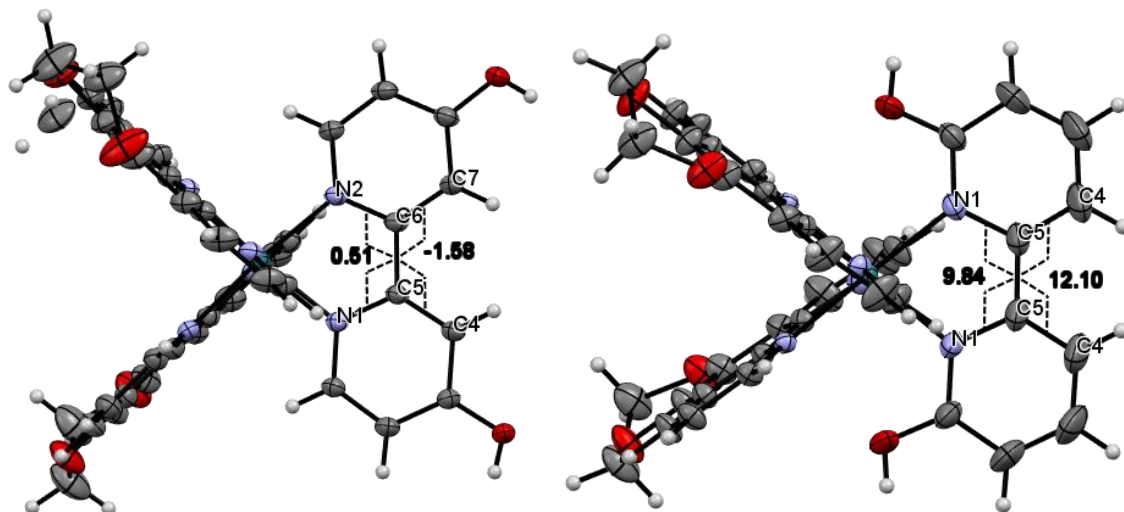


Figure 4.10. **Left:** Top-down view of the X-Ray crystal structure of $[(\text{dop})_2\text{Ru}(4,4'\text{-dhbp})]^{2+}$ (**8_A**). **Right:** Top-down view of the X-Ray crystal structure of $[(\text{dop})_2\text{Ru}(6,6'\text{-dhbp})]^{2+}$ (**3_A**). The torsion angle from C4 to C4' of the 6,6'-dhbp ligand (**3_A**) was 12.1° while the corresponding angle on 4,4'-dhbp (**8_A**) is -1.58°. The Ru-N bond lengths of the dhbp ligand on **3_A** averaged 2.098 Å while **8_A** had shorter average bond lengths of 2.057 Å.

Table 4.3. Selected bond lengths (Å) and angles (°) for compound **8_A**. Complete crystallographic information can be found in the appendix (Section 4A.4).

Selected Bond or Angle	Bond Length (Å) or Angle (°)
Ru1—N1	2.053(2)
Ru1—N2	2.060(2)
Ru1—N3	2.060(2)
Ru1—N4	2.061(2)
Ru1—N5	2.071(2)
Ru1—N6	2.051(2)
O1—C3	1.336(3)
O2—C8	1.341(3)
N6—Ru1—N2	89.95(9)
N1—C5—C6—N2	0.5(3)
C4—C5—C6—C7	-1.5(4)

Table 4.4. Comparison of preliminary Φ_{Δ} data form complexes **1-3** and **8** in acetonitrile. **1B-3B** Φ_{Δ} (and repeated measurements) are planned for future study.

Compound	Structure	Φ_{Δ} in MeCN ¹	
		X _A	X _B
1	[(bpy) ₂ Ru(6,6'-dhbp)] ²⁺	0.027	--
2	[(phen) ₂ Ru(6,6'-dhbp)] ²⁺	0.019	--
3	[(dop) ₂ Ru(6,6'-dhbp)] ²⁺	0.018	--
8	[(dop) ₂ Ru(4,4'-dhbp)] ²⁺	0.37	0.09

¹Acetonitrile is a coordinating solvent that can increase photodissociation. For compounds that photodissociate, only one measurement per sample has been carried out to avoid decomposition of the sample with excitation.

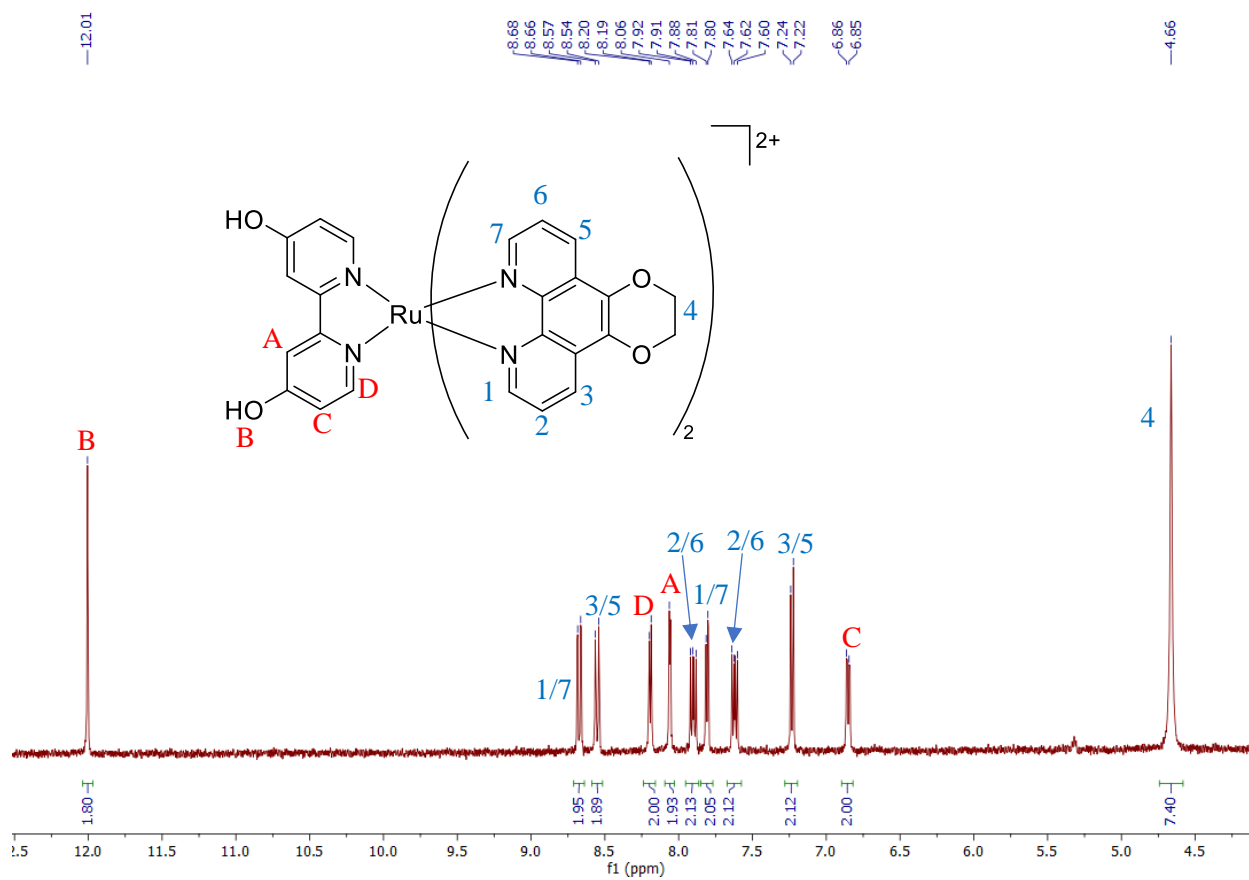


Figure 4.11. ^1H NMR spectrum of $[(\text{dop})_2\text{Ru}(4,4'\text{-dhbp})]^{2+}$ (**8_A**) in $\text{DMSO-}[d_6]$ with assignments. Solvent peak has been omitted for clarity.

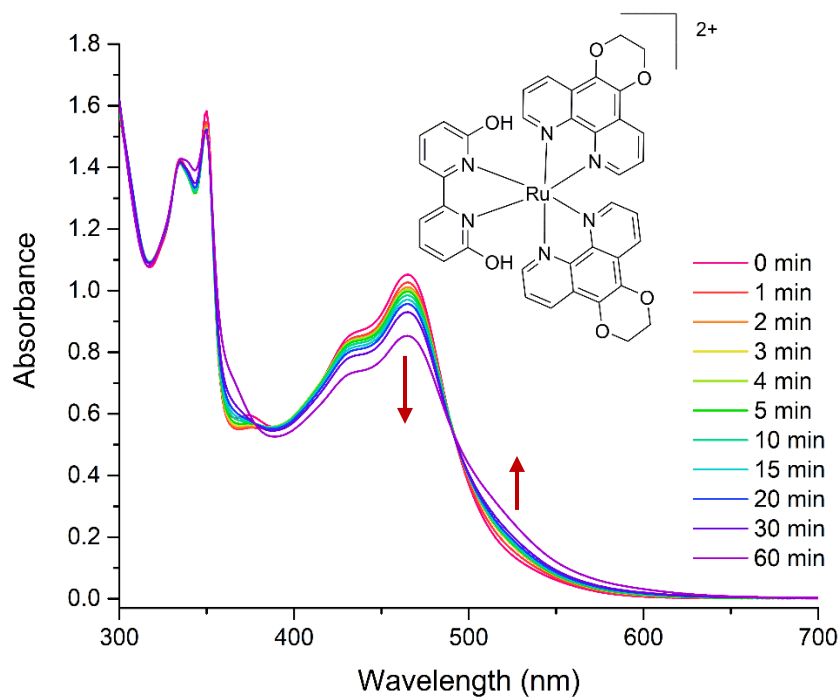
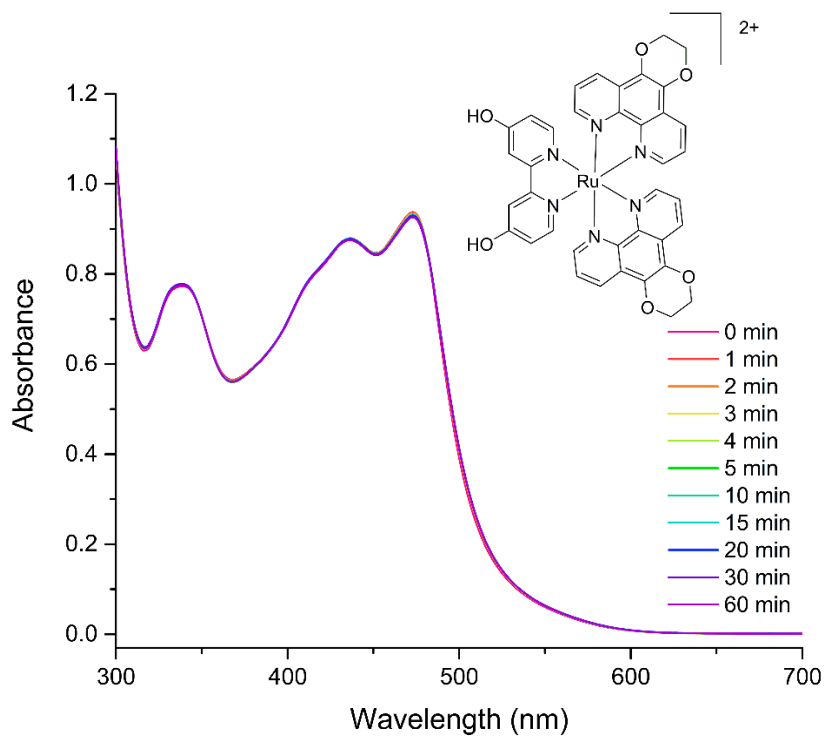


Figure 4.12 UV-Vis spectra of photodissociation of **8_A** (top) and **3_A** (bottom) in MeOH with respective structures inserted. A slight increase in absorbance of 0.019 was observed at 498 nm from $t = 0$ min to $t = 60$ min for **8_A**, otherwise little to no change was observed in the spectra. Unlike **3_A**, **8_A** undergoes limited photodissociation.

4.3.6 Luminescent Measurements of compound **2**

Ruthenium complexes can produce singlet oxygen or photodissociate to reach the ground state from the excited $^3\text{MLCT}$ or ^3MC states, respectively. However, ruthenium complexes are also known emit light from the $^3\text{MLCT}$ state as a means of relaxation (Figure 4.13).²³⁻²⁶ These luminescent pathways can potentially compete with both singlet oxygen and photodissociation pathways. The wavelength at which maximum luminescence is observed (λ_{max}) may prove useful in determining the relative energy of the excited states for compounds **1-3**. The luminescence of **2** is measured in aqueous solvents at both pH 7.4 (mostly **2_B** and physiological pH) and pH 4.0 (**2_A**). For both pH values, compound **2** emitted weak luminescence with a λ_{max} around 610 nm (Figures 4.14 & 4.15). As these spectra have similar λ_{max} 's, both solutions likely have the same “major species” in solution; however, a small shoulder was observed around 700 nm for pH 7.40. It is hypothesized that the luminescence at $\lambda_{\text{max}} = \sim 610$ nm corresponds to **2_A** while the shoulder observed at 700 nm (at pH 7.40) likely corresponds to the monodeprotonated or fully deprotonated (**2_B**) species. For these experiments, **2_A** was added to the relevant buffer solution (pH 4.0 or 7.4) to allow for the formation of the studied species in solution (**2_A** or **2_B**, respectively). Unfortunately, this experiment was not repeated under these conditions due to COVID-19 related shutdowns. Subsequent luminescent studies by other members of the Papish group, in which the isolated **2_A** or **2_B** were directly added to diH₂O, have since been carried out. In diH₂O, **2_A** has a $\lambda_{\text{max}} = 628$ nm while **2_B** has a $\lambda_{\text{max}} = 696$ nm (Figure 4.16). This red shift in the λ_{max} signifies a $^3\text{MLCT}$ state that is lower in relative energy for **2_B** when compared to **2_A**. This conclusion is further supported by computational studies by the Webster group and Dr. Qu (Appendix, 4A.3), which have calculated the relative free energies of the ^3MC and $^3\text{MLCT}$ states for complexes **2** and **3** (Figures 4A.3 & 4A.5). Their work found that, for **2_A** and **3_A**, the ^3MC state (1.7 eV) was downhill of the $^3\text{MLCT}$

state allowing for favorable photodissociation. However, for **2_B** and **3_B**, the ³MC state (1.9 eV) was energetically uphill from the ³MLCT state leading to favorable ¹O₂ production from the ³MC state.. Luminescence experiments in methanol are underway in order to directly compare to TR-NIR studies by the McFarland group as well as investigating other compounds.

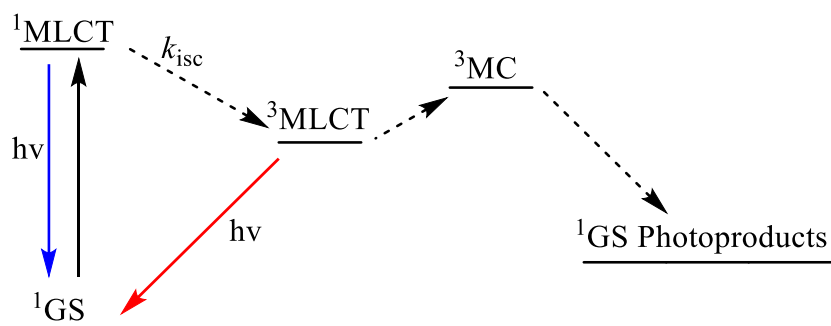


Figure 4.13. Typical Jablonski diagram detailing the potential light emissive relaxation pathway (blue arrow, fluorescence; red arrows, phosphorescence) for ruthenium complexes upon excitation. Luminescent pathways can compete with singlet oxygen or photodissociation pathways.

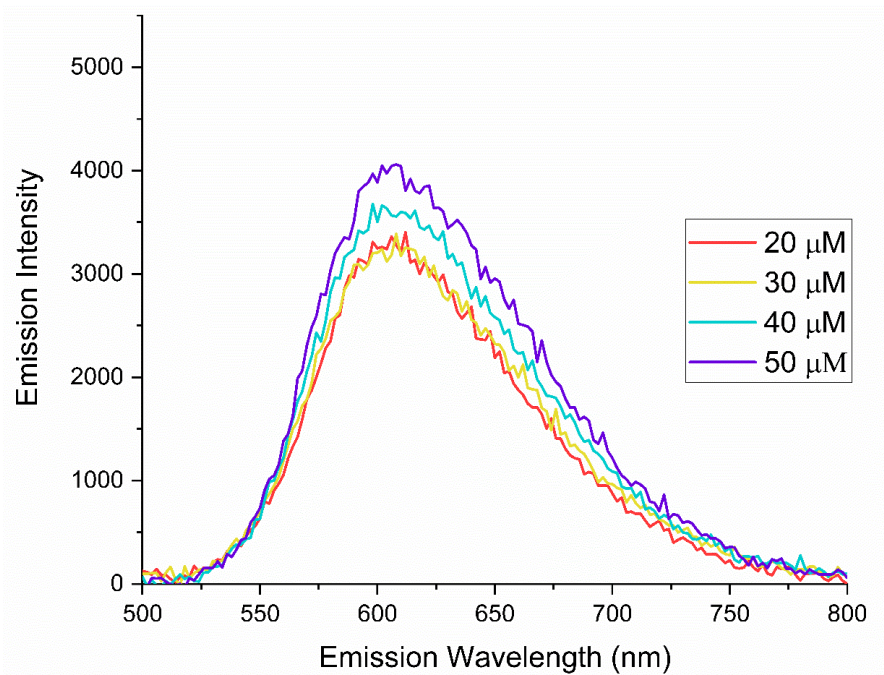


Figure 4.14. Emission spectra of **2** at pH 4.0 (**2_A**) (0.1 M acetate buffer) upon excitation at 450 nm.

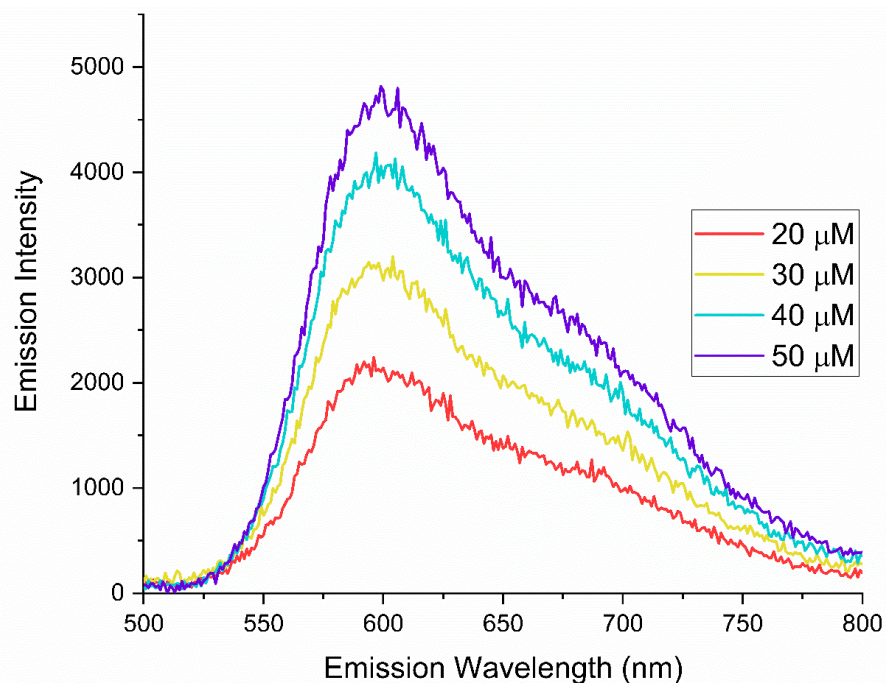


Figure 4.15 Emission spectra of **2** at pH 7.4 (0.1 M phosphate buffer) upon excitation at 450 nm. The shoulder at approximately 700 nm most likely corresponds to a monodeprotonated or fully deprotonated species which formed in solution. The λ_{max} of ~610 nm indicates that the major species in solution is likely **2_A**.

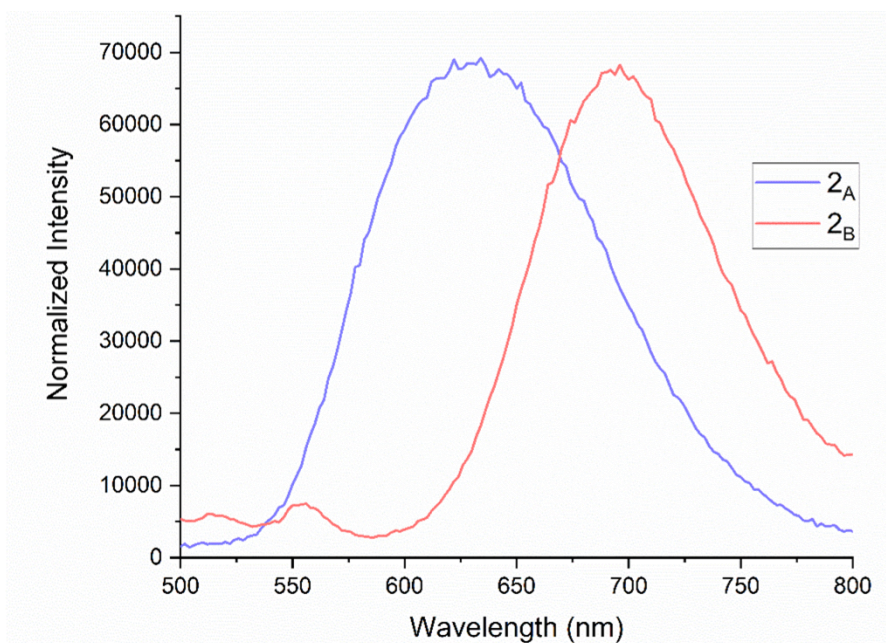
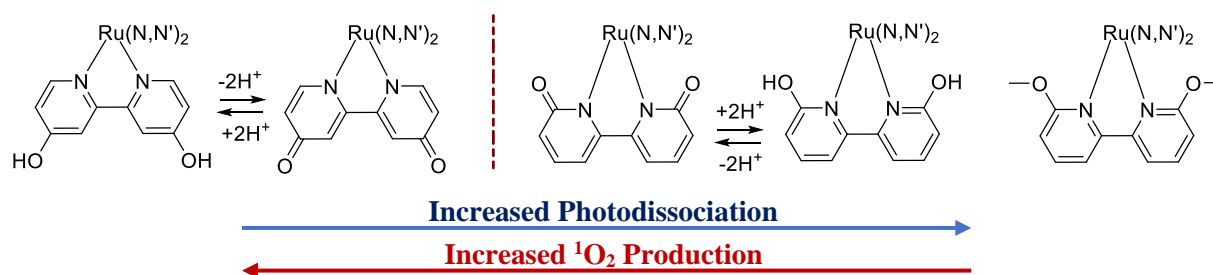


Figure 4.16 Emission spectra of **2_A** and **2_B** in diH₂O upon excitation at 450 nm measured by Olaitain Oladipupo (Papish Group, UA) and Yifei Xu (Bonizzoni Group, UA). The λ_{max} of **2_B** is noticeably red shifted from **2_A**, indicating a ³MLCT excited state lower in relative energy.

4.4 Conclusions

As singlet oxygen is produced via a catalytic light-activated pathway, it can be generated in relatively high concentrations compared to initial concentration of photosensitizer. Unfortunately, due to its short lifetime, it is difficult to detect without the use of specialized equipment or trapping molecules. Trapping molecules can provide an advantage in detecting $^1\text{O}_2$ by using common laboratory visualization techniques (such as UV-Vis or fluorescence spectroscopy); however, none of the methods utilized worked for this system. In all cases, either the probe failed under experiment conditions or an un-intended interaction between the probe and the target compound of study is observed. Thankfully, with the help of the McFarland group, we were successfully able to measure Φ_Δ and found a near 20-fold increase in Φ_Δ for **2_B** and **3_B** when compared to their respective **X_A** forms. An inverse relationship between rates of photodissociation and Φ_Δ is observed. Supporting computational work by the Webster group and Dr. Qu measured lower $^3\text{MLCT}$ energies for **3_B** and **2_B**; explaining why the **X_A** forms of the compound favor photodissociation and the **X_B** forms favor singlet oxygen production (Appendix 4A.3). This is further supported by luminescent studies of **2** which exhibits a red-shifted λ_{max} upon deprotonation. Complex **8** was found to be a highly efficient producer of $^1\text{O}_2$, and preliminary EC_{50} studies are currently in progress. In summary, this data has shown how small structural changes can affect PDT or PACT pathways and ultimately, light-driven toxicity (Scheme 4.2).



Scheme 4.2. Changes in the -OR group at the 6,6' or 4,4' positions on the bipyridine ligand dictate the dominant pathway.

With the data discussed in this chapter, it is evident that these compounds kill breast cancer cells through a pathway that is dominated by the production of singlet oxygen and not photodissociation. Furthermore, it has been determined which factors have the greatest influence on the production of singlet oxygen. A compound that is less likely to photodissociate will stand a better chance at phototoxicity against cancer cells. Incorporation of the 6,6'-dhbp ligand may result in some compound lost to less-toxic photodissociation pathways; however, it has led to a first of its kind fundamental study on the effects of ligand charge on singlet oxygen formation and has been submitted for publication to *Inorganic Chemistry*. These new discoveries have also aided in the design of what we believe to be exciting new complexes that will be discussed in further chapters.

4.5 Materials and Methods

4.5.1. General Synthetic and Characterization Methods

Complexes **1-3** were prepared without modification according to previously published procedures.¹³ Complex **8_A** was synthesized with few modifications to published procedures.¹³ While shielded from light, (dop)₂RuCl₂ (0.086 mmol, 1.0 eq) and 4,4'-dihydroxy-2,2'-bipyridine (4,4'-dhbp) (0.10 mmol, 1.1 eq) were added to a 100 mL oven-dried Schlenk flask equipped with a stir bar and purged with nitrogen. Degassed EtOH/DI H₂O (1:1, 10 mL) was transferred into

the flask via syringe before adding a condenser and heating the solution to reflux for 5 hours. Upon completion, the solution was cooled to room temperature before adding a few drops of 5 M HCl to precipitate out any unreacted 4,4'-dhbp ligand. The solution was filtered and washed with DI H₂O (5 mL x 3). The filtrate was dried completely by rotary evaporation before collecting the red-orange solid. Dark red X-ray quality crystals were grown by vapor diffusion of Et₂O into a saturated ethanol solution. Yield: 43.5 mg, 0.0520 mmol, 60.3 % yield. ¹H NMR (360 MHz, DMSO-[d₆]) δ 12.01 (s, 2H), 8.68 (d, 2H), 8.57 (d, 2H), 8.20 (d, 2H), 8.06 (s, 2H), 7.92 (t, 2H), 7.81 (d, 2H), 7.64 (t, 2H), 7.24 (d, 2H), 6.86 (d, 2H), 4.66 (d, 8H). MALDI-ToF MS: [C₃₈H₂₆N₆O₆RuH]⁺ m/z = 765.3 (Calculated m/z = 765.1).

NMR spectra were recorded in a Bruker AVANCE 360 (360 MHz, ¹H frequency) NMR spectrometer. FT-IR spectra were recorded on a Bruker Alpha ATR-IR spectrophotometer. Mass spectra were obtained in a Waters AutoSpec-Ultima NT mass spectrometer or Waters Xero G2-XS QTOF. UV-Vis spectra were recorded with an Ocean Optics FLAME-CHEM-UV-VIS or a Perkin Elmer Lambda 35 instrument using a quartz cuvette of 1 cm path length under ambient atmosphere.

4.5.2 Typical synthesis of the deprotonated complexes (*X_B* = *1_B*, *2_B*, *3_B*)

While protected from light, approximately 10-20 mg of the **X_A** complex (**1_A**, **2_A**, or **3_A**) was dissolved in a minimum amount of MeOH before adding an excess of NaOH (approximately 4-5 drops of 5 M NaOH_(aq)) until a color change from red-orange to darker purple was observed. The methanol solution was then recrystallized via vapor diffusion with diethyl ether to yield crystals of **X_B**. The solid was collected by filtration and washed with diethyl ether before drying completely under vacuum. Typical yield was 90 %. Purity and identity of the samples was confirmed by UV-Vis, ESI-MS, and IR.

4.5.3 Singlet Oxygen Measurement via EPR Detectable Formation of TEMPO^{17, 28}

Continuous wave (CW) EPR spectra were measured on a Bruker ELEXSYS E540 X-band spectrometer with an ER 4102 ST resonator. Unless otherwise noted, CW spectra were measured at a nominal microwave frequency of 9.45 GHz with 3.341 mW of power using 100 kHz magnetic field modulation with an amplitude of 1.00 mT. Spectra were recorded at room temperature. EPR samples were prepared from a 0.5 mM **3_A**/50 mM TEMP stock solution in ethanol. One hundred μ L of the sample solution was placed in 3 mm outside diameter quartz EPR tubes. For aerobic experiments, the ethanol was first degassed (freeze, pump, thaw x3) and the sample was prepared under N₂ atmosphere in the glovebox.

4.5.4 Singlet Oxygen Measurement Via UV-Vis/DPBF

A 10 mL solution of 1 μ M **3_A** and 100 μ M DPBF in ethanol were prepared fresh for each trial. 3.5 mL of this solution was then used for analysis. The sample was irradiated with a blue light panel (450 nm) in the cuvette and precautions to limit exposure to outside light were employed. The absorbance of the solution was measured at various time points of irradiation before being plotted.

4.5.5. Fluorescence/SOSG

A stock solution of SOSG was prepared in MeOH according to manufacturer protocols. A solution of SOSG (1 μ M) and the ruthenium complex of study (10 μ M) was prepared at a total volume of 5 mL with 3 mL being utilized for study in an aqueous buffered solution. The solution was irradiated at intervals of 1 minute with white light before measuring the fluorescence. (Ex λ = 501 nm, Em λ = 525 nm). The sample was shielded from ambient light.

4.5.6 Singlet Oxygen Quantum Yield Measurements-McFarland Group

Singlet oxygen quantum yields (Φ_{Δ}) were measured by the emissive actinometric method that has worked well in the past with other polypyridyl-type Ru(II) complexes.^{10, 29, 30} A PTI Quantamaster spectrometer equipped with a Hamamatsu R5509-42 near-infrared detector (cooled to -80 °C) was used to measure the intensity of the $^1\text{O}_2$ emission that occurs at around 1276 nm. The quantum yield was calculated by the relative actinometric method in Equation 1, using $[\text{Ru}(\text{bpy})_3](\text{PF}_6)_2$ as the standard ($\Phi_{\Delta} = 0.56$ in aerated MeCN)³¹

$$\Phi_{\Delta} = \Phi_{\Delta,S} \left(\frac{I}{I_S} \right) \left(\frac{A_S}{A} \right) \left(\frac{\eta^2}{\eta_S^2} \right) \quad (1)$$

Where I is the emission integration, A is the absorption of the solution at the excitation wavelength, and η is the refractive index of the solvent. The standard is indicated by the subscript S . The samples were measured in deuterated methanol solution, and the standard in acetonitrile. The excitation wavelength was the longest in the excitation spectrum to maximize the emission at 1276 nm. The emission spectrum was recorded between 1200–1350 nm with a 1000 nm long pass filter, and internally corrected for variations in the illumination source and detector output. The spectra were signal averaged over multiple scans to reduce noise and were baseline corrected.

4.5.7 General Photodissociation Procedure for compounds 8_A and 3_A

A 50 μM solution of the compound was prepared in methanol while shielding from light. Approximately 3 mL of the solution was transferred to a cuvette and used for analysis. The sample was irradiated with blue light (450 nm, Philips, goLITE BLU) for 1 hour and a UV-Vis

spectrum was obtained at various time points over the course of total irradiation. Data was analyzed in Origin 2020 graphing software.

4.5.8 Luminescence Measurements of compound 2

Degassed solutions of compound **2** were prepared at various concentrations with either 0.1 M acetate buffer (pH 4.0) or 0.1 M phosphate buffer (pH 7.4). All samples were handled under low light conditions. Emission was measured from 500-800 nm after excitation at 456 nm. The data was then plotted in Origin 2020 graphing software. Special thanks to Michael Idhe and the Bonizzoni Group for helping me collect this data.

4.5.9 EC₅₀ Measurement of 8 – Kim Group

MDA-MB-231, MCF7, and MCF10A were seeded at a density of 20,000 cells per well in 100 μ L of media in 96-well plates and incubated for 48 h to adhere to plate. Compounds were dissolved in DMSO and diluted in media to avoid cytotoxic effect from DMSO on cells. Final concentration of DMSO was set to less than 1 % (v/v). Cells were treated with 100 μ L of serially diluted compounds and incubated for 48 h in the dark. After 48 h, cells were washed with Phosphate-buffered saline (PBS 200 μ L x 3) and irradiated for two hours with white light (STASUN 200W LED Flood Light, 100-256V, 20000lm). Cells were then provided with 100 μ L of fresh media per well and incubated in the dark for a total of 24 h. Cytotoxic effects of the compounds were measured using a Cell Counting Kit-8 according to the manufacturer's protocol (Enzo Life Sciences). The EC₅₀ of each cell line was determined using a Minitab 17. Complex **8** was found to be non-toxic and not light activated.

References

- [1] Weishaupt, K. R., Gomer, C. J., and Dougherty, T. J. (1976) Photoradiation therapy. 3. Identification of singlet oxygen as the cytotoxic agent in photo-inactivation of a murine tumor, *Cancer Res.* *36*, 2326-2329.
- [2] Singh, T. N., and Turro, C. (2004) Photoinitiated DNA Binding by cis-[Ru(bpy)₂(NH₃)₂]²⁺, *Inorg. Chem.* *43*, 7260-7262.
- [3] Ford, P. C. (1970) Properties and reactions of ruthenium(II) amine complexes, *Coord. Chem. Rev.* *5*, 75-99.
- [4] Ford, P. C. (1982) The ligand field photosubstitution reactions of d₆ hexacoordinate metal complexes, *Coord. Chem. Rev.* *44*, 61-82.
- [5] Collins, J. G., Sleeman, A. D., Aldrich-Wright, J. R., Greguric, I., and Hambley, T. W. (1998) A ¹H NMR Study of the DNA Binding of Ruthenium(II) Polypyridyl Complexes, *Inorg. Chem.* *37*, 3133-3141.
- [6] Albani, B. A., Pena, B., Leed, N. A., de Paula, N. A. B. G., Pavani, C., Baptista, M. S., Dunbar, K. R., and Turro, C. (2014) Marked Improvement in Photoinduced Cell Death by a New Tris-heteroleptic Complex with Dual Action: Singlet Oxygen Sensitization and Ligand Dissociation, *J. Am. Chem. Soc.* *136*, 17095-17101.
- [7] Lincoln, R., Kohler, L., Monroe, S., Yin, H., Stephenson, M., Zong, R., Chouai, A., Dorsey, C., Hennigar, R., Thummel, R. P., and McFarland, S. A. (2013) Exploitation of Long-Lived ³IL Excited States for Metal-Organic Photodynamic Therapy: Verification in a Metastatic Melanoma Model, *J. Am. Chem. Soc.* *135*, 17161-17175.
- [8] McFarland, S. A., Mandel, A., Dumoulin-White, R., and Gasser, G. (2020) Metal-based photosensitizers for photodynamic therapy: the future of multimodal oncology?, *Curr. Opin. Chem. Biol.* *56*, 23-27.
- [9] Monroe, S., Colon, K. L., Yin, H., Roque, J., Konda, P., Gujar, S., Thummel, R. P., Lilge, L., Cameron, C. G., and McFarland, S. A. (2019) Transition Metal Complexes and Photodynamic Therapy from a Tumor-Centered Approach: Challenges, Opportunities, and Highlights from the Development of TLD1433, *Chem. Rev. (Washington, DC, U. S.)* *119*, 797-828.
- [10] Roque III, J., Havrylyuk, D., Barrett, P. C., Sainuddin, T., McCain, J., Colón, K., Sparks, W. T., Bradner, E., Monroe, S., Heidary, D., Cameron, C. G., Glazer, E. C., and

- McFarland, S. A. (2020) Strained, Photoejecting Ru(II) Complexes that are Cytotoxic Under Hypoxic Conditions, *Photochem. Photobiol.* 96, 327-339.
- [11] Roque, J. A., Barrett, P. C., Cole, H. D., Lifshits, L. M., Shi, G., Monro, S., von Dohlen, D., Kim, S., Russo, N., Deep, G., Cameron, C. G., Alberto, M. E., and McFarland, S. A. (2020) Breaking the barrier: an osmium photosensitizer with unprecedented hypoxic phototoxicity for real world photodynamic therapy, *Chem. Sci.* 11, 9784-9806.
- [12] Hufziger, K. T., Thowfeik, F. S., Charboneau, D. J., Nieto, I., Dougherty, W. G., Kassel, W. S., Dudley, T. J., Merino, E. J., Papish, E. T., and Paul, J. J. (2014) Ruthenium dihydroxybipyridine complexes are tumor activated prodrugs due to low pH and blue light induced ligand release, *J. Inorg. Biochem.* 130, 103-111.
- [13] Qu, F., Park, S., Martinez, K., Gray, J. L., Thowfeik, F. S., Lundeen, J. A., Kuhn, A. E., Charboneau, D. J., Gerlach, D. L., Lockart, M. M., Law, J. A., Jernigan, K. L., Chambers, N., Zeller, M., Piro, N. A., Kassel, W. S., Schmehl, R. H., Paul, J. J., Merino, E. J., Kim, Y., and Papish, E. T. (2017) Ruthenium Complexes are pH-Activated Metallo Prodrugs (pHAMPs) with Light-Triggered Selective Toxicity Toward Cancer Cells, *Inorg. Chem.* 56, 7519-7532.
- [14] Qu, F., Martinez, K., Arcidiacono, A. M., Park, S., Zeller, M., Schmehl, R. H., Paul, J. J., Kim, Y., and Papish, E. T. (2018) Sterically demanding methoxy and methyl groups in ruthenium complexes lead to enhanced quantum yields for blue light triggered photodissociation, *Dalton Trans.* 47, 15685-15693.
- [15] Park, S., Gray, J. L., Altman, S. D., Hairston, A. R., Beswick, B. T., Kim, Y., and Papish, E. T. (2020) Cellular uptake of protic ruthenium complexes is influenced by pH dependent passive diffusion and energy dependent efflux, *J. Inorg. Biochem.* 203, 110922.
- [16] Dolmans, D. E. J. G. J., Fukumura, D., and Jain, R. K. (2003) TIMELINE: Photodynamic therapy for cancer, *Nat. Rev. Cancer* 3, 380-387.
- [17] Lion, Y., Delmelle, M., and Van de Vorst, A. (1976) New method of detecting singlet oxygen production, *Nature (London)* 263, 442-443.
- [18] Nardi, G., Manet, I., Monti, S., Miranda, M. A., and Lhiaubet-Vallet, V. (2014) Scope and limitations of the TEMPO/EPR method for singlet oxygen detection: the misleading role of electron transfer, *Free Radical Biol. Med.* 77, 64-70.
- [19] Zhou, Q.-X., Lei, W.-H., Chen, J.-R., Li, C., Hou, Y.-J., Wang, X.-S., and Zhang, B.-W. (2010) A New Heteroleptic Ruthenium(II) Polypyridyl Complex with Long-Wavelength Absorption and High Singlet-Oxygen Quantum Yield, *Chem. - Eur. J.* 16, 3157-3165, S3157/3151-S3157/3111.

- [20] Gollmer, A., Arnbjerg, J., Blaikie, F. H., Pedersen, B. W., Breitenbach, T., Daasbjerg, K., Glasius, M., and Ogilby, P. R. (2011) Singlet Oxygen Sensor Green: photochemical behavior in solution and in a mammalian cell, *Photochem. Photobiol.* *87*, 671-679.
- [21] Entradas, T., Waldron, S., and Volk, M. (2020) The detection sensitivity of commonly used singlet oxygen probes in aqueous environments, *J. Photochem. Photobiol. B* *204*, 111787.
- [22] Kim, S., Fujitsuka, M., and Majima, T. (2013) Photochemistry of Singlet Oxygen Sensor Green, *J. Phys. Chem. B* *117*, 13985-13992.
- [23] Bhasikuttan, A. C., Suzuki, M., Nakashima, S., and Okada, T. (2002) Ultrafast Fluorescence Detection in Tris(2,2'-bipyridine)ruthenium(II) Complex in Solution: Relaxation Dynamics Involving Higher Excited States, *J. Am. Chem. Soc.* *124*, 8398-8405.
- [24] Campen, A. K., Rest, A. J., and Yoshihara, K. (1991) Luminescence spectra and lifetimes of tris-(2,2'-bipyridine)ruthenium(II) dichloride and potassium hexacyanochromate(III) in polymer films and hydrocarbon mulls at approximately 77 K: evaluation of alternative host media for studying unstable species in photochemical reaction pathways originating from nonvolatile substrates, *J. Photochem. Photobiol., A* *55*, 301-317.
- [25] Puckett, C. A., and Barton, J. K. (2008) Mechanism of Cellular Uptake of a Ruthenium Polypyridyl Complex, *Biochemistry* *47*, 11711-11716.
- [26] Anuja, P. K., and Paira, P. (2020) Luminescent anticancer Ru(II)-arenebipyridine and phenanthroline complexes: Synthesis, characterization, DFT studies, biological interactions and cellular imaging application, *J. Inorg. Biochem.* *208*, 111099.
- [27] Charboneau, D. J., Piro, N. A., Kassel, W. S., Dudley, T. J., and Paul, J. J. (2015) Structural, electronic and acid/base properties of $[\text{Ru}(\text{bpy})(\text{bpy}(\text{OH})_2)_2]^{2+}$ (bpy = 2,2'-bipyridine, $\text{bpy}(\text{OH})_2$ = 4,4'-dihydroxy-2,2'-bipyridine), *Polyhedron* *91*, 18-27.
- [28] Conner, K. P., Cruce, A. A., Krzyaniak, M. D., Schimpf, A. M., Frank, D. J., Ortiz de Montellano, P., Atkins, W. M., and Bowman, M. K. (2015) Drug Modulation of Water-Heme Interactions in Low-Spin P450 Complexes of CYP2C9d and CYP125A1, *Biochemistry* *54*, 1198-1207.
- [29] Monroe, S., Cameron, C. G., Zhu, X., Colón, K. L., Yin, H., Sainuddin, T., Hetu, M., Pinto, M., Fuller, A., Bennett, L., Roque III, J., Sun, W., and McFarland, S. A. (2019) Synthesis, Characterization and Photobiological Studies of Ru(II) Dyads Derived from α -Oligothiophene Derivatives of 1,10-Phenanthroline, *Photochem. Photobiol.* *95*, 267-279.
- [30] McCain, J., Colón, K. L., Barrett, P. C., Monroe, S. M. A., Sainuddin, T., Roque Iii, J., Pinto, M., Yin, H., Cameron, C. G., and McFarland, S. A. (2019) Photophysical Properties and Photobiological Activities of Ruthenium(II) Complexes Bearing π -Expansive Cyclometalating Ligands with Thienyl Groups, *Inorg. Chem.* *58*, 10778-10790.

- [31] DeRosa, M. C., and Crutchley, R. J. (2002) Photosensitized singlet oxygen and its applications, *Coord. Chem. Rev.* 233-234, 351-371.
- [32] Frisch, M. J. T., G. W.; Schlegel, H. B.; Scuseria, G. E.; Robb, M. A.; Cheeseman, J. R.; Scalmani, G.; Barone, V.; Petersson, G. A.; Nakatsuji, H.; Li, X.; Caricato, M.; Marenich, A. V.; Bloino, J.; Janesko, B. G.; Gomperts, R.; Mennucci, B.; Hratchian, H. P.; Ortiz, J. V.; Izmaylov, A. F.; Sonnenberg, J. L.; Williams-Young, D.; Ding, F.; Lipparini, F.; Egidi, F.; Goings, J.; Peng, B.; Petrone, A.; Henderson, T.; Ranasinghe, D.; Zakrzewski, V. G.; Gao, J.; Rega, N.; Zheng, G.; Liang, W.; Hada, M.; Ehara, M.; Toyota, K.; Fukuda, R.; Hasegawa, J.; Ishida, M.; Nakajima, T.; Honda, Y.; Kitao, O.; Nakai, H.; Vreven, T.; Throssell, K.; Montgomery, J. A., Jr.; Peralta, J. E.; Ogliaro, F.; Bearpark, M. J.; Heyd, J. J.; Brothers, E. N.; Kudin, K. N.; Staroverov, V. N.; Keith, T. A.; Kobayashi, R.; Normand, J.; Raghavachari, K.; Rendell, A. P.; Burant, J. C.; Iyengar, S. S.; Tomasi, J.; Cossi, M.; Millam, J. M.; Klene, M.; Adamo, C.; Cammi, R.; Ochterski, J. W.; Martin, R. L.; Morokuma, K.; Farkas, O.; Foresman, J. B.; Fox, D. J. (2016) Gaussian 16 C.01, Gaussian, Inc., Wallingford, CT, USA.
- [33] Adamo, C., and Barone, V. (1999) Toward reliable density functional methods without adjustable parameters: The PBE0 model, *J. Chem. Phys.* 110, 6158-6170.
- [34] Stefan, G. (2006) Semiempirical GGA-type density functional constructed with a long-range dispersion correction, *J. Comput. Chem.* 27, 1787-1799.
- [35] Grimme, S., Ehrlich, S., and Goerigk, L. (2011) Effect of the damping function in dispersion corrected density functional theory, *J. Comput. Chem.* 32, 1456-1465.
- [36] Couty, M., and Hall, M. B. (1996) Basis sets for transition metals: Optimized outer p functions, *J. Comput. Chem.* 17, 1359-1370.
- [37] Hay, P. J., and Wadt, W. R. (1985) Ab initio effective core potentials for molecular calculations. Potentials for K to Au including the outermost core orbitals, *J. Chem. Phys.* 82, 299-310.
- [38] Hehre, W. J., Ditchfield, R., and Pople, J. A. (1972) Self—Consistent Molecular Orbital Methods. XII. Further Extensions of Gaussian—Type Basis Sets for Use in Molecular Orbital Studies of Organic Molecules. , *J. Chem. Phys.* 56 2257-2261.
- [39] Hariharan, P. C., and Pople, J. A. (1973) The influence of polarization functions on molecular orbital hydrogenation energies, *Theor. Chim. Acta* 28, 213-222.
- [40] Petersson, G. A., and Al-Laham, M. A. (1991) A complete basis set model chemistry. II. Open-shell systems and the total energies of the first-row atoms, *J. Chem. Phys.* 94, 6081-6090.
- [41] McLean, A. D., and Chandler, G. S. (1980) Contracted Gaussian basis sets for molecular calculations. I. Second row atoms, Z=11–18, *J. Chem. Phys.* 72, 5639-5648.

- [42] Petersson, G. A., and Al-Laham, M. A. (1991) A complete basis set model chemistry. II. Open-shell systems and the total energies of the first-row atoms, *J. Chem. Phys.* *94*, 6081-6090.
- [43] Marques, M. A. L., and Gross, E. K. U. (2004) Time-Dependent Density Functional Theory, *Annu. Rev. Phys. Chem.* *55*, 427-455.
- [44] Press, W. H. (1992) *Numerical recipes in FORTRAN : the art of scientific computing*, 2nd ed., Cambridge University Press, Cambridge England ; New York, NY, USA.
- [45] Chemcraft - graphical software for visualization of quantum chemistry computations.
- [46] Sheldrick, G. M. (2008) A short history of SHELX, *Acta Crystallogr., Sect. A: Found. Crystallogr.* *64*, 112-122.
- [47] Huebschle, C. B., Sheldrick, G. M., and Dittrich, B. (2011) ShelXle: a Qt graphical user interface for SHELXL, *J. Appl. Crystallogr.* *44*, 1281-1284.
- [48] Sheldrick, G. M. (2014) SADABS, University of Göttingen, Germany.
- [49] Sheldrick, G. M. (2015) Crystal structure refinement with SHELXL, *Acta Crystallogr., Sect. C: Struct. Chem.* *71*, 3-8.

4A. Appendix

Some of the work discussed in the appendix appears in the submitted publication:

Qu, F.^{a,1}; Lamb, R. W.^{b,1}; Cameron, C. G.^c; Park, S.^d; Oladipupo, O. E.^a; Gray, J. L.^a; Kim, Y.^d; McFarland, S. A.^c; Webster, C. E.^b; Papish, E. T.^a, Singlet Oxygen Formation vs. Photodissociation for Protic Ruthenium Anticancer Compounds: The Oxygenated Substituent Determines which Pathway Dominates. *Inorg. Chem.*, **2021**, *Accepted*.

^a*Department of Chemistry and Biochemistry, The University of Alabama, Tuscaloosa, AL 35487, USA.*

^b*Department of Chemistry, Mississippi State University, Mississippi State, MS 39762, USA.*

^c*Department of Chemistry and Biochemistry, University of Texas Arlington, Arlington, TX 76019, USA.*

^d*Department of Chemical and Biological Engineering, The University of Alabama, Tuscaloosa, AL 35487, USA.*

¹*These authors contributed equally*

4A.1 Qualitative Photodissociation study of **8B** in Methanol

An 80 μ M solution of **8B** was prepared in methanol while shielding from light.

Approximately 3 mL of the solution was transferred to a cuvette and used for analysis. The sample was irradiated with blue light (450 nm, Philips, goLITE BLU) for 1 hour and a UV-Vis spectrum was obtained at various time points over the course of total irradiation. Data was analyzed in Origin 2020 graphing software.

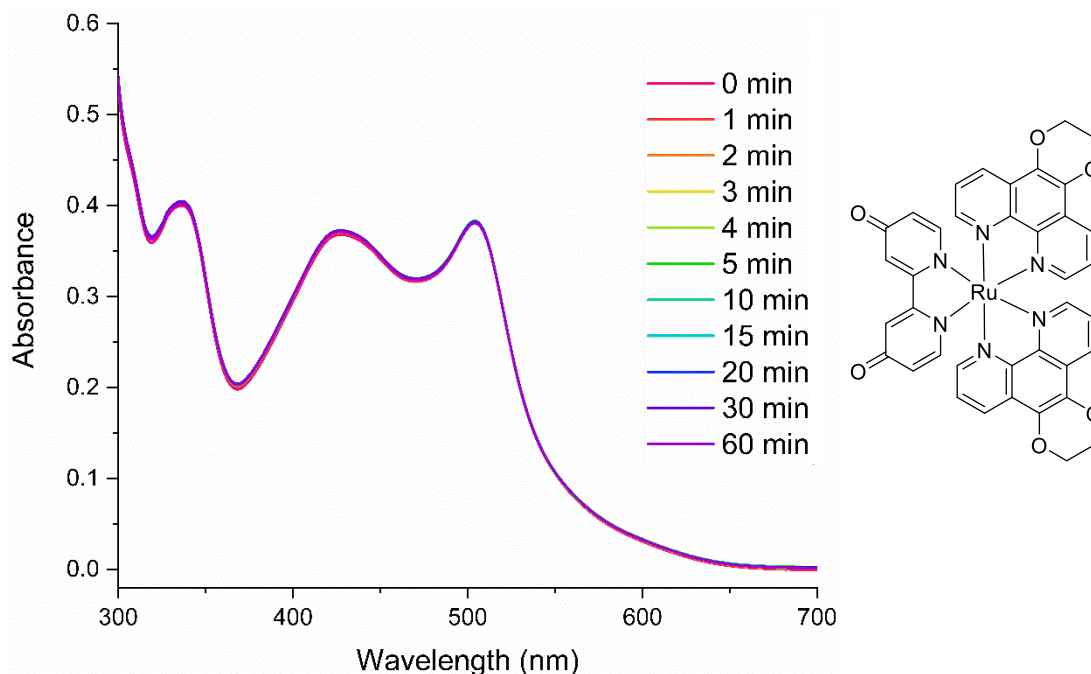


Figure 4A.1. Photodissociation of **8B** in MeOH with structure shown on the right. Over the course of 1 hour of irradiation (450 nm) a maximum change in absorbance was observed at 302 nm ($\Delta\text{Abs}_{\text{max}} = 7.79 \times 10^{-3}$).

4A.2 Qualitative Photodissociation Study of **2** with White Light Source

A 45 μM solution of **2** was prepared in pH 8.0, 0.1 M phosphate buffer. Approximately 3 mL of the solution was transferred to a cuvette and used for analysis. The sample was placed directly on the light source (STASUN 200W LED Flood Light, 100-256V, 20000lm), and an UV-Vis spectrum was obtained at various time points over the course of 10 minutes total irradiation. The reaction was stopped after 10 minutes as little to no change in spectra was further observed.

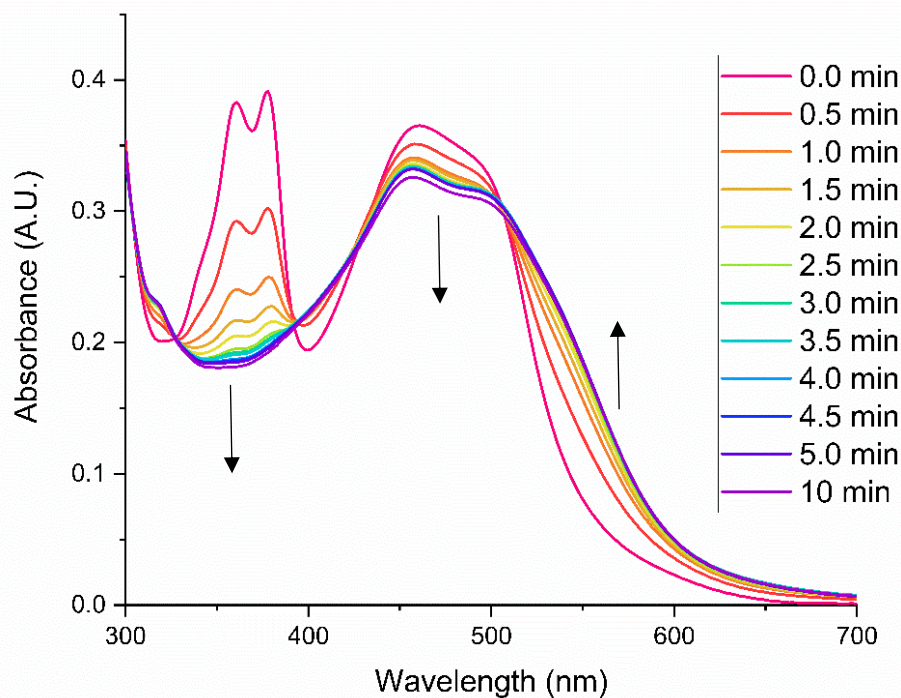


Figure 4A.2. Photodissociation spectra of **2** at pH 8.0 (0.1 M Phosphate buffer) upon irradiation with a white light source (STASUN 200W LED Flood Light, 100-256V, 20000lm). The UV-Vis spectra of the sample was obtained at various time points over the course of 10 minutes of irradiation.

4A.3. Computational Studies of the Excited States Generated Upon Irradiation- Dr. Qu and Webster Group

All computations were carried out using Revision C.01 of the Gaussian 16³² suite of programs with default (10^{-8}) SCF convergence criteria. The PBE0 functional³³ was used in conjunction with Grimme's D3 empirical dispersion³⁴ and Becke-Johnson damping³⁵ [EMP=GD3BJ] for all computations. The basis set combination (BS1) is defined as follows: for Ru, the Couty and Hall modification³⁶ (mod-LANL2DZ) to the valence basis set of LANL2DZ+ECP combination,³⁷ and for C, H, N, and O the 6-31G(d')³⁸⁻⁴⁰ basis sets (the 6-31G(d') basis sets have the d polarization functions taken from the 6-311G(d)⁴¹ basis sets rather than the default value of 0.8⁴² for C, N, and O). Spherical harmonic d functions were used

throughout; *i.e.* 5 angular basis functions exist per d function. Excited state optimizations were carried out as variational triplets, 1 TD-DFT, and 3 TD-DFT. Optimizations with TD-DFT were carried out using analytical gradients and the first 3 excitations were solved iteratively [TD(SINGLETS,ROOT=1) or TD(TRIPLET,ROOT=1)]. All stationary points were confirmed to be minima by an analytical frequency computation at the same level of theory. UV-VIS absorption spectra were simulated using TD-DFT⁴³ single points on the optimized geometries (TD-DFT//PBE0-D3BJ/BS1). To simulate the absorption spectra, the first 30 vertical excitations were solved iteratively [TD(ROOT=1,NSTATES=30)]. Simulated absorption spectra were generated using an in-house Fortran program by convoluting⁴⁴ the computed excitation energies and oscillator strengths with a Gaussian line-shape and a broadening of 20 nm. Orbital images were generated in Chemcraft⁴⁵ using an isovalue of 0.02.

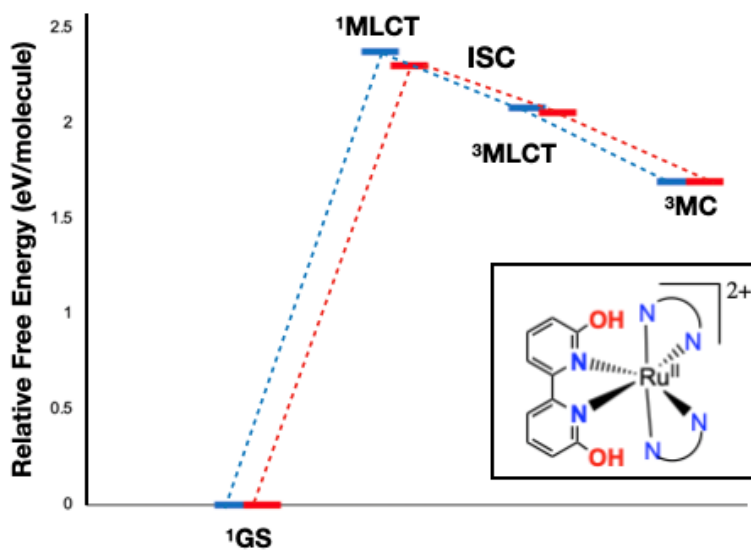


Figure 4A.3. Free energy diagram for energetically accessible excited states of **2_A** (in blue) and **3_A** (in red) by the PBE-D3/B1 method. The lowest energy, thermally accessible triplet excited state is 3 MC, which leads to ligand loss and photodissociation products. The 3 MLCT state would lead to singlet oxygen and luminescence, but this most likely quickly converts to 3 MC for **2_A** and **3_A** before it encounters oxygen.

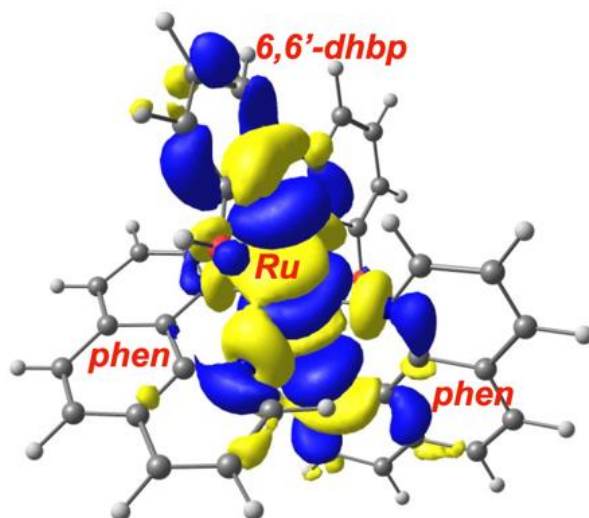


Figure 4A.4. Orbital depiction of the ^3MC excited state for 2_{A} shows that this state is antibonding between Ru and 6,6'-dhbp.

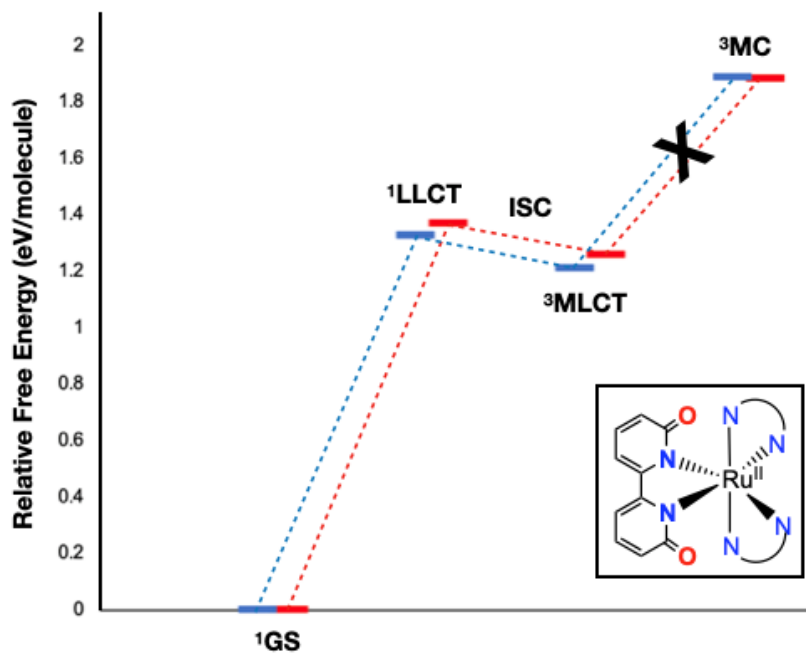


Figure 4A.5. Free energy diagram for energetically accessible excited states of 2_{B} (in blue) and 3_{B} (in red) by the PBE1-D3/B1 method. The $^3\text{MLCT}$ state is readily accessed and should lead to singlet oxygen formation and luminescence. Furthermore, the ^3MC (which leads to ligand loss) is not accessible and this explains the relative lack of photodissociation for 2_{B} and 3_{B} .

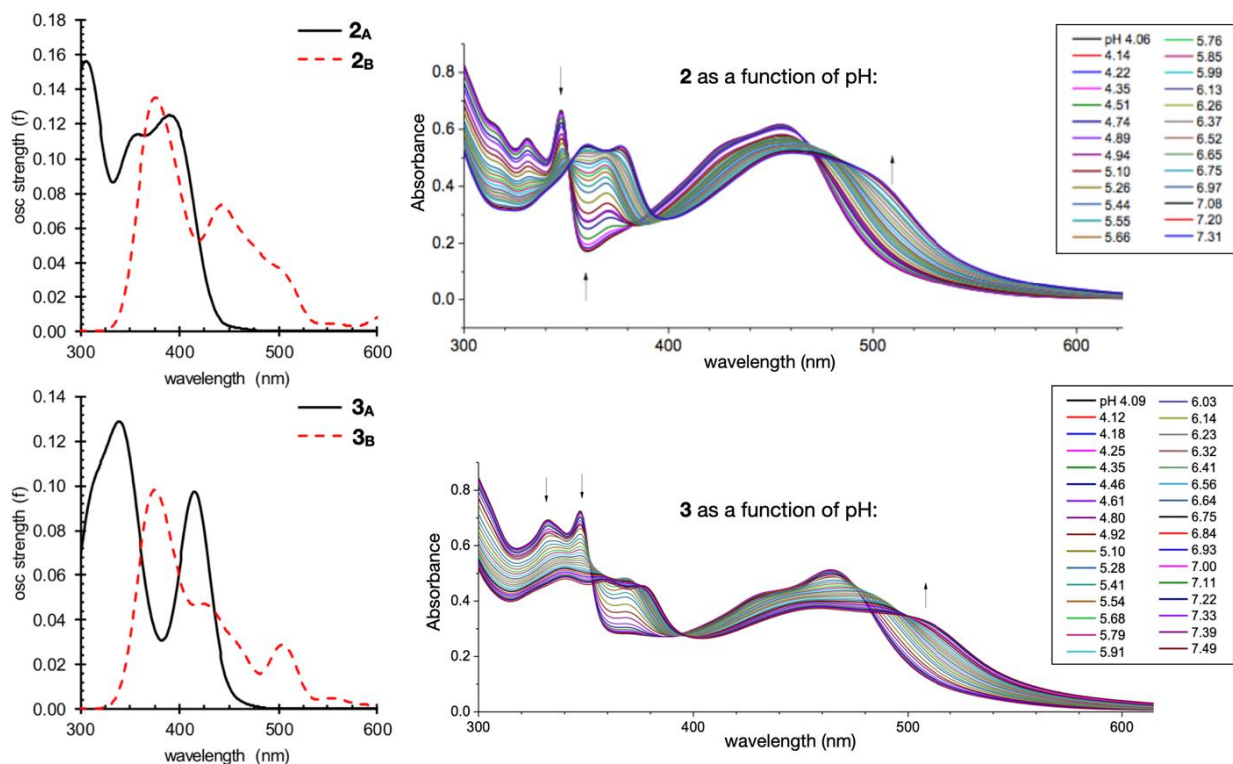


Figure 4A.6. Left: Simulated UV-Vis absorption spectra for complex **2** (top) and complex **3** (bottom) from TD-PBE0-D3//PBE0-D3/BPS1 **Right:** Experimental UV-Vis absorption spectra for complex **2** (top) and complex **3** (bottom) as a function of pH as previously reported.¹⁵

4A.4 Crystallographic Data for $[(dop)_2Ru(4,4'-dhbp)]Cl_2$ (**8_A**)

Dark-red crystals of **8_A** were generated via vapor diffusion of Et₂O into a saturated ethanol solution. Each asymmetric unit contains three water molecules and two chloride counter ions. Each unit cell contains approximately 8 asymmetric units.⁴⁶⁻⁴⁹

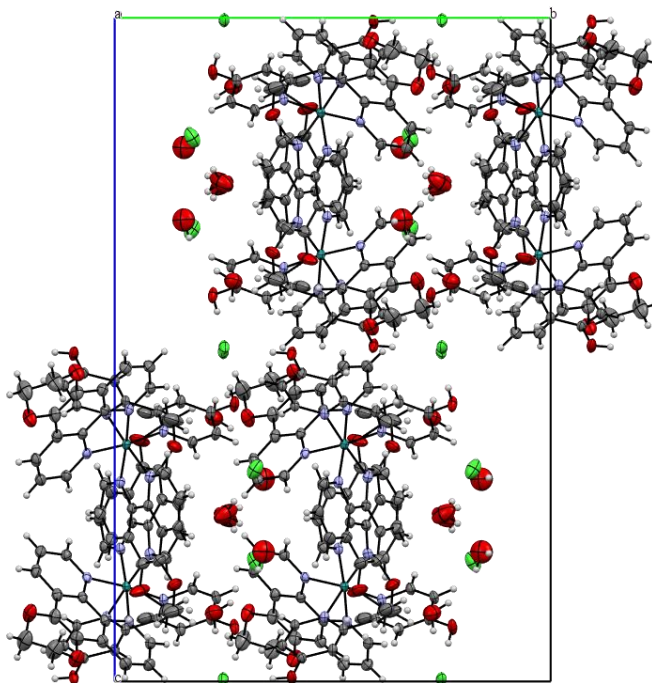


Figure 4A.7 Full unit cell for **8_A** as viewed along the *a* axis. Each unit cell contains approximately 8 asymmetric units. Each asymmetric unit is composed of the ruthenium complex, 3 water molecules, and 2 chloride counter ions.

Table 4A.1 Crystal data for **8_A**

$C_{38}H_{28}N_6O_6Ru \cdot 2(Cl) \cdot 3(H_2O)$	
$M_r = 890.68$	$D_x = 1.599 \text{ Mg m}^{-3}$
Orthorhombic, <i>Pbca</i>	
Hall symbol: $-P\ 2ac\ 2ab$	Mo $K\alpha$ radiation, $\lambda = 0.71073 \text{ \AA}$
$a = 13.5194 (2) \text{ \AA}$	Cell parameters from 27050 reflections
$b = 18.9737 (2) \text{ \AA}$	$\theta = 2.3\text{--}32.6^\circ$
$c = 28.8521 (4) \text{ \AA}$	$\mu = 0.63 \text{ mm}^{-1}$
$V = 7400.94 (17) \text{ \AA}^3$	$T = 100 \text{ K}$
$Z = 8$	Block, dark red
$F(000) = 3632$	$0.15 \times 0.10 \times 0.07 \text{ mm}$

Table 4A.2 Data collection for **8_A**

XtaLAB Synergy R, DW system, HyPix diffractometer	8573 reflections with $I > 2\sigma(I)$
Radiation source: Rotating Anode mirror monochromator	$R_{\text{int}} = 0.037$
	$\theta_{\text{max}} = 30.5^\circ$, $\theta_{\text{min}} = 2.2^\circ$

N/A	$h = -1918$
Absorption correction: gaussian <i>CrysAlis</i> PRO 1.171.40.49a (Rigaku Oxford Diffraction, 2019) Numerical absorption correction based on gaussian integration over a multifaceted crystal model	$k = -2719$
Empirical absorption correction using spherical harmonics, implemented in SCALE3 ABSPACK scaling algorithm.	
$T_{\min} = 0.936$, $T_{\max} = 1.000$	$l = -2941$
59667 measured reflections	Standard reflections: N/A
11227 independent reflections	

Table 4A.3 Refinement information for **8_A**

Refinement on F^2	Secondary atom site location: difference Fourier map
Least-squares matrix: full	Hydrogen site location: mixed
$R[F^2 > 2\sigma(F^2)] = 0.048$	H-atom parameters constrained
$wR(F^2) = 0.139$	$w = 1/[\sigma^2(F_o^2) + (0.0724P)^2 + 10.9016P]$ where P $= (F_o^2 + 2F_c^2)/3$
$S = 1.04$	$(\Delta/\sigma)_{\max} = 0.002$
11227 reflections	$\Delta\rho_{\max} = 1.61 \text{ e } \text{\AA}^{-3}$
526 parameters	$\Delta\rho_{\min} = -1.26 \text{ e } \text{\AA}^{-3}$
0 restraints	Extinction correction: none
Primary atom site location: dual	

Table 4A.4 Fractional atomic coordinates and isotropic or equivalent isotropic displacement parameters (\AA^2)

	x	y	z	$U_{\text{iso}}^*/U_{\text{eq}}$	Occ. (<1)
Ru1	0.63819(2)	0.47308(2)	0.35717(2)	0.01973(7)	
Cl1	1.04758(6)	0.25093(4)	0.49642(3)	0.03663(17)	
Cl2	0.56392(8)	0.17781(6)	0.31957(4)	0.0599(3)	
O1	0.94517(17)	0.59389(10)	0.49400(8)	0.0325(5)	
H1	0.942502	0.636964	0.495953	0.049*	
O2	0.90564(17)	0.22518(10)	0.41793(8)	0.0349(5)	
H2	0.933562	0.23478	0.44236	0.052*	
O3	0.27801(19)	0.69458(13)	0.39705(10)	0.0485(6)	

O4	0.24534(19)	0.58743(14)	0.46556(10)	0.0498(7)
O5	0.5593(2)	0.36244(14)	0.14586(8)	0.0468(6)
O6	0.7371(3)	0.44282(19)	0.13676(9)	0.0683(10)
O7	0.4818(3)	0.27206(18)	0.39675(11)	0.0648(8)
H7A	0.494348	0.23457	0.38163	0.097*
H7B	0.507529	0.269251	0.42352	0.097*
O8	0.6628(3)	0.6584(3)	0.19536(16)	0.0897(12)
H8A	0.604397	0.642033	0.193074	0.135*
H8B	0.683188	0.670931	0.168739	0.135*
O9	0.7253(3)	0.2454(2)	0.25255(15)	0.0931(13)
H9A	0.757068	0.213553	0.238158	0.140*
H9B	0.684901	0.226383	0.27129	0.140*
N1	0.73536(17)	0.51843(11)	0.40301(8)	0.0213(4)
N2	0.72244(16)	0.38769(11)	0.37683(8)	0.0217(4)
N3	0.55861(17)	0.56330(11)	0.34357(8)	0.0218(4)
N4	0.53407(17)	0.46708(11)	0.40920(8)	0.0233(4)
N5	0.55597(17)	0.41943(11)	0.30796(8)	0.0241(4)
N6	0.72682(17)	0.48705(11)	0.30022(8)	0.0243(5)
C1	0.7360(2)	0.58681(13)	0.41543(9)	0.0233(5)
H1A	0.687884	0.616396	0.403087	0.028*
C2	0.8045(2)	0.61516(13)	0.44555(10)	0.0255(5)
H2A	0.802697	0.662792	0.4531	0.031*
C3	0.8761(2)	0.57127(13)	0.46440(9)	0.0244(5)
C4	0.8751(2)	0.49968(14)	0.45259(10)	0.0256(5)
H4	0.921439	0.468933	0.465211	0.031*
C5	0.8047(2)	0.47541(12)	0.42200(9)	0.0219(5)
C6	0.7966(2)	0.40047(13)	0.40702(9)	0.0233(5)
C7	0.8605(2)	0.34814(14)	0.42153(10)	0.0271(6)
H7	0.91125	0.358555	0.442164	0.032*
C8	0.8483(2)	0.27945(13)	0.40507(10)	0.0269(6)
C9	0.7739(2)	0.26733(13)	0.37333(11)	0.0283(6)
H9	0.765367	0.222651	0.360698	0.034*

C10	0.7128(2)	0.32147(13)	0.36051(10)	0.0263(5)
H10	0.662148	0.312109	0.339569	0.032*
C11	0.4817(2)	0.57338(13)	0.37334(9)	0.0231(5)
C12	0.5728(2)	0.61085(14)	0.30966(10)	0.0269(5)
H12	0.624989	0.604439	0.289109	0.032*
C13	0.5111(2)	0.66990(15)	0.30429(11)	0.0311(6)
H13	0.523054	0.701832	0.280476	0.037*
C14	0.4343(2)	0.68052(15)	0.33375(11)	0.0320(6)
H14	0.393266	0.719536	0.330283	0.038*
C15	0.4174(2)	0.63161(15)	0.36966(11)	0.0290(6)
C16	0.3381(2)	0.63695(17)	0.40219(13)	0.0358(7)
C17	0.2172(3)	0.7057(2)	0.43826(18)	0.0611(12)
H17A	0.166337	0.740411	0.431787	0.073*
H17B	0.257854	0.723177	0.46346	0.073*
C18	0.1706(3)	0.6375(2)	0.45176(18)	0.0604(12)
H18A	0.125013	0.645194	0.477227	0.073*
H18B	0.133386	0.618752	0.425789	0.073*
C19	0.3232(2)	0.58626(17)	0.43507(12)	0.0354(7)
C20	0.3888(2)	0.52762(15)	0.43959(11)	0.0295(6)
C21	0.3784(2)	0.47484(16)	0.47354(12)	0.0335(6)
H21	0.326715	0.476587	0.494788	0.040*
C22	0.4458(2)	0.42074(16)	0.47475(11)	0.0329(6)
H22	0.440096	0.385676	0.497108	0.039*
C23	0.5232(2)	0.41810(14)	0.44244(10)	0.0282(6)
H23	0.56849	0.381271	0.444072	0.034*
C24	0.4677(2)	0.52172(13)	0.40839(10)	0.0244(5)
C25	0.5960(2)	0.42313(13)	0.26490(10)	0.0243(5)
C26	0.4724(2)	0.38261(15)	0.31331(11)	0.0298(6)
H26	0.4446	0.379038	0.342709	0.036*
C27	0.4254(2)	0.34932(16)	0.27607(12)	0.0345(7)
H27	0.367614	0.323818	0.281027	0.041*
C28	0.4640(2)	0.35410(16)	0.23260(11)	0.0341(7)

H28	0.431847	0.333104	0.207664	0.041*	
C29	0.5525(2)	0.39100(15)	0.22586(10)	0.0308(6)	
C30	0.6019(3)	0.39759(17)	0.18224(11)	0.0377(7)	
C31	0.6179(4)	0.3656(3)	0.10530(14)	0.0689(14)	
H31C	0.608404	0.321557	0.088827	0.083*	0.487(11)
H31D	0.590571	0.40253	0.085899	0.083*	0.487(11)
H31A	0.667196	0.328551	0.107246	0.083*	0.513(11)
H31B	0.575686	0.354696	0.079089	0.083*	0.513(11)
C32A	0.7202(8)	0.3773(5)	0.1080(3)	0.056(3)	0.487(11)
H32A	0.747523	0.383599	0.077181	0.067*	0.487(11)
H32B	0.752534	0.337146	0.122309	0.067*	0.487(11)
C32	0.6674(7)	0.4291(5)	0.0955(2)	0.054(3)	0.513(11)
H32C	0.620419	0.467371	0.092166	0.065*	0.513(11)
H32D	0.70493	0.424903	0.066951	0.065*	0.513(11)
C33	0.6878(3)	0.43513(19)	0.17789(11)	0.0426(8)	
C34	0.7327(3)	0.46796(15)	0.21726(11)	0.0328(6)	
C35	0.8208(3)	0.50696(17)	0.21519(12)	0.0399(8)	
H35	0.852177	0.514546	0.186933	0.048*	
C36	0.8600(3)	0.53360(16)	0.25509(13)	0.0364(7)	
H36	0.918517	0.559315	0.25414	0.044*	
C37	0.8124(2)	0.52234(14)	0.29715(11)	0.0299(6)	
H37	0.841021	0.539906	0.324096	0.036*	
C38	0.6873(2)	0.46019(13)	0.26053(10)	0.0251(5)	

Table 4A.5 Atomic displacement parameters (\AA^2)

	U^{11}	U^{22}	U^{33}	U^{12}	U^{13}	U^{23}
Ru1	0.02070(11)	0.01553(10)	0.02296(11)	-0.00189(7)	-0.00030(8)	-0.00091(7)
C11	0.0487(4)	0.0216(3)	0.0395(4)	-0.0045(3)	-0.0125(3)	0.0009(3)
C12	0.0527(6)	0.0526(5)	0.0744(7)	0.0025(4)	-0.0082(5)	-0.0215(5)
O1	0.0380(12)	0.0187(8)	0.0409(12)	0.0004(8)	-0.0167(10)	-0.0039(8)
O2	0.0359(12)	0.0173(8)	0.0515(14)	0.0037(8)	-0.014(1)	-0.0029(8)
O3	0.0378(13)	0.0405(13)	0.0672(17)	0.0169(11)	0.0170(12)	0.0117(12)

O4	0.0379(13)	0.0499(14)	0.0616(16)	0.0101(11)	0.0211(13)	0.0123(12)
O5	0.0612(17)	0.0474(14)	0.0317(12)	-0.0126(13)	-0.0008(11)	-0.0123(10)
O6	0.087(2)	0.086(2)	0.0318(13)	-0.044(2)	0.0225(14)	-0.0189(14)
O7	0.074(2)	0.0673(19)	0.0529(17)	-0.0065(17)	0.0045(17)	0.0017(15)
O8	0.061(2)	0.103(3)	0.105(3)	0.024(2)	-0.001(2)	0.001(3)
O9	0.086(3)	0.111(3)	0.082(3)	-0.045(3)	0.016(2)	-0.035(2)
N1	0.0225(10)	0.0167(9)	0.0249(10)	-0.0005(8)	-0.0003(9)	-0.0005(8)
N2	0.0222(10)	0.0156(9)	0.0273(11)	-0.0018(8)	0.0011(9)	-0.0015(8)
N3	0.0222(10)	0.0183(9)	0.0248(10)	-0.0027(8)	-0.0047(9)	-0.0024(8)
N4	0.0246(11)	0.0181(9)	0.0271(11)	-0.0029(8)	0.0001(9)	-0.0024(8)
N5	0.0251(11)	0.0199(9)	0.0273(11)	-0.0007(8)	0.0004(9)	-0.0015(8)
N6	0.0259(11)	0.0175(9)	0.0295(11)	-0.0013(8)	0.0014(9)	-0.0013(8)
C1	0.0259(13)	0.0162(10)	0.0279(12)	0.0000(9)	-0.0014(11)	0.0004(9)
C2	0.0302(14)	0.0163(10)	0.0299(13)	-0.0005(10)	-0.0026(11)	-0.0018(9)
C3	0.0279(13)	0.0188(11)	0.0264(13)	-0.0025(10)	-0.0041(11)	-0.0018(9)
C4	0.0268(13)	0.0170(11)	0.0329(14)	0.0003(10)	-0.0029(11)	0.0002(10)
C5	0.0230(12)	0.0153(10)	0.0275(12)	0.0001(9)	0.0002(10)	-0.0009(9)
C6	0.0244(12)	0.0166(10)	0.0289(13)	-0.0013(9)	0.0014(11)	-0.0024(9)
C7	0.0274(13)	0.0183(11)	0.0356(15)	-0.0014(10)	-0.0055(12)	-0.0019(10)
C8	0.0287(14)	0.0166(11)	0.0356(15)	0.0005(10)	0.0001(12)	0.0001(10)
C9	0.0330(14)	0.0175(11)	0.0346(14)	-0.0016(10)	-0.0014(12)	-0.0061(10)
C10	0.0291(13)	0.0190(11)	0.0308(14)	-0.0026(10)	-0.0035(11)	-0.0042(10)
C11	0.0222(12)	0.0212(11)	0.0260(12)	-0.0021(9)	-0.0024(10)	-0.0021(9)
C12	0.0298(14)	0.0228(12)	0.0282(13)	-0.0026(10)	-0.0022(11)	0.0004(10)
C13	0.0371(16)	0.0239(12)	0.0324(14)	0.0004(11)	-0.0044(13)	0.0029(11)
C14	0.0341(16)	0.0230(12)	0.0390(16)	0.0042(11)	-0.0056(13)	0.0039(11)
C15	0.0265(13)	0.0248(12)	0.0356(14)	0.0013(11)	-0.0040(12)	-0.0011(11)
C16	0.0274(14)	0.0304(14)	0.0496(19)	0.0062(12)	0.0026(14)	0.0019(13)
C17	0.048(2)	0.051(2)	0.084(3)	0.0207(19)	0.024(2)	0.013(2)
C18	0.039(2)	0.063(3)	0.079(3)	0.0186(19)	0.023(2)	0.015(2)
C19	0.0267(14)	0.0357(15)	0.0438(18)	0.0032(12)	0.0088(13)	0.0002(13)
C20	0.0261(13)	0.0277(13)	0.0347(15)	-0.0026(11)	0.0035(12)	-0.0017(11)
C21	0.0320(15)	0.0324(14)	0.0361(16)	-0.0058(12)	0.0081(13)	-0.0012(12)
C22	0.0386(16)	0.0285(13)	0.0316(14)	-0.0054(12)	0.0061(13)	0.0031(11)
C23	0.0319(14)	0.0232(12)	0.0294(13)	-0.0034(11)	0.0007(12)	0.0006(10)
C24	0.0233(12)	0.0218(11)	0.0282(13)	-0.0039(10)	-0.0009(10)	-0.0025(10)
C25	0.0262(13)	0.0189(11)	0.0278(13)	-0.0001(10)	-0.0018(11)	-0.0017(9)
C26	0.0262(14)	0.0288(13)	0.0345(15)	-0.0068(11)	0.0002(12)	-0.0040(11)
C27	0.0297(15)	0.0304(14)	0.0434(17)	-0.0070(12)	-0.0041(13)	-0.0054(12)
C28	0.0370(16)	0.0280(13)	0.0373(16)	-0.0026(12)	-0.0088(13)	-0.0077(12)
C29	0.0376(16)	0.0241(12)	0.0306(14)	-0.0005(11)	-0.0050(13)	-0.0045(10)

C30	0.050(2)	0.0336(15)	0.0293(15)	-0.0053(14)	-0.0027(14)	-0.0071(12)
C31	0.084(3)	0.090(4)	0.0321(19)	-0.028(3)	0.008(2)	-0.020(2)
C32A	0.075(7)	0.055(5)	0.037(4)	-0.013(5)	0.012(4)	-0.014(3)
C32	0.069(6)	0.066(6)	0.026(3)	-0.015(4)	0.002(3)	-0.012(3)
C33	0.057(2)	0.0415(17)	0.0289(15)	-0.0109(16)	0.0085(15)	-0.0066(13)
C34	0.0434(18)	0.0254(13)	0.0295(14)	-0.0025(12)	0.0059(13)	-0.0028(11)
C35	0.050(2)	0.0316(15)	0.0380(17)	-0.0092(14)	0.0189(16)	-0.0018(13)
C36	0.0360(16)	0.0292(14)	0.0440(18)	-0.0091(12)	0.0141(14)	-0.0017(12)
C37	0.0288(14)	0.0258(13)	0.0350(15)	-0.0060(11)	0.0038(12)	-0.0022(11)
C38	0.0293(14)	0.0191(11)	0.0269(13)	0.0004(10)	0.0027(11)	-0.0015(9)

Table 4A.6 Geometric parameters (Å, °)

Ru1—N1	2.053(2)	C11—C15	1.410(4)
Ru1—N2	2.060(2)	C11—C24	1.421(4)
Ru1—N3	2.060(2)	C12—H12	0.93
Ru1—N4	2.061(2)	C12—C13	1.405(4)
Ru1—N5	2.071(2)	C13—H13	0.93
Ru1—N6	2.051(2)	C13—C14	1.358(5)
O1—H1	0.82	C14—H14	0.93
O1—C3	1.336(3)	C14—C15	1.410(4)
O2—H2	0.82	C15—C16	1.429(5)
O2—C8	1.341(3)	C16—C19	1.366(5)
O3—C16	1.370(4)	C17—H17A	0.97
O3—C17	1.461(5)	C17—H17B	0.97
O4—C18	1.443(5)	C17—C18	1.491(6)
O4—C19	1.372(4)	C18—H18A	0.97
O5—C30	1.371(4)	C18—H18B	0.97
O5—C31	1.415(5)	C19—C20	1.428(4)
O6—C32A	1.513(8)	C20—C21	1.408(4)
O6—C32	1.541(8)	C20—C24	1.400(4)
O6—C33	1.369(4)	C21—H21	0.93
O7—H7A	0.8514	C21—C22	1.373(4)
O7—H7B	0.8485	C22—H22	0.93
O8—H8A	0.8511	C22—C23	1.403(4)
O8—H8B	0.8499	C23—H23	0.93
O9—H9A	0.8495	C25—C29	1.409(4)
O9—H9B	0.8489	C25—C38	1.427(4)
N1—C1	1.346(3)	C26—H26	0.93
N1—C5	1.358(3)	C26—C27	1.399(4)
N2—C6	1.350(4)	C27—H27	0.93
N2—C10	1.348(3)	C27—C28	1.361(5)

N3—C11	1.362(4)	C28—H28	0.93
N3—C12	1.344(3)	C28—C29	1.401(4)
N4—C23	1.343(4)	C29—C30	1.430(5)
N4—C24	1.371(3)	C30—C33	1.368(5)
N5—C25	1.357(4)	C31—H31C	0.97
N5—C26	1.338(4)	C31—H31D	0.97
N6—C37	1.340(4)	C31—H31A	0.97
N6—C38	1.362(4)	C31—H31B	0.97
C1—H1A	0.93	C31—C32A	1.403(11)
C1—C2	1.379(4)	C31—C32	1.406(10)
C2—H2A	0.93	C32A—H32A	0.97
C2—C3	1.388(4)	C32A—H32B	0.97
C3—C4	1.401(4)	C32—H32C	0.97
C4—H4	0.93	C32—H32D	0.97
C4—C5	1.378(4)	C33—C34	1.431(5)
C5—C6	1.490(3)	C34—C35	1.403(5)
C6—C7	1.380(4)	C34—C38	1.399(4)
C7—H7	0.93	C35—H35	0.93
C7—C8	1.397(4)	C35—C36	1.364(5)
C8—C9	1.379(4)	C36—H36	0.93
C9—H9	0.93	C36—C37	1.390(4)
C9—C10	1.370(4)	C37—H37	0.93
C10—H10	0.93		
N1—Ru1—N2	78.38(8)	O3—C17—H17A	109.9
N1—Ru1—N3	96.24(8)	O3—C17—H17B	109.9
N1—Ru1—N4	89.49(9)	O3—C17—C18	109.0(4)
N1—Ru1—N5	172.40(9)	H17A—C17—H17B	108.3
N2—Ru1—N4	97.69(9)	C18—C17—H17A	109.9
N2—Ru1—N5	95.68(9)	C18—C17—H17B	109.9
N3—Ru1—N2	174.24(9)	O4—C18—C17	110.3(3)
N3—Ru1—N4	80.09(9)	O4—C18—H18A	109.6
N3—Ru1—N5	89.85(9)	O4—C18—H18B	109.6
N4—Ru1—N5	96.06(9)	C17—C18—H18A	109.6
N6—Ru1—N1	95.06(9)	C17—C18—H18B	109.6
N6—Ru1—N2	89.95(9)	H18A—C18—H18B	108.1
N6—Ru1—N3	92.58(9)	O4—C19—C20	115.5(3)
N6—Ru1—N4	171.78(9)	C16—C19—O4	123.1(3)
N6—Ru1—N5	80.08(9)	C16—C19—C20	121.4(3)
C3—O1—H1	109.5	C21—C20—C19	123.8(3)
C8—O2—H2	109.5	C24—C20—C19	118.4(3)
C16—O3—C17	111.2(3)	C24—C20—C21	117.8(3)
C19—O4—C18	111.8(3)	C20—C21—H21	120.6
C30—O5—C31	112.2(3)	C22—C21—C20	118.9(3)
C33—O6—C32A	108.3(4)	C22—C21—H21	120.6
C33—O6—C32	110.8(4)	C21—C22—H22	119.8

H7A—O7—H7B	109.4	C21—C22—C23	120.3(3)
H8A—O8—H8B	109.4	C23—C22—H22	119.8
H9A—O9—H9B	109.6	N4—C23—C22	122.1(3)
C1—N1—Ru1	125.41(18)	N4—C23—H23	119
C1—N1—C5	117.9(2)	C22—C23—H23	119
C5—N1—Ru1	116.71(16)	N4—C24—C11	116.5(2)
C6—N2—Ru1	116.55(16)	N4—C24—C20	123.2(3)
C10—N2—Ru1	125.67(19)	C20—C24—C11	120.3(3)
C10—N2—C6	117.7(2)	N5—C25—C29	122.9(3)
C11—N3—Ru1	113.28(17)	N5—C25—C38	116.8(2)
C12—N3—Ru1	128.5(2)	C29—C25—C38	120.2(3)
C12—N3—C11	118.2(2)	N5—C26—H26	119
C23—N4—Ru1	129.24(19)	N5—C26—C27	122.0(3)
C23—N4—C24	117.6(2)	C27—C26—H26	119
C24—N4—Ru1	113.14(18)	C26—C27—H27	119.9
C25—N5—Ru1	112.86(18)	C28—C27—C26	120.3(3)
C26—N5—Ru1	129.1(2)	C28—C27—H27	119.9
C26—N5—C25	118.0(2)	C27—C28—H28	120.4
C37—N6—Ru1	128.5(2)	C27—C28—C29	119.2(3)
C37—N6—C38	118.0(2)	C29—C28—H28	120.4
C38—N6—Ru1	113.33(18)	C25—C29—C30	118.1(3)
N1—C1—H1A	118.4	C28—C29—C25	117.5(3)
N1—C1—C2	123.2(2)	C28—C29—C30	124.4(3)
C2—C1—H1A	118.4	O5—C30—C29	115.8(3)
C1—C2—H2A	120.6	C33—C30—O5	122.7(3)
C1—C2—C3	118.8(2)	C33—C30—C29	121.5(3)
C3—C2—H2A	120.6	O5—C31—H31C	107.1
O1—C3—C2	123.0(2)	O5—C31—H31D	107.1
O1—C3—C4	118.3(2)	O5—C31—H31A	107.8
C2—C3—C4	118.7(2)	O5—C31—H31B	107.8
C3—C4—H4	120.4	H31C—C31—H31D	106.8
C5—C4—C3	119.1(2)	H31A—C31—H31B	107.1
C5—C4—H4	120.4	C32A—C31—O5	120.9(5)
N1—C5—C4	122.3(2)	C32A—C31—H31C	107.1
N1—C5—C6	114.0(2)	C32A—C31—H31D	107.1
C4—C5—C6	123.7(2)	C32—C31—O5	118.0(5)
N2—C6—C5	114.4(2)	C32—C31—H31A	107.8
N2—C6—C7	122.1(2)	C32—C31—H31B	107.8
C7—C6—C5	123.6(2)	O6—C32A—H32A	110.1
C6—C7—H7	120.2	O6—C32A—H32B	110.1
C6—C7—C8	119.6(3)	C31—C32A—O6	108.0(7)
C8—C7—H7	120.2	C31—C32A—H32A	110.1
O2—C8—C7	123.7(3)	C31—C32A—H32B	110.1
O2—C8—C9	118.5(2)	H32A—C32A—H32B	108.4
C9—C8—C7	117.8(3)	O6—C32—H32C	110.5

C8—C9—H9	120.2	O6—C32—H32D	110.5
C10—C9—C8	119.6(2)	C31—C32—O6	106.3(6)
C10—C9—H9	120.2	C31—C32—H32C	110.5
N2—C10—C9	123.1(3)	C31—C32—H32D	110.5
N2—C10—H10	118.4	H32C—C32—H32D	108.7
C9—C10—H10	118.4	O6—C33—C34	115.8(3)
N3—C11—C15	122.2(2)	C30—C33—O6	123.2(3)
N3—C11—C24	117.0(2)	C30—C33—C34	120.9(3)
C15—C11—C24	120.8(3)	C35—C34—C33	123.8(3)
N3—C12—H12	119	C38—C34—C33	118.4(3)
N3—C12—C13	122.1(3)	C38—C34—C35	117.8(3)
C13—C12—H12	119	C34—C35—H35	120.4
C12—C13—H13	119.9	C36—C35—C34	119.3(3)
C14—C13—C12	120.2(3)	C36—C35—H35	120.4
C14—C13—H13	119.9	C35—C36—H36	120
C13—C14—H14	120.5	C35—C36—C37	120.0(3)
C13—C14—C15	119.1(3)	C37—C36—H36	120
C15—C14—H14	120.5	N6—C37—C36	122.3(3)
C11—C15—C16	118.0(3)	N6—C37—H37	118.9
C14—C15—C11	118.1(3)	C36—C37—H37	118.9
C14—C15—C16	123.9(3)	N6—C38—C25	116.7(2)
O3—C16—C15	115.5(3)	N6—C38—C34	122.6(3)
C19—C16—O3	123.4(3)	C34—C38—C25	120.7(3)
C19—C16—C15	121.1(3)		
Ru1—N1—C1—C2	-178.3(2)	C13—C14—C15—C11	0.0(4)
Ru1—N1—C5—C4	178.8(2)	C13—C14—C15—C16	-179.1(3)
Ru1—N1—C5—C6	-1.6(3)	C14—C15—C16—O3	-1.0(5)
Ru1—N2—C6—C5	0.9(3)	C14—C15—C16—C19	177.3(3)
Ru1—N2—C6—C7	-177.6(2)	C15—C11—C24—N4	-179.9(2)
Ru1—N2—C10—C9	176.9(2)	C15—C11—C24—C20	0.7(4)
Ru1—N3—C11—C15	-179.3(2)	C15—C16—C19—O4	-176.8(3)
Ru1—N3—C11—C24	-0.1(3)	C15—C16—C19—C20	2.8(5)
Ru1—N3—C12—C13	179.2(2)	C16—O3—C17—C18	-48.2(5)
Ru1—N4—C23—C22	-178.1(2)	C16—C19—C20—C21	178.4(3)
Ru1—N4—C24—C11	-1.2(3)	C16—C19—C20—C24	-2.0(5)
Ru1—N4—C24—C20	178.2(2)	C17—O3—C16—C15	-164.7(3)
Ru1—N5—C25—C29	-179.6(2)	C17—O3—C16—C19	17.0(5)
Ru1—N5—C25—C38	2.0(3)	C18—O4—C19—C16	13.8(5)
Ru1—N5—C26—C27	179.8(2)	C18—O4—C19—C20	-165.8(3)
Ru1—N6—C37—C36	-173.4(2)	C19—O4—C18—C17	-45.8(5)
Ru1—N6—C38—C25	-4.1(3)	C19—C20—C21—C22	-180.0(3)
Ru1—N6—C38—C34	175.9(2)	C19—C20—C24—N4	-179.1(3)
O1—C3—C4—C5	-179.8(3)	C19—C20—C24—C11	0.3(4)
O2—C8—C9—C10	178.3(3)	C20—C21—C22—C23	-0.4(5)
O3—C16—C19—O4	1.4(6)	C21—C20—C24—N4	0.6(4)

O3—C16—C19—C20	-179.0(3)	C21—C20—C24—C11	179.9(3)
O3—C17—C18—O4	64.8(5)	C21—C22—C23—N4	-0.7(5)
O4—C19—C20—C21	-2.0(5)	C23—N4—C24—C11	179.1(2)
O4—C19—C20—C24	177.6(3)	C23—N4—C24—C20	-1.6(4)
O5—C30—C33—O6	2.1(6)	C24—N4—C23—C22	1.6(4)
O5—C30—C33—C34	-176.6(3)	C24—C11—C15—C14	-179.1(3)
O5—C31—C32A—O6	-52.8(9)	C24—C11—C15—C16	0.0(4)
O5—C31—C32—O6	60.2(8)	C24—C20—C21—C22	0.5(4)
O6—C33—C34—C35	1.0(5)	C25—N5—C26—C27	-0.9(4)
O6—C33—C34—C38	-178.2(3)	C25—C29—C30—O5	176.8(3)
N1—C1—C2—C3	-0.5(4)	C25—C29—C30—C33	-1.4(5)
N1—C5—C6—N2	0.5(3)	C26—N5—C25—C29	1.0(4)
N1—C5—C6—C7	179.0(3)	C26—N5—C25—C38	-177.4(2)
N2—C6—C7—C8	-0.5(4)	C26—C27—C28—C29	1.8(5)
N3—C11—C15—C14	0.1(4)	C27—C28—C29—C25	-1.6(4)
N3—C11—C15—C16	179.1(3)	C27—C28—C29—C30	177.8(3)
N3—C11—C24—N4	0.9(4)	C28—C29—C30—O5	-2.6(5)
N3—C11—C24—C20	-178.5(2)	C28—C29—C30—C33	179.2(3)
N3—C12—C13—C14	-0.1(4)	C29—C25—C38—N6	-177.1(2)
N5—C25—C29—C28	0.2(4)	C29—C25—C38—C34	2.9(4)
N5—C25—C29—C30	-179.2(3)	C29—C30—C33—O6	-179.8(4)
N5—C25—C38—N6	1.4(4)	C29—C30—C33—C34	1.5(6)
N5—C25—C38—C34	-178.6(3)	C30—O5—C31—C32A	23.8(8)
N5—C26—C27—C28	-0.5(5)	C30—O5—C31—C32	-38.5(7)
C1—N1—C5—C4	-0.9(4)	C30—C33—C34—C35	179.8(3)
C1—N1—C5—C6	178.7(2)	C30—C33—C34—C38	0.7(5)
C1—C2—C3—O1	-179.7(3)	C31—O5—C30—C29	-173.9(4)
C1—C2—C3—C4	-0.9(4)	C31—O5—C30—C33	4.3(5)
C2—C3—C4—C5	1.3(4)	C32A—O6—C33—C30	-31.3(7)
C3—C4—C5—N1	-0.4(4)	C32A—O6—C33—C34	147.5(5)
C3—C4—C5—C6	-180.0(3)	C32—O6—C33—C30	20.9(7)
C4—C5—C6—N2	-180.0(3)	C32—O6—C33—C34	-160.3(5)
C4—C5—C6—C7	-1.5(4)	C33—O6—C32A—C31	52.8(8)
C5—N1—C1—C2	1.4(4)	C33—O6—C32—C31	-48.3(7)
C5—C6—C7—C8	-178.9(3)	C33—C34—C35—C36	-177.1(3)
C6—N2—C10—C9	0.3(4)	C33—C34—C38—N6	177.2(3)
C6—C7—C8—O2	-178.8(3)	C33—C34—C38—C25	-2.8(4)
C6—C7—C8—C9	2.2(4)	C34—C35—C36—C37	-0.3(5)
C7—C8—C9—C10	-2.5(4)	C35—C34—C38—N6	-2.0(4)
C8—C9—C10—N2	1.3(5)	C35—C34—C38—C25	178.0(3)
C10—N2—C6—C5	177.8(2)	C35—C36—C37—N6	-1.6(5)
C10—N2—C6—C7	-0.7(4)	C37—N6—C38—C25	-179.8(2)
C11—N3—C12—C13	0.1(4)	C37—N6—C38—C34	0.2(4)
C11—C15—C16—O3	179.9(3)	C38—N6—C37—C36	1.6(4)
C11—C15—C16—C19	-1.7(5)	C38—C25—C29—C28	178.6(3)

C12—N3—C11—C15	-0.1(4)	C38—C25—C29—C30	-0.8(4)
C12—N3—C11—C24	179.1(2)	C38—C34—C35—C36	2.0(5)
C12—C13—C14—C15	0.1(5)		

Table 4A.7 Hydrogen bond geometry (Å, °)

D—H...A	D—H	H...A	D...A	D—H...A
O9—H9A...O8i	0.85	1.95	2.781 (6)	167
Symmetry code: (i) $-x+3/2, y-1/2, z$.				

CHAPTER 5

DEVELOPMENT OF NEW RUTHENIUM PDT AGENTS INCORPORATING BATHOPHENANTHROLINEDISULFONIC ACID AND BATHOPHENANTHROLINE LIGANDS

5.1 Abstract

$[(\text{BPS})_2\text{Ru}(6,6'\text{-dhbp})]^{2-}$ (**9_A**), $[(\text{BPhen})_2\text{Ru}(6,6'\text{-dhbp})]^{2+}$ (**10_A**), and $[(\text{BPhen})_2\text{Ru}(4,4'\text{-dhbp})]^{2+}$ (**11_A**) were synthesized and studied as potential light activated anticancer agents. All compounds are novel; however, their syntheses are small modifications of previously published procedures. Compound **9_A**, a highly hydrophilic and negatively charged complex, was synthesized and screened in cells; however, it was non-toxic and was not light activated. A preliminary study of this complex showed that it may photodissociate upon irradiation, potentially preventing it from producing significant amounts of singlet oxygen. Compounds **10** and **11**; however, were significantly more toxic than complexes that have been discussed in previous chapters. Both complexes showed excellent light selectivity as seen by PI values ranging from ~7 (compound **10**) to over 1,600 (complex **11**). Complex **11** had an EC₅₀ value of $0.30 \pm 0.03 \mu\text{M}$ in MDA-MB-231 breast cancer stem cells. Research on these complexes is still ongoing, and data on hydrophobicity, photodissociation, and singlet oxygen production are in progress or planned for future work.

5.2 Introduction

While the study of platinum-based anticancer drugs is common, there have also been advances in the development of ruthenium-based anticancer drugs with potentially fewer side effects than Pt-based treatments. To date only three ruthenium complexes have advanced to clinical trials, and only one is light activated (Figure 1.1).¹⁻⁴ TLD-1433 is a Ru(II) light-triggered complex classified as a photodynamic therapy (PDT) agent to treat non-muscle invasive bladder cancer.^{5, 6} This complex has shown great promise and produces $^1\text{O}_2$ at near quantitative efficiency. Light has been used to treat certain cancers using PCT which allows for precise spatial delivery of drug to cancer cells by only affecting the area of irradiation. As discussed in previous chapters, PCT includes both PDT and PACT (Scheme 1.1).⁷

In *Inorganic Chemistry* 2017, the Papish group developed and studied a series of complexes originally designed as PACT agents (compounds **1-3**), which were found to be highly toxic against breast cancer cells once irradiated (Table 1.1).^{8, 9} Subsequent studies showed that complexes **1-3** did not photodissociate at significant rates but were excellent producers of singlet oxygen (Chapter 4, Table 4.2) with the highest observed Φ_Δ for **2B** (0.89 in CD_3OD).¹⁰ This led to the conclusion that compounds **1-3** behaved as PDT agents and not PACT agents. Furthermore, the hydrophobicity of a complex played a significant role in uptake and toxicity (Chapter 2).¹¹

With the information that has been collected on protic anticancer compounds, ruthenium complexes with increased hydrophobicity, lower rates of photodissociation, and potentially increased rates of singlet oxygen production have been synthesized. These new complexes continue to include 6,6'-dhbp and its derivatives as it is known to aid in controlling the PDT vs PACT pathway, and overall hydrophobicity based on the pH. For these new complexes, the

ligands Bathophenanthrolinedisulfonic acid (BPS) and Bathophenanthroline are incorporated (BPhen, sometimes referred to as “Dip” in literature) (Figure 5.1).

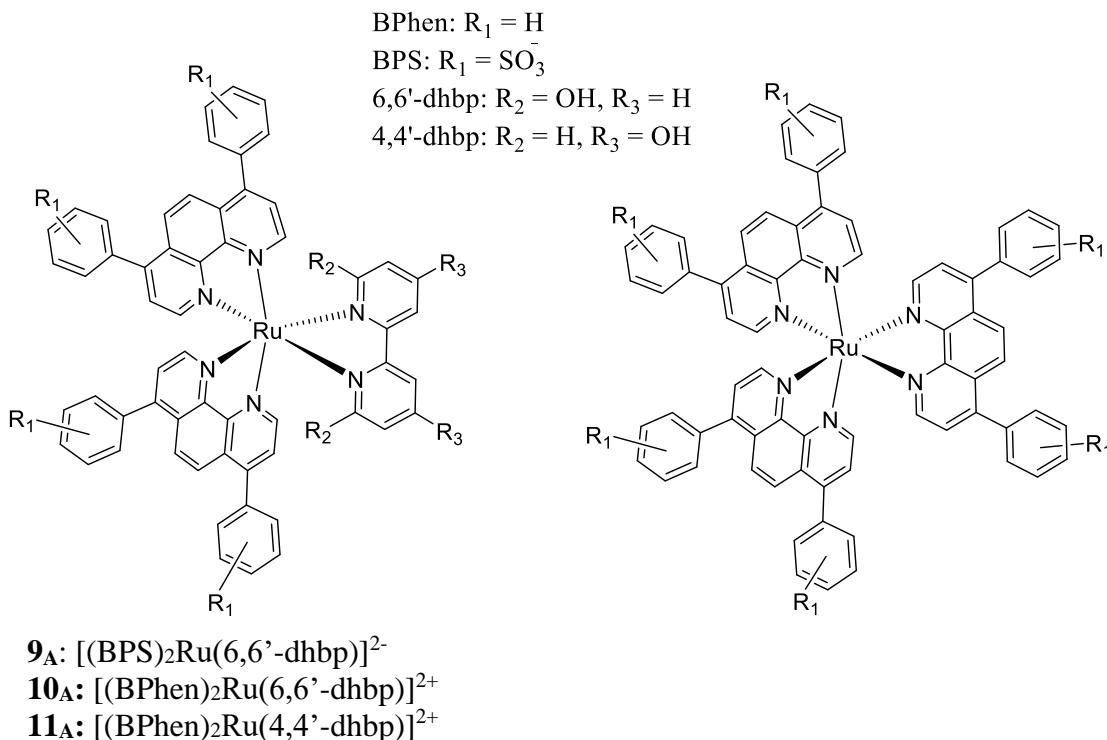


Figure 5.1. Left: Structure of BPS and BPhen complexes (**9_A**-**11_A**) that are discussed in this chapter. Right: Structures studied by Glazer ($[Ru(BPS)_3]^{4-}$ or $[Ru(BPhen)_3]^{2+}$) were light activated anticancer compounds capable of producing singlet oxygen.

Glazer and co-workers did a comparative study of two light-activated ruthenium complexes, $[Ru(BPS)_3]^{4-}$ and $[Ru(BPhen)_3]^{2+}$.¹² Both complexes showed cytotoxic activity upon irradiation and were capable of producing 1O_2 . Glazer’s BPhen complex was hydrophobic (Log P = 1.80) with an IC_{50} of 0.075 μM while the negatively charged BPS complex had a Log P value of -2.2 with an IC_{50} of 3.31 μM (both complexes were tested against Jurkat lymphatic cancer cells).¹² By using a similar system that incorporates the protic ligand, 6,6'-dhbp, the complex’s uptake, toxicity, and 1O_2 production as a function of charge can be studied. The target complexes will contain the 2- ligand, BPS, or the neutral ligand, BPhen, while also incorporating

dihydroxybipyridine derivatives. $[\text{Ru}(\text{BPS})_3]^{4+}$ or $[\text{Ru}(\text{BPhen})_3]^{2+}$ complexes are widely reported in the literature as fluorescent probes for cellular imaging applications and in-gel protein staining.¹³⁻¹⁶ Di-substituted complexes (bis BPhen complexes, in particular) have been studied as anticancer agents with significant toxicity towards melanoma, pharynx carcinoma, and breast cancer cell lines (MDA-MB-435S, FaDU, and MCF-7 respectively) as studied by Gasser and co-workers (Figure 5.2).¹⁷⁻¹⁹ These ruthenium BPhen complexes also showed increased uptake into melanoma and breast cancer cell lines compared to cisplatin as measured by ICP-MS but were not toxic through light-activated mechanisms (*Inorg. Chem.* 2020).¹⁸ SAR studies by Paira and co-workers have found that the incorporating BPhen increased the lipophilicity of their ruthenium complexes and was crucial for toxicity.¹³ Similarly, Barton and co-workers have demonstrated that $[(\text{BPhen})_2\text{Ru}(\text{dppz})]^{2+}$ was able to enter HeLa cells via passive diffusion.²⁰

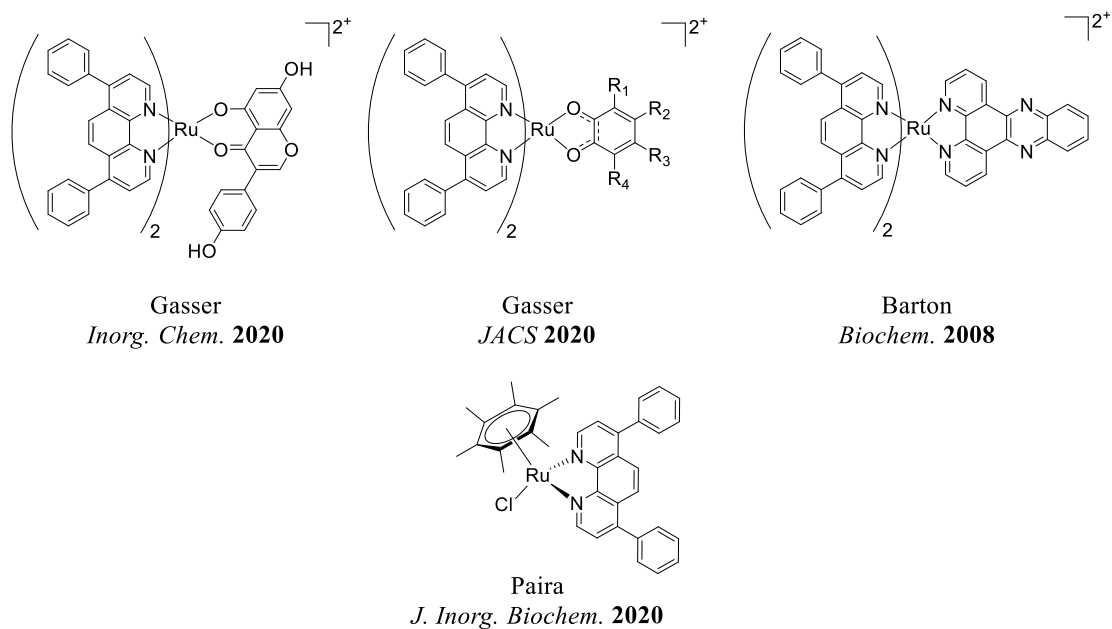


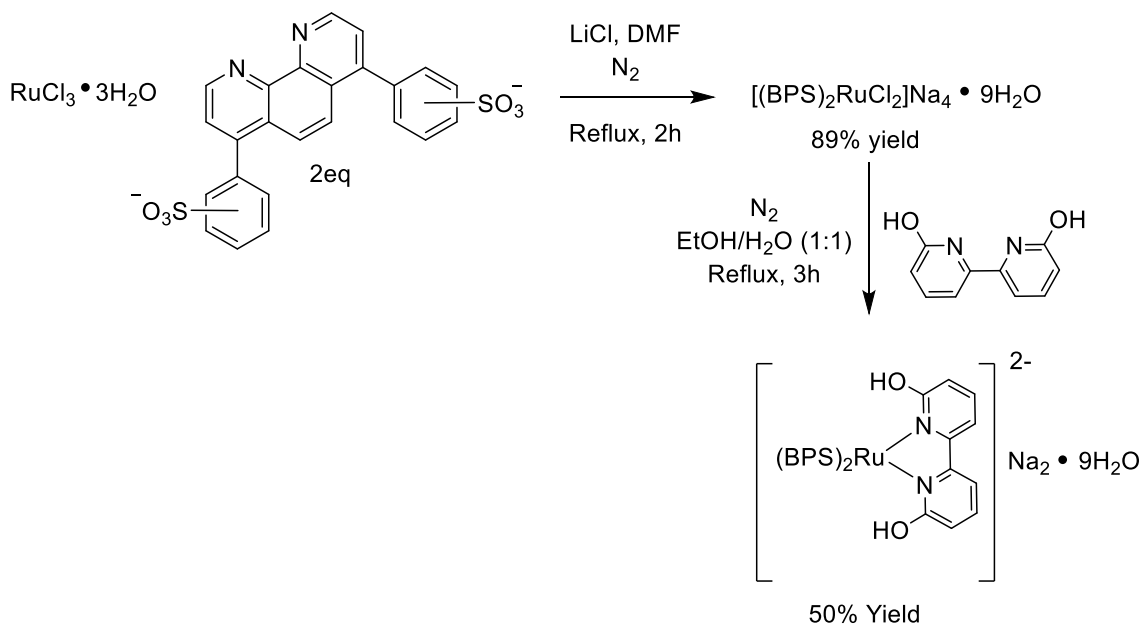
Figure 5.2. Structures of BPhen complexes in the literature that have been studied by Gasser, Barton, and Paira.

In this chapter, I will discuss the complexes $[(BPS)_2Ru(6,6'\text{-dhbp})]Na_2$ (**9_A**), $[(BPhen)_2Ru(6,6'\text{-dhbp})]Cl_2$ (**10_A**), and $[(BPhen)_2Ru(4,4'\text{-dhbp})]Cl_2$ (**11_A**) (Figure 5.1). Like complexes **1-3**, complexes **9-11** can become protonated or deprotonated at the dhbp ligand and are denoted as **X_A** or **X_B**, respectively; however, it should be noted that the pK_a of compounds **9-11** is currently TBD. Compound **9** was chosen as a point of comparison. The inclusion of negatively charged ligands will make the complex range from an overall charge of -2 or -4 depending on protonation state. As a result, complex **9** is predicted to have increased hydrophilicity and potentially less uptake and toxicity (this is no guarantee as has been demonstrated by Glazer's work). Compounds **10** and **11** have the potential to be more hydrophobic than complexes **1-3** due to an extended pi system on the BPhen ligand and potentially higher uptake into cells. By moving the -OH substituents of dhbp from the 6,6' positions to the 4,4' positions, complex **11** will have less steric bulk (compared to **10**) near the metal center and may undergo less photodissociation and increased singlet oxygen production. While this study is currently ongoing, this chapter will cover the preliminary synthesis, characterization, and toxicity data for complexes **9-11**.

5.3 Results and Discussion

5.3.1. Synthesis and Characterization of $[(BPS)_2Ru(6,6'\text{-dhbp})]Na_2$ (**9_A**)

Unlike previously studied compounds, complex **9** will have a relatively high negative charge. This charge will result in increased hydrophilicity and potentially less uptake into cells via passive diffusion. While this may affect the mode of uptake for the complex, similar complexes are capable of producing singlet oxygen and light-activity toxicity towards cancer cells.¹² Synthesis of complex **9_A** was carried out with minimal modification to a synthesis described by Ciana *et al.* in 2010 (Scheme 5.1).¹⁶



Scheme 5.1. Proposed synthesis scheme for the target complex $[(\text{BPS})_2\text{Ru}(6,6'\text{-dhbp})]^{2-}$ (**9A**).

The synthesis of the dichloride intermediate was performed with little modification apart from isolating the final product under inert, dry atmosphere.¹⁶ The final BPS ruthenium complex had the high proclivity to collect atmospheric moisture. Once synthesized, the complex was analyzed via inductively coupled plasma mass spectrometry (ICP-MS) and NMR. The sulfonate groups on BPS are not located at a set position on the ligand and the final complex is isolated as a mixture of isomers. As a result, NMR assignments of the BPS ligand can be difficult with only 1D ^1H NMR and attempts to isolate an x-ray quality crystal for analysis were unsuccessful. ^1H NMR and mass spectroscopy evidence showed that the isolated di-chloride intermediate complex was the *trans*- $(\text{BPS})_2\text{RuCl}_2$ complex and not the *cis* isomer (Figure 5.3). Individual peak assignment can be difficult due to overlap within the aromatic region as seen on 2D ^1H NMR (Figure 5.4). Electrospray ionization mass spectrometry (ESI-MS) data of the product also matched simulated spectra with $[(\text{BPS})_2\text{Ru}(6,6'\text{-dhbp})]^{2-}$ $m/z = 636.2$. Peaks for $[\mathbf{9}]^{3-}$ and $[\mathbf{9}\text{-Na}]^{2-}$ were also observed at $m/z = 423.2$ and 646.2 respectively (Figure 5.5).

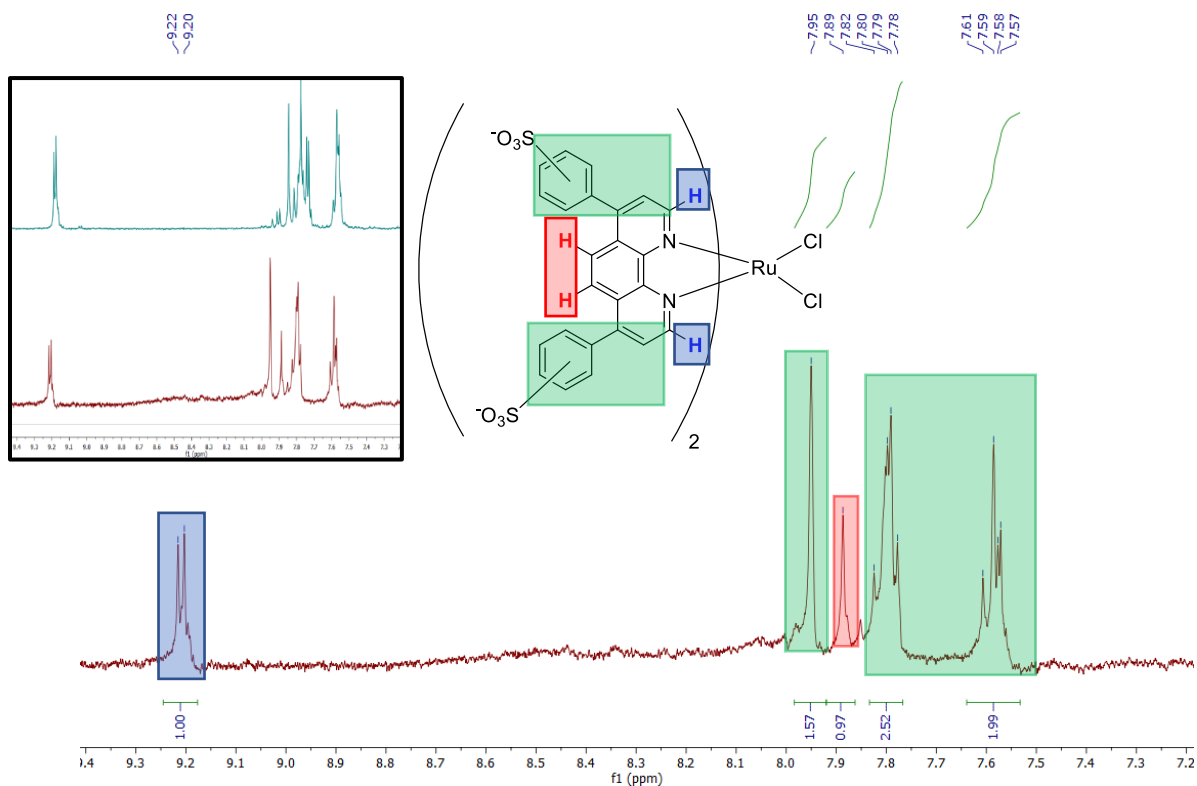


Figure 5.3. ¹H NMR spectrum of [(BPS)₂RuCl₂]⁴⁻ intermediate in DMSO-[d₆] (Solvent peak omitted for clarity). **Insert:** Stacked comparison of stock BPS ligand (green) to the collected dichloride product (red). All NMR shown were taken in DMSO-[d₆] at 360 MHz. A rough assignment of peaks was determined using ChemDraw ¹H NMR prediction. The similarity in spectra for the free BPS ligand and the (BPS)₂RuCl₂ complex indicates that a trans complex was formed.

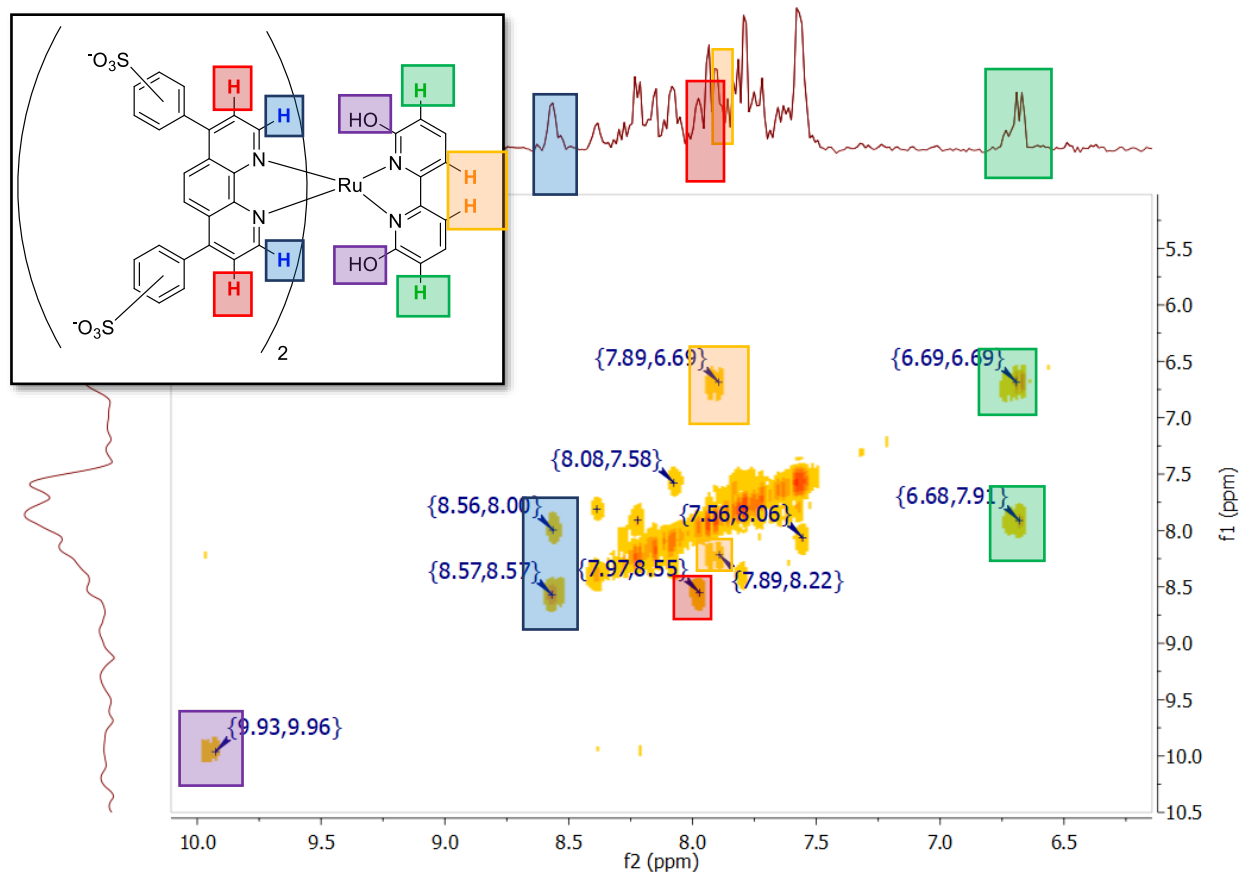


Figure 5.4. 2D COSY ^1H NMR spectrum of $[(\text{BPS})_2\text{Ru}(6,6'\text{-dhbp})]^{2-}$ (**9A**) in DMSO- $[\text{d}_6]$ (Solvent peak omitted for clarity). Significant overlap of aromatic peaks prevent assignment for all hydrogens within the complex; however, based off information from the 2D NMR, ChemDraw simulated NMR's, and known relative shifts for 6,6'-dhbp, some assignments can be made.

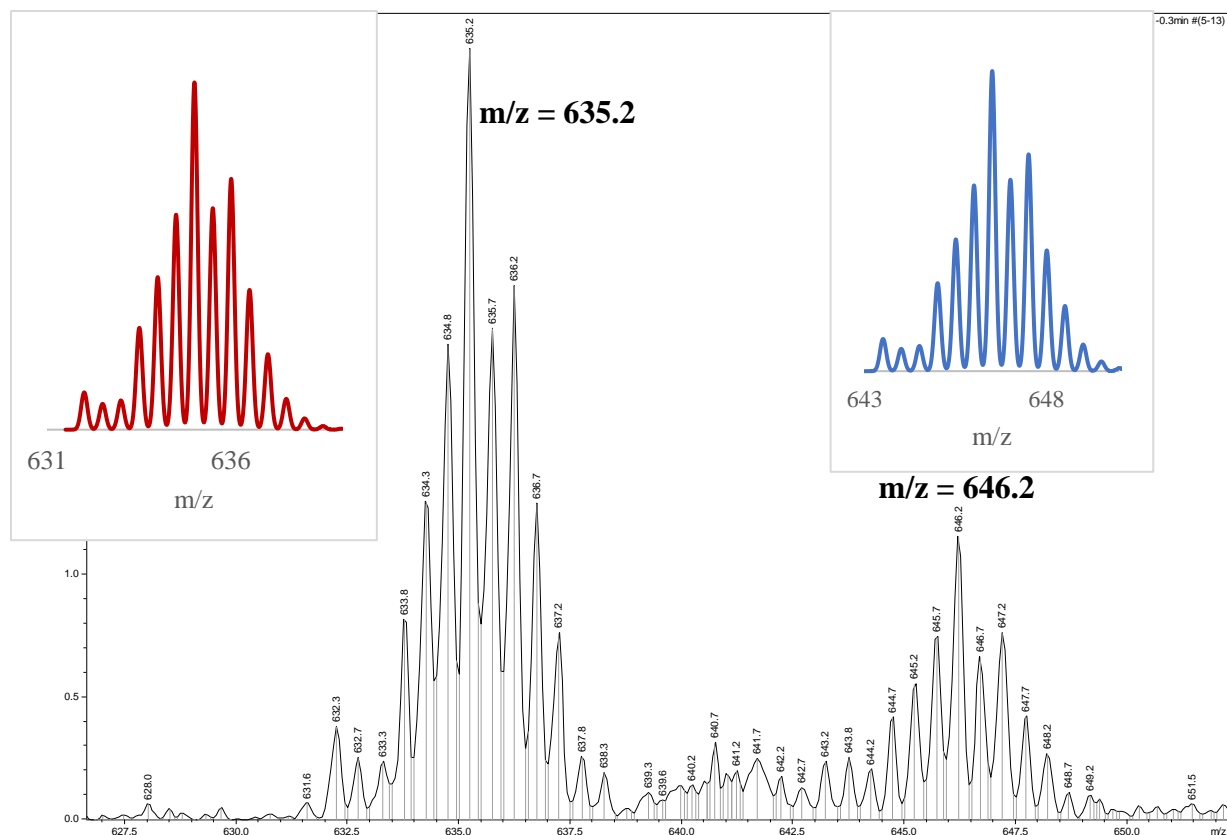


Figure 5.5. ESI-MS spectrum of $[(\text{BPS})_2\text{Ru}(6,6'\text{-dhbp})]\text{Na}_2$ (**9A**). The peak at m/z 635.2 corresponds to $[\text{M}]^{2-}$ (simulated in red) while the peak at m/z 646.2 corresponds to $[\text{M-Na}]^{2-}$ (simulated in blue). Another peak observed at m/z 423.2 corresponds to $[\text{M}]^{3-}$ but is omitted for clarity.

$[(\text{BPS})_2\text{Ru}(6,6'\text{-dhbp})]^{2-}$ (**9A**) was screened against MDA-MB-231 cell lines by the Kim group at a concentration of $5\mu\text{M}$ in both light and dark conditions but was found to be non-toxic at that concentration and not light activated. A qualitative photodissociation study was carried out in distilled deionized H_2O and monitored via UV-Vis. The sample was irradiated with blue light (450 nm) over the course of two hours and monitored for any change via UV-Vis spectroscopy (Figure 5.6). The spectra changed significantly over the course of irradiation indicating photo-induced physical changes within the complex, most likely photodissociation. As photodissociation and singlet oxygen production are inversely related, **9** is not likely to produce singlet oxygen: a potential explanation for its lack of toxicity.

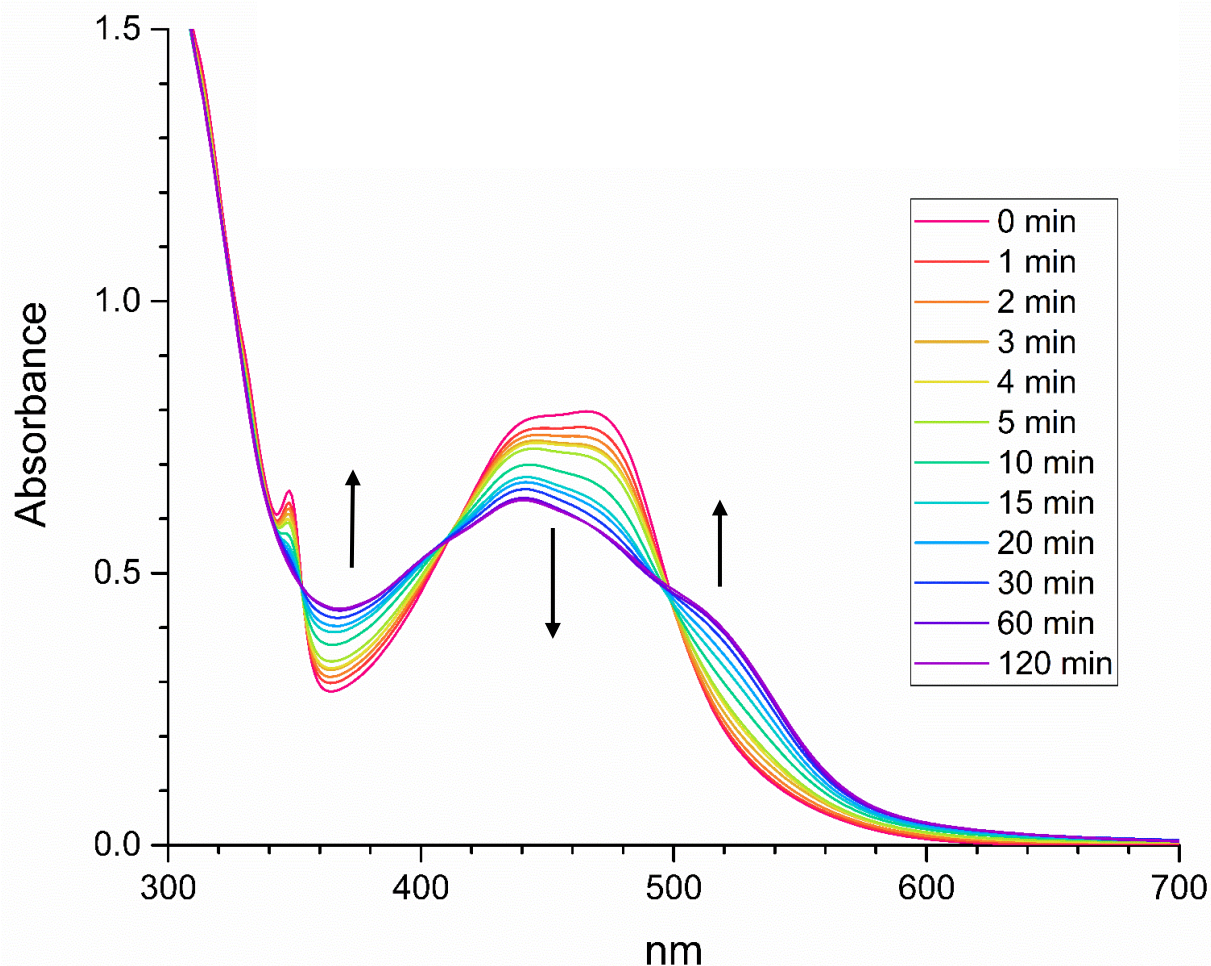


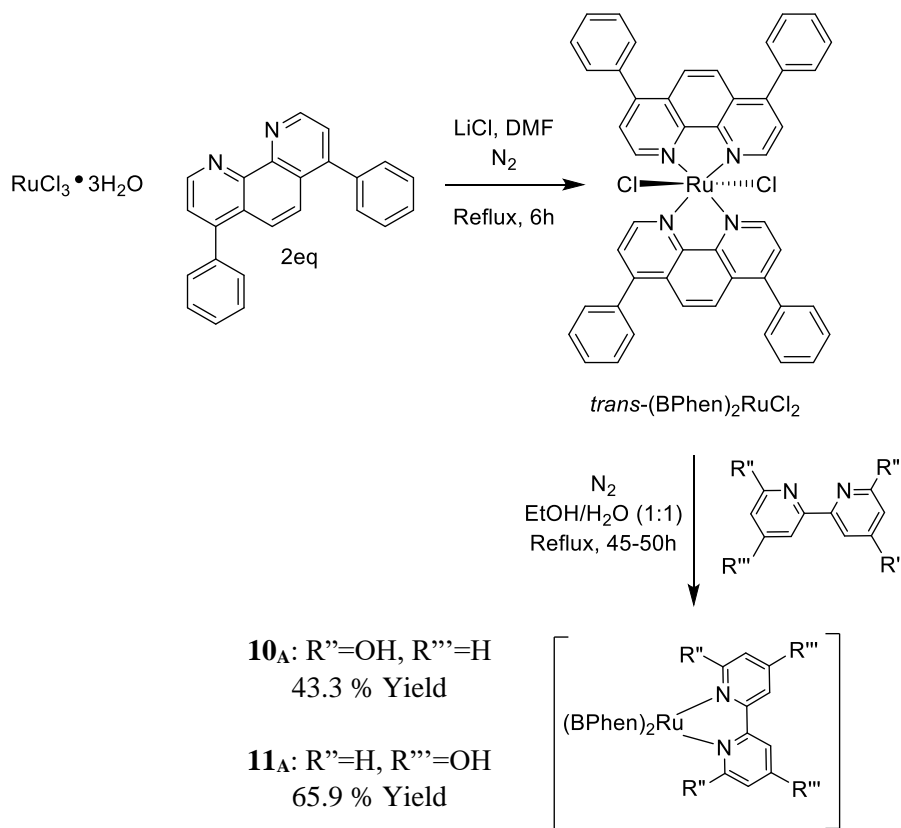
Figure 5.6. Photodissociation of $[(\text{BPS})_2\text{Ru}(6,6'\text{-dhbp})]^{2-}$ (**9_A**) diH_2O . The solution was irradiated with blue light (450 nm) and over the course of 2 hours with UV-Vis spectrum taken at various points throughout. Significant change in the spectra indicates that the complex is most likely undergoing photodissociation upon irradiation.

5.3.2. Synthesis and Characterization of $[(\text{BPhen})_2\text{Ru}(6,6'\text{-dhbp})]^{2+}$ (**10_A**) and $[(\text{BPhen})_2\text{Ru}(4,4'\text{-dhbp})]^{2+}$ (**11_A**)

Studies by Paira and Gasser have shown that the inclusion of the BPhen ligand can greatly increase hydrophobicity yielding a beneficial effect on toxicity.^{15,19-21} Glazer has shown that ruthenium BPhen complexes can produce singlet oxygen and be effective as light-activated anticancer agents.¹⁴ As opposed to the BPS analogue (**9**), both **10** and **11** will have overall charges ranging from 2+ to 0 depending on the protonation state of the dhbp ligand. The

incorporation of the neutral BPhen ligand will also allow for an increase in hydrophobicity.

Complexes **10_A** and **11_A** follow similar synthetic routes as compound **9_A** (Scheme 5.2).



Scheme 5.2. Proposed synthesis scheme for the target complex $[(\text{BPhen})_2\text{Ru}(6,6'\text{-dhbp})]^{2+}$ (**10_A**) and $[(\text{BPhen})_2\text{Ru}(4,4'\text{-dhbp})]^{2+}$ (**11_A**).

The synthesis of the intermediate, $(\text{BPhen})_2\text{RuCl}_2$, was carried out according to published literature.^{18, 21} The synthesis of $[(\text{BPhen})_2\text{Ru}(6,6'\text{-dhbp})]^{2+}$ (**10_A**) or $[(\text{BPhen})_2\text{Ru}(4,4'\text{-dhbp})]^{2+}$ (**11_A**) was based off synthesis for complexes **1-3** and was monitored for completion via NMR. The final reaction was typically run for 45-50 hours to allow for a *cis-trans* isomerization of the BPhen ligands. 2D ¹H NMR of **10_A** showed significant overlap of aromatic peaks from both BPhen and 6,6'-dhbp, making assignment of all hydrogens difficult; however, some can be assigned with the help of 2D ¹H NMR and simulation software (Figures 5.7-5.9). Unlike with

BPhen, BPhen complexes do not typically form a mixture of isomers and a crystal structure of **10_A** was isolated by Ambar Shrestha (formerly of the Papish group) and analyzed via X-ray diffraction (Figure 5.10). Current work towards investigating photodissociation and potential singlet oxygen production for complexes **10** and **11** is currently ongoing.

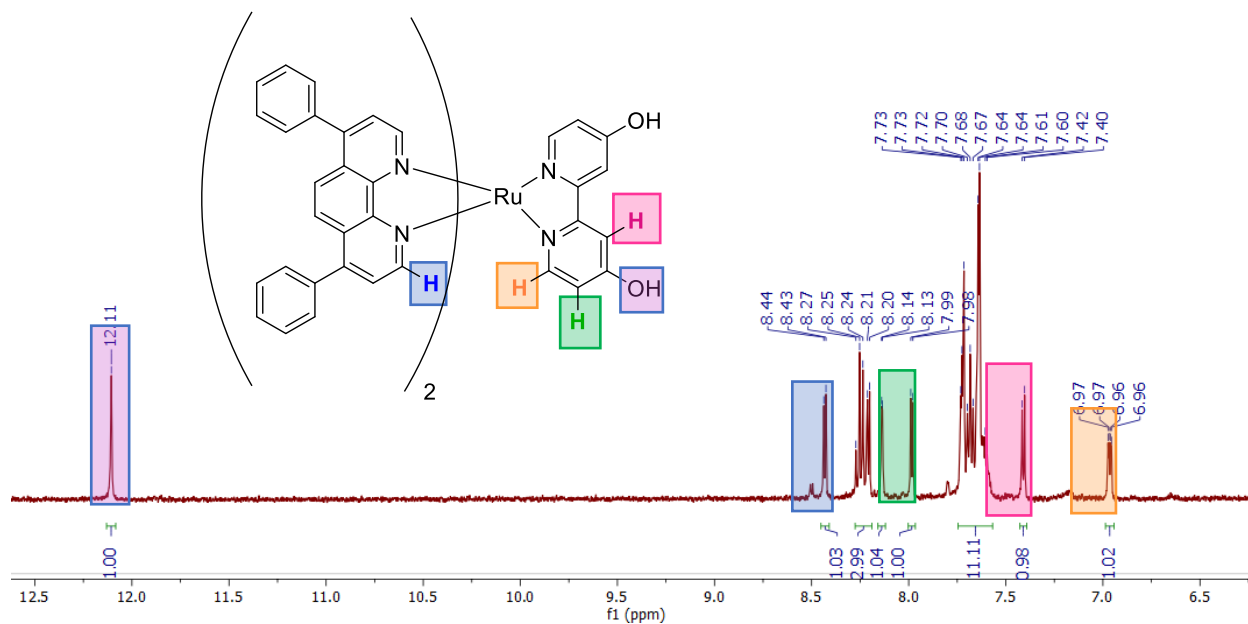


Figure 5.7. ^1H NMR (360 MHz) spectrum of $[(\text{BPhen})_2\text{Ru}(4,4'\text{-dhbp})]\text{Cl}_2$ (**11_A**) in $\text{DMSO-}[d_6]$. Solvent peak omitted for clarity. The given assignments are based off ChemDraw's ^1H NMR simulation software. Significant overlap within the BPhen ligand makes individual assignment difficult.

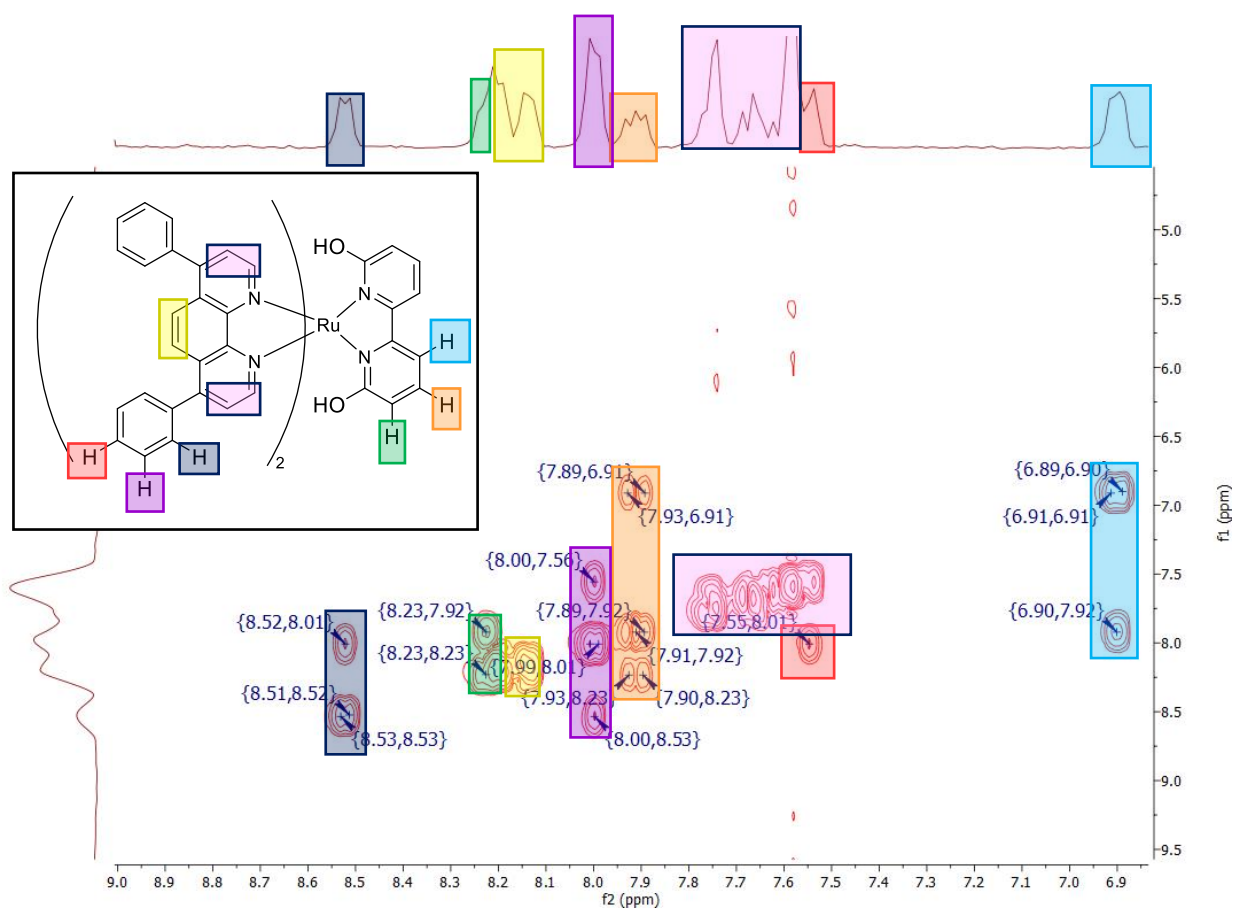


Figure 5.9. 2D COSY ^1H NMR (360 MHz) spectrum of $[(\text{BPhen})_2\text{Ru}(6,6'\text{-dhbp})]\text{Cl}_2$ (**10_A**) in $\text{DMSO-}[d_6]$ with most probable assignments. Solvent peak omitted for clarity.

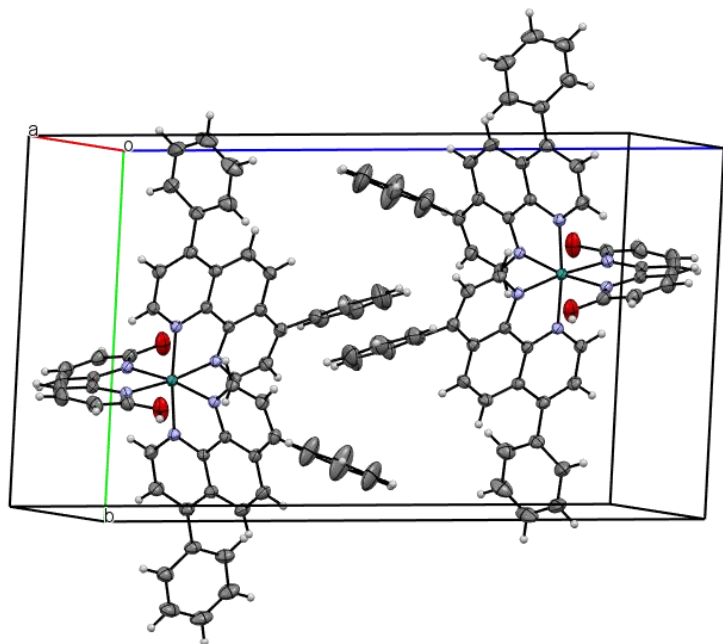


Figure 5.10. X-ray crystal structure of $[(\text{BPhen})_2\text{Ru}(6,6'\text{-dhbp})]^{2+}$ (**10_A**) generated by Ambar Shrestha. Shown is the unit cell as viewed along the *a*-axis. Benzonitrile (which co-crystallized with **10_A**) and chloride counter ions have been removed for clarity.

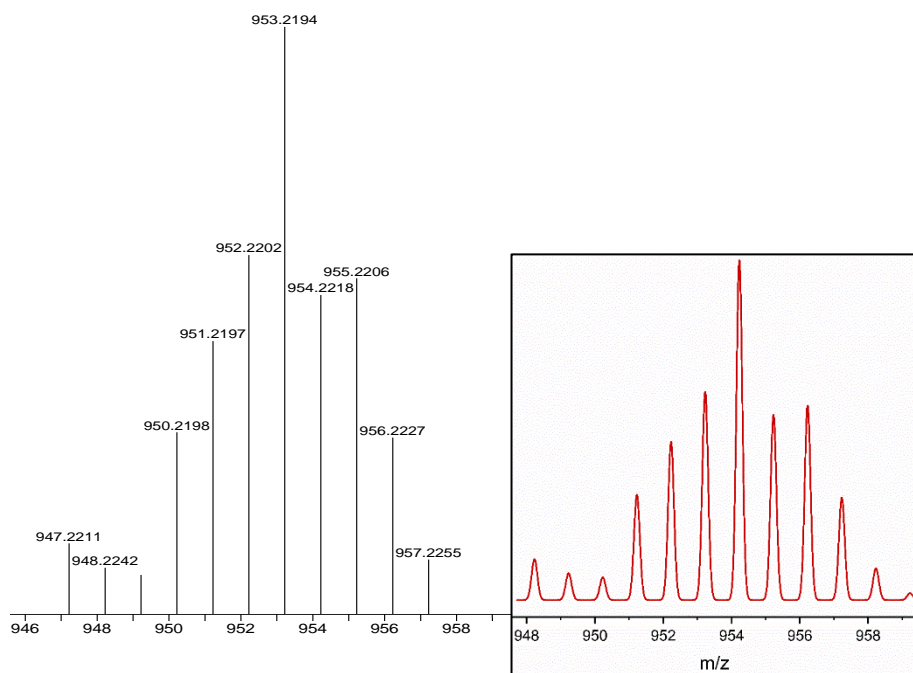


Figure 5.11. Left: ESI-MS of $[(\text{BPhen})_2\text{Ru}(6,6'\text{-dhbp})]^{2+}$ (**10_A**). The peak at m/z 935.2 corresponds to $\text{C}_{58}\text{H}_{40}\text{N}_6\text{O}_2\text{Ru} [\text{M}-\text{H}]^+$ **Right:** Simulated spectra of **10_A** $[\text{M}-\text{H}]^+$

Once synthesized, complexes $[(\text{BPhen})_2\text{Ru}(6,6'\text{-dhbp})]^{2+}$ (**10_A**) and $[(\text{BPhen})_2\text{Ru}(4,4'\text{-dhbp})]^{2+}$ (**11_A**) were sent to collaborators in the Kim group for analysis in cancer cells. Initial screenings at 5 μM yielded promising results for both complexes to warrant full EC_{50} measurements. Compound **10** had $\text{EC}_{50 \text{ light}}$ values as low as 0.82 μM in MDA-MB-231 breast cancer stem cells and a phototoxicity index of 23 (Table 5.1, Figure 5.12). This compound also had toxicity in healthy breast cells (MCF10A) but the toxicity was significantly increased once irradiated. Given past results with similar complexes (complexes studied in the Papish group and other similar published complexes), the likely mode of action for this complex is via a pathway that produces singlet oxygen. $\text{Log}(D_{o/w})$ studies were attempted for this complex, but solubility issues prevented acquisition of a usable measurement (unable to dissolve the complexes in a solvent to make a stock solution for study. Refer to chapter 2 for procedural details). If complex **10** has similar characteristics to other complexes containing 6,6'-dhbp (such as compound **1-3**), **10** may still be able to photodissociate once irradiated, limiting the potential to produce singlet oxygen. Complex **11**; however, incorporates 4,4'-dhbp to limit possible photodissociation. By moving the -OH substituents to the 4,4' positions from the 6,6', steric bulk near the metal center is reduced allowing for better light stability; a characteristic that has also been observed in $[(\text{dop})_2\text{Ru}(4,4'\text{-dhbp})]^{2+}$ (**8_A**, Chapter 4). This is likely why complex **11** had even better toxicity results than **10** (Table 5.1). While $\text{EC}_{50 \text{ light}}$ values are generally comparable to **10** (except in MCF7 for which **11** performed better), complex **11** had significantly better phototoxicity indices. Against cancer cells, **11** had the best performance against MDA-MB-231 breast cancer stem cells ($\text{EC}_{50 \text{ light}} = 0.30 \mu\text{M}$, $\text{PI} = 102$). Against healthy MCF10A cells, **11** had $\text{EC}_{50 \text{ light}}$ values of 0.08 μM but a phototoxicity index of over 470 indicating significant light activated toxicity. Furthermore, compound **11** had PI values of >1600 against MCF7 breast cancer cells. To date,

10 and **11** are the most toxic complexes for this system and exhibit the best PI values. $\text{Log}(D_{o/w})$ have not yet been determined for **11**; however, it is clear that this complex will be more hydrophobic than complexes **1-3**. Studies on these complexes are still ongoing and measurements on singlet oxygen production, photodissociation, and uptake are still required.

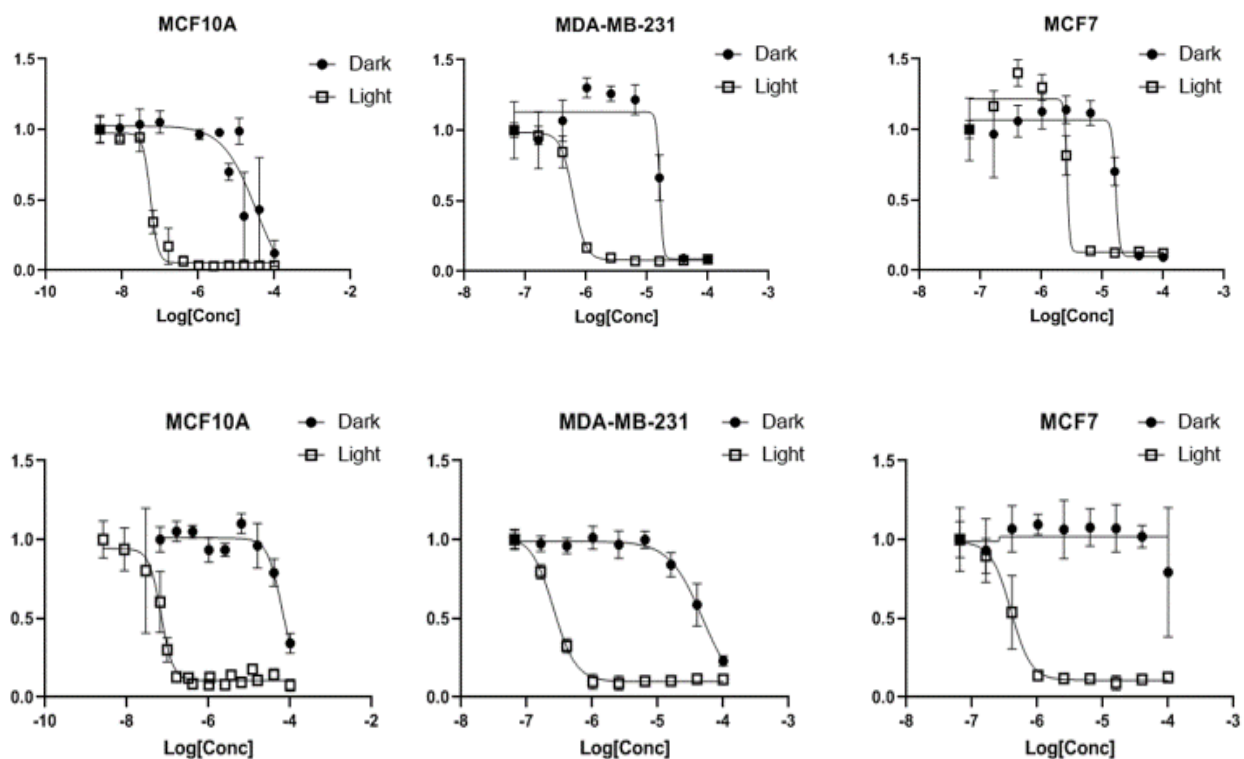


Figure 5.12. Top Row: EC_{50} data plots for complex **10**. Bottom Row: EC_{50} data plots for complex **11**.

Table 5.1 Toxicity data for complexes **10** and **11**. All EC₅₀'s is listed in μM. The phototoxicity index (PI) is a ratio of EC₅₀ dark/EC₅₀ light and indicates light selectivity.

MDA-MB-231 (Breast CSC)				MCF7 (Breast Cancer)		
Compound	EC ₅₀ Dark	EC ₅₀ Light	PI	EC ₅₀ Dark	EC ₅₀ Light	PI
10	19 ± 3	0.82 ± 0.1	23	25 ± 5	3.7 ± 0.6	6.7
11	30 ± 4	0.30 ± 0.03	100	>1000	0.63 ± 1	>1600

MCF10A (Normal)			
Compound	EC ₅₀ Dark	EC ₅₀ Light	PI
10	20 ± 3	0.05 ± 0.004	400
11	38 ± 7	0.08 ± 0.008	475

5.4 Conclusion

In the literature, only a few ruthenium BPS complexes are utilized as anticancer agents, let alone for PDT applications. Unfortunately, the BPS complex (**9**) was determined to be non-toxic (at least EC₅₀ > 5 μM) and appeared to undergo photodissociation and not likely to produce significant amounts of singlet oxygen. More research has been conducted on BPhen anticancer complexes, but most are not light activated. The BPhen complexes, **10** and **11**, not only showed toxicity in the sub-micromolar range but also had significant light activated toxicity. Research on these complexes is still ongoing and data on hydrophobicity, photodissociation, and singlet oxygen production are in progress or planned for future work. These complexes have proven to be better performers than complexes discussed in previous chapters. The data gathered on these complexes may prove useful in developing even more toxic and light selective complexes.

5.5 Materials and Methods

5.5.1 Synthesis of [(BPS)₂RuCl₂]Na₄¹⁶

Synthesis of [(BPS)₂RuCl₂]Na₄ was performed with minimal modification to published procedures. RuCl₃-xH₂O (47.5 mg, 0.182 mmol), BPS-Na₂ (198.3 mg, 0.3599 mmol), and LiCl (38.5 mg, 0.917 mmol) were added to an oven-dried Schlenk flask and purged with nitrogen.

DMF (3 mL, collected from SPS) was transferred into the flask whereupon a condenser was added, and the solution was heated to reflux for 2 h under N₂. After 10 minutes, the solution had changed color from brown/green to dark red. Once complete, the reaction was cooled to room temperature before being transferred into the glovebox. The red solution was then added dropwise to 150 mL stirring acetone to crash out the solid which was collected by vacuum filtration. The solid was washed with Et₂O and dried under vacuum to yield a red solid. Yield 226.4 mg, 0.1605 mmol (88.19 %). Yield was calculated as the nonahydrate, which had been previously published.

5.5.2 Synthesis of [(BPS)₂Ru(6,6'-dhbp)]Na₂ (**9_A**)¹⁶

[(BPS)₂RuCl₂]Na₄ (100 mg, 0.082 mmol) and 6,6-dhbp (19 mg, 0.10 mmol) were added to an oven-dried amber Schlenk flask and purged with nitrogen. 10 mL of degassed EtOH/H₂O (1:1) was cannula transferred into the flask. A condenser was added, and the solution was heated to reflux for 3 hours under N₂. After 3 hours, the flask was cooled to room temperature and dried down via rotary evaporation. The resulting solid was re-dissolved in 2 mL of MeOH and added dropwise to 200 mL rapidly stirring Et₂O to crash out the solid which was then collected by vacuum filtration. Once dry, the solid is then re-dissolved in water then filtered to remove excess dhbp. The filtrate was acidified with 1 mL 5 M HCl before being dried down via rotary evaporation. Yield 49.8 mg, 0.0357 mmol (46.2 %, crude).

5.5.3 Synthesis of *trans*-(BPhen)₂RuCl₂²²

Synthesis of (BPhen)₂RuCl₂ was performed without modification to published procedures. RuCl₃·xH₂O (80.1 mg, 0.306 mmol), BPhen (203 mg, 0.612 mmol), and LiCl (21.2 mg, 0.500 mmol) were added to an oven-dried Schlenk flask and purged with nitrogen. DMF (2

mL, collected from SPS) was transferred into the flask whereupon a condenser was added, and the solution was heated to reflux for 6 hours under N₂. Once complete, the solution was cooled to room temperature before adding 10 mL acetone and the solution was left to precipitate at -20°C for 18 hours. The resulting solid was collected by filtration and washed with cold distilled deionized H₂O (3 x 10 mL) and Et₂O (3 x 10 mL) and dried under vacuum. Typical yield 66 %. ESI-MS C₄₈H₃₂N₄ClRu [M]⁺ m/z = 801.13 (Calculated m/z = 801.14).

5.5.4 Synthesis of [(BPhen)₂Ru(6,6'-dhbp)]Cl₂ (**10**_A) and [(BPhen)₂Ru(4,4'-dhbp)]Cl₂ (**11**_A)⁹

Syntheses of complexes **10**_A and **11**_A were performed with minimal modification to synthesis of complexes **1**_A-**3**_A as reported in *Inorganic Chemistry*, 2017.⁹ The whole process was protected from light, as the final product is sensitive to light. (BPhen)₂RuCl₂ (1 eq) and the dihydroxybipyridine ligand (1.2 eq. **10**: 6,6'-dhbp; **11**: 4,4'-dhbp) were added to an oven dried Schlenk flask and purged with nitrogen. 10 mL of a degassed solution of H₂O/EtOH (1:1) was added by cannula transfer. The solution was heated to reflux for 50 hours for complex **10**_A or 45 hours for complex **11**_A. Once complete the solution was cooled to room temperature before being acidified with 5 M HCl and filtered. For complex **10**_A, the final product can be precipitated out of the filtrate at low temperatures. Complex **11**_A precipitates out of the reaction solution once it is acidified. The isolated red-orange solid was collected, washed with Et₂O, and dried under vacuum. Calculated m/z of [(BPhen)₂Ru(N,N'-dhbp)]⁰ = 952.2.

10_A. Yield: 43.3 %. ESI-MS C₅₈H₃₈N₆O₂Ru [M-H]⁺ m/z = 953.2

11_A. Yield: 65.9 %. ESI-MS C₅₈H₃₈N₆O₂Ru [M-H]⁺ m/z = 953.2

5.5.5 *EC₅₀ Measurements – Kim Group*

MDA-MB-231, MCF7, and MCF10A were seeded at a density of 20,000 cells per well in 100 μ L of media in 96-well plates and incubated for 48 h to adhere to plate. Compounds were dissolved in DMSO and diluted in media to avoid cytotoxic effect from DMSO on cells. Final concentration of DMSO was set to less than 1 % (v/v). Cells were treated with 100 μ L of serially diluted compounds and incubated for 48 h in the dark. After 48 h, cells were washed with Phosphate-buffered saline (PBS 200 μ L x 3) and irradiated for two hours with white light (STASUN 200W LED Flood Light, 100-256V, 20000lm). Cells were then provided with 100 μ L of fresh media per well and incubated in the dark for a total of 24 h. Cytotoxic effects of the compounds were measured using a Cell Counting Kit-8 according to the manufacturer's protocol (Enzo Life Sciences). The EC_{50} of each cell line was determined using a Minitab 17.

References

- [1] Alessio, E. (2017) Thirty Years of the Drug Candidate NAMI-A and the Myths in the Field of Ruthenium Anticancer Compounds: A Personal Perspective, *Eur. J. Inorg. Chem.* 2017, 1549-1560.
- [2] Trondl, R., Heffeter, P., Kowol, C. R., Jakupec, M. A., Berger, W., and Keppler, B. K. (2014) NKP-1339, the first ruthenium-based anticancer drug on the edge to clinical application, *Chem. Sci.* 5, 2925-2932.
- [3] Leijen, S., Burgers, S. A., Baas, P., Pluim, D., Tibben, M., van Werkhoven, E., Alessio, E., Sava, G., Beijnen, J. H., and Schellens, J. H. M. (2015) Phase I/II study with ruthenium compound NAMI-A and gemcitabine in patients with non-small cell lung cancer after first line therapy, *Invest. New Drugs* 33, 201-214.
- [4] Burris, H. A., Bakewell, S., Bendell, J. C., Infante, J., Jones, S. F., Spigel, D. R., Weiss, G. J., Ramanathan, R. K., Ogden, A., and Von Hoff, D. (2016) Safety and activity of IT-139, a ruthenium-based compound, in patients with advanced solid tumours: a first-in-human, open-label, dose-escalation phase I study with expansion cohort, *ESMO Open* 1., e000154.
- [5] Monro, S., Colón, K. L., Yin, H., Roque, J., Konda, P., Gujar, S., Thummel, R. P., Lilge, L., Cameron, C. G., and McFarland, S. A. (2019) Transition Metal Complexes and Photodynamic Therapy from a Tumor-Centered Approach: Challenges, Opportunities, and Highlights from the Development of TLD1433, *Chem. Rev.* 119, 797-828.
- [6] McFarland, S. A., Mandel, A., Dumoulin-White, R., and Gasser, G. (2020) Metal-based photosensitizers for photodynamic therapy: the future of multimodal oncology?, *Curr. Opin. Chem. Biol.* 56, 23-27.
- [7] White, J. K., Schmechl, R. H., and Turro, C. (2017) An overview of photosubstitution reactions of Ru(II) imine complexes and their application in photobiology and photodynamic therapy, *Inorg. Chim. Acta* 454, 7-20.
- [8] Hufziger, K. T., Thowfeik, F. S., Charboneau, D. J., Nieto, I., Dougherty, W. G., Kassel, W. S., Dudley, T. J., Merino, E. J., Papish, E. T., and Paul, J. J. (2014) Ruthenium dihydroxybipyridine complexes are tumor activated prodrugs due to low pH and blue light induced ligand release, *J. Inorg. Biochem.* 130, 103-111.
- [9] Qu, F., Park, S., Martinez, K., Gray, J. L., Thowfeik, F. S., Lundeen, J. A., Kuhn, A. E., Charboneau, D. J., Gerlach, D. L., Lockart, M. M., Law, J. A., Jernigan, K. L., Chambers,

- N., Zeller, M., Piro, N. A., Kassel, W. S., Schmehl, R. H., Paul, J. J., Merino, E. J., Kim, Y., and Papish, E. T. (2017) Ruthenium Complexes are pH-Activated Metallo Prodrugs (pHAMPs) with Light-Triggered Selective Toxicity Toward Cancer Cells, *Inorg. Chem.* *56*, 7519-7532.
- [10] Qu, F., Martinez, K., Arcidiacono, A. M., Park, S., Zeller, M., Schmehl, R. H., Paul, J. J., Kim, Y., and Papish, E. T. (2018) Sterically demanding methoxy and methyl groups in ruthenium complexes lead to enhanced quantum yields for blue light triggered photodissociation, *Dalton Trans.* *47*, 15685-15693.
- [11] Park, S., Gray, J. L., Altman, S. D., Hairston, A. R., Beswick, B. T., Kim, Y., and Papish, E. T. (2020) Cellular uptake of protic ruthenium complexes is influenced by pH dependent passive diffusion and energy dependent efflux, *J. Inorg. Biochem.* *203*, 110922.
- [12] Dickerson, M., Sun, Y., Howerton, B., and Glazer, E. C. (2014) Modifying Charge and Hydrophilicity of Simple Ru(II) Polypyridyl Complexes Radically Alters Biological Activities: Old Complexes, Surprising New Tricks, *Inorg. Chem.* *53*, 10370-10377.
- [13] Anuja, P. K., and Paira, P. (2020) Luminescent anticancer Ru(II)-arenebipyridine and phenanthroline complexes: Synthesis, characterization, DFT studies, biological interactions and cellular imaging application, *J. Inorg. Biochem.* *208*, 111099.
- [14] Babak, M. V., Le Faouder, P., Trivelli, X., Venkatesan, G., Bezzubov, S. I., Kadjout, M., Gushchin, A. L., Hanif, M., Poizat, O., Vezin, H., and Rolando, C. (2020) Heteroleptic Ruthenium(II) Complexes with Bathophenanthroline and Bathophenanthroline Disulfonate Disodium Salt as Fluorescent Dyes for In-Gel Protein Staining, *Inorg. Chem.* *59*, 4527-4535.
- [15] Rabilloud, T., Strub, J.-M., Luche, S., Van Dorselaer, A., and Lunardi, J. (2001) A comparison between sypro ruby and ruthenium II tris (batho-phenanthroline disulfonate) as fluorescent stains for protein detection in gels, *Proteomics* *1*, 699-704.
- [16] Della Ciana, L., Zanarini, S., Perciaccante, R., Marzocchi, E., and Valenti, G. (2010) Neutral and Dianionic Ru(II) Bathophenanthroline disulfonate Complexes: A Route To Enhance Electrochemiluminescence Performance in Aqueous Media, *J. Phys. Chem. C* *114*, 3653-3658.
- [17] Karges, J., Blacque, O., Jakubaszek, M., Goud, B., Goldner, P., and Gasser, G. (2019) Systematic investigation of the antiproliferative activity of a series of ruthenium terpyridine complexes, *J. Inorg. Biochem.* *198*, 110752.
- [18] Munteanu, A.-C., Notaro, A., Jakubaszek, M., Cowell, J., Tharaud, M., Goud, B., Uivarosi, V., and Gasser, G. (2020) Synthesis, Characterization, Cytotoxic Activity, and Metabolic Studies of Ruthenium(II) Polypyridyl Complexes Containing Flavonoid Ligands, *Inorg. Chem.* *59*, 4424-4434.

- [19] Notaro, A., Jakubaszek, M., Rotthowe, N., Maschietto, F., Vinck, R., Felder, P. S., Goud, B., Tharaud, M., Ciofini, I., Bedioui, F., Winter, R. F., and Gasser, G. (2020) Increasing the Cytotoxicity of Ru(II) Polypyridyl Complexes by Tuning the Electronic Structure of Dioxo Ligands, *J. Am. Chem. Soc.* *142*, 6066-6084.
- [20] Puckett, C. A., and Barton, J. K. (2008) Mechanism of Cellular Uptake of a Ruthenium Polypyridyl Complex, *Biochemistry* *47*, 11711-11716.
- [21] Karges, J., Heinemann, F., Jakubaszek, M., Maschietto, F., Subecz, C., Dotou, M., Vinck, R., Blacque, O., Tharaud, M., Goud, B., Vinuelas Zahinos, E., Spingler, B., Ciofini, I., and Gasser, G. (2020) Rationally Designed Long-Wavelength Absorbing Ru(II) Polypyridyl Complexes as Photosensitizers for Photodynamic Therapy, *J. Am. Chem. Soc.* *142*, 6578-6587.
- [22] Al-Rawashdeh, N. A. F., Chatterjee, S., Krause, J. A., and Connick, W. B. (2014) Ruthenium Bis-diimine Complexes with a Chelating Thioether Ligand: Delineating 1,10-Phenanthrolyl and 2,2'-Bipyridyl Ligand Substituent Effects, *Inorg. Chem.* *53*, 294-307.

CHAPTER 6

CRYSTAL STRUCTURE OF (PERCHLORATO- κ O)(1,4,7,10-TETRAAZACYCLODODECANE- κ^4 N)COPPER(II) PERCHLORATE

Adapted from: Gray, Jessica L.; Gerlach, Deidra L.; Papish, Elizabeth T., *Acta Cryst.*, **2017**, *E73*, 31-34

6.1 Abstract

The crystal structure of the title salt, [Cu(ClO₄)(C₈H₂₀N₄)]ClO₄, is reported. The Cu(II) ion exhibits a square-pyramidal geometry and is coordinated by the four N atoms of the neutral 1,4,7,10-tetraazacyclododecane (cyclen) ligand and an O atom from one perchlorate anion, with the second perchlorate ion hydrogen-bonded to one of the amine N atoms of the cyclen ligand. Additional N—H···O hydrogen bonds between the amine H atoms and the coordinating and non-coordinating perchlorate groups create a three-dimensional network structure. Crystals were grown from a concentrated methanol solution at ambient temperature, resulting in no co-crystallization of solvent.

6.2 Chemical Context

Azamacrocyclic ligands, including 1,4,7,10-tetraazacyclododecane (cyclen), are of significant importance in research due to their ability to form stable metal complexes, allowing for their use in a wide range of applications. Some of these complexes have been studied for their use as chemical sensors, contrast agents in MRI and PET, antimicrobial agents and as biomimetic catalysts.^{1, 2} Copper–cyclen complexes have been studied extensively for their ability

to perform catalytic DNA cleavage and peptide hydrolysis.³⁻⁵ Although the synthesis of a similar Cu(II) complex has been reported previously, no crystal structure of the complex, [Cu(1,4,7,10-tetraazacyclododecane)](ClO₄)₂ (Figure 6.1), has previously been published.⁶

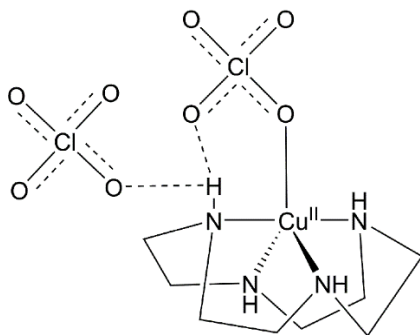


Figure 6.1 Chemdraw figure of [Cu(1,4,7,10-tetraazacyclododecane)](ClO₄)₂.

6.3 Structural Commentary

In the title complex (Figures 6.1 & 6.2), the copper(II) ion coordinated by the four nitrogen atoms of the cyclen ligand and one oxygen atom of a perchlorate ligand. The five-coordinate cupric ion shows a nearly ideal square-pyramidal geometry ($\tau_5 = 0.049$; Addison et al., 1984).⁷ The Cu—N bond lengths range from 2.004(1) to 2.015(1) Å, which are typical values. The Cu(II) ion exhibits a tetragonal distortion that leads to a longer apical bond with Cu1—O1 = 2.266(1) Å, which is 0.12 Å longer than the average Cu—O distance.^{8,9} The average N—Cu—O bond angle is 103.8(8)°. Three hydrogen bonds are present within the asymmetric unit, with two extending from O2 and O3 of the bound perchlorate anion to N1—H1 and N2—H2, respectively. The third hydrogen bond extends from N2—H2 to O8 of the unbound anion; the numerical details are given in Table 6.1.

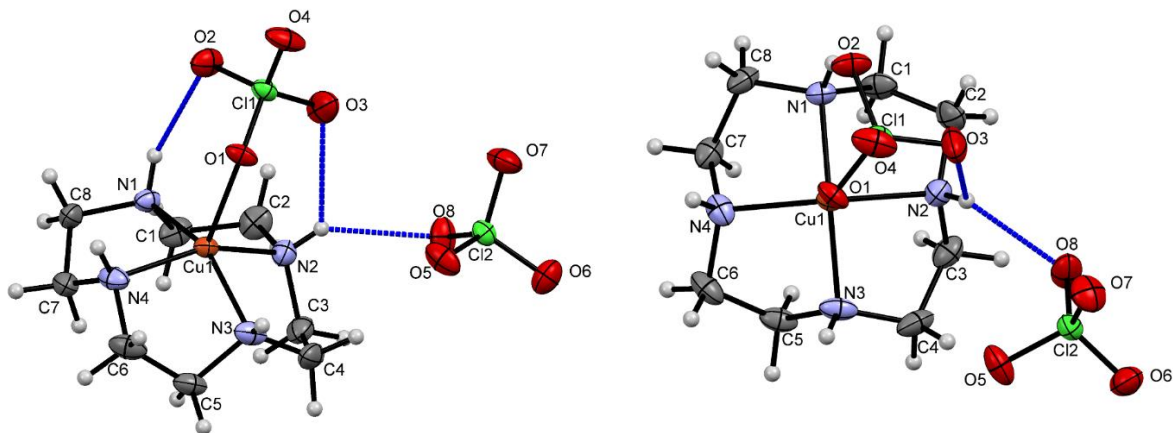


Figure 6.2. Side (left) and top (right) views, as defined by the cyclen ligand ring, of $[\text{Cu}(\text{cyclen})](\text{ClO}_4)_2$ represented with ellipsoids at the 50 % probability level. Hydrogen bonds are drawn in blue.

6.4 Supramolecular Features

The crystal structure exhibits three unique symmetry elements: an inversion center, a twofold screw axis and a glide plane. The complex cations of two asymmetric units hydrogen-bond across an inversion center, which is clearly visible when viewed along the a axis (Figure 6.3), creating a dimer. These hydrogen bonds ($\text{N3}\cdots\text{H3}\cdots\text{O1}$, $\text{N3}\cdots\text{H3}\cdots\text{O4}$, $\text{N4}\cdots\text{H4}\cdots\text{O5}$) have an average $\text{N}\cdots\text{O}$ distance of 3.16 Å (Figure 6.4). The complexes assemble in rows parallel to the b axis (Figure 6.5) due in part to weak electrostatic interactions between the bound perchlorate anion and a neighboring cyclen ligand. A hydrogen bond between the cyclen ligand and a neighboring perchlorate anion ($\text{N1}\cdots\text{H1}\cdots\text{O3}$) allows the building units to assemble parallel to the a axis (Figure 6.6).

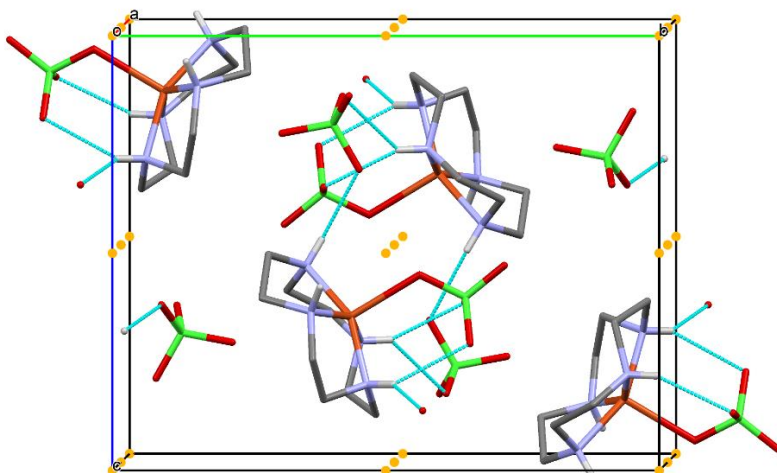


Figure 6.3 View of the unit cell along the a axis. An inversion center (yellow dots) exists between two asymmetric units, creating the dimeric unit defined at the center of the unit cell. Hydrogen bonds are drawn in blue.

Table 6.1 Hydrogen-bond geometry (\AA° , $^\circ$)

D—H...A	D—H	H...A	D...A	D—H...A
N1—H1...O6 ⁱ	0.86(1)	2.50(2)	3.171(1)	135(1)
N1—H1...O2	0.86(1)	2.39(1)	3.093(1)	139(1)
N2—H2...O8 ⁱⁱ	0.88(2)	2.31(2)	3.050(1)	142(1)
N2—H2...O3	0.88(2)	2.44(2)	3.052(2)	127(1)
N3—H3...O1 ⁱⁱ	0.86(2)	2.40(1)	3.245(1)	169(2)
N3—H3...O4 ⁱⁱ	0.86(2)	2.55(2)	3.132(1)	126(1)
N4—H4...O5	0.86(2)	2.36(1)	3.096(1)	143(1)

Symmetry codes: (i) $-x+1, -y+1, -z+1$; (ii) $-x, -y+1, -z+1$.

6.5 Database Survey

A database survey resulted in several similar Cu–cyclen complexes with five-coordinate copper(II). Four structures chosen for further analysis contained a copper(II) ion coordinated by either five nitrogen atoms or four nitrogen atoms and one oxygen atom.⁹⁻¹² Where applicable, the complexes have similar Cu—O bond lengths to that of the title complex, with only slight deviations. The title complex and surveyed complexes have similar Cu—N distances with a standard deviation of 0.018 \AA .

6.6 Synthesis and Crystallization

The title complex was synthesized by a modified method as reported by Kruppa *et al.*⁶ Under a nitrogen atmosphere, 1,4,7,10-tetraazacyclododecane (247 mg, 1.40 mmol) and copper(II) perchlorate hexahydrate (527 mg, 1.40 mmol) were separately dissolved in 2.8 mL anhydrous methanol each and combined. The resulting purple solution formed a precipitate. The reaction mixture was heated to reflux for 30 minutes then filtered. The filtrate was evaporated to dryness to yield a purple amorphous solid. X-ray quality crystals were grown by dissolving the solid in a minimum amount of methanol followed by slow evaporation at ambient temperature. The title complex $[\text{Cu}(\text{cyclen})](\text{ClO}_4)_2$ was isolated as purple crystals in 84 % yield (1.20 mmol, 526 mg). IR [ATR, ν (cm^{-1})]: 3281, 2939, 1478, 1072, 617. MS (MALDI–ToF, MeOH): $m/z = 334.2$ $[\text{Cu}(\text{cyclen})^{2+} + \text{ClO}_4^-]^-$ (Calculated $[\text{C}_8\text{H}_{20}\text{N}_4\text{CuClO}_4]^-$ $m/z = 334.1$).

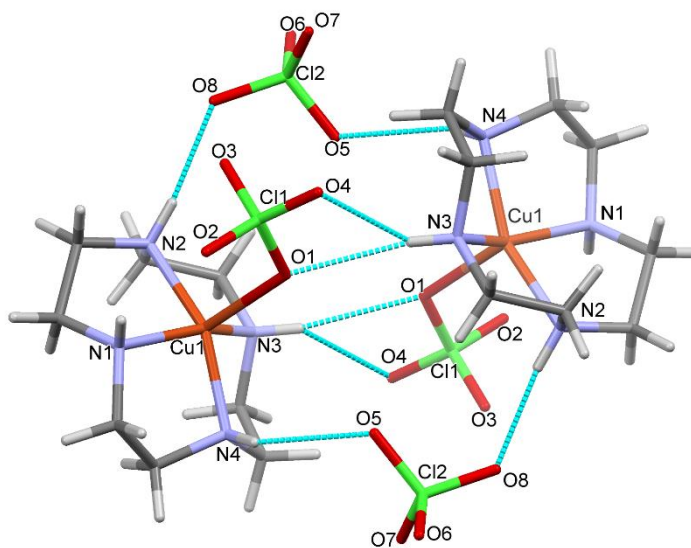


Figure 6.4 A view of hydrogen bonding within a dimer pair. Hydrogen bonds are drawn in blue. Carbon and hydrogen atom labels have been omitted for clarity.

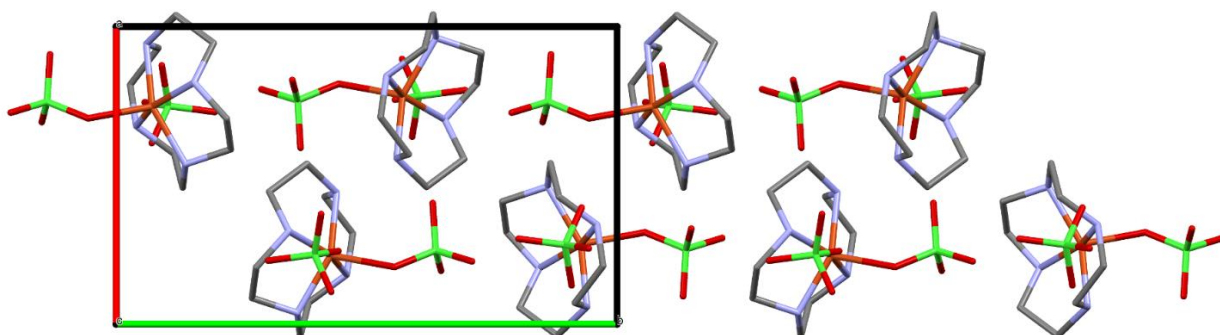


Figure 6.5 Packing of the complex cations, as viewed along the *c* axis of the unit cell. The *a* axis is drawn in red and the *b* axis is drawn in green.

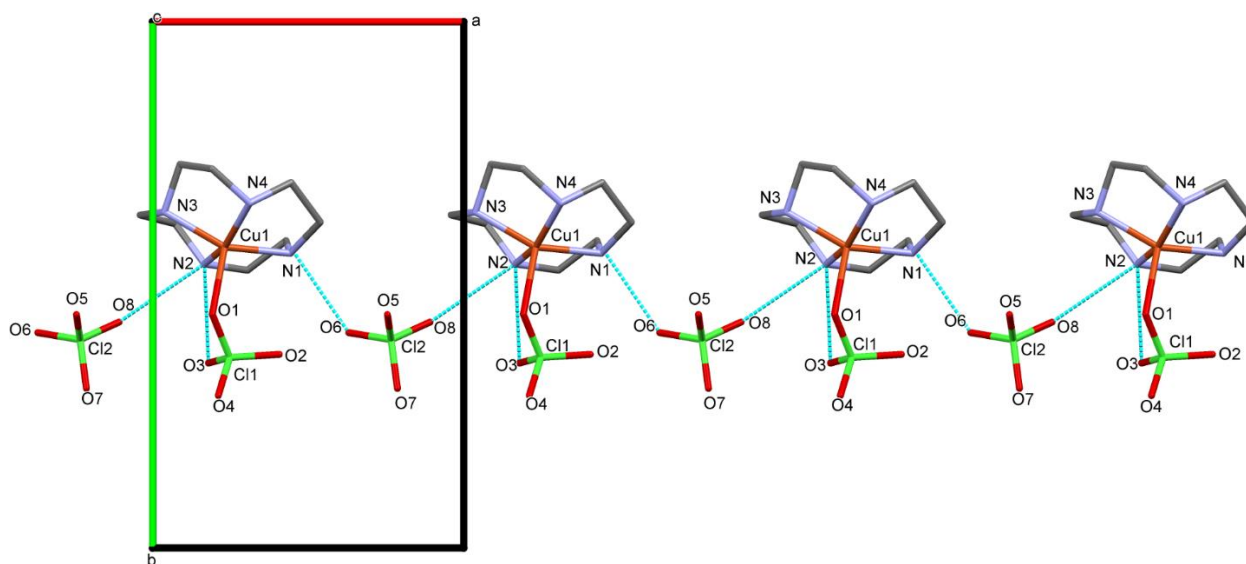


Figure 6.6 Hydrogen bonding between complex cations and anions, as viewed along the *c* axis. Hydrogen bonds are drawn in blue. The *a* axis is drawn in red and the *b* is drawn in green.

Table 6.2 Experimental Details

Crystal Data	
Chemical formula	[Cu(ClO ₄)(C ₈ H ₂₀ N ₄)]ClO ₄
M_r	434.72
Crystal system, space group	Monoclinic, $P2_1/n$
Temperature (K)	173
a, b, c (Å)	8.9387(2), 15.0607(4), 11.9235(3)
β (°)	92.949 (1)
V (Å ³)	1603.05 (7)
Z	4
Radiation type	Mo $K\alpha$
μ (mm ⁻¹)	1.74
Crystal size (mm)	0.23 × 0.21 × 0.18
Data collection	
Diffractometer	Bruker SMART APEXII CCD
Absorption correction	Multi-scan (SADABS; Sheldrick, 2014) ¹³
T_{\min}, T_{\max}	0.667, 0.747
No. of measured, independent and observed [$I > 2\sigma(I)$] reflections	43306, 7519, 6655
R_{int}	0.021
$(\sin \theta/\lambda)_{\text{max}}$ (Å ⁻¹)	0.830
Refinement	
$R[F^2 > 2\sigma(F^2)], wR(F^2), S$	0.025, 0.068, 1.02
No. of reflections	7519
No. of parameters	221
No. of restraints	6
H-atom treatment	H atoms treated by a mixture of independent and constrained refinement
$\Delta\rho_{\text{max}}, \Delta\rho_{\text{min}}$ (e Å ⁻³)	0.60, -0.44

Computer programs: APEX2 and SAINT-Plus (Bruker, 2013),¹⁴ SHELXT (Sheldrick, 2008),¹⁵ SHELXL2014 (Sheldrick, 2015)¹⁵ and SHELXLE (Hübschle *et al.*, 2011).¹⁶

6.7 Refinement

Crystal data, data collection and structure refinement details are summarized in Table 6.2.

H atoms attached to carbon were positioned geometrically and constrained to ride on their parent

atoms. The H atoms attached to nitrogen were located in a difference map and restrained to have comparable bond lengths. $U_{\text{iso}}(\text{H})$ values were set to $1.2U_{\text{eq}}(\text{C/N})$.

Acknowledgements

Special thanks to The University of Alabama Department of Chemistry for funding and facilities. We also thank the Undergraduate Creativity and Research Academy (UCRA) at UA, the Research Grants Committee (RGC) at UA, and acknowledge the NSF EPSCoR Track 2 Seed Grant to ETP (PI N. Hammer, grant No. OIA-1539035) for generous financial support.

References

- [1] De Leon-Rodriguez, L. M., Viswanathan, S., and Sherry, A. D. (2010) Improved synthesis of DOTA tetraamide ligands for lanthanide(III) ions: a tool for increasing the repertoire of potential PARACEST contrast agents for MRI and/or fluorescent sensors, *Contrast Media Mol. Imaging* 5, 121-125.
- [2] Yoo, S. H., Lee, B. J., Kim, H., and Suh, J. (2005) Artificial Metalloprotease with Active Site Comprising Aldehyde Group and Cu(II)Cyclen Complex, *J. Am. Chem. Soc.* 127, 9593-9602.
- [3] Zhang, X., Liu, X., Phillips, D. L., and Zhao, C. (2016) Mechanistic Insights Into the Factors That Influence the DNA Nuclease Activity of Mononuclear Facial Copper Complexes Containing Hetero-Substituted Cyclens, *ACS Catal.* 6, 248-257.
- [4] Li, S., Chen, J.-X., Xiang, Q.-X., Zhang, L.-Q., Zhou, C.-H., Xie, J.-Q., Yu, L., and Li, F.-Z. (2014) The synthesis and activities of novel mononuclear or dinuclear cyclen complexes bearing azole pendants as antibacterial and antifungal agents, *European Journal of Medicinal Chemistry* 84, 677-686.
- [5] Hormann, J., Perera, C., Deibel, N., Lentz, D., Sarkar, B., and Kulak, N. (2013) Straightforward approach to efficient oxidative DNA cleaving agents based on Cu(II) complexes of heterosubstituted cyclens, *Dalton Trans.* 42, 4357-4360.
- [6] Kruppa, M., Frank, D., Leffler-Schuster, H., and König, B. (2006) Screening of metal complex–amino acid side chain interactions by potentiometric titration, *Inorganica Chim. Acta* 359, 1159-1168.
- [7] Addison, A. W., Rao, T. N., Reedijk, J., Van Rijn, J., and Verschoor, G. C. (1984) Synthesis, structure, and spectroscopic properties of copper(II) compounds containing nitrogen-sulfur donor ligands: the crystal and molecular structure of aqua[1,7-bis(N-methylbenzimidazol-2'-yl)-2,6-dithiaheptane]copper(II) perchlorate, *J. Chem. Soc., Dalton Trans.*, 1349-1356.
- [8] Clay, R., Murray-Rust, P., and Murray-Rust, J. (1979) Nitrate(1,4,7,10-tetraazacyclododecane)copper(II) nitrate, *Acta Crystallogr., Sect. B* B35, 1894-1895.
- [9] Rohde, D., and Merzweiler, K. (2010) (1,4,7,10-Tetraazacyclododecane-κ4N1,N4,N7,N10)(tetraoxidomolybdato-κO)copper(II) monohydrate, *Acta Crystallogr., Sect. E: Struct. Rep. Online* 66, m894.

- [10] Sarma, M., Chatterjee, T., and Das, S. K. (2010) A copper-cyclen coordination complex associated with a polyoxometalate anion: Synthesis, crystal structure and electrochemistry of [Cu(cyclen)(MeCN)][W₆O₁₉], *Inorg. Chem. Commun.* *13*, 1114-1117.
- [11] Perez-Toro, I., Dominguez-Martin, A., Choquesillo-Lazarte, D., Vilchez-Rodriguez, E., Gonzalez-Perez, J. M., Castineiras, A., and Niclos-Gutierrez, J. (2015) Lights and shadows in the challenge of binding acyclovir, a synthetic purine-like nucleoside with antiviral activity, at an apical-distal coordination site in copper(II)-polyamine chelates, *J. Inorg. Biochem.* *148*, 84-92.
- [12] Guo, J.-F., Yeung, W.-F., Gao, S., Lee, G.-H., Peng, S.-M., Lam, M. H.-W., and Lau, T.-C. (2008) Coordination polymers constructed from [Mn(N)(CN)₄]²⁻: synthesis, structures, and magnetic properties, *Eur. J. Inorg. Chem.*, 158-163.
- [13] Sheldrick, G. M. (2014) SADABS, University of Göttingen, Germany.
- [14] Bruker. (2013) SAINT-Plus and APEX2, Bruker AXS Inc., Madison, Wisconsin, USA.
- [15] Sheldrick, G. M. (2008) A short history of SHELX, *Acta Crystallogr., Sect. A: Found. Crystallogr.* *64*, 112-122.
- [16] Hübschle, C. B., Sheldrick, G. M., and Dittrich, B. (2011) ShelXle: a Qt graphical user interface for SHELXL, *J. Appl. Crystallogr.* *44*, 1281-1284.
- [17] Sheldrick, G. M. (2015) Crystal structure refinement with SHELXL, *Acta Crystallogr., Sect. C: Struct. Chem.* *71*, 3-8.

6A. Appendix

6A.1 Computing Details

Data collection: APEX2 (Bruker, 2013)¹⁴; cell refinement: SAINT-Plus (Bruker, 2013)¹⁴; data reduction: SAINT-Plus (Bruker, 2013)¹⁴; program(s) used to solve structure: SHELXT (Sheldrick, 2008)¹⁵; program(s) used to refine structure: SHELXL2014 (Sheldrick, 2015)¹⁷ and SHELXLE (Hübschle et al., 2011).¹⁶

6A.2 Special Details

Geometry: All esds (except the esd in the dihedral angle between two l.s. planes) are estimated using the full covariance matrix. The cell esds are taken into account individually in the estimation of esds in distances, angles and torsion angles; correlations between esds in cell parameters are only used when they are defined by crystal symmetry. An approximate (isotropic) treatment of cell esds is used for estimating esds involving l.s. planes.

Table 6A.1 Crystal Data

[Cu(ClO ₄)(C ₈ H ₂₀ N ₄)]ClO ₄	$F(000) = 892$
Mr = 434.72	Dx = 1.801 Mg m ⁻³
Monoclinic, $P2_1/n$	Mo $K\alpha$ radiation, $\lambda = 0.71073 \text{ \AA}$
$a = 8.9387(2) \text{ \AA}$	Cell parameters from 9899 reflections
$b = 15.0607(4) \text{ \AA}$	$\theta = 2.3\text{--}35.9^\circ$
$c = 11.9235(3) \text{ \AA}$	$\mu = 1.74 \text{ mm}^{-1}$
$\beta = 92.949(1)^\circ$	$T = 173 \text{ K}$
$V = 1603.05(7) \text{ \AA}^3$	Block, purple
$Z = 4$	$0.23 \times 0.21 \times 0.18 \text{ mm}$

Table 6A.2 Data Collection

Bruker SMART APEXII CCD Diffractometer	6655 reflections with $I > 2\sigma(I)$
Radiation source: fine focus sealed tube	$R_{\text{int}} = 0.021$
phi and ω scans	$\theta_{\text{max}} = 36.2^\circ$, $\theta_{\text{min}} = 2.2^\circ$
Absorption correction: multi-scan (SADABS; Sheldrick, 2014) ¹³	$h = -14 \rightarrow 13$
$T_{\text{min}} = 0.667$, $T_{\text{max}} = 0.747$	$k = -24 \rightarrow 24$
43306 measured reflections	$l = -19 \rightarrow 12$
7519 independent reflections	

Table 6A.3 Refinement

Refinement on F^2	Secondary atom site location: difference Fourier map
Least-squares matrix: full	Hydrogen site location: mixed
$R[F^2 > 2\sigma(F^2)] = 0.025$	H atoms treated by a mixture of independent and constrained refinement
$wR(F^2) = 0.068$	$w = 1/[\sigma^2(F_o^2) + (0.0357P)^2 + 0.4526P]$ where $P = (F_o^2 + 2F_c^2)/3$
$S = 1.02$	$(\Delta/\sigma)_{\text{max}} = 0.003$
7519 reflections	$\Delta\rho_{\text{max}} = 0.60 \text{ e } \text{\AA}^{-3}$
221 parameters	$\Delta\rho_{\text{min}} = -0.44 \text{ e } \text{\AA}^{-3}$
6 restraints	Extinction correction: SHELXL2014 (Sheldrick, 2015) ¹⁷ , $\text{Fc}^* = k\text{Fc}[1 + 0.001x\text{Fc}^2\lambda^3/\sin(2\theta)]^{-1/4}$
Primary atom site location: structure-invariant direct methods	Extinction coefficient: 0.0025(3)

Table 6A.4 Fractional atomic coordinates and isotropic or equivalent isotropic displacement parameters (\AA^2)

	x	y	z	$U_{\text{iso}}^*/U_{\text{eq}}$
C1	0.42855(13)	0.41595(9)	0.83806(10)	0.0315(2)
H1A	0.524	0.4277	0.8813	0.038*
H1B	0.4043	0.3521	0.845	0.038*
C2	0.30439(15)	0.47211(10)	0.88238(9)	0.0341(2)
H2A	0.285	0.454	0.9601	0.041*
H2B	0.3344	0.5354	0.8835	0.041*
C3	0.07219(14)	0.38402(9)	0.83922(11)	0.0330(2)

H3A	0.0198	0.3977	0.9083	0.040*
H3B	0.1353	0.3308	0.8533	0.040*
C4	-0.04050(12)	0.36717(8)	0.74254(13)	0.0353(3)
H4A	-0.0945	0.311	0.7554	0.042*
H4B	-0.1148	0.416	0.7378	0.042*
C5	0.08786(13)	0.27094(7)	0.60632(10)	0.0297(2)
H5A	0.0006	0.2334	0.5836	0.036*
H5B	0.1415	0.2431	0.672	0.036*
C6	0.19107(16)	0.27947(8)	0.51035(10)	0.0345(2)
H6A	0.2356	0.2209	0.4943	0.041*
H6B	0.1335	0.2998	0.442	0.041*
C7	0.44486(13)	0.30541(7)	0.60226(11)	0.0302(2)
H7A	0.5046	0.2707	0.55	0.036*
H7B	0.4126	0.2651	0.662	0.036*
C8	0.53867(12)	0.38048(8)	0.65356(12)	0.0315(2)
H8A	0.6201	0.3558	0.7037	0.038*
H8B	0.5847	0.4147	0.5934	0.038*
H1	0.4734(19)	0.4937(9)	0.7172(14)	0.038*
H2	0.1146(18)	0.5097(10)	0.8063(14)	0.038*
H3	-0.0155(19)	0.3802(12)	0.5781(13)	0.038*
H4	0.3389(19)	0.3719(11)	0.4820(12)	0.038*
N1	0.44205(10)	0.43993(6)	0.71871(8)	0.02310(15)
N2	0.16614(10)	0.46012(7)	0.80849(8)	0.02595(16)
N3	0.03746(11)	0.36146(6)	0.63546(9)	0.02866(19)
N4	0.31208(12)	0.34444(6)	0.54087(8)	0.02774(18)
O1	0.19181(10)	0.55583(5)	0.55695(6)	0.02513(14)
O2	0.40695(9)	0.63197(6)	0.62923(8)	0.03461(19)
O3	0.17927(13)	0.64843(8)	0.71488(9)	0.0461(3)
O4	0.21084(11)	0.71021(6)	0.53609(9)	0.0388(2)
O5	0.24547(13)	0.44353(6)	0.31635(7)	0.0375(2)
O6	0.36978(11)	0.40926(8)	0.15317(8)	0.0381(2)
O7	0.21333(13)	0.30342(6)	0.23229(9)	0.0411(2)
O8	0.10864(11)	0.42926(7)	0.14227(8)	0.0380(2)
Cl1	0.24776(3)	0.63777(2)	0.61025(2)	0.02082(4)
Cl2	0.23354(3)	0.39588(2)	0.21099(2)	0.02216(5)
Cu1	0.23119(2)	0.42802(2)	0.65438(2)	0.01773(3)

Table 6A.5 Atomic Displacement Parameters (\AA^2)

	U^{11}	U^{22}	U^{33}	U^{12}	U^{13}	U^{23}
C1	0.0265(5)	0.0390(6)	0.0278(5)	-0.0022(4)	-0.0100(4)	0.0095(4)
C2	0.0368(6)	0.0465(7)	0.0184(4)	-0.0037(5)	-0.0038(4)	-0.0015(4)
C3	0.0296(5)	0.0328(5)	0.0375(6)	0.0004(4)	0.0110(4)	0.0077(4)
C4	0.0176(4)	0.0285(5)	0.0600(8)	-0.0005(4)	0.0049(5)	0.0049(5)
C5	0.0299(5)	0.0191(4)	0.0386(5)	-0.0049(3)	-0.0117(4)	0.0052(4)
C6	0.0523(7)	0.0237(5)	0.0266(5)	-0.0087(5)	-0.0064(5)	-0.0022(4)
C7	0.0307(5)	0.0206(4)	0.0402(6)	0.0008(4)	0.0099(4)	0.0013(4)
C8	0.0199(4)	0.0252(5)	0.0501(7)	-0.0006(3)	0.0081(4)	0.0014(4)
N1	0.0190(3)	0.0217(3)	0.0282(4)	-0.0023(3)	-0.0021(3)	0.0033(3)
N2	0.0241(4)	0.0280(4)	0.0259(4)	0.0011(3)	0.0030(3)	0.0013(3)
N3	0.0236(4)	0.0208(4)	0.0400(5)	-0.0022(3)	-0.0134(3)	0.0065(3)
N4	0.0403(5)	0.0208(4)	0.0224(4)	-0.0040(3)	0.0032(3)	0.0018(3)
O1	0.0361(4)	0.0155(3)	0.0227(3)	-0.0025(3)	-0.0091(3)	-0.0012(2)
O2	0.0213(4)	0.0348(4)	0.0466(5)	-0.0019(3)	-0.0095(3)	0.0080(4)
O3	0.0542(6)	0.0452(6)	0.0408(5)	-0.0136(5)	0.0192(4)	-0.0216(4)
O4	0.0420(5)	0.0181(3)	0.0538(5)	-0.0016(3)	-0.0219(4)	0.0084(3)
O5	0.0614(6)	0.0281(4)	0.0222(3)	0.0054(4)	-0.0054(4)	-0.0058(3)
O6	0.0258(4)	0.0516(6)	0.0371(4)	-0.0021(4)	0.0033(3)	0.0019(4)
O7	0.0536(6)	0.0203(4)	0.0493(5)	-0.0032(4)	0.0031(5)	-0.0015(4)
O8	0.0302(4)	0.0538(6)	0.0295(4)	0.0164(4)	-0.0042(3)	-0.0005(4)
Cl1	0.02111(9)	0.01695(8)	0.02384(9)	-0.00122(7)	-0.00426(7)	-0.00201(7)
Cl2	0.02481(10)	0.02058(9)	0.02081(9)	0.00237(7)	-0.00149(7)	-0.00166(7)
Cu1	0.01806(5)	0.01641(5)	0.01824(5)	-0.00136(3)	-0.00382(4)	0.00267(3)

Table 6A.6 Geometric Parameters (Å, °)

C1—N1	1.4791(14)	C7—H7A	0.99
C1—C2	1.5122(19)	C7—H7B	0.99
C1—H1A	0.99	C8—N1	1.4901(15)
C1—H1B	0.99	C8—H8A	0.99
C2—N2	1.4913(15)	C8—H8B	0.99
C2—H2A	0.99	N1—Cu1	2.0061(9)
C2—H2B	0.99	N1—H1	0.858(14)
C3—N2	1.4781(16)	N2—Cu1	2.0145(9)
C3—C4	1.513(2)	N2—H2	0.876(14)
C3—H3A	0.99	N3—Cu1	2.0036(9)
C3—H3B	0.99	N3—H3	0.859(13)
C4—N3	1.4881(18)	N4—Cu1	2.0099(10)
C4—H4A	0.99	N4—H4	0.859(13)
C4—H4B	0.99	O1—Cl1	1.4644(7)
C5—N3	1.4826(15)	O1—Cu1	2.2664(7)
C5—C6	1.5118(19)	O2—Cl1	1.4320(8)
C5—H5A	0.99	O3—Cl1	1.4267(10)
C5—H5B	0.99	O4—Cl1	1.4321(9)
C6—N4	1.4898(15)	O5—Cl2	1.4459(9)
C6—H6A	0.99	O6—Cl2	1.4441(10)
C6—H6B	0.99	O7—Cl2	1.4285(9)
C7—N4	1.4835(16)	O8—Cl2	1.4409(9)
C7—C8	1.5174(17)		
N1—C1—C2	107.30(9)	C1—N1—C8	115.66(9)
N1—C1—H1A	110.3	C1—N1—Cu1	102.97(7)
C2—C1—H1A	110.3	C8—N1—Cu1	107.77(7)
N1—C1—H1B	110.3	C1—N1—H1	107.1(11)
C2—C1—H1B	110.3	C8—N1—H1	110.9(12)
H1A—C1—H1B	108.5	Cu1—N1—H1	112.2(11)
N2—C2—C1	109.06(9)	C3—N2—C2	114.31(10)
N2—C2—H2A	109.9	C3—N2—Cu1	103.55(7)

C1—C2—H2A	109.9	C2—N2—Cu1	107.38(7)
N2—C2—H2B	109.9	C3—N2—H2	111.3(12)
C1—C2—H2B	109.9	C2—N2—H2	109.4(12)
H2A—C2—H2B	108.3	Cu1—N2—H2	110.7(11)
N2—C3—C4	107.81(10)	C5—N3—C4	114.55(9)
N2—C3—H3A	110.1	C5—N3—Cu1	102.42(7)
C4—C3—H3A	110.1	C4—N3—Cu1	108.34(7)
N2—C3—H3B	110.1	C5—N3—H3	106.1(12)
C4—C3—H3B	110.1	C4—N3—H3	113.6(12)
H3A—C3—H3B	108.5	Cu1—N3—H3	111.3(12)
N3—C4—C3	109.92(9)	C7—N4—C6	114.37(9)
N3—C4—H4A	109.7	C7—N4—Cu1	102.84(7)
C3—C4—H4A	109.7	C6—N4—Cu1	107.10(8)
N3—C4—H4B	109.7	C7—N4—H4	110.1(12)
C3—C4—H4B	109.7	C6—N4—H4	110.2(12)
H4A—C4—H4B	108.2	Cu1—N4—H4	112.0(12)
N3—C5—C6	107.69(9)	Cl1—O1—Cu1	116.92(4)
N3—C5—H5A	110.2	O3—Cl1—O2	109.65(7)
C6—C5—H5A	110.2	O3—Cl1—O4	111.02(7)
N3—C5—H5B	110.2	O2—Cl1—O4	109.85(6)
C6—C5—H5B	110.2	O3—Cl1—O1	108.78(6)
H5A—C5—H5B	108.5	O2—Cl1—O1	109.36(5)
N4—C6—C5	109.55(9)	O4—Cl1—O1	108.14(5)
N4—C6—H6A	109.8	O7—Cl2—O8	109.87(7)
C5—C6—H6A	109.8	O7—Cl2—O6	109.78(7)
N4—C6—H6B	109.8	O8—Cl2—O6	109.12(6)
C5—C6—H6B	109.8	O7—Cl2—O5	109.49(6)
H6A—C6—H6B	108.2	O8—Cl2—O5	109.95(6)
N4—C7—C8	108.37(9)	O6—Cl2—O5	108.61(6)
N4—C7—H7A	110	N3—Cu1—N1	151.33(4)
C8—C7—H7A	110	N3—Cu1—N4	87.11(4)
N4—C7—H7B	110	N1—Cu1—N4	87.14(4)
C8—C7—H7B	110	N3—Cu1—N2	86.24(4)

H7A—C7—H7B	108.4	N1—Cu1—N2	86.52(4)
N1—C8—C7	109.56(9)	N4—Cu1—N2	153.54(4)
N1—C8—H8A	109.8	N3—Cu1—O1	104.87(3)
C7—C8—H8A	109.8	N1—Cu1—O1	103.78(3)
N1—C8—H8B	109.8	N4—Cu1—O1	103.79(3)
C7—C8—H8B	109.8	N2—Cu1—O1	102.66(3)
H8A—C8—H8B	108.2		
N1—C1—C2—N2	54.05(13)	C6—C5—N3—C4	-168.48(9)
N2—C3—C4—N3	50.52(13)	C6—C5—N3—Cu1	-51.42(9)
N3—C5—C6—N4	53.24(12)	C3—C4—N3—C5	89.53(11)
N4—C7—C8—N1	51.48(13)	C3—C4—N3—Cu1	-24.09(11)
C2—C1—N1—C8	-169.09(9)	C8—C7—N4—C6	-165.51(10)
C2—C1—N1—Cu1	-51.82(10)	C8—C7—N4—Cu1	-49.77(10)
C7—C8—N1—C1	89.34(12)	C5—C6—N4—C7	87.24(12)
C7—C8—N1—Cu1	-25.21(11)	C5—C6—N4—Cu1	-26.00(11)
C4—C3—N2—C2	-166.49(10)	Cu1—O1—Cl1—O3	-58.89(8)
C4—C3—N2—Cu1	-50.00(10)	Cu1—O1—Cl1—O2	60.85(7)
C1—C2—N2—C3	87.01(12)	Cu1—O1—Cl1—O4	-179.55(6)
C1—C2—N2—Cu1	-27.24(11)		

CHAPTER 7

CONCLUSIONS AND FUTURE WORK

7.1 Summary of Findings and Future Works

In 2017, the Papish group published a study in *Inorganic Chemistry* that highlighted three protic anticancer compounds (**1-3**) and influenced much of the research and findings that have been discussed in this dissertation.¹ These compounds were originally designed as anticancer agents capable of PACT driven toxicity. However, no direct correlation between an increase in photodissociation and toxicity was found leading to the conclusion that these complexes were ineffective PACT agents, despite their moderate toxicity (**3**: EC₅₀ Light = 4.1 μM in MDA-MB-231 breast cancer stem cells).¹⁻⁶ My work since this publication has focused on understanding which characteristics of these compounds have the highest impact on toxicity and using that information to design and synthesize more effective anticancer compounds capable of light-driven toxicity.

The work in Chapter 2 reported on the hydrophobicity (Log(D_{o/w})), mode of uptake, and subcellular localization of compounds **1-3**.⁷ The Log(D_{o/w}) was measured for **1-3** from pH 4.00 to 8.00 and it was found that the Log(D_{o/w}) (and thus hydrophobicity) of each compound increased with pH (Table 2.3). Overall, compound **3** was the most hydrophobic (and most toxic), which may lead to greater uptake by passive diffusion relative to **2** or **1**. ATP inhibition studies resulted in an increased concentration of **3** in MDA-MB-231 cell lines indicating an efflux mechanism that affects how much compound is found within the cells (Figure 2.8). Once within

the cell, complex **3** localized within the nucleus as seen by confocal microscopy (Figure 2.9) and the highest uptake of **3** appears to lead to the highest dark toxicity in MCF10A (healthy cells). However, the data does not suggest an explanation for why greater light activated toxicity is seen in certain cell lines (MDA-MB-231 and MCF7). Most likely, this relates to the inherent vulnerability of these cell lines to generated ROS rather than simply being correlated with uptake alone. Good uptake is required for toxicity, and this chapter explored the factors (passive diffusion and efflux) that influence uptake, but uptake alone is not sufficient for light driven toxicity. Research on this project was completed and published in *Journal of Inorganic Biochemistry* in early 2020 and future experiments will focus on conducting similar Log(D_{o/w}) and uptake studies on new compounds.

In chapter 3, I attempted to synthesize ruthenium PACT agents containing the potentially toxic and photolabile ligands 5-FU and 5-CNU.⁸⁻¹⁵ Attempted syntheses of a 5-FU containing complex were ultimately unsuccessful. Attempted synthesis of [(tpy)Ru(5-CNU)(6,6'-dhbp)]²⁺ (**6**) instead produced [(tpy)Ru(dhbp-CNU)]²⁺ (**7**), which arose from an intermolecular reaction with 6,6'-dhbp and 5-CNU to form a new tridentate ligand (Figure 3.9). Complex **7** was analyzed by XRD but the solved structure was not of publishable quality. This complex was never isolated in pure enough quality for screening in cancer cells; however, it may be possible to directly synthesize **7** by extending the duration of the reaction or by adding base to the reaction solution.

Chapter 4 sought to address the mode of toxicity for complexes **1-3**. Research conducted on complexes **2**^{OMe} and **3**^{OMe} by Dr. Qu showed that an increase in photodissociation did not yield an increase in toxicity.⁶ Similar complexes in the literature were capable of both photodissociation and producing singlet oxygen.^{2, 5, 16-20} Due to the short lifetime of ¹O₂, I studied singlet oxygen quantum yields (Φ_Δ) via indirect detection methods. The tested methods,

TEMP/EPR, UV-Vis/DPBF, and Fluorescence/SOSG, ultimately proved to be ineffective with this system due to possible side reactions or photobleaching of the selected probes. Thankfully, direct detection methods carried out by the McFarland group showed significant singlet oxygen production (highest observed: **2_B** Φ_{Δ} = 0.89) for all complexes that increased once the complexes were deprotonated. Conversely, complexes that exhibited higher relative photodissociation, produced less singlet oxygen and had lower toxicity.

With this information I studied a complex analogous to complex **3_A**, [(dop)₂Ru(4,4'-dhbp)]²⁺ (**8_A**) which was similar in structure to a non-toxic complex ([(phen)₂Ru(4,4'-dhbp)]²⁺ EC_{50 light} = \geq 100 μ M in MCF7) that had been studied in the 2017 *Inorganic Chemistry* study.¹ Complex **8_A** has little to no photodissociation when compared to complex **3_A** (Figure 4.12), most likely due to less steric strain near the metal center and less rotation within the dhbp ligand as observed in its crystal structure (Figure 4.10). In CD₃OD, **8_A** and **8_B** have Φ_{Δ} 's like that of the standard used, [Ru(bpy)₃](PF₆)₂. As a general trend, Φ_{Δ} in CD₃OD for complexes **1-3** are higher for their deprotonated **X_B** forms than for their fully protonated **X_A** form. In MeCN; however, **8** exhibited the opposite trend with **8_A** having a higher Φ_{Δ} than **8_B** (0.37 vs 0.09 respectively). Complex **8_A** had higher Φ_{Δ} 's than compounds **1_A-3_A** in acetonitrile; however, it is yet to be determined how **8_B** compares to **1_B-3_B** in MeCN.

Collaborative work from the Webster group and Dr. Qu found that **2_B** and **3_B** have relatively inaccessible ³MC states, favoring a PDT driven pathway (Chapter 4 appendix, Figures 4A.3 and 4A.5). This work was supported by luminescence emission studies of compound **2** (Figures 4.17-4.19). The λ_{\max} of for luminescence upon irradiation for **2_B** was red shifted from the λ_{\max} of **2_A** indicating a ³MLCT excited state that is lower in energy when compared to **2_A**.

This work partially contributed to a publication submitted to *Inorganic Chemistry* this year, but there is still more data to be collected. Future work is focusing on completing fluorescence measurements for complexes **1-3** as these were initially interrupted by COVID-19 related shutdowns. In order to make a through comparison between **1-3** and **8**, Φ_{Δ} measurements need to be completed for complexes **1B-3B** in acetonitrile.

Research to develop new compounds that utilize the insights from chapters 2-4 was discussed in Chapter 5. The ligands BPS and BPhen were chosen to study the effects of charge, hydrophobicity, and singlet oxygen production on toxicity.²¹⁻²⁶ [(BPS)₂Ru(6,6'-dhbp)]²⁻ (**9A**), [(BPhen)₂Ru(6,6'-dhbp)]²⁺ (**10A**), and [(BPhen)₂Ru(4,4'-dhbp)]²⁺ (**11A**) were synthesized for study. Complex **9A**, a negatively charged hydrophilic compound, was observed to undergo photodissociation upon irradiation with blue light (450 nm) (Figure 5.5). This may explain why the complex was non-toxic against a 5 μ M screen. Complexes **10A** and **11A**; however, showed the best toxicity to date for this system with EC₅₀ light values in the sub-micromolar range (Table 5.3) and PI values >1600. Research on these complexes is still ongoing, and data on hydrophobicity, photodissociation, and singlet oxygen production will be the focus of future research. These complexes have proven to be better performers than complexes **1-3** discussed in previous chapters. The data gathered on these complexes will prove useful in developing even more toxic and light selective complexes.

Lastly, chapter 6 focused on the crystal structure of [Cu(ClO₄)(cyclen)](ClO₄). Copper cyclen complexes are known to perform catalytic DNA cleavage and peptide hydrolysis.²⁷⁻²⁹ Similar crystal structures are reported in the literature but this was the first reported instance of a [Cu(cyclen)] structure isolated with perchlorate counterions. The Cu(II) ion exhibits a square-pyramidal geometry and is coordinated by the four N atoms of the neutral 1,4,7,10-

tetraazacyclododecane (cyclen) ligand and an O atom from one perchlorate anion, with the second perchlorate ion hydrogen-bonded to one of the amine N atoms of the cyclen ligand. This work was published in *Acta Crystallography* in 2017.³⁰

7.2 Closing Remarks

In closing, the work reported in this dissertation has contributed to significant findings in the field of ruthenium anticancer research. While initial compounds were designed as PACT agents, studies show that they are in fact effective PDT agents capable of significant Φ_{Δ} when deprotonated. When protonated (\mathbf{X}_A) or with increased steric bulk near the metal center, the complexes have higher rates of photodissociation allowing for significant tuning of favorability for PACT and/or PDT pathways. The significance of hydrophobicity on toxicity, uptake, was investigated and found that compounds **1-3** are capable of subcellular localization in the nucleus. This information has led to the development of new complexes (**10** and **11**) that are capable of significant light activated toxicity. By only exhibiting toxicity upon irradiation, these complexes can reduce off target toxicity and potentially limiting some of the more severe side-effects associated with many chemotherapy agents.

References

- [1] Qu, F., Park, S., Martinez, K., Gray, J. L., Thowfeik, F. S., Lundeen, J. A., Kuhn, A. E., Charboneau, D. J., Gerlach, D. L., Lockart, M. M., Law, J. A., Jernigan, K. L., Chambers, N., Zeller, M., Piro, N. A., Kassel, W. S., Schmehl, R. H., Paul, J. J., Merino, E. J., Kim, Y., and Papish, E. T. (2017) Ruthenium Complexes are pH-Activated Metallo Prodrugs (pHAMPs) with Light-Triggered Selective Toxicity Toward Cancer Cells, *Inorg. Chem.* *56*, 7519-7532.
- [2] Knoll, J. D., Albani, B. A., and Turro, C. (2015) New Ru(II) Complexes for Dual Photoreactivity: Ligand Exchange and $^{1}O_2$ Generation, *Acc. Chem. Res.* *48*, 2280-2287.
- [3] Knoll, J. D., Albani, B. A., and Turro, C. (2015) Excited state investigation of a new Ru(II) complex for dual reactivity with low energy light, *Chem. Commun. (Cambridge, U. K.)* *51*, 8777-8780.
- [4] White, J. K., Schmehl, R. H., and Turro, C. (2017) An overview of photosubstitution reactions of Ru(II) imine complexes and their application in photobiology and photodynamic therapy, *Inorg. Chim. Acta* *454*, 7-20.
- [5] Toupin, N. P., Nadella, S., Steinke, S. J., Turro, C., and Kodanko, J. J. (2020) Dual-Action Ru(II) Complexes with Bulky π -Expansive Ligands: Phototoxicity without DNA Intercalation, *Inorg. Chem.* *59*, 3919-3933.
- [6] Qu, F., Martinez, K., Arcidiacono, A. M., Park, S., Zeller, M., Schmehl, R. H., Paul, J. J., Kim, Y., and Papish, E. T. (2018) Sterically demanding methoxy and methyl groups in ruthenium complexes lead to enhanced quantum yields for blue light triggered photodissociation, *Dalton Trans.* *47*, 15685-15693.
- [7] Park, S., Gray, J. L., Altman, S. D., Hairston, A. R., Beswick, B. T., Kim, Y., and Papish, E. T. (2020) Cellular uptake of protic ruthenium complexes is influenced by pH dependent passive diffusion and energy dependent efflux, *J. Inorg. Biochem.* *203*, 110922.
- [8] Peters, G. J., Backus, H. H. J., Freemantle, S., van Triest, B., Codacci-Pisanelli, G., van der Wilt, C. L., Smid, K., Lunec, J., Calvert, A. H., Marsh, S., McLeod, H. L., Bloemena, E., Meijer, S., Jansen, G., van Groeningen, C. J., and Pinedo, H. M. (2002) Induction of thymidylate synthase as a 5-fluorouracil resistance mechanism, *Biochim. Biophys. Acta, Mol. Basis Dis.* *1587*, 194-205.

- [9] Garner, R. N., Gallucci, J. C., Dunbar, K. R., and Turro, C. (2011) [Ru(bpy)₂(5-cyanouracil)₂]²⁺ as a Potential Light-Activated Dual-Action Therapeutic Agent, *Inorg. Chem.* *50*, 9213-9215.
- [10] Shobana, S., Dharmaraja, J., and Selvaraj, S. (2013) Mixed ligand complexation of some transition metal ions in solution and solid state: spectral characterization, antimicrobial, antioxidant, DNA cleavage activities and molecular modeling, *Spectrochim. Acta A. Mol. Biomol. Spectrosc.* *107*, 117-132.
- [11] Ellipilli, S., Palvai, S., and Ganesh, K. N. (2016) Fluorinated peptide nucleic acids with fluoroacetyl side chain bearing 5-(F/CF₃)-uracil: Synthesis and cell uptake studies, *J. Org. Chem.* *81*, 6364-6373.
- [12] Gonchar, M. R., Matnurov, E. M., Burdina, T. A., Zava, O., Ridel, T., Milaeva, E. R., Dyson, P. J., and Nazarov, A. A. (2020) Ruthenium(II)-arene and triruthenium-carbonyl cluster complexes with new water-soluble phosphites based on glucose: Synthesis, characterization and antiproliferative activity, *J. Organomet. Chem.* *919*, 121312.
- [13] Marelis, D. C., Bhagan, S., Charboneau, D. J., Schroeder, K. M., Kamdar, J. M., McGettigan, A. R., Freeman, B. J., Moore, C. E., Rheingold, A. L., Cooksy, A. L., Smith, D. K., Paul, J. J., Papish, E. T., and Grotjahn, D. B. (2014) How Do Proximal Hydroxy or Methoxy Groups on the Bidentate Ligand Affect [(2,2';6',2''-Terpyridine)Ru(N,N)X] Water-Oxidation Catalysts? Synthesis, Characterization, and Reactivity at Acidic and Near-Neutral pH, *Eur. J. Inorg. Chem.* *2014*, 676-689.
- [14] Carrington, S. J., Chakraborty, I., Bernard, J. M. L., and Mascharak, P. K. (2016) A Theranostic Two-Tone Luminescent PhotoCORM Derived from Re(I) and (2-Pyridyl)-benzothiazole: Trackable CO Delivery to Malignant Cells, *Inorg. Chem.* *55*, 7852-7858.
- [15] Albani, B. A., Durr, C. B., and Turro, C. (2013) Selective Photoinduced Ligand Exchange in a New Tris-Heteroleptic Ru(II) Complex, *J. Phys. Chem. A* *117*, 13885-13892.
- [16] Loftus, L. M., White, J. K., Albani, B. A., Kohler, L., Kodanko, J. J., Thummel, R. P., Dunbar, K. R., and Turro, C. (2016) New RuII Complex for Dual Activity: Photoinduced Ligand Release and ¹O₂ Production, *Chem. - Eur. J.* *22*, 3704-3708.
- [17] Shi, G., Monroe, S., Hennigar, R., Colpitts, J., Fong, J., Kasimova, K., Yin, H., DeCoste, R., Spencer, C., Chamberlain, L., Mandel, A., Lilge, L., and McFarland, S. A. (2015) Ru(II) dyads derived from α-oligothiophenes: A new class of potent and versatile photosensitizers for PDT, *Coord. Chem. Rev.* *282-283*, 127-138.
- [18] Sainuddin, T., McCain, J., Pinto, M., Yin, H., Gibson, J., Hetu, M., and McFarland, S. A. (2016) Organometallic Ru(II) Photosensitizers Derived from π-Expansive Cyclometalating Ligands: Surprising Theranostic PDT Effects, *Inorg. Chem.* *55*, 83-95.

- [19] Ghosh, G., Colon, K. L., Fuller, A., Sainuddin, T., Bradner, E., McCain, J., Monroe, S. M. A., Yin, H., Hetu, M. W., Cameron, C. G., and McFarland, S. A. (2018) Cyclometalated Ruthenium(II) Complexes Derived from α -Oligothiophenes as Highly Selective Cytotoxic or Photocytotoxic Agents, *Inorg. Chem.* *57*, 7694-7712.
- [20] Monroe, S., Colon, K. L., Yin, H., Roque, J., Konda, P., Gujar, S., Thummel, R. P., Lilge, L., Cameron, C. G., and McFarland, S. A. (2019) Transition Metal Complexes and Photodynamic Therapy from a Tumor-Centered Approach: Challenges, Opportunities, and Highlights from the Development of TLD1433, *Chem. Rev. (Washington, DC, U. S.)* *119*, 797-828.
- [21] Dickerson, M., Sun, Y., Howerton, B., and Glazer, E. C. (2014) Modifying Charge and Hydrophilicity of Simple Ru(II) Polypyridyl Complexes Radically Alters Biological Activities: Old Complexes, Surprising New Tricks, *Inorg. Chem.* *53*, 10370-10377.
- [22] Babak, M. V., Le Faouder, P., Trivelli, X., Venkatesan, G., Bezzubov, S. I., Kadjout, M., Gushchin, A. L., Hanif, M., Poizat, O., Vezin, H., and Rolando, C. (2020) Heteroleptic Ruthenium(II) Complexes with Bathophenanthroline and Bathophenanthroline Disulfonate Disodium Salt as Fluorescent Dyes for In-Gel Protein Staining, *Inorg. Chem.* *59*, 4527-4535.
- [23] Rabilloud, T., Strub, J.-M., Luche, S., Van Dorselaer, A., and Lunardi, J. (2001) A comparison between sypro ruby and ruthenium II tris (batho-phenanthroline disulfonate) as fluorescent stains for protein detection in gels, *Proteomics* *1*, 699-704.
- [24] Della Ciana, L., Zanarini, S., Perciaccante, R., Marzocchi, E., and Valenti, G. (2010) Neutral and Dianionic Ru(II) Bathophenanthroline disulfonate Complexes: A Route To Enhance Electrochemiluminescence Performance in Aqueous Media, *J. Phys. Chem. C* *114*, 3653-3658.
- [25] Karges, J., Blacque, O., Jakubaszek, M., Goud, B., Goldner, P., and Gasser, G. (2019) Systematic investigation of the antiproliferative activity of a series of ruthenium terpyridine complexes, *J. Inorg. Biochem.* *198*, 110752.
- [26] Munteanu, A.-C., Notaro, A., Jakubaszek, M., Cowell, J., Tharaud, M., Goud, B., Uivarosi, V., and Gasser, G. (2020) Synthesis, Characterization, Cytotoxic Activity, and Metabolic Studies of Ruthenium(II) Polypyridyl Complexes Containing Flavonoid Ligands, *Inorg. Chem.* *59*, 4424-4434.
- [27] Zhang, X., Liu, X., Phillips, D. L., and Zhao, C. (2016) Mechanistic Insights Into the Factors That Influence the DNA Nuclease Activity of Mononuclear Facial Copper Complexes Containing Hetero-Substituted Cyclens, *ACS Catal.* *6*, 248-257.
- [28] Li, S., Chen, J.-X., Xiang, Q.-X., Zhang, L.-Q., Zhou, C.-H., Xie, J.-Q., Yu, L., and Li, F.-Z. (2014) The synthesis and activities of novel mononuclear or dinuclear cyclen complexes

- bearing azole pendants as antibacterial and antifungal agents, *Eur. J. Med. Chem.* **84**, 677-686.
- [29] Hormann, J., Perera, C., Deibel, N., Lentz, D., Sarkar, B., and Kulak, N. (2013) Straightforward approach to efficient oxidative DNA cleaving agents based on Cu(II) complexes of heterosubstituted cyclens, *Dalton Trans.* **42**, 4357-4360.
- [30] Gray, J. L., Gerlach, D. L., and Papish, E. T. (2017) Crystal structure of (perchlorato- κ O)(1,4,7,10-tetraazacyclododecane- κ 4N)copper(II) perchlorate, *Acta Crystallogr., Sect. E: Crystallogr. Commun.* **73**, 31-34.